

Yttrium bismuth titanate pyrochlore mixed oxides for photocatalytic hydrogen production

Von der Naturwissenschaftlichen Fakultät
der Gottfried Wilhelm Leibniz Universität Hannover
zur Erlangung des Grades

Doktor der Naturwissenschaften

- Dr. rer. nat. -

genehmigte Dissertation

von

Dipl.-Chem. Oliver Merka

geboren am 01.03.1983 in Alfeld (Leine)

2012

Referent: Prof. Dr. Michael Wark

Koreferent: Prof. Dr. Detlef W. Bahnemann

Tag der Promotion: 18.10.2012

Für meine Eltern

Erklärung

Hiermit erkläre ich, dass ich die vorliegende Dissertation „**Yttrium bismuth titanate pyrochlore mixed oxides for photocatalytic hydrogen production**“ als Mitarbeiter des Instituts für Physikalische Chemie und Elektrochemie der Gottfried Wilhelm Leibniz Universität Hannover selbstständig verfasst und alle benutzten Hilfsmittel sowie evtl. zur Hilfeleistung herangezogene Institutionen vollständig angegeben habe.

Die Dissertation wurde nicht schon als Diplom- oder ähnliche Prüfungsarbeit verwendet.

Hannover, den 26.07.2012

Dipl.-Chem. Oliver Merka

Danksagung

An dieser Stelle möchte ich mich bei allen bedanken, die mich auf diesem Weg begleitet haben und zum Gelingen dieser Arbeit beigetragen haben.

Zuerst möchte ich mich bei Prof. Dr. Michael Wark für die hervorragende Betreuung meiner Doktorarbeit in den vergangenen dreieinhalb Jahren bedanken. Insbesondere danke ich für die Möglichkeit, die Entwicklung meiner Konzepte selbstständig zu gestalten, während die Arbeit zu gegebener Zeit durch viele kritische Diskussionen wie auch gezielte Motivation fokussiert wurde.

Weiterhin bedanke ich mich bei Prof. Dr. Detlef W. Bahnemann für die zahlreichen fachlichen Diskussionen und die Übernahme des Koreferats.

Ich danke Prof. Dr. Jürgen Caro für die Möglichkeit, in seinem Arbeitskreis zu promovieren, für seine Diskussionsbereitschaft sowie für die Übernahme des Drittprüferamtes.

Ich bedanke mich bei Prof. Dr. Thomas Bredow für eine interessante Woche der Einarbeitung in Crystal09 an der Universität Bonn. Weiterhin möchte ich mich bei Dr. Dirk Hollmann vom LIKAT in Rostock für die Charakterisierung meiner Proben mittels Raman Spektroskopie und Elektronenspinresonanz danken. Ich bedanke mich bei Prof. Dr. Armin Feldhoff für die Hilfestellung sowohl in der Elektronenmikroskopie als auch in der Röntgendiffraktometrie. Meiner Projektpartnerin Olga Raisch aus der Technischen Chemie danke ich für zahlreiche Diskussionen und die gute Zusammenarbeit. Mein Dank geht auch an Ann-Christin Möller für die Mitarbeit an dieser Dissertation während ihrer Diplomarbeit.

Besonders möchte ich mich bei Dr. Viktor Yarovyi, Frank Steinbach, Dr. Monir Sharifi, Dr. Konstantin Efimov, Tobias Klande und Olga Ravkina für die Präparation und Messung der Proben am TEM, für die kompetente Hilfestellung am REM, für die Durchführung der Stickstoffadsorptionsmessungen und für die interessanten Gespräche in Labor und Büro bedanken. Mein Dank gilt auch Kerstin Janze für die schnelle Beschaffung von Laborgeräten und Chemikalien. Ich möchte Yvonne Gabbey-Uebe für ihr Engagement bei der Lösung bürokratischer Probleme danken. Den Mitarbeitern der

Elektronikwerkstatt und der Feinmechanik danke ich für die zahlreichen Spezialanfertigungen.

Ich danke Dr. Britta Seelandt, Dr. Jana Panke, Dr. Florian Bittner und Christian Dunkel für die gemeinsame Zeit in den Nebenfachpraktika. Weiterhin möchte ich allen weiteren Mitarbeitern des Instituts für Physikalische Chemie und Elektrochemie für ihre Hilfsbereitschaft und die gute Zusammenarbeit danken.

Für die finanzielle Unterstützung danke ich der Deutschen Forschungsgemeinschaft (DFG).

Ich möchte mich bei meinen Freunden und bei meiner Familie bedanken, insbesondere bei meinen Eltern, die mir während des Studiums und während der Promotion ein bedingungsloser Rückhalt waren. Ich danke meiner Freundin Stefanie, die mich stets motiviert und unterstützt hat.

Kurzzusammenfassung

Die Wasserstoffproduktion durch Photokatalyse stellt eine von wenigen Schlüsseltechnologien für umweltfreundliche Energiegewinnung dar. Es werden hochaktive Photokatalysatoren gesucht, die speziell auf die Anforderungen des anspruchsvollen Prozesses der Wasserstoffentwicklung zugeschnitten sind. Diese Katalysatoren sollten nicht nur durch den UV Bereich, sondern auch durch den sichtbaren Teil des Sonnenspektrums aktivierbar sein. Auch die Langzeitstabilität gegenüber Fotokorrosion und chemischer Zersetzung im wässrigen Medium müssen gewährleistet sein. Obwohl Materialien, die in der $A_2B_2O_6$ Pyrochlorstruktur kristallisieren, häufig in weniger anspruchsvollen photokatalytischen Abbaureaktionen verwendet werden, kamen sie in der Wasserstoffproduktion bislang nur selten zum Einsatz.

Diese Arbeit berichtet über die Sol-Gel Synthese von neuen nicht-stöchiometrischen Pyrochlor Titanaten und über ihre Anwendung in der photokatalytischen Wasserstoffproduktion. Die Aktivierbarkeit im sichtbaren Bereich des Lichts wird zum einen durch den Einbau von Bismut-Ionen auf dem A-Gitterplatz und zum anderen durch die Dotierung des B-Gitterplatzes mit Übergangsmetallkationen erreicht, die über partiell gefüllte d-Orbitale verfügen.

Die Arbeit fokussiert sich auf den Zusammenhang zwischen der photokatalytischen Aktivität und Verschiebungen im Kristallgitter, die durch systematische Stöchiometrieänderungen im Pyrochlor induziert werden.

Die Photokatalysatoren wurden sowohl auf ihre optischen als auch strukturellen Eigenschaften untersucht. Es zeigte sich, dass weitreichende Stöchiometrieänderungen durch die Pyrochlorstruktur toleriert werden. Stöchiometrieänderungen in A_2O_3 -reichen Zusammensetzungen werden durch Kationenaustausch kompensiert, wenn kleinere Y^{3+} Kationen die A-Position besetzen. Es bildet sich eine Nebenphase, wenn größere Bismut-Ionen die A-Position einnehmen. Bei TiO_2 -reichen nicht-stöchiometrischen Zusammensetzungen bilden sich Vakanzen auf den A- und/oder O-Gitterplätzen.

Es wird gezeigt, dass Pyrochlor Oxide im Yttrium-Bismut-Titan-System hochaktive Photokatalysatoren darstellen, wenn sie zuvor präzise optimiert wurden. Eine Erhöhung des TiO_2 -Überschusses führt zu einer deutlichen Erhöhung der Aktivität sowohl bei $Y_2Ti_2O_7$ als auch $Bi_2Ti_2O_7$, aber die Gründe dafür sind grundverschieden. Ein steigender TiO_2 -Überschuss in $Bi_2Ti_2O_7$ beeinflusst das Sauerstoffanionengitter und optimiert die TiO_6 Oktaedergeometrie, während er im $Y_2Ti_2O_7$ zu einer Reinigung des TiO_6 Oktaedernetzwerkes von Y^{3+} -Ionen führt. Letzteres wird durch Versuche bestätigt, in denen eine Dotierung der Titan-Position mit Cr^{3+} , Mn^{3+} und Fe^{3+} nicht zu der erhofften Aktivitätssteigerung durch verbesserte Absorptionseigenschaften führte, sondern zu einer deutlichen Abnahme eben dieser.

Während $Y_2Ti_2O_7$ stabile Wasserstoffproduktionsraten liefert, verringerten sich die an $YBi_2Ti_2O_7$ und $Bi_2Ti_2O_7$ gemessenen Aktivitäten mit der Zeit, da sie instabil unter Bestrahlung waren. Dieser Nachteil wurde durch Abscheiden eines Co-Katalysatorsystems, bestehend aus einem Edelmetallkern und einer Cr_2O_3 -Schale, kompensiert.

SCHLAGWÖRTER: Wasserstoffproduktion, Photokatalyse, Pyrochlor

Abstract

Photocatalytic hydrogen production is supposed to be one of the future key technologies for environmental friendly energy generation. The development of highly active photocatalytic materials is under investigation, which are developed to specifically meet the requirements of the challenging process of hydrogen production. Moreover, the photocatalysts should not only be excitable by UV irradiation, but also by the visible part of the solar spectrum and have to provide long term stability against photodegradation as well as chemical degradation in aqueous media. Materials crystallizing in the pyrochlore structure type of $A_2B_2O_6O'$ are frequently used in less demanding photocatalytic degradation reactions, but so far almost ignored for application in photocatalytic hydrogen production.

In this work, the sol-gel synthesis of new non-stoichiometric pyrochlore titanates and their application in photocatalytic hydrogen production is reported. Visible light response is achieved by introducing bismuth on the A site or by doping the B site by transition metal cations featuring partially filled d orbitals.

This work clearly focusses on atomic scale structural changes induced by the systematical introduction of non-stoichiometry in pyrochlore mixed oxides and the resulting influence on the activity in photocatalytic hydrogen production.

The materials were characterized in detail regarding their optical properties and their atomic structure. The pyrochlore structure tolerates tremendous stoichiometry variations. The non-stoichiometry in A_2O_3 rich compositions is compensated by distortions in the cationic sub-lattice for the smaller Y^{3+} cation and by evolution of a secondary phase for the larger Bi^{3+} cation on the A site. For TiO_2 rich compositions, the non-stoichiometry leads to a special vacancy formation in the A and optionally O' sites.

It is shown that pyrochlore mixed oxides in the yttrium bismuth titanate system represent very active and promising materials for photocatalytic hydrogen production, if precisely and carefully tuned. The increase of the TiO_2 excess leads to greatly improved photocatalytic activities for non-stoichiometric $Y_2Ti_2O_7$ and $Bi_2Ti_2O_7$, but the reasons are completely different. The TiO_2 rich non-stoichiometry leads to a special vacancy generation in $Bi_2Ti_2O_7$ re-arranging the oxygen sub-lattice and optimizing the TiO_6 octahedral geometry. For $Y_2Ti_2O_7$, the purification of the TiO_6 octahedral network induced by non-stoichiometry is important. This thesis is corroborated by the finding that doping the titanium position with Cr^{3+} , Mn^{3+} or Fe^{3+} does not lead to the desired effect of higher activities due to improved absorption properties, but to a decrease of activity due to a contamination of the TiO_6 octahedral network.

Whereas $Y_2Ti_2O_7$ yields stable hydrogen production rates over time, the bismuth richer compounds of $YBiTi_2O_7$ and $Bi_2Ti_2O_7$ are found to be not stable under irradiation. This drawback is overcome by applying a special co-catalyst system consisting of a precious metal core and a Cr_2O_3 shell on the photocatalysts.

KEYWORDS: hydrogen production, photocatalysis, pyrochlore

Table of Contents

1	INTRODUCTION	1
2	FUNDAMENTALS	7
2.1	Band theory	7
2.2	Photocatalysis	10
2.2.1	Process of photocatalysis	10
2.2.2	Inhibiting charge carrier recombination	13
2.3	The cubic pyrochlore structure	14
2.4	Band gap engineering	18
2.5	Reactor design and reaction settings	25
2.6	Photocatalyst evaluation	27
2.6.1	Photonic efficiency ^[101]	27
2.6.2	The process of photocurrent-doubling	29
3	EXPERIMENTAL	31
3.1	Analytical methods	31
3.1.1	Nitrogen adsorption using the BET model	31
3.1.2	Diffuse UV-vis spectroscopy	32
3.1.3	X-ray diffraction (XRD)	33
3.1.4	Rietveld refinement method	33
3.2	Photocatalysis setup	36
3.2.1	Photocatalytic hydrogen production using blank co-catalysts	38
3.2.2	Photocatalysis using Cr ₂ O ₃ -shelled co-catalysts	38
3.2.3	Potassium ferrioxalate actinometry	39
3.3	Preparation of mixed oxides	40
3.3.1	Importance of precursor solutions for the sol-gel synthesis	40
3.3.2	Preparation of Y ₂ Ti ₂ O ₇ with different Ti/Y ratios (Y _{2-x} Ti ₂ O _{7-1.5x})	41
3.3.3	Preparation of Y _{1.5} Bi _{0.5} Ti ₂ O ₇ with different Ti/(Y+Bi) ratios ((Y _{1.5} Bi _{0.5}) _{1-x} Ti ₂ O _{7-3x})	42

3.3.4	Preparation of YBiTi_2O_7 with different Ti/(Y+Bi) ratios ($(\text{YBi})_{1-x}\text{Ti}_2\text{O}_{7-3x}$)	43
3.3.5	Preparation of bismuth titanates with different Ti/Bi ratios ($\text{Bi}_{2-x}\text{Ti}_{0.75x}$) Ti_2O_7 , $\text{Bi}_4\text{Ti}_3\text{O}_{12}$ and $\text{Bi}_2\text{Ti}_4\text{O}_{11}$	45
3.3.6	Preparation of $\text{Y}_{1.86}\text{Ti}_2\text{O}_{6.80}$ doped with Cr^{3+} , Mn^{3+} , Fe^{3+}	46
3.3.7	Preparation of $\text{Y}_{1.86}\text{Ti}_{1.6}\text{Ta}_{0.4}\text{O}_7$ and $\text{Y}_{1.86}\text{Ti}_{1.8}\text{W}_{0.2}\text{O}_7$	47
3.3.8	Preparation of $\text{Y}_2\text{Ta}_2\text{O}_5\text{N}_2$ via the pre-stage of M^-YTaO_4	48
4	RESULTS AND DISCUSSION	51
4.1	Non-stoichiometric $\text{Y}_2\text{Ti}_2\text{O}_7$	51
4.1.1	Characterization of non-stoichiometric $\text{Y}_2\text{Ti}_2\text{O}_7$	51
4.1.2	Photocatalytic hydrogen production with $\text{Y}_{2-x}\text{Ti}_2\text{O}_{7-1.5x}$	60
4.1.3	Structure related photocatalysis in $\text{Y}_{2-x}\text{Ti}_2\text{O}_{7-1.5x}$	64
4.1.4	Optimum co-catalyst loading and stability of $\text{Y}_{1.867}\text{Ti}_2\text{O}_{6.80}$	68
4.2	Non-stoichiometric $\text{Y}_{1.5}\text{Bi}_{0.5}\text{Ti}_2\text{O}_7$ and YBiTi_2O_7	70
4.2.1	Characterization of non-stoichiometric yttrium bismuth titanates	70
4.2.2	Photocatalytic hydrogen production with $(\text{Y}_{1.5}\text{Bi}_{0.5})_{1-x}\text{Ti}_2\text{O}_{7-3x}$	80
4.2.3	Photocatalytic hydrogen production with $(\text{YBi})_{1-x}\text{Ti}_2\text{O}_{7-3x}$	82
4.2.4	Optimum co-catalyst loading and stability of non-stoichiometric yttrium bismuth titanates	84
4.2.5	Photonic efficiencies of non-stoichiometric yttrium bismuth titanates	87
4.3	Non-stoichiometric $\text{Bi}_2\text{Ti}_2\text{O}_7$ and other bismuth titanates	90
4.3.1	Characterization of non-stoichiometric bismuth titanate	90
4.3.2	The vacancy structure in non-stoichiometric “ $\text{Bi}_2\text{Ti}_2\text{O}_7$ ”	95
4.3.3	Photocatalytic hydrogen production	100
4.3.4	Structure-photocatalysis relation	103
4.3.5	Pt/ Cr_2O_3 core-shell co-catalyst	107
4.4	Ti-site doping in structure-optimized $\text{Y}_{1.867}\text{Ti}_2\text{O}_{6.80}$	110
4.4.1	B-site doping of $\text{Y}_{1.867}\text{Ti}_2\text{O}_{6.80}$ with Cr^{3+} , Mn^{3+} and Fe^{3+}	110
4.4.2	Optimum dopant level in Cr^{3+} doped $\text{Y}_{1.867}\text{Ti}_2\text{O}_{6.80}$	117
4.4.3	B-site doping of $\text{Y}_{1.867}\text{Ti}_2\text{O}_{6.80}$ with Ta^{5+} and W^{6+}	121
4.5	Nitrogen doped $\text{Y}_2\text{Ta}_2\text{O}_5\text{N}_2$	129
5	CONCLUSION AND OUTLOOK	133
6	REFERENCES	139

7	APPENDIX	147
7.1	Additional information	147
7.1.1	Additional Figures	147
7.1.2	Additional Tables	158
7.2	Abbreviations and symbols	165
7.3	Table of Figures	167
7.4	Tables	175
7.5	Scientific publications	178
7.5.1	Journal publications	178
7.5.2	Talks on conferences	179
7.5.3	Posters on conferences	179
7.6	Curriculum vitae	181

1 Introduction

As the world population and the degree of industrialization are growing steadily, the demand for energy is growing concomitantly.^[1] This leads to the predicted depletion of fossil fuels in the foreseeable future.^[2] Thus, the time is short to research new technologies for renewable energy generation.^[3] Moreover, renewable energy sources provide the advantage of being neutral in terms of CO₂ balance per definition. Besides the sources of wind energy^[4] and geothermal energy^[5], especially solar light is supposed to be the energy source of the future.^[6, 7] The two main areas of solar energy utilization are the “direct” energy conversion by photovoltaics, i. e., solar cells, and the “indirect” energy conversion by photocatalysis.^[8] In terms of energy conversion efficiency, the photovoltaics gathered a significant advance, as solar cells do already provide efficiencies of about 40 % (multijunction GaAs), 25 % (monocrystalline silicon) and 20 % (multicrystalline silicon)^[9]. The process of photocatalysis is applicable in many areas of subject. Especially in the field of pollutant degradation^[10-12], in which organic compounds are ideally decomposed completely into carbon dioxide and water^[13, 14], photocatalysis plays an important role and a plentitude of commercial products are already available. However, also energy conversion can be obtained by means of photocatalysis. In a photocatalytic reaction, an electron-hole pair (exciton) is generated by irradiating a semi-conductor with a photon of suitable energy. The electron and the hole located at the edges of the conduction band and the valence band, respectively, are involved in a redox reaction with adsorbed species. If the reduction potential of electrons is suitable for reducing protons to molecular hydrogen and the oxidation potential of holes is sufficient to form molecular oxygen from water, this process is called *overall water splitting* and states a pure form of clean energy conversion.^[15] This artificial photosynthesis, which is difficult to accomplish and often referred to as the “holy grail” in chemistry^[16], is a thermodynamically uphill-reaction ($\Delta G_R = +237.2 \text{ kJ/mol}$).^[17, 18] The process of *overall water splitting* facilitates the two individual steps of photovoltaics and water electrolysis in a single reaction step. In the photocatalytic hydrogen production organic substances like methanol are utilized as sacrificial reagents. Although this process consumes fossil fuels as well, it is much more environmental friendly than the process of steam reforming, as hydrogen generation from methanol or methane is still an “uphill reaction”, which is compensated by the energy of irradiated photons in

photocatalysis, but by temperature and pressure of about 500 K and 30 bar, respectively, in steam reforming.^[19]

The goal of this work is to prove the suitability of materials crystallizing in the pyrochlore structure $A_2B_2O_6O'$ for the purpose of photocatalytic energy conversion. Materials should be developed, which are active in photocatalytic hydrogen production utilizing methanol as sacrificial reagent under UV and visible light irradiation. An additional activity in *overall water splitting* is desired, but not mandatory. Thus, photocatalysts are developed to specifically meet the requirements of the challenging process of photocatalytic hydrogen production, in which the potentials of electrons and holes are of importance.^[20] Less demanding degradation reactions, in which oxygen acts as electron scavenger^[21], were not considered.

The pyrochlore structure type is so far almost ignored in terms of photocatalysis. Abe et al.^[22] investigated overall water splitting over mixed oxides of R_3MO_7 and $R_2Ti_2O_7$ ($R = Y, Gd, La$, $M = Nb, Ta$). Surprisingly, the pyrochlore $Y_2Ti_2O_7$ yielded the highest activity, which was even superior to the $La_2Ti_2O_7$ perovskite. However, further work on pyrochlores was rather disappointing, as pyrochlores of R_3MO_7 and $Bi_2(In, Al, Ga)NbO_7$ ^[23] were almost inactive, which was attributed to the disadvantageous occupation of the B site by two different cations. Thus, the chemical compositions of pyrochlores prepared in this work were chosen to involve only a single cation species on the B site. As a single work is only expected to scratch the surface of capability, pyrochlore $Y_2Ti_2O_7$ was chosen as the starting point and developed specifically. In the Y_2O_3 - TiO_2 system, Mizutani et al.^[24] reported about a small stability range for non-stoichiometric cubic pyrochlores of $Y_2Ti_2O_7$ below 1723 K and a phase transition into a cubic defect fluorite solid solution of $Y_xTi_{1-x}O_{2-x/2}$ (with x ranging from 0.62 to 0.80) at higher temperatures. In this work, the influence of stoichiometry changes on the structure of $Y_2Ti_2O_7$ is examined focusing on TiO_2 rich compositions of $Y_{2-x}Ti_2O_{7-1.5x}$ with A, O' site vacancies, but also including the analysis of the transition from the pyrochlore into the defect fluorite structure leading to stuffed pyrochlores of $Y_2(Ti_{2-x}Y_x)O_{7-0.5x}$.

Pyrochlore $Y_2Ti_2O_7$ suffers from the disadvantage of being a wide band gap semiconductor ($E_{bg} = 3.6$ eV).^[22] To develop pyrochlore materials providing the capability of absorbing in the visible light region of the solar spectrum, three concepts are applied.

First, the yttrium position in $Y_2Ti_2O_7$ is subsequently substituted by bismuth. The shift of the absorption edge towards the visible is supposed to correlate with the degree of

bismuth substitution. As the decrease of the band gap energy by bismuth insertion is achieved by raising the valence band top, the reduction potential of photogenerated electrons should be not affected. Moreover, it should be examined, if the bismuth content in the structure influences the stability range of non-stoichiometric $Y_{1.5}Bi_{0.5}Ti_2O_7$ and $YBiTi_2O_7$, and thus, the photocatalytic activity. The stability range of the pyrochlore phase in the ternary Bi_2O_3 - Y_2O_3 - TiO_2 system was investigated by Knop and Brisse^[25]. Pure pyrochlore phases of $(Y_{1-x}Bi_x)_2Ti_2O_7$ were obtained up to $x = 0.75$, at higher bismuth content a non-identified by-phase was observed. Kunej and Suvorov reported that bismuth insertion has to be accomplished by vacancy generation in the A,O` sites leading to $(Bi_{1.6-0.8x})Y_xTi_2O_{6.4+0.3x}$ with $0.03 < x < 2$.^[26] As this vacancy generation is supposed to extend the stability range of TiO_2 rich non-stoichiometric compositions, the stability range of non-stoichiometric pyrochlores in the Bi_2O_3 - Y_2O_3 - TiO_2 system is investigated herein. Compared to yttrium containing titanate pyrochlores, the literature regarding bismuth titanates is rather contradictory, although the Aurivillius phase of $Bi_4Ti_3O_{12}$ ^[27] and two monoclinic phases of $Bi_2Ti_4O_{11}$ ^[28] are described sufficiently. The electronic properties as well as the stoichiometry in “stoichiometric” pyrochlore $Bi_2Ti_2O_7$ is often characterized the wrong way, as a contamination by a secondary phase of $Bi_4Ti_3O_{12}$ is sometimes concealed or not recognized.^[29] The existence of another compound, namely $Bi_2Ti_3O_9$, is controversially discussed. Yordanov et al.^[30] reported on its existence but did not discuss a suitable crystal structure, whereas Zaremba could not obtain a $Bi_2Ti_3O_9$ stoichiometry.^[31] Although the bismuth titanate phases of $Bi_4Ti_3O_{12}$ ^[32], $Bi_2Ti_2O_7$ ^[33] and $Bi_2Ti_4O_{11}$ ^[34] were shown to be active in less challenging dye degradation reactions, Kudo and Hiji^[35] reported that $Bi_4Ti_3O_{12}$ and the pyrochlore $Bi_2Ti_2O_7$ were inactive in photocatalytic hydrogen production. Contrarily, Murugesan et al.^[36] conducted a DFT study on pyrochlore $Bi_2Ti_2O_7$ proving that, hypothetically, all requirements are met to be a good photocatalyst for hydrogen production and even *overall water splitting*. This work examines the phase stability of TiO_2 rich compositions of pyrochlore bismuth titanate, reinvestigates their suitability for photocatalytic hydrogen production and gives a comparison to other bismuth titanate modifications.

As a second possibility of reducing the band gap energy, the titanium position in $Y_2Ti_2O_7$ is doped with the transition metal cations of Cr^{3+} , Mn^{3+} and Fe^{3+} providing partially filled d-orbitals, which leads to donor or acceptor levels within the energy band gap. Furthermore, the proposed O` site vacancy generation in $Y_{2-x}Ti_2O_{7-1.5x}$ should facilitate the incorporation of transition metal cations with similar effective ionic radii, but higher

oxidation states, i. e., Ta^{5+} and W^{6+} . The substitution limit is given by the complete refill of the O' position. Chemical compositions of $Y_{1.867}Ti_{1.6}Ta_{0.4}O_7$ and $Y_{1.867}Ti_{1.8}W_{0.2}O_7$ are obtained for a (Ti+Ta+W)/Y ratio of 1.075. Although the incorporation of Ta^{5+} and W^{6+} is not supposed to change the optical properties of yttrium titanate material significantly, this kind of titanium substitution should not only examine the influence of the substitution on the photocatalytic activity, but should also provide evidence for the proposed A,O' vacancy structure in $Y_{2-x}Ti_2O_{7-1.5x}$. Also considering the yttrium self-doping in $Y_2(Ti_{2-x}Y_x)O_{7-0.5x}$, the systematical substitution of the titanium site by a variety of transition metal cations should lead to an evaluation of pyrochlore doping.

The third possibility of reducing the band gap energy is based on the formation of oxynitrides by thermal ammonolysis. As both titanium and bismuth are reduced under the conditions of ammonolysis, the pyrochlore $Y_2Ta_2O_5N_2$ should be prepared and subsequently tested in photocatalytic hydrogen production. The monoclinic M'-YTaO₄ is in-situ transformed into the pyrochlore phase during ammonolysis.

In general, the structure chemistry and the corresponding vacancy structure in pyrochlores are supposed to be very complex, a function of the chemical composition and there exists a need for further investigations. Thus, this work should provide new insights into the pyrochlore structure. Moreover, new concepts should be introduced to explain the correlation between structure changes on the atomistic level of pyrochlores and the resulting photocatalytic activities.

Naturally, the influence of the preparation procedure on the properties of the photocatalysts is examined. Most of the research in photocatalysis is still conducted on materials prepared by a conventional solid state reaction (SSR). Although a high degree of crystallinity and a low defect concentration are achievable by the SSR, the need for high temperature annealing leads inevitably to crystallite sizes in the micrometer range. To achieve crystallite sizes in the nanometer scale, hydrothermal or sol-gel chemistry has to be utilized. The sol-gel process is preferred for preparing mixed oxides, as chelating agents lead to a homogenous distribution of cations already in the stage of gel formation. Thus, less energy is needed for the formation of crystalline mixed oxides and the heat treatment conditions are significantly moderated compared to the SSR. Contrary to binary oxides, nano-structured materials of mixed oxides are very hard to accomplish even by sol-gel chemistry. Thus, this work focused on the preparation of bulk complex mixed oxides with crystallite sizes in the nanometer scale. To achieve this, temperature and period of annealing play an important role. Annealing just above the temperature of

crystallization should lead to the smallest average crystallite sizes and to the largest active surface area, but higher temperature and/or prolonged heat treatment will result in a lower defect concentration and higher degree of crystallinity. As all of these characteristics are supposed to be advantageous to the photocatalytic activity, optimum annealing conditions are examined for each material.

Besides the elaborated evaluation of the photocatalysts itself, this work also investigates the photocatalytic hydrogen producing test reaction regarding stability and comparability. Usually, closed gas circulation systems are applied for evaluating photocatalytic hydrogen production rates. In this kind of setup, the hydrogen pressure increases with the reaction time, which may lead to an inaccurate determination of the activity getting even higher, if a syringe is used as sampler. Thus, the design of a special flow-through reactor system was necessary maintaining a constant hydrogen pressure in the gas phase to accurately determine variations in the hydrogen production rate occurring over time. The comparability of photocatalytic activities achieved by different photocatalysts is hindered by the use of the meaningless unit of $\mu\text{mol/h}$ in most publications. This hydrogen production rate is determined not only by the used photocatalyst, but also by the photocatalysis setup, the reactor geometry and mainly by the applied irradiation source. Besides the power output, especially the type of lamp plays a crucial role. Whereas a xenon arc lamp provides a uniform energy emission in the range from 250 to 750 nm being close to the solar spectrum^[37], a low-pressure mercury lamp offers three very intense emission lines in the UV at 254, 310 and 370 nm.^[38] Therefore, mercury lamps are preferentially used in the literature for evaluation of wide band gap semi-conductors to achieve delusively high hydrogen production rates without considering efficiencies. Thus, in this work a xenon arc lamp is utilized, as *solar* hydrogen production is the final objective. Moreover, hydrogen production rates are strictly converted into photonic efficiencies to facilitate the comparability of the investigated photocatalysts among themselves and compared to measurements conducted in other laboratories.

2 Fundamentals

2.1 Band theory

Atoms being isolated or far-off each other offer discrete energy levels. If these atoms converge, electrostatic interactions between their electron shells arise and the atom orbitals of the isolated atoms, which were formerly equivalent in energy, start to form a narrow distribution of energy levels referred as an energy band.^[39]

The bonding in solids is characterized by the entirety of all molecular orbitals of participating atoms. Regarding the band theory, ionic bonding and covalent bonding are special cases.

To understand the scheme of band structure formation, a linear chain of $N + 1$ equidistant hydrogen atoms is considered. By linear combining the $1s$ functions of the hydrogen atoms, a sum of $N + 1$ wavefunction is obtained each belonging to one electron. The wavefunctions may be compared to the vibrations of a linkage of $N + 1$ spheres connected by springs. This linkage of spheres is able to express a definite number of oscillation states determined by the number of oscillation nodes. Different oscillation states are numbered by means of k' values. Each sphere in the linkage (ranging from $n = 0$ up to $n = N$) oscillates with an amplitude of:

$$A_n = A_0 \cos 2\pi \frac{k'n}{2N} \quad (1)$$

A wavelength of $\lambda_{k'}$ is attributed to each stationary wave, whereas the distance between two spheres in the linkage is referred to as a :

$$\lambda_{k'} = \frac{2Na}{k'} \quad (2)$$

To become independent from the number of atoms in the linkage, that is N , the k' value is substituted by the wavenumber k :

$$k = \frac{2\pi}{\lambda_{k'}} = \frac{\pi k'}{Na} \quad (3)$$

Therefore, the wavefunction is defined in the range between 0 and $\pi/2$. The wavefunctions for the other values of the wavenumber are k obtained accordingly corresponding to the remaining electrons in the linkage of hydrogen atoms.

In terms of their $1s$ functions, every atom contributes to the BLOCH function being the sum of each single contribution χ_n . The BLOCH function is referred to as follows:

$$\psi_k = \sum_{n=0}^N \chi_n \cos(nka) \quad (4)$$

By means of the wavenumber k , the De-Broglie equation assigns a momentum to each electron:

$$k = \frac{2\pi}{\lambda} = \frac{2\pi p}{h} \quad (5)$$

The character of the wavefunction with $k = 0$ is binding, while that of the wavefunction with $k = \pi/a$ is anti-binding, as shown in Figure 1.

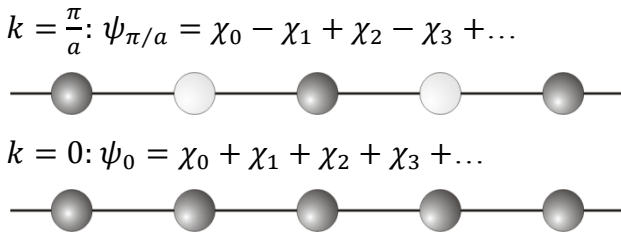


Figure 1: Wavefunctions

Each wavefunction is connected to a dedicated energy value of $E(k)$. As the number of atoms in the lattice is equal to the number of generated wavefunctions, an energy band is formed consisting of an equal number of energy levels, which are located between $E(0)$ and $E(\pi/a)$. Indeed, the energy levels are not allocated at equidistant intervals within the energy band. A high gradient in the energy band characterizes a dense sequence of energy levels resulting in a high *density of states (DOS)*. Naturally, energy levels located at lower energies correspond to binding states and energy levels at higher energies to non-binding states in the solid. In the case of hydrogen, the principle of Pauli predicts that the electrons exactly occupy the energy levels in the lower half of the energy band. The *highest occupied molecular orbital (HOMO)* is referred as the Fermi energy level. If the Fermi level is located in the middle of an energy band, the compound exhibits metallic conductivity. The excitation of an electron from an occupied energy level beneath into an unoccupied energy level above the Fermi energy is facilitated by a minimum of thermal energy leading to a high mobility of electrons even at lower temperatures. However, hydrogen is not a metallic conductor, as the Peierls distortion makes an equidistant linkage of hydrogen atoms unstable leading to a pairwise approach of the atoms. Thus, a band gap is formed between binding and non-binding states in the 1s energy band.

The band width is referred to as the difference in energy between the highest and the lowest energy state with both being located in the same energy band. In general, the stronger the interactions between the atoms are, the higher the overlap between their atomic orbitals. Moreover, the band width is an indicator for the degree of localization of

the bonding within the solid. If the character of the bonding is more localized, the narrow bands are not able to overlap leading to the generation of large interband gaps. If the Fermi level is located above such a band, all energy states within this particular band are defined to be occupied resulting in an electric insulator. An electric insulator is characterized by a band gap energy of at least 4 eV. This value describes the minimum amount of energy, which is needed to excite an electron from an occupied energy band into an unoccupied energy band.

For a proper description of the bonding characteristics in a 3-dimensional structure, the three lattice parameters and, additionally, rather the wavevector \vec{k} built up from three directional components than the wavenumber have to be taken into consideration. Actually, the application of a vector leads to the coincidence of the directions of the wavevector and the momentum. As the wavevector \vec{k} corresponds to a reciprocal wavelength, one can imagine a reciprocal space, which is stretched by a factor of 2π when compared to the reciprocal space used in crystallography. The reciprocal space, in which k is examined, is referred to as the first Brillouin zone describing a polyhedra. Each specific point in the Brillouin zone is dedicated to a possible state of an electron. A diagram characterizing the band structure is obtained by passing the energy states in the Brillouin zone in a specific way. By constructing a vector contour among all significant points in the k space, the whole symmetry of the Brillouin zone and thus, the symmetry of the crystal lattice are captured within the band structure.

Materials exhibiting a band gap energy of less than 4 eV are usually referred to as semi-conductors. The group of semi-conductors is divided into the subgroup of thermal semi-conductors being excitable by heat ($E_{bg} \leq 1$ eV) and the subgroup of photo semi-conductors being only excitable by irradiation (1 eV $< E_{bg} < 4$ eV). A semi-conductor is referred to as a direct semi-conductor, if the excitation of an electron from the conduction band into the valence band occurs at the same wavevector, i. e., the excited electron does not change its momentum. A semi-conductor is referred to as an indirect one, if the electron has to change its momentum during the transition from the valence band into the conduction band. This change in momentum has to be compensated by a lattice oscillation, also known as phonon, to conserve the momentum. In principle, the same fits for the process of electron-hole recombination. The recombination occurs without change in the momentum in direct semi-conductors leading to the possibility of photon emittance, known as fluorescence. In indirect semi-conductors, the recombination has to proceed under participation of a phonon to change the momentum of the electron. This

occurs in particular at lattice defect sites. Thus, the recombination rate increases with increasing defect concentration in the semi-conductor.

2.2 Photocatalysis

2.2.1 Process of photocatalysis

The process of photocatalysis in a semi-conductor exhibiting an indirect band gap transition is departed in three fundamental reaction steps^[40], which are illustrated in Figure 2:

- (1) An electron is excited from the valence band (*VB*) into the conduction band (*CB*), if the semi-conductor is irradiated with light containing photons of suitable wavelengths. The transition of the photo-excited electron e^- generates a hole h^+ in the valence band. The photons have to meet the requirement of being equal or higher in energy than the band gap energy of the semi-conductor to facilitate electron-hole pair generation (step (1) in Figure 2). This very fast electron-hole pair generation occurs on the time scale of femtoseconds.^[41, 42] The first way of electron hole recombination may occur as direct band gap recombination. This recombination process is preferred in direct semi-conductors leading to the phenomena of luminescence by emitting photons. In semi-conductors featuring an indirect band gap, this transition is unlikely, as the wavevector is not changed in this process. However, Novikov et al.^[43] report that a correlation between the band gap energy E_{bg} and the recombination rate k_r exists for semi-conductors providing an indirect band gap transition as well:

$$k_r = k_r^0 e^{-\alpha_r E_{bg}} \quad \text{with} \quad \alpha_r \approx 1.5 \text{ eV}^{-1} \quad (6)$$

The recombination behavior of six selected semi-conductors each featuring an indirect band gap transition could be described by this equation excellently. It was shown that the recombination rate increases with decreasing band gap energy. Although this equation is purely empirical, it fits well with other experimental data obtained by Sermakasheva^[44].

- (2) In the second reaction step, photogenerated electrons and holes have to migrate through the particle to the surface of the photocatalyst (cf. to step (2) in Figure 2). The time required for reaching the surface sites depends on the excitation energy as well as on the particle size. Usually, charge migration occurs in the time scale of picoseconds.^[45, 46] Within this diffusion process, the charge carriers may be

trapped at lattice or surface defect sites in shallow traps, which are energetically located near the conduction or valence band, or in deep traps, which are located below or above the conduction or valence band, respectively.^[47] Shallowly-trapped charge species have a short lifetime, deeply-trapped species are long-living. In general, trapped charge carriers may recombine involving Auger-processes (cf. to step (3) in Figure 2).^[48, 49] This recombination of an electron-hole pair proceeds via the excitation of another electron transferring additional energy into the lattice. In the case of a semi-conductor with indirect band gap transition, this kind of recombination prevails. The processes of charge trapping and relaxation occur over a broad time scale from picoseconds to milliseconds and compete with the process of charge recombination proceeding in the same time scale.^[47]

As the charge carrier recombination is the major drawback in photocatalysis, many attempts of inhibiting the recombination rate in the bulk were performed. The most frequently used methods are the generation of special nanostructured materials and/or the deposition of a co-catalyst, which is part of the illustration in Figure 2. Both models are described more in detail in chapter 2.2.2 (vide infra).

- (3) In the final step of the photocatalytic process, the photogenerated charge carriers may be involved in redox reactions at surface sites, if electrons possess suitable reduction potentials and if suitable oxidation potentials are provided by the corresponding holes. Photogenerated charge carriers may be trapped by adsorbed species directly, i. e., a chemical reaction, transferred to a co-catalyst particle like platinum (cf. to step (4) in Figure 2) or trapped by surface sites. The latter leads to Ti^{3+} centers for trapped electrons and to surface-bound radicals ($>\text{Ti}^{\text{IV}}\text{-OH}\cdot$) for trapped holes.^[8, 46] Both surface sites may be regenerated by reacting with adsorbed species or, of course, by recombination. The processes of interfacial charge transfer occur in a broad time scale from picoseconds to seconds depending on the complexity of the chemical reaction. The electron trapping by protons forming molecular hydrogen and the methanol oxidation by holes are quite fast in the micro- to millisecond scale, whereas the challenging 4-hole process of water oxidation takes nearly one second.^[47, 50]

To facilitate the process of hydrogen production, the photocatalytic reaction must indeed be performed in de-aerated solutions, as oxygen acts as an effective

electron scavenger forming superoxide anions. The same behavior is known from nitrogen.

If the solution, in which the photocatalytic process is performed, contains organic material, the hole possessing a positive charge may oxidize the organics directly to form radical cations (cf. to step (5) in Figure 2). The holes may also oxidize water or hydroxide ions to hydroxyl radicals, which can on their part, oxidize the organics. If the solution does not contain organics, the holes have to be strong enough in their oxidation potential to facilitate the further oxidation of hydroxyl radicals to molecular oxygen. This is a complicate process involving four holes, which is only managed by very few photocatalysts (vide infra, chapter 2.4).

As also shown in Figure 2, the oxidation potential of holes and the reduction potential of electrons derive directly from the absolute positions of the valence band and of the conduction band with respect to the normal hydrogen electrode (vs. NHE), respectively. The more positive vs. NHE the valence band top, the higher the oxidation potential of photogenerated holes. Vice versa, the more negative vs. NHE the conduction band bottom, the higher the reduction potential of photogenerated electrons. As the absolute band energies do play such an important role in photocatalysis, the different ways of changing the band positions are described in chapter 2.4 (vide infra) more in detail.

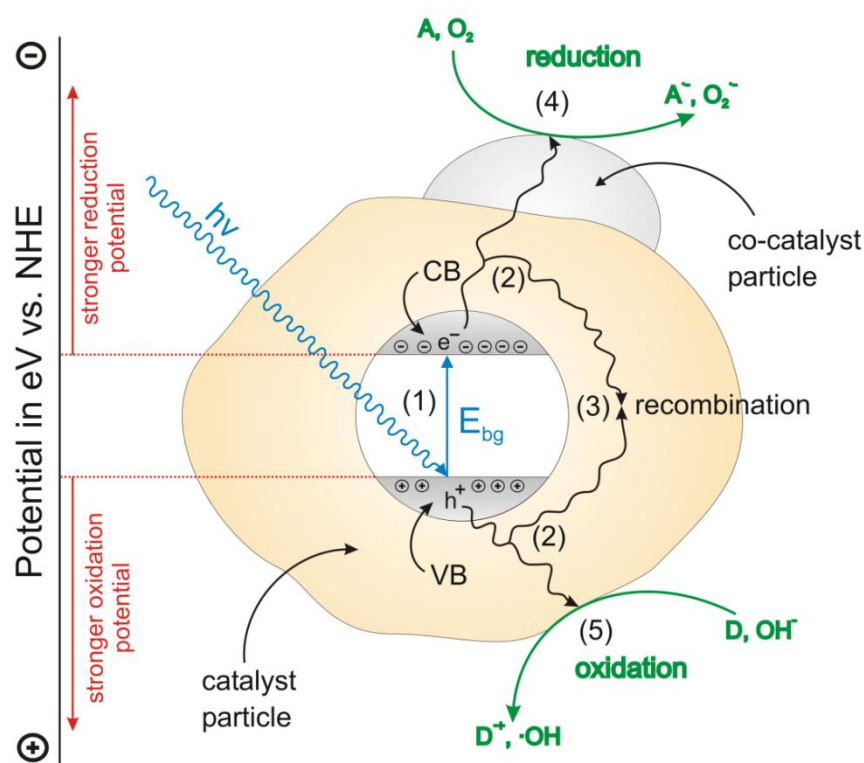


Figure 2: Fundamental reaction steps in the process of photocatalysis.

2.2.2 Inhibiting charge carrier recombination

The recombination in the particle bulk is the major drawback in photocatalysis. Usually, only a fractional amount of the photogenerated electron-hole pairs reaches the active surface sites. The bigger part of electron-hole pairs recombines in the bulk making them no longer utilizable for the photocatalytic purpose. The most common way to inhibit charge carrier recombination is to deposit a co-catalyst on the surface of the photocatalyst. The deposition process can be performed by impregnation like in the case of the prominent Ni/NiO^[51] co-catalyst system or by reductive photodeposition. In the process of photodeposition, usually, inorganic salts containing the cation of the desired metal species are applied, which are photo-reduced in a kind of photocatalytic step involving the concomitant photo-oxidation of an organic sacrificial reagent. In many respects precious metals are the most suitable candidates. Most importantly, precious metals generate strong electronic sinks in their local environment by which electrons are adducted separating photogenerated electrons from holes. From the chemical point of view, precious metals feature very high redox potentials vs. NHE making them easy to deposit and, more importantly, very hard to oxidize. The redox potentials vs. NHE of the frequently used precious metals of gold and platinum are given as follows^[52]: $E_0(Au^+|Au) = +1.69 V$ and $E_0(Pt^{2+}|Pt) = +1.18 V$. Although the redox potential of rhodium ($E_0(Rh^{3+}|Rh) = +0.76 V$)^[52] is not ideal, it is known to act as co-catalyst very effectively. The redox potential of nickel is even negative ($E_0(Ni^{2+}|Ni) = -0.24 V$)^[52], but the NiO shell is supposed stabilize the Ni core against oxidation. Although much smaller co-catalyst particle sizes are obtained by photodeposition than by the impregnation method, the electron adducting character of as-deposited particles leads to the disadvantage of further particles being preferentially deposited in the surrounding of already existing particles, which is illustrated in Figure 3 using the example of platinum.

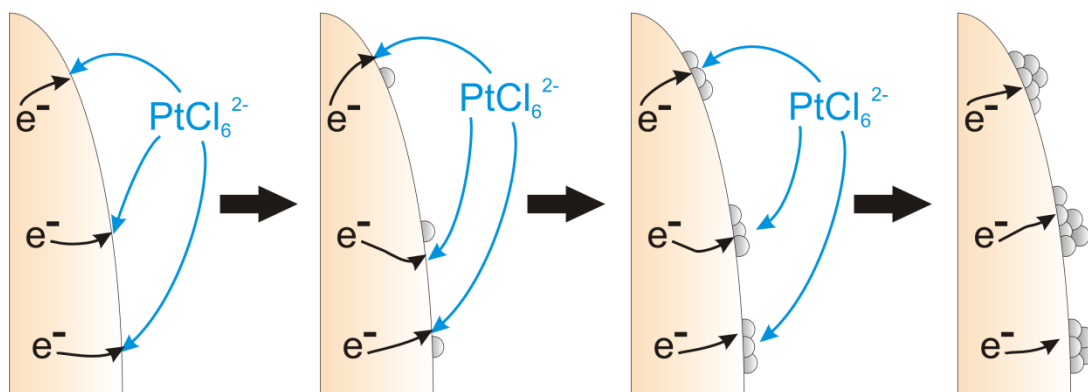


Figure 3: The process of platinum co-catalyst photodeposition.

Another way of decreasing the probability of charge carrier recombination is to design nanostructured materials. Sayama et al. report about a layered structure of $K_4Nb_6O_{17}$, which facilitate the intercalation of interstitial water or co-catalyst nanoparticles of nickel^[53] or platinum^[54] between the niobate sheets. The charge carrier separation was improved by decreasing the distance that photogenerated electrons have to pass for reaching the co-catalyst particles leading to an increase in the photocatalytic activity. A similar finding was obtained by Shimizu et al.^[55], who prepared the Ruddlesden-Popper perovskite of $H_2La_{2/3}Ta_2O_7$. The subsequent impregnation with NiO led to the selective intercalation of NiO nanoclusters in-between the perovskite layers, by which the diffusion length of electrons to active sites of NiO are shortened improving the charge separation. Kato and Kudo^[56, 57] performed La^{3+} doping on the perovskite of $NaTaO_3$. A structure directing influence of the La^{3+} doping was found, by what a stepped nanostructure was formed on the surface. The NiO co-catalyst was selectively deposited at the edges of the steps, which was again proposed to improve the charge separation.

2.3 The cubic pyrochlore structure

In the process of photocatalysis, the crystal structure plays an important role. As the crystal structure influences the electronic and optical properties of the photocatalysts, it significantly affects the separation of charge carriers and their subsequent migration to active surface sites. According to Abe et al.^[22], especially the availability of a corner-sharing octahedral network of transition metal cations (MO_6) leads to an improved separation and migration of photogenerated electrons and holes. Besides the cubic pyrochlore structure, many perovskite structures (cubic, tetragonal, monoclinic) and the orthorhombic Weberite structure also provide a corner-sharing octahedral network.

As a lot of work was done in the field of photocatalysis using perovskites, the focus of this thesis is attached to materials crystallizing in the cubic pyrochlore structure. The pyrochlore structure was named after the corresponding mineral with a chemical composition of $(Na,Ca)_2(Nb,Ti)_2O_6(OH,F)$. The ideal pyrochlore structure crystallizes in space group $Fd\bar{3}m$ with the general chemical composition of $A_2B_2X_6Y$. In mixed metal oxides, the A and B positions are occupied by cations and the positions of X and Y by oxygen ($A_2B_2O_6O^\cdot$).

The crystallographic origin of the pyrochlore cell is usually placed on the Wyckoff site $16c$ (with coordinates of 0, 0, 0). Beside the $16c$ site also the Wyckoff sites of

$16d$ ($1/2, 1/2, 1/2$) and $8a$ ($1/8, 1/8, 1/8$) are highly symmetric, i.e., these sites do not have any positional parameters. For undistorted pyrochlores like $Y_2Ti_2O_7$, the A cations are placed on the $16c$ site, the B cations on $16d$ and the O⁻ anion on $8a$.^[58] Only the O anions occupy sites with a positional parameter, namely $48f$ ($x, 1/8, 1/8$).^[25] The B cation (titanium, tantalum) is sixfold coordinated by $48f$ oxygen forming a corner-sharing MO_6 octahedral network. Due to the larger ionic radius, the A cation (yttrium, bismuth) is located in the center of a puckered hexagonal bipyramid^[59]. Figure 4 shows the network of corner-sharing TiO_6 octahedra.

In order to obtain a pyrochlore structure, the smaller transition metal B cations have to provide an effective ionic radius between 0.6 \AA and 0.8 \AA ^[60]. Considering a coordination number of 6, Ti^{4+} (61 pm) as well as Ta^{5+} (64 pm) satisfy this demand.

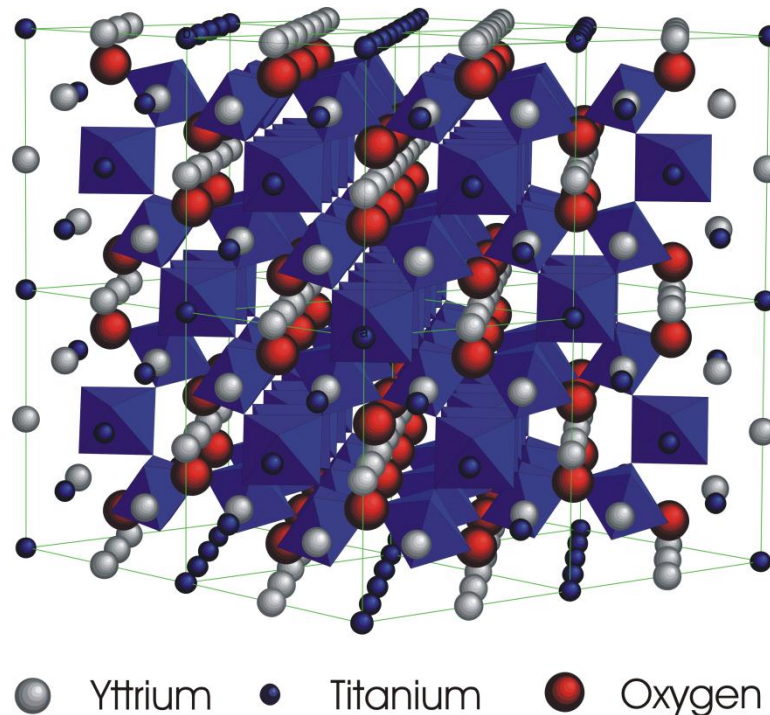


Figure 4: Corner-sharing network of TiO_6 octahedra in the cubic pyrochlore structure of $Y_2Ti_2O_7$.

The cubic pyrochlore structure is often described as an anion defect fluorite structure^[61]. Usually, the “standard” fluorite structure has the chemical composition AO_2 and crystallizes in spacegroup $Fm\bar{3}m$ ^[62]. Adopting the pyrochlore stoichiometry, one vacancy per eight anions has to be considered leading to $AO_{1.75}$ for the defect fluorite. A perfect defect fluorite with a randomized cation distribution is found for $YZrO_{3.5}$ ^[63]. Like in the pyrochlore structure, the anion vacancy can alternatively be placed on eight possible anion positions leading to a $2 \times 2 \times 2$ supercell of the “standard” fluorite with a doubled lattice parameter for defect fluorite. Actually, pyrochlore and defect fluorite differ in the

degree of cation order. The pyrochlore structure type provides two distinct crystallographic positions for cations, in the defect fluorite exists only one cation lattice site. However, the cations are arranged in the same way in both lattices. Both structures differ more in their anion sub-lattice. In the defect fluorite structure, all anions (usually oxygen) are placed on the Wyckoff site $8c$ (0.25,0.25,0.25). Due to the higher degree of cation order in the pyrochlore, the anions rearrange resulting in two distinct anion lattice sites, namely the $48f$ and $8a$.

ion		pyrochlore structure				defect fluorite structure			
		Wyckoff site	coordinates			Wyckoff site	coordinates		
			x	y	z		x	y	z
A	Y ³⁺	16c	0	0	0	4a	0	0	0
			0	1/2	1/2		0	1/2	1/2
			1/2	0	1/2		1/2	0	1/2
			1/2	1/2	0		1/2	1/2	0
			0	1/4	1/4		0	1/4	1/4
			1/4	1/4	0		1/4	1/4	0
			1/4	0	1/4		1/4	0	1/4
B	Ti ⁴⁺	16d	1/2	1/2	1/2	4a	1/2	1/2	1/2
			1/2	0	0		1/2	0	0
			0	1/2	0		0	1/2	0
			0	0	1/2		0	0	1/2
			1/2	1/4	1/4		1/2	1/4	1/4
			1/4	1/4	1/2		1/4	1/4	1/2
			1/4	1/2	1/4		1/4	1/2	1/4
O	O ²⁻	48f	0.4201	1/8	1/8	8c	3/8	1/8	1/8
			3/8	0.1701	3/8		3/8	1/8	3/8
			0.1701	3/8	3/8		3/8	1/8	3/8
			3/8	3/8	0.1701		3/8	3/8	1/8
			1/8	0.4201	1/8		1/8	3/8	1/8
			1/8	1/8	0.4201		1/8	1/8	3/8
O ⁻	O ²⁻	8a	1/8	1/8	1/8	8c	1/8	1/8	1/8

Table 1: Changes in the crystallographic coordinates of Y³⁺, Ti⁴⁺ and O²⁻ in a hypothetical phase transition of Y₂Ti₂O₇ from the pyrochlore structure into the parental defect fluorite structure. In this process, the metal cations remain in their lattice positions, while the x positional parameter of O oxygen changes from 0.4201 to 0.375 (3/8). The fractional coordinates of the defect fluorite structure were halved to fit into an eighth of a pyrochlore unit cell.

The close relation between both structures is indicated in Table 1 showing the coordinates of cations and anions of $Y_2Ti_2O_7$ in an eighth of a unit cell of a perfect pyrochlore as well as of an imaginary defect fluorite structure. In a phase transition from pyrochlore into the defect fluorite structure the cations are not affected. However, by changing the x positional parameter from 0.4201 to 0.375, the $48f$ oxygen is moved into the highly symmetric lattice position of $8a$. As this x parameter is variable, the structure remains in the pyrochlore type throughout the phase transition. The movements of the O oxygen ions are presented in Figure 5. It should be noticed that even a complete randomized distribution of cations will not lead to a perfect defect fluorite lattice of oxygen anions, as the remaining oxygen vacancy weakens the movement of the oxygen ions towards the highly symmetrical positions.^[64] By means of X-ray diffraction, such a lattice is misleadingly believed to be defect fluorite in the anion sub-lattice as well, as only the cation sub-lattice is “visible”. Moreover, a complete cationic phase transition from pyrochlore into defect fluorite is rather unusual.

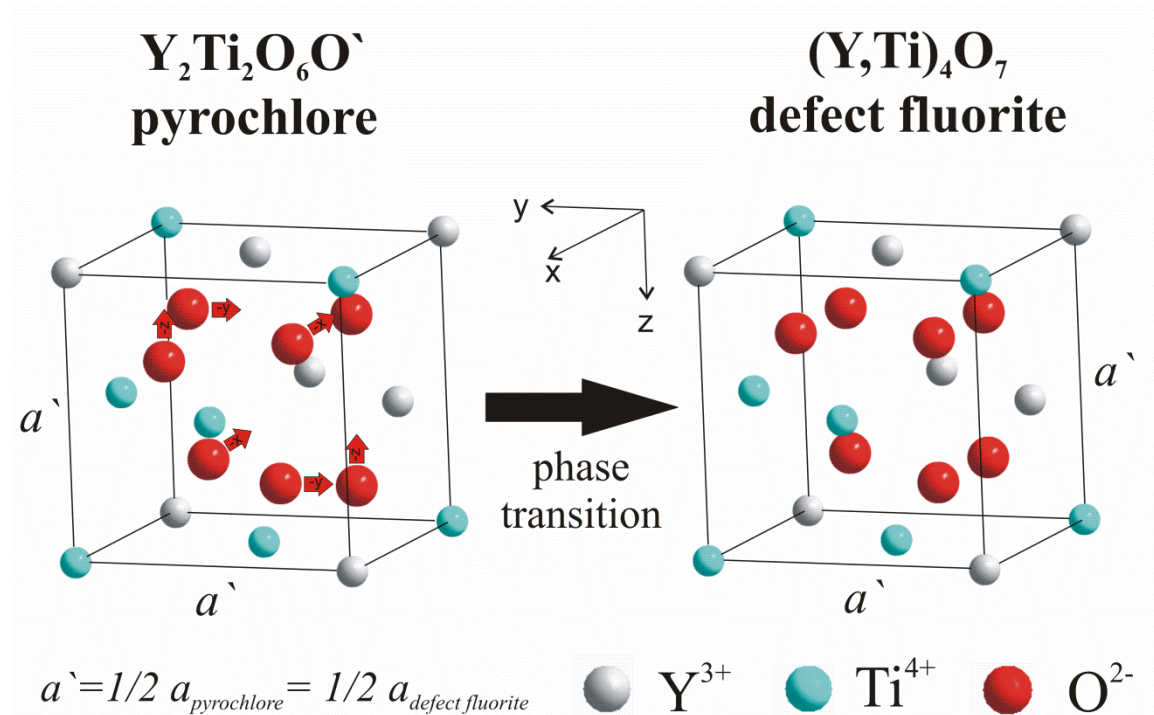


Figure 5: Scheme of the hypothetical phase transition of $Y_2Ti_2O_7$ from the pyrochlore structure into the parental defect fluorite structure. The metal cations remain on their lattice positions, while O oxygen moves towards the highly symmetrical Wyckoff site of $8a$. As only $1/8$ of a unit cell is presented, the disordered distribution of cations in the defect fluorite structure is not illustrated in this scheme.

2.4 Band gap engineering

In order to engineer an effective photocatalyst one should consider that the wavelengths of photons which are utilizable by the catalyst are limited by the band gap energy. The photons have to feature equal or higher energies when compared to the band gap energy. Thus, only a specific fraction of the whole photon spectrum provided by solar irradiation, which extends into the near IR region, can lead to an excitation, which limits the achievable photocatalytic *efficiency* (vice versa, chapter 2.6) of solar irradiation in general.

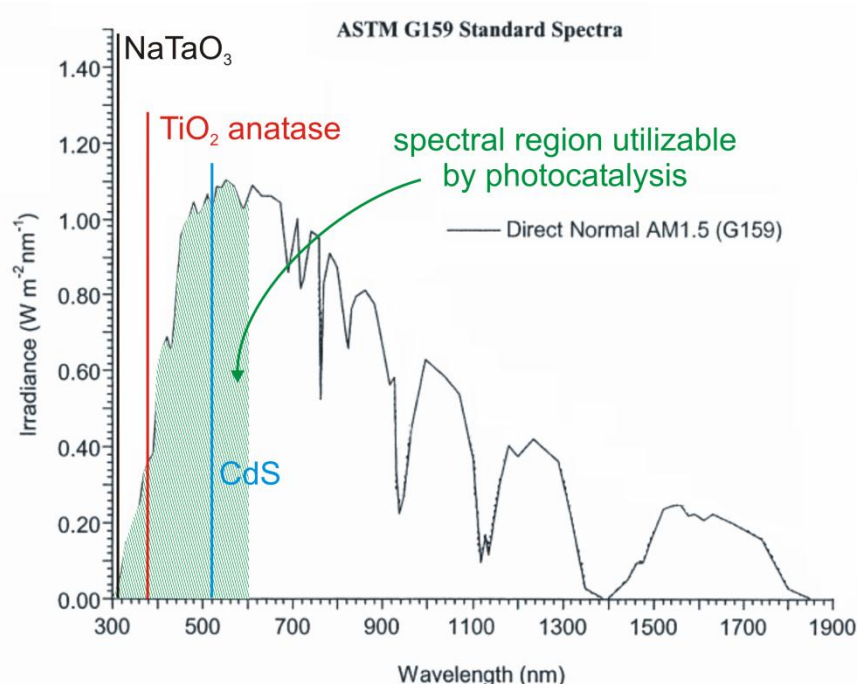


Figure 6: ASTM standard spectra^[65] AM1.5 (G159) being in good accordance with the overall yearly average irradiation in mid-latitude regions.

The spectrum of solar irradiation^[65] is presented in Figure 6 in the so-called air mass description featuring an atmospheric factor of 1.5 (AM1.5), which implies a solar zenith angle of $z = 48.2^\circ$ being in good accordance with the overall yearly average irradiation in mid-latitude regions. The atmospheric factors of AM0 and AM1 correspond to zero atmosphere, that is, outer space, and exactly one atmosphere, which belongs to equatorial irradiation ($z = 0^\circ$), respectively. The infrared region and the red fraction of the visible light region are per se not utilizable by photocatalysis, because these photons feature energies which are too less to activate a semi-conductor. On the other hand, the region in the visible light spectrum ranging from 370 nm to about 600 nm is of special interest, as being suitable for photocatalytic purposes. To absorb in this region, a semi-conductor has

to be designed with a band gap energy situated between 2.1 eV and 3.0 eV. For a better comparability, the band gap energies of some prominent photocatalysts are inserted into the spectrum, namely, NaTaO₃ ($E_{bg} = 4.0 \text{ eV}$)^[66], TiO₂ anatase ($E_{bg} = 3.2 \text{ eV}$)^[67] and CdS ($E_{bg} = 2.4 \text{ eV}$)^[68].

Based on the energy distribution over the solar spectrum, it is obvious that wide band semi-conductors like NaTaO₃ are only able of absorbing a marginal part of the spectrum. Interestingly, successful *overall water splitting* is achieved almost exclusively by wide band gap semi-conductors. Among diverse structures like Sr₂Ta₂O₇^[69] preferentially perovskites such as SrTiO₃^[70, 71], NaTaO₃^[72, 73] and the quite expensive AgTaO₃^[74] were found to be active in *overall water splitting*. All of these materials share the disadvantage of being wide band gap semi-conductors with band gap energies between 3.4 eV and 4.5 eV. Fujishima and Honda initially observed the phenomena of *overall water splitting* in a photoelectrochemical cell by means of a TiO₂ electrode.^[75] Up to now, the TiO₂ modifications of anatase and brookite are frequently used in photocatalytic hydrogen production, in which these materials are highly active, but not in *overall water splitting*. Kaniel et al. reported a better suitability of the brookite modification by providing a more negative conduction band level (vs. NHE).^[76] However, exhibiting band gap energies of 3.2 eV and 3.1 eV^[77], respectively, even TiO₂ can only be excited by UV irradiation, which is about 4 %^[78] of the solar energy reaching the surface of the earth. The modification of the band gap of wide gap semi-conductors for the purpose of reaching a lower gap energy poses some problems and have to be valued as a compromise between raising the valence band edge or lowering the conduction band edge, which leads to decreasing redox potentials of photogenerated holes or electrons, respectively (cf. to Figure 2). Unfortunately, most of the semi-conducting oxides suffer from the disadvantage of high band gap energies, as the valence band is usually built up from occupied $2p$ orbitals of oxygen, which determine the absolute position of the valence band top to be located at about +3.0 eV^[79]. This indeed leads to very strong oxidation potentials of photogenerated holes. The conduction band in mixed oxides is usually formed by empty d orbitals of transition metal cations like Ti⁴⁺ ($3d^0$), Nb⁵⁺ ($4d^0$), or Ta⁵⁺ and W⁶⁺ (both $5d^0$). To facilitate hydrogen generation by mixed oxides, the conduction band level has to be more negative vs. NHE than the redox potential of $E_0(2H^+|H_2) = 0 \text{ V}$. The conduction band level is not only a function of the d^0 transition metal cations, but also of the lattice structure confirmed by the prominent phases of TiO₂, anatase, brookite and rutile, which do not differ in their valence band positions, but in

their conduction band levels leading to different energy band gaps of 3.2 eV, 3.1 eV and 3.0 eV^[67], respectively. The influence of changing the lattice structure on the conduction band level is not easily predictable. On the other hand, the conduction band level is altered to more negative values vs. NHE, if a transition metal cation from a lower period is substituted by one from a higher period of the periodic system. When comparing TiO₂ anatase with ZrO₂, the bottom of the conduction band is changed from -0.2 eV to -1.0 eV vs. NHE by substituting Ti⁴⁺ by Zr⁴⁺.^[80] Most of the d^0 transition metal cations generate a conduction band that is located only slightly above the redox potential of the redox pair of $E_0(2H^+|H_2)$ as shown in Figure 7 presenting the conduction band positions of some commonly used d^0 transition metal cations. Thus, the attempt of decreasing the band gap energy by lowering the conduction band bottom may lead to the complete deactivation in photocatalytic hydrogen production for some d^0 cations. Thus, methods have to be investigated to decrease the band gap energy by raising the position of the valence band top of a semi-conducting oxide, while letting its conduction band level unchanged.

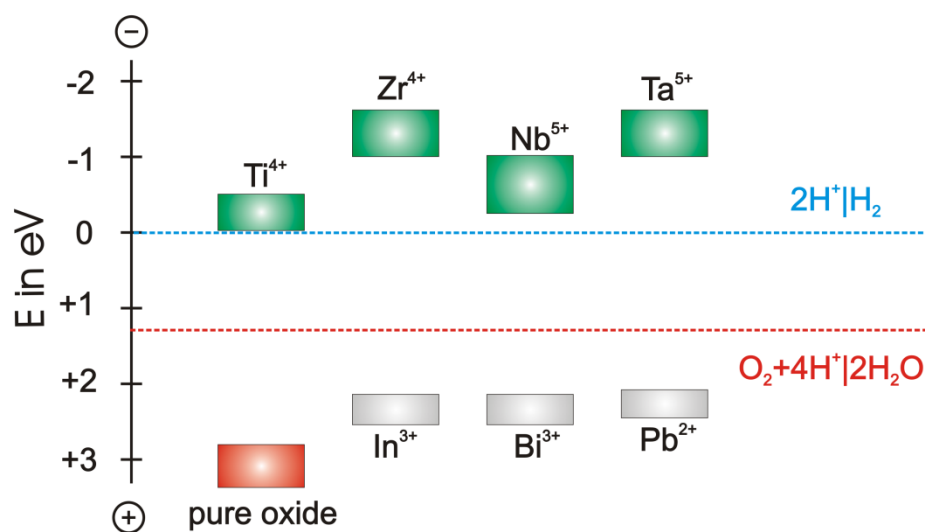


Figure 7: The positions of the conduction band bottom and the valence band top proposed for binary oxides using the band of pure oxygen as valence band position and for ternary oxides, in which selected ns^2 or $(n+1)s^0nd^{10}$ cations occupy the A position. The B position is occupied by selected nd^0 transition metal cations. For each band, a range of possible band positions is presented, as the actual band position is not only influenced strongly by the lattice structure, but even slightly by other characteristics like the crystallite size.

Some binary compounds such as CdS and Bi₂O₃ exhibit visible light activity inherently, with band gap energies of 2.5^[81] and 2.8^[82] eV, respectively, but none of these small band gap semi-conductors were found to be active in *overall water splitting*. Hydrogen

production can be performed with CdS, but only in a sulphide solution, which prevents photocorrosion. In literature, several attempts of raising the valence band top of oxide semi-conductors have been conducted. Beside the possibility of introducing a dopant on the transition metal cation position, the synthesis of complex oxides providing two or more cation crystallographic positions being distinguishable from each other is a prerequisite for extending the options of band gap engineering. The most prominent mixed oxide structure is the perovskite structure of ABO_3 , whereas potential applications of the pyrochlore structure of $A_2B_2O_7$ are only barely investigated up to now. A structure providing two distinguishable crystallographic positions for two cation species is only formed, if the cations differ significantly in their effective ionic radii. Otherwise, a higher symmetric binary structure is established instead. In general, mixed oxides are supposed to be more stable than doped photocatalysts and may exhibit a lower degree of defects and thus, of recombination centers, which should be beneficial for an effective charge carrier separation^[83]. Often in mixed oxides, the d^0 transition metal cation B possesses the by far smaller radius than the cation A and forms a three-dimensional network of corner- or edge-sharing octahedra being considered favorable for photocatalytic activity^[22]. The major advantage of using complex mixed oxides is founded in the presence of the second cation position A, which does not influence the octahedral BO_6 network, but may indeed have a significant effect on the band structure. Three methods of raising the valence band top are presented as follows and the influence on the valence band by applying methods (1) or (2) is illustrated in Figure 7 as well.

- (1) By introducing cations with ns^2 configuration like Pb^{2+} ^[84] or Bi^{3+} ^[85] (both $6s^2$) on the A position the occupied $Pb6s$ or $Bi6s$ band of Pb^{2+} or Bi^{3+} cations hybridize with the $O2p$ band of oxygen leading to a shift of the valence band top to more negative energies vs. NHE.
- (2) The introduction of cations with $(n+1)s^0nd^{10}$ configuration like Ag^+ ^[86] or In^{3+} ^[87] (both $5s^04d^{10}$) on the A position leads a hybridization of the fully occupied d band with the $O2p$ band of oxygen. Thus, the valence band top is energetically altered to more negative values vs. NHE once again.
- (3) The doping of one of the oxygen positions by another anion species like nitrogen or sulfur leads to the raise of the valence band top as well. The newly emerging bands of $N2p$ of nitrogen anions or $S3p$ of sulfide anions hybridize with the $O2p$ oxygen band. The nitrogen and sulfur doped anatase structures of $TiO_{2-(3/2)x}N_x$ ^[88] and $TiO_{2-x}S_x$ ^[89] were investigated intensively.

If an nd^0 transition metal cation is chosen as the B cation species, the bottom of the conduction band is composed of empty d orbitals. As the small transition metal cations are usually coordinated octahedrally by oxygen ions, an octahedral splitting of the crystal field is observed for the d orbitals forming the e_g and t_{2g} orbitals being higher and lower in energy, respectively, when compared to the d orbitals in a spherical field. The bottom of the conduction band is characterized by the t_{2g} state. The absolute position of the t_{2g} state depends on the interactions between these d orbitals and the oxygen ligands, which are a function of the ionic radius and the charge of the transition metal cation, the extend of the crystal field splitting and the shielding of the nuclear charge. These interactions indeed represent the energy needed for a charge-transfer transition from an O2p orbital of oxygen into a low energy d orbital of the transition metal cation, which is referred to as a band gap transition with the corresponding band gap energy E_{bg} .

However, the influence of the crystal structure on the band gap transition must not be neglected, as dependent on the crystal structure the top of the valence band and the bottom of the conduction band are located at special k points in an individual Brillouin zone. Thus, the influence of substituting one cation species for another is highly dependent on the lattice structure and only hard to predict.

Instead of substituting with $ns^2/(n+1)s^0nd^{10}$ cations or nitride/sulfide anions, the doping with transition metal cations featuring partially filled d orbitals may lead to a shift of the band gap energy to facilitate activity under visible light irradiation as well. However, the influence of this type of doping on the band structure is not easy to predict. As was true for the nd^0 transition metals, the cations with partially filled d orbitals are also affected by the octahedral crystal field splitting, but the low energy t_{2g} orbitals accommodating electrons and the usually unoccupied high energy e_g orbitals may now be located within the energy band gap of the pure material. Beside the standard band gap excitation, up to two additional photon induced transitions leading to charge generation are facilitated in a doped semi-conductor, which are the photoexcitation of valence band electrons into the acceptor level of the dopant and the transition from the dopant donor energy level into the conduction band:



These photon induced transitions are presented in Figure 8 as reaction (1) utilizing the pyrochlore $Y_2Ti_2O_7$ as the host material and Fe^{3+} as dopant. The absolute conduction

band and valence band edge positions of $Y_2Ti_2O_7$ are supposed to be located at -0.6 eV and $+3.0$ eV vs. NHE, respectively, considering an energy band gap of 3.6 eV reported by Abe et al.^[22]. Being dependent on the possible oxidation states provided, the dopant cations also act as electron and/or hole traps, if the cation is reducible and/or oxidizable, respectively (cf. to reaction (2) in Figure 8):

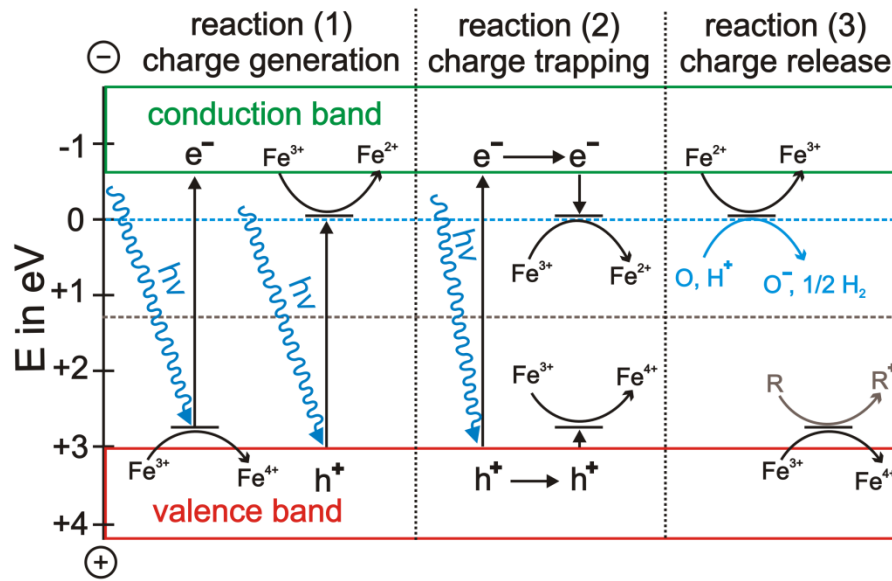
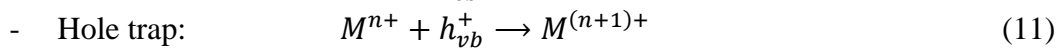
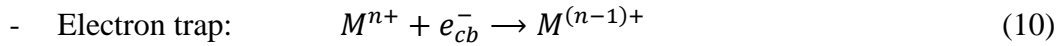
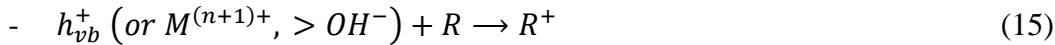
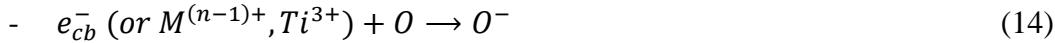
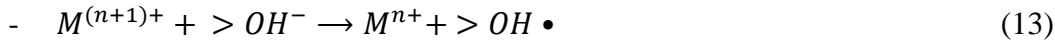


Figure 8: The additional transitions and reaction steps in $Y_2Ti_2O_7$ doped by transition metal cations. Reaction (1) shows the additional excitation modes from the donor energy level into the conduction band and from the valence band into the acceptor level of the dopant. Reaction (2) describes the charge trapping mechanism by acceptor and donor levels of the dopant being located near the conduction and valence band, respectively. Reaction (3) shows the charge release out of the dopant traps regenerating the original valence state of the dopant cation.

The energy levels of electron traps $M^{n+}/M^{(n-1)+}$ lie below the conduction band bottom and the energy levels of hole traps $M^{n+}/M^{(n+1)+}$ are located above the valence band top. The energy levels of dopants utilized or found in this work are proposed in Figure 9 on the basis of published results obtained with the TiO_2 phase rutile. As rutile crystallizes in another structure type and the conduction band is located at a different energy, the doping levels inside $Y_2Ti_2O_7$ will be located differently as well, and should be regarded as approximation. However, the relative differences in energy level positions of the dopants should be consistent leading to an order of $E(Fe^{3+/4+}) < E(Cr^{3+/4+}) < E(Mn^{3+/4+}) < E(Mn^{2+/3+}) < E(Fe^{2+/3+})$ vs. NHE^[90]. The cationic dopants of Fe^{3+} and Mn^{3+} can act

as electron as well as hole traps, whereas Cr^{3+} can only trap holes, but not electrons.^[91] The energy level of a possible Ti^{3+} self-doping state is located above the conduction band edge.^[91] Reactions (1) and (2) presented in Figure 8 lead to excited states of the cation dopant, from which the trapped charge might migrate and finally, be released as shown in reaction (3):



Electron acceptors and donors are referred to as O and R , respectively, and M^{n+} is the transition metal dopant featuring partially filled d orbitals.

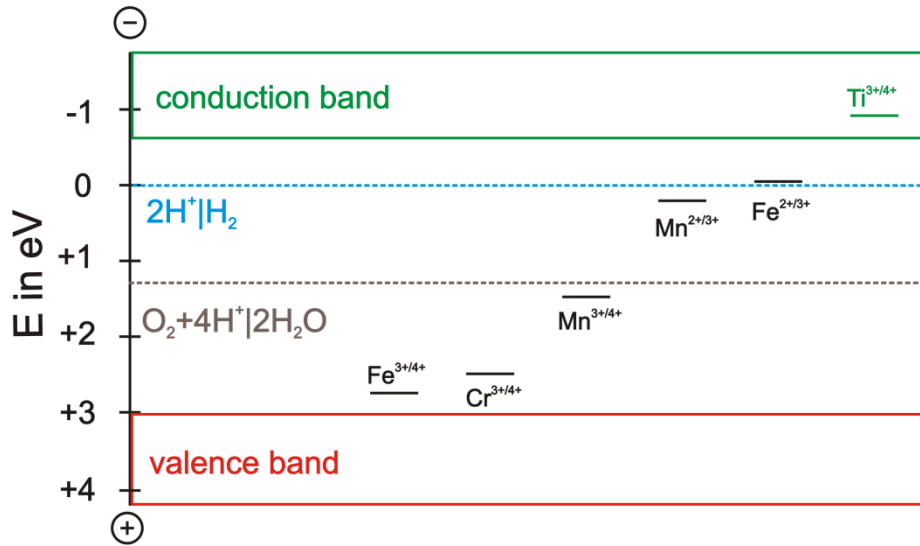


Figure 9: The proposed positions of energy levels created by doping the pyrochlore $\text{Y}_2\text{Ti}_2\text{O}_7$ with Fe^{3+} , Cr^{3+} , Mn^{3+} and Ti^{3+} . The data are taken from results^[90] obtained with the TiO_2 phase rutile. As the structure type of rutile is another and the conduction band is located at a different energy, the doping levels inside $\text{Y}_2\text{Ti}_2\text{O}_7$ will be located differently and should be regarded as approximation. However, the relative differences in energy level positions of the dopants should not be changed compared to the rutile source.

Figure 9 also shows redox potentials of the two important half-reactions of *overall water splitting* forming molecular hydrogen and oxygen from pure water:



When examining the process of hydrogen production under aid of a sacrificial reagent like methanol, the hydrogen producing half-reaction is untouched, whereas the oxidation of methanol to formaldehyde is conducted at more positive energies vs. NHE. Thus,

hydrogen production is much easier to accomplish by a photocatalyst. However, the dopant energy level of $E(Mn^{2+/3+})$ is supposed to be located below the redox potential of hydrogen generation, which would lead to the fact that trapped electrons will no longer provide a sufficient reduction potential inhibiting the hydrogen formation. A similar proposal might also count for the Fe^{3+} doping. As Cr^{3+} cannot trap an electron, this kind of doping is considered favorable for hydrogen production. One should note that these thoughts only fit for hydrogen production performed under deaerated conditions. From the thermodynamic point of view, for the cleavage of organic compounds a completely different behavior is supposed, as the reduction of oxygen acting as an electron scavenger needs clearly less energy than the proton reduction step.

Photocatalysts showing any kind of activity in *overall water splitting* under visible light irradiation are still rare. Successful water splitting by visible light irradiation was achieved over $InVO_4$ ^[92] loaded with NiO as co-catalyst. Recently, Maeda et al. reported about visible light driven water splitting with the solid solution of $(Ga_{1-x}Zn_x)(N_{1-x}O_x)$ loaded with a new co-catalyst system of core-shell Rh/ Cr_2O_3 .^[93, 94] Especially the Cr_2O_3 shell is supposed to be important for the high photocatalytic activity by preventing the back reaction usually taking place on the surface of noble metals like platinum or rhodium. The Cr_2O_3 shell was shown to be permeable for water and molecular hydrogen, but not for molecular oxygen.^[95]

2.5 Reactor design and reaction settings

A number of parameters influencing the photocatalytic activity should be referred to as *intrinsic*, as these factors are only determined by the photocatalyst itself. The chemical composition and the crystal structure are the most important *intrinsic* characteristics predetermining the electronic and optical properties of a photocatalyst. Naturally, also the crystallite size and shape and the concentration of surface active sites directly influence the photocatalytic activity and is referred to as *intrinsic*. If these *intrinsic* characteristics of a photocatalyst were considered and photocatalytic reactions were performed in a standardized procedure using a standardized reactor, the results would be perfectly comparable. However, up to now only a few procedures are standardized and the „results“ regarding hydrogen production are almost exclusively published in the unit $\mu\text{mol/h}$. Unfortunately, these results are often more determined by the applied lamp as

well as by the shape and size of the reactor than by the photocatalytic properties of the material. In summary, it is very difficult to evaluate the quality of a photocatalyst.

Beside the *intrinsic* properties influencing photocatalysis, there exist some extrinsic factors, which are highly dependent of the reactor design and the reaction procedure.

- Changing the pH value has a significant influence on the properties of a photocatalyst. First, the amount of surface *OH*-groups is a function of the pH value. Moreover, by decreasing or increasing the pH value, the *OH*-groups are also protonated or deprotonated forming OH_2^+ - or O^- -groups, respectively. At a special pH value referred to as the zero point of charge (ZPC), the surface is uncharged, as shown in Figure 10.

Dhananjeyan et al.^[96] show that increasing the pH value also shifts the positions of the valence band as well as of the conduction band to more negative values vs. NHE. Thus, an increase in the pH value leads to an increase in the reduction potential of photogenerated electrons, but also to a decrease in the oxidation potential of the corresponding holes. For a decrease in the pH value, the opposite is observed for the potentials of photogenerated electron/hole pairs.

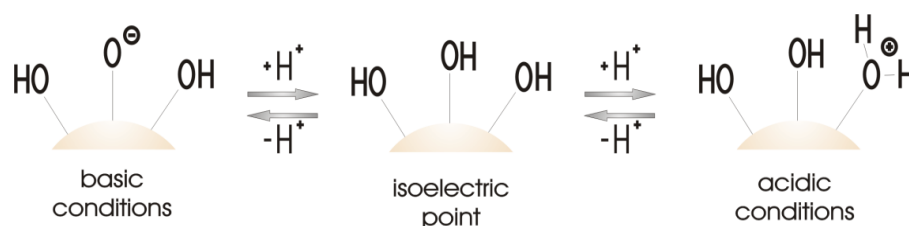


Figure 10: Alteration of the surface charge by changing the pH value.

- Many investigations^[97, 98] report about an optimum of the photocatalytic activity when examined as a function of increasing catalyst loading, which is primarily a function of the reactor design. At higher catalyst loadings, the advantage of more active surface sites has to be traded against the disadvantages of increasing light scattering in suspension as well as the stronger particle aggregation, which leads to a decrease in surface area. Thus, an optimum catalyst loading results. However, Abdullah et al.^[99] report that the optimum catalyst loading is also a function of the pH value and the concentrations of the reactants and other ions in solution.

A similar trend is found for the co-catalyst loading also exhibiting a specific maximum dependent on the intrinsic ability of the photocatalyst regarding charge separation, but not dependent on the reactor design. If this intrinsic ability is provided only insufficiently by the photocatalyst itself, applying a higher amount

of co-catalyst countervails by strengthening the attracting forces exerted on photogenerated electrons. As soon as the co-catalyst loading is adjusted too high, more and more co-catalyst particles cover the surface absorbing photons and thus, inhibiting the excitation of the actual photocatalyst. Moreover, only the reductive redox reaction consuming photogenerated electrons is supplied by the co-catalyst system. The oxidative reaction consuming the corresponding holes has to be performed at free active surface sites of the mixed oxide photocatalyst.

- There exists also an optimum for the light intensity, which indeed again depends on the reactor design. For comparably small light intensities, the photocatalytic activity increases proportionally with increasing illumination intensity. At higher intensities, the increase in activity is only proportional to the square root of the light intensity due to a significant increase of the charge carrier concentration in the semi-conductor leading to a higher recombination rate, as found by Wei and Wan^[100].
- The reaction rate r_{rxn} of a photocatalytic reaction is also influenced by the reaction temperature as described by the standard equation of Arrhenius:

$$-r_{rxn} = A_{app} \cdot e^{-E_A/RT} \quad (18)$$

To transfer this concept into the field of photocatalysis, the variable A_{app} is determined to be a function of the light intensity, the concentrations of relevant species in solution and in the gas phase, the pH value and the catalyst loading. An important difference to thermally activated reactions exists in the fact that photocatalytic reactions need by far less activation energy E_A , because active surface sites are involved in the mechanism. The most important difference consists in the feasibility of endergonic reactions being thermodynamically unfavored, but facilitated in photocatalysis by utilizing the energy provided by irradiated photons.

2.6 Photocatalyst evaluation

2.6.1 Photonic efficiency^[101]

In order to compare different photocatalysts, a definition for the efficiency of a photocatalytic process has to be established. The universal *energy conversion efficiency* used for evaluation of solar cells is very difficult to access in photocatalysis, as the wavelength dependency of a photocatalytic process can only be analyzed by an action

spectrum^[102], which is very time-consuming and needs a special experimental setup. Even the *overall quantum yield* $\Phi_{overall}$ expressed as the rate of reaction to the rate of absorbed photons is hard to access, as the processes of reflection, scattering and transmission occurring in the suspension have to be known. Thus, the *actual photonic efficiency* ζ_{actual} defined by dividing the rate of photocatalytic reaction steps by the rate of photons incident inside the reaction cell is used. Only the particular wavelength region is considered, which can in principle lead to an excitation of the photocatalyst. As secondary optical processes like scattering are not part of the *actual photonic efficiency*, the value of ζ_{actual} is always lower than the *overall quantum yield* and can be considered as lower limit.

The rate of photons reaching the reaction cell called photon flux can be quantified by the potassium ferrioxalate actinometry^[103]. The absorbance of the actinometer solution can only be adjusted marginally by changing its concentration and/or the optical path length of the reactor. The ferrioxalate actinometry quantifies the amount of photons in the spectral region ranging from 200 nm to about 500 nm. As the investigated photocatalysts are only able of absorbing photons up to a wavelength of about 350-400 nm, the calculated photonic efficiencies are underestimated once again. Figure 11 shows the typical irradiation spectrum of a xenon arc lamp. Xenon arc lamps provide a very uniform energy distribution in the spectral range from 200 to 800 nm, by which solar irradiation can be reproduced almost perfectly (cf. to Figure 6).

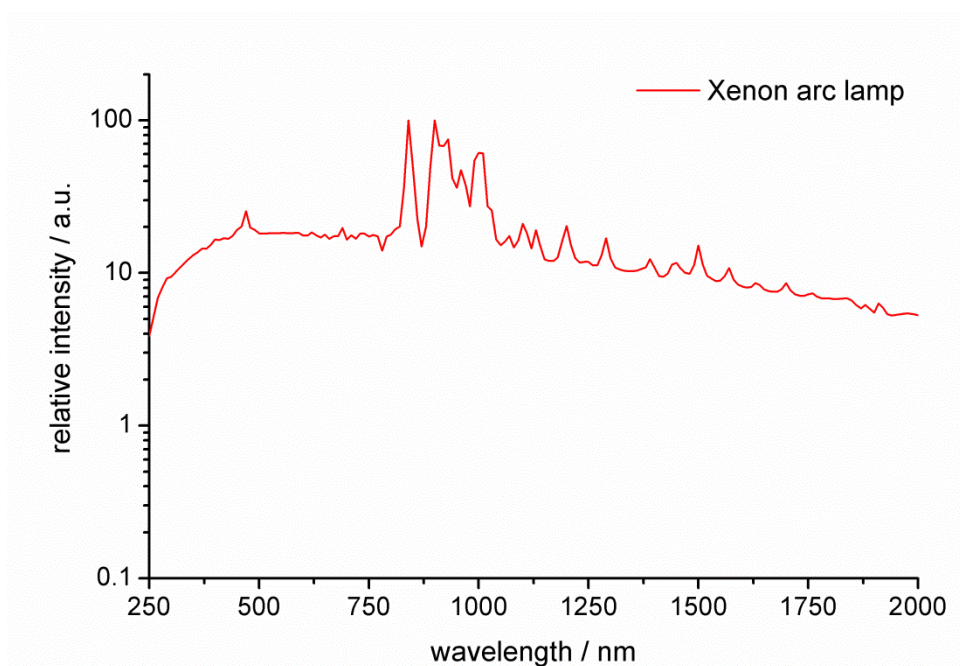


Figure 11: The typical irradiation spectrum of a xenon arc lamp.

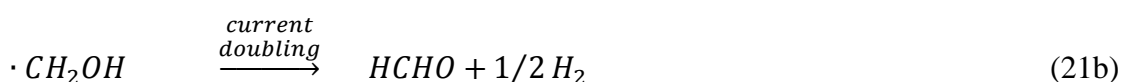
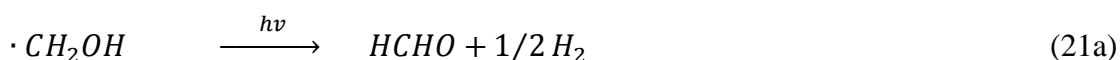
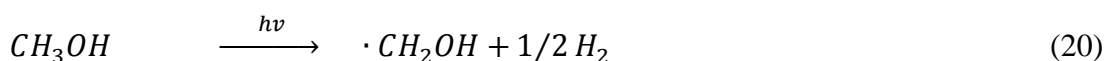
As the formation of a molecule of hydrogen H_2 is a two electron reduction step, the reaction rate should in principle correspond to the doubled hydrogen production rate expressed in $\mu\text{mol/h}$. However, a special mechanism called photocurrent-doubling^[104] (vice versa, chapter 2.6.2) has to be taken into consideration. Current-doubling does not change the definition of the photonic efficiency, but leads to an uncertainty, whether one or two photons are needed to produce one molecule of H_2 . The actual amount of needed photons will most likely lie in between one and two, thus, the photonic efficiency is calculated by assuming one photon per H_2 and again regarded as a lower limit:

$$\zeta(\%) = \frac{\text{hydrogen production rate}}{\text{photon flux}} \times 100 \quad (19)$$

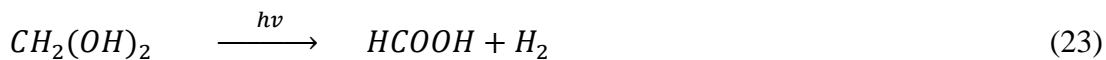
If the methanol concentration is not reduced significantly during the photocatalytic process, the photocatalytic hydrogen production follows pseudo-zero order reaction kinetics resulting in a constant hydrogen production rate. This *actual photonic efficiency* should be almost irrespective of the applied source of illumination, but still a function of the reactor geometry.

2.6.2 The process of photocurrent-doubling

The mechanism of photocurrent-doubling described by Wang et al.^[104] for TiO_2 anatase is expected to occur in the photocatalytic hydrogen production involving the oxidation of methanol while working under oxygen-free conditions. The methanol oxidation mechanism under oxygen-free conditions is given as follows.^[105] After excitation of the semi-conductor, methanol is most likely oxidized to a $\cdot CH_2OH$ radical intermediate (equation 20). The $\cdot CH_2OH$ radical intermediate may be converted into formaldehyde by a conventional photocatalytic step (equation 21a) or by the dark process of electron injection into the conduction band of the semi-conductor called photocurrent-doubling (equation 21b). As electron injection into the conduction band of TiO_2 anatase is thermodynamically allowed and the conduction bands of the investigated pyrochlore titanates consist of unoccupied $Ti3d$ orbitals as well, electron injection is considered possible for all materials.



After oxidation of methanol to formaldehyde, the latter can be further oxidized leading to HCOOH and finally to CO₂^[106, 107] with both of these processes involving the current-doubling mechanism once again.



In conclusion, current-doubling facilitates the formation of molecular hydrogen H₂ involving two electron reduction per absorption of a single photon. As radical intermediates might be oxidized by photogenerated holes in the normal photocatalytic manner as well, the actual amount of needed photons will most likely lie in between one and two.

3 Experimental

3.1 Analytical methods

The materials probed in photocatalytic hydrogen production were characterized by the techniques of powder X-ray diffraction, UV-vis reflectance spectroscopy, CHN elemental analysis, nitrogen adsorption and electron microscopy.

3.1.1 Nitrogen adsorption using the BET model

In order to determine the specific surface area of the used photocatalysts, nitrogen adsorption measurements were performed. An adsorption isotherm is obtained by examining the adsorbed amount of nitrogen as a function of the nitrogen partial pressure at a constant temperature. Based on the properties of the materials, Brunauer classified five kinds of isotherms. As the synthesized catalysts obtained by aqueous sol-gel synthesis do not provide an ordered pore system, the corresponding adsorption isotherms correspond to type II^[108, 109], which do not show a hysteresis loop at high partial pressures.

The BET model invented by Brunauer, Emmett and Teller^[110], describes multi-layer adsorption on a homogenous surface. The gas volume V_m necessary for monolayer coverage of the surface is given by the BET equation:

$$\frac{p/p_0}{V_a(1-p/p_0)} = \frac{1}{V_m C} + \frac{C-1}{V_m C} \cdot \frac{p}{p_0} \quad (25)$$

The specific surface O_{sp} is calculated by multiplying the monolayer volume V_m by the Avogadro constant N_A and by the area on the surface needed per adsorbed nitrogen molecule a_m (0.162 nm²)^[111]:

$$O_{sp} = V_m \cdot N_A \cdot a_m \quad (26)$$

The BET measurements were performed by a Quantachrome Autosorb 3B apparatus applying the multi-point measuring method. The nitrogen adsorption/desorption isotherms were collected at 77 K. Prior to the adsorption measurements the samples were degased at 473 K for 24 hours.

3.1.2 Diffuse UV-vis spectroscopy

If a photon hits a surface consisting of very small particles, several processes may occur, in which the photon transfers more or less energy into the lattice of the particles. Firstly, a photon might be reflected directly on the surface of the particle. Moreover, the photon might be scattered on the particle, either in reflection or in transmission. Lastly, the photon might be absorbed by the particle.

Kubelka and Munk invented a theory in order to describe the behavior of scattering and absorption in solids. The sample has to be as thick as transmission is inhibited. Thus, a correlation between the ability of reflection (R_∞) and the quotient of absorption (K) and scattering (S) is obtained, referred to as the Kubelka-Munk function $F(R_\infty)$.

$$\frac{K}{S} = \frac{(1-R_\infty)^2}{2 \cdot R_\infty} \equiv F(R_\infty) \quad (27)$$

The knowledge of the Kubelka-Munk function facilitates the calculation of the band gap energy E_{bg} . Close to the absorption edge, the band gap energy E_{bg} is directly proportional to the reciprocal optical absorption coefficient α . This empirical relation is known as the Tauc-plot^[112-114].

$$\alpha \cdot hv \propto const(hv - E_{bg})^n \quad (28)$$

The reciprocal optical absorption coefficient α itself is proportional to the Kubelka-Munk function (R_∞):

$$(F(R_\infty) \cdot hv)^{1/n} \propto const(hv - E_{bg}) \quad (29)$$

The exponent n values to 2 for an indirect band gap transition, whereas a direct transition leads to $n = 1/2$. If an indirect band gap transition exists, which counts for all materials crystallizing in the pyrochlore structure, the band gap energy is obtained from the intersection point of the linear part of the plot $(F(R_\infty) \cdot hv)^{1/2}$ vs. hv with the energy axis.

The UV-vis diffuse reflectance spectra were measured on a Varian Cary 4000 UV-vis spectrophotometer in the spectral range from 200 – 800 nm utilizing an Ulbricht sphere. In order to fulfill the Lambert-Beer equation^[115], the scattered radiation is reflected at the inner surface of an Ulbricht sphere^[116] very frequently, by what an almost ideal diffusivity is achieved when leaving the sphere.

3.1.3 X-ray diffraction (XRD)

In X-ray diffraction, electrons emitted from a tungsten filament are accelerated onto a copper anode leading to the generation of Cu K α X-ray radiation ($\lambda_{K\alpha} = 1.54 \text{ \AA}$), which is focused on the probe. As the wavelength corresponds closely to the distances of lattice planes d in solids, the Cu K α radiation is diffracted. If the difference in path length of two diffracted X-ray photons corresponds to a multiple of the wavelength, a glancing angle is accomplished, constructive interference results and the Bragg law is fulfilled^[117]. The interference is of a destructive character if the Bragg law is not fulfilled.

$$n \cdot \lambda = 2d \cdot \sin\theta \quad (30)$$

Based on the lattice plane distances d and the indexing of the X-ray reflections, the lattice structure can be solved. The correlation between a particular lattice plane distance d , the corresponding Miller indices h, k, l and the lattice parameter a in the cubic pyrochlore structure (SG: $Fd3m$) is given as follows:

$$\frac{1}{d_{h,k,l}^2} = \frac{h^2+k^2+l^2}{a^2} \quad (31)$$

The X-ray powder diffraction was performed at room temperature with Cu K α radiation on a Bruker D8 Advance instrument in the 2θ range of $10^\circ - 80^\circ$ in Bragg-Brentano geometry (θ - θ scan). The stepsize was chosen to be 0.02° and 1.5 seconds was accounted for time per step. A fixed divergence slit of 0.3° was applied. In order to minimize scattered radiation, soller slits of 2.5° were applied on the X-ray tube side as well as on the detector side. An ultrafast Lynx-Eye *linear position-sensitive detector* (linear PSD) is applied permanently counting the diffracted radiation in a 2θ region of 3° .

3.1.4 Rietveld refinement method

Some properties of a solid, namely the crystal symmetry and the lattice parameter can be directly obtained from the X-ray diffraction data without utilizing the Rietveld refinement, as these properties are only determined by the angular positions of the reflections, but not of their intensities. For determination of the average crystallite size only the peak shape of reflections, i. e., the *full width at half maximum* (FWHM) is of interest, but not the angular position. However, these properties can also be analyzed by means of the Rietveld refinement method more easily. Moreover, the Rietveld refinement method also provides the feasibility of performing a quantitative analysis and of calculating the microstructure with both depending on the angular positions and the

X-ray intensities of the reflections as well as on the chemical composition. Even if a space group is pre-determined like $Fd\bar{3}m$ in the case of the cubic pyrochlore structure, there exists a variety of possible crystallographic positions in the lattice. Some symmetry relevant positions have to be occupied; some other positions might be occupied and might be additionally free in positioning of one crystallographic parameter. Usually, those positions being of high symmetry are occupied. However, if distortions are introduced into a lattice like cations featuring a lone electron pair, these cations might be allowed to deviate slightly from their intended high symmetry position without changing the symmetry at all. In the X-ray diffraction pattern, only the relative intensities of the reflections change, but not their angular positions. If the multiplicity of the crystallographic position is changed in the course of such a transition, the occupation number is changed as well. The Rietveld refinement method provides the exact determination of occupied crystallographic positions in the lattice and their occupation numbers by which also the geometry of coordination polyhedra can be constructed. As the applicability of X-ray diffraction is determined by the atomic scattering factor^[118], which increases markedly with increasing atomic number, the changes in the cationic sublattice can be far better identified than changes in the oxygen sublattice.

The Rietveld refinements were conducted using TOPAS V4.2 from Bruker AXS. The Cu $K\alpha$ radiation is simulated using the Cu- $K\alpha$ -5 emission profile assembled by Berger providing the significant contributions of copper $K\alpha_1$, $K\alpha_2$ and $K\alpha_3$ by fitting five wavelengths. The background is fitted by the combination of a Chebyshev polynomial function of 7th order and a $1/x$ function emulating the contribution of the primary beam. A Lorentz polarization (LP) factor of 0 was pre-determined and the zero error was allowed to refine. For each Rietveld refinement, a structure file was developed including initial values for crystallographic positions, occupation numbers and the lattice parameter. All initial structure files applied for describing a $A_2B_2O_6O'$ pyrochlore are based on the structure of $Y_2Ti_2O_7$ published by Knop et al.^[25] exhibiting no distortions in the lattice, while placing the ions on highly symmetrical crystallographic positions with yttrium occupying the crystallographic origin at the Wyckoff site $16c$ (with the coordinates of 0, 0, 0). The structure file is summarized in Table 2.

Wyckoff site		ion	coordinates			occupancy	thermal expans. coeff.
			x	y	z		
A	$16c$	Y^{3+}, Bi^{3+}	0	0	0	1	1
B	$16d$	Ti^{4+}	1/2	1/2	1/2	1	1
O	$48f$	O^{2-}	$x(0.4201)$	1/8	1/8	1	1
O'	$8a$	O^{2-}	1/8	1/8	1/8	1	1

Table 2: Summary of the crystal information file of $Y_2Ti_2O_7$ published by Knop et al.^[25] proposing a highly symmetric structure.

The Wyckoff sites of $16c$ (0, 0, 0), $16d$ (1/2, 1/2, 1/2) and $8a$ (1/8, 1/8, 1/8) occupied in $Y_2Ti_2O_7$ by Y^{3+} , Ti^{4+} and O^{2-} , respectively, are highly symmetric, i.e., these sites do not have any refinable positional parameters. Only the other O anion occupies a site with a positional parameter, namely $48f$ (x , 1/8, 1/8), which is allowed to refine. Knop et al.^[25] predicted an x positional parameter of 0.4201 and a lattice parameter of 10.095 Å for $Y_2Ti_2O_7$. As no reliable data were available for the thermal behaviour of yttrium bismuth titanate pyrochlores, the thermal expansion coefficients were fixed to 1 in all refinements. For the calculation of average crystallite sizes, the Rietveld method utilizes the Scherrer equation describing a broadening of the peak profile with decreasing average crystallite size.

$$D \approx \frac{k \cdot \lambda_{K\alpha}}{\beta \cdot \cos\theta} \quad (32)$$

In the Scherrer equation, an average crystallite size D is assigned to the integrated peak width β considering the wavelength of Cu $K\alpha$ radiation $\lambda_{K\alpha}$ and the Scherrer constant k valuing to 0.89 for crystallites with spherical shape^[119]. To determine the integrated peak width, the reflection peak is fitted with a Lorentz function.

However, under real conditions, also the diffractometer itself makes a contribution to the peak broadening. This deviation is automatically corrected by the Rietveld refinement program superseding a reference measurement with a silicon single crystal. To achieve reliable results with the Scherrer equation, the average crystallite size may not exceed 100 nm.

Based on pre-determined parameters and a particular number of refinable variables, the Rietveld refinement method simulates a crystal lattice and the corresponding X-ray diffraction pattern, which is subsequently compared to the measured one. By altering the refinable variables, the combination of variables is presumed as fitting best, if the smallest deviation between calculated and measured pattern is achieved. The quality of a Rietveld refinement may be evaluated by the goodness of fit value (GOF), which is

calculated as the quotient of the weighted profile R-factor R_{wp} and the expected R-factor R_{exp} . Measurement parameters like step size and time per step have a significant influence on the R_{exp} . In order to achieve a reliable structure, the number of refinable variables should be as low as possible and the number of induced restrictions should be as high as possible. Introducing a higher amount of refinable variables will indeed lead to a better *GOF* value, but it may also lead to misleading results.

3.2 Photocatalysis setup

For the photocatalytic test reactions, a 100 mL quartz reactor equipped with a cooling mantle maintaining the temperature of the reaction mixture at 288 K was used. The irradiation was conducted by a LOT Oriel 300 W xenon arc lamp equipped with a 10 cm water filter bath to intercept photons of the IR region and hence prevent heat effects. The reaction was performed in a flow-through reactor system connected to a Shimadzu GC-2014 gas chromatograph (GC) as shown in Figure 12.

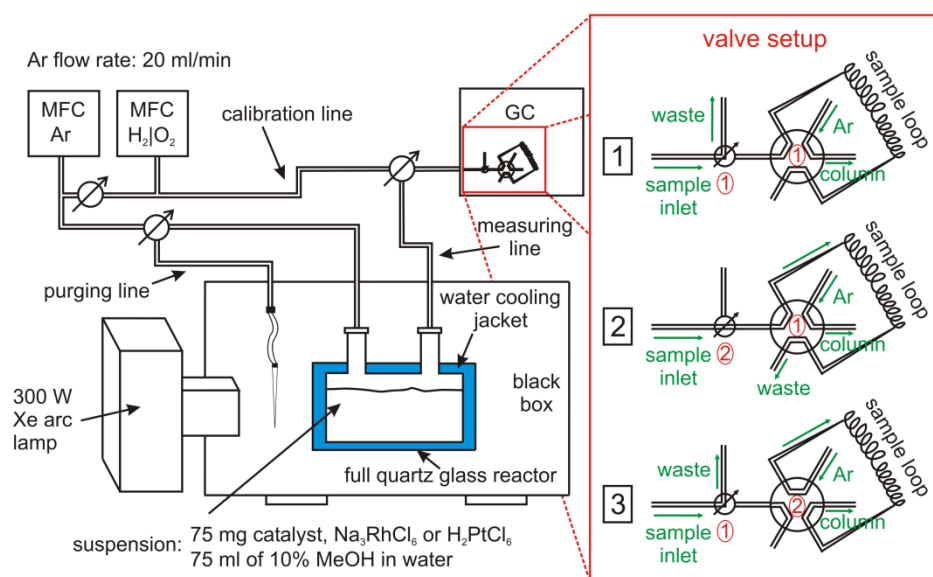


Figure 12: Photocatalysis setup used for the photocatalytic reactions of overall water splitting and hydrogen production with methanol acting as sacrificial reagent. The different states captured by the special valve setup, which is installed in the gas chromatograph, are shown on the right-hand side.

As the photocatalytic reactions are performed in a flow through reactor system, the setup is equipped with a calibration line facilitating a calibration of the gas chromatograph with Ar/H₂ and Ar/O₂ mixtures of different compositions. As the H₂ and O₂ concentrations reaching the GC during reaction were very low, gas bottles with argon gas mixtures

containing 5 % H₂ or 6 % O₂ were used and further diluted with Ar for calibration. Pre-calibrated Bronkhorst Mättig mass flow controllers were applied for regulating the flow rates of gases. A three-way valve fed the Ar flow either into the reactor or into the purging line realized by a syringe, which is used for degasing the suspension prior to illumination. Except of the syringe the whole system is built up from stainless steel tubings from Swagelok. The introduced Ar flow of defined flow rate is mixed with H₂ and/or O₂ in the quartz reactor and the concentrations are determined by GC. The overall flow rate reaching the GC is slightly increased by the gases produced by photocatalysis, which is already considered in the calibration procedure.

The gas stream reaching the GC exhibits a pressure being dependent on the amounts of products formed. Thus, a special self-assembled valve setup had to be utilized consisting of a three-way valve and a 6-port valve both being tempered at 423 K. The different states of valve switching are shown on the right-hand side of Figure 12. In state 1 the valves are in standard conditions representing the period between two measurements in which the gas stream is directly conducted to the outlet. The pre-run is started by purging the sample loop (500 µL) for 4 minutes by switching the three-way valve leading to state 2. Switching the three-way valve back induces pressure compensation against outer atmosphere in the sample loop (state 1). After 30 seconds, the gas volume of defined pressure captured in the sample loop is injected into the column by switching the 6-port valve (state 3) and the measurement itself is started. A micro-packed column (ShinCarbon ST 100/120, Restek) was used. As the photocatalytic reactions are performed under Ar stream, the GC is operated with Ar as carrier gas as well.

In each GC measurement, the separation of permanent gases of H₂ and/or O₂ is conducted in the first 5 minutes of retention time at 308 K. Afterwards, the temperature is increased to 408 K (135 °C) with a ramp of 50 K/min and the temperature is held for 2 minutes to desorb water from the column. Water desorption after each measurement is inevitable for the long-term stability of a column when operated under water rich gas streams. The high water content leads to the disadvantage of carbon dioxide being no longer separable by the column, which makes a quantification of CO₂ impossible. Finally, the temperature is again decreased to 308 K by -10 K/min and held for additional 5 minutes. Considering the pre-run phase of 5 minutes and an equilibrium time needed by the GC of one minute, the GC measurement needs 30 minutes at all, which determines the time interval between two measurements. However, adequate information about the co-catalyst photodeposition as well as the consistency of photocatalytic H₂ production rates was gathered.

3.2.1 Photocatalytic hydrogen production using blank co-catalysts

The determination of the photocatalytic H₂ production rate was performed in 75 mL of an aqueous solution containing 10 vol.-% of methanol corresponding to a methanol concentration of 2.47 mol/L. In a typical run, 75 mg of the photocatalyst were added to the methanol/water mixture containing an appropriate amount of Na₃RhCl₆·6H₂O or H₂PtCl₆·6H₂O previously prepared as highly diluted aqueous solutions containing 100 mg salt per 100 mL. Co-catalyst loadings of 0.40 %, 0.75 %, 1.35 %, 2.00 %, 3.00 % and 4.00 % regarding the wt.-% of pure metal were applied and the needed volumes of co-catalyst solutions are given in the appendix in Table A1. The suspension was left at the natural pH value adjusted by the Pt- or Rh-salt. De-aeration was achieved by bubbling argon into the solution using the purging line with a flow rate of 50 mL/min over a period of 45 minutes. A blind measurement was performed after de-aeration to prove oxygen free conditions followed by adjusting the Ar-flow rate to 20 mL/min using the measuring line and turning on the light source. The photocatalytic reaction was performed for a total time of 300 minutes. The co-catalysts rhodium or platinum were photodeposited within the initial phase of irradiation. Depending on the photocatalyst, the photodeposition phase was sometimes completed within 30 minutes or needed more than 300 minutes. The gas stream leaving the reactor was analyzed at irradiation time intervals of 30 minutes to gather adequate information about the co-catalyst photodeposition as well as the consistency of photocatalytic H₂ production rates.

3.2.2 Photocatalysis using Cr₂O₃-shelled co-catalysts

Beside the blank metal co-catalysts, also the metal/Cr₂O₃ core-shell model was tested as co-catalyst on pyrochlore mixed oxides. As the chromium shell cannot be easily deposited within the initial phase of a photocatalytic reaction, the preparation and test procedure is a little bit more complicated. Moreover, the metal/Cr₂O₃ core-shell loaded photocatalysts were tested in overall water splitting and subsequently in hydrogen production using methanol as sacrificial reagent.

The photodeposition of the metal/Cr₂O₃ core-shell co-catalyst system was performed in the same 100 mL quartz reactor used for overall water splitting and the hydrogen producing test reaction. A 100 mg of the photocatalyst were dispersed in 75 mL of a water/methanol (10 vol.-%) mixture containing the appropriate volume of the Na₃RhCl₆·6H₂O or H₂PtCl₆·6H₂O precursor solution. After de-aerating the solution with

a flow rate of 50 mL/min using the purging line for 45 minutes, a blind measurement is performed. As all catalysts were previously tested in hydrogen production under aid of methanol, the specific time of complete co-catalyst deposition corresponding to the highest temporal activity is well-known. The solution is irradiated for this specific time to deposit the metal core, while measurements of the hydrogen production rate are conducted every 30 minutes for comparison to the previous measurement. Afterwards, the illumination is intercepted and a specific volume of the diluted K_2CrO_4 solution prepared from 500 mg salt per 100 mL is added. The wt.-%-ratio of Cr to metal is adjusted to 1.5. After de-aerating the solution with an Ar flow rate of 50 mL/min for 30 minutes using the measuring line, the illumination is resumed. The Cr_2O_3 photodeposition was conducted over a period of 300 minutes, in which the gas stream of the reactor is analyzed every 30 minutes by gas chromatography. After completed metal/ Cr_2O_3 photodeposition, the photocatalyst is filtrated, thoroughly washed with distilled water and dried overnight. The residual chromium solution is analyzed by UV-vis spectroscopy to determine the actual amount of chromium photodeposited. For overall water splitting, 75 mg of the catalyst were dispersed in 75 mL of pure water and the measurement itself was performed in the same way described for the hydrogen producing test reaction applying methanol as sacrificial reagent (cf. to chapter 3.2.1). After completing the overall water splitting reaction, the metal/ Cr_2O_3 loaded catalyst was allowed to sediment, 7.5 mL of water were exchanged by methanol and the catalyst was further tested in hydrogen production as described in chapter 3.2.1. The applied volumes of Rh-, Pt- and Cr-precursor solutions are given in the appendix in Table A2.

3.2.3 Potassium ferrioxalate actinometry

The photon flux of the LOT Oriel 300 W xenon arc lamp under full arc irradiation was quantified by using the standard potassium ferrioxalate actinometer as initially proposed by Hatchard and Parker. Measurements were carried out under Argon atmosphere and at 293 K in the same 100 mL quartz reactor used for the photocatalytic tests. A 0.02 mol/L potassium ferrioxalate solution was prepared by mixing self-synthesized and twice recrystallized $\text{K}_3\text{Fe}(\text{C}_2\text{O}_4)\cdot 3\text{H}_2\text{O}$ with 0.05 mol/L sulphuric acid under dark conditions. Applying the quartz reactor with an optical path length of 80 mm, the actinometer solution used here is capable of absorbing photons up to a wavelength of 485 nm completely. A 75 mL of the actinometer solution was irradiated for a period of

90 seconds. For the 0.02 mol/L potassium ferrioxalate actinometer solution a quantum efficiency of 1.1 was used.

3.3 Preparation of mixed oxides

3.3.1 Importance of precursor solutions for the sol-gel synthesis

All mixed oxides of $Y_{2-x}Ti_2O_{7-1.5x}$, $(Y_{1.5}Bi_{0.5})_{1-x}Ti_2O_{7-3x}$, $(YBi)_{1-x}Ti_2O_{7-3x}$, $Bi_{2-x}Ti_2O_{7-1.5x}$, $Y_{1.867}Ti_{1.6}Ta_{0.4}O_7$, $Y_{1.867}Ti_{1.8}W_{0.2}O_7$ and, $Y_{1.867}Ti_2O_{6.80}$ doped with Cr^{3+} , Mn^{3+} or Fe^{3+} were prepared by a modified aqueous Pechini sol-gel route^[120]. Citric acid monohydrate and ethylenediaminetetraacetic acid (EDTA) were used as complexing agents. To ensure a high accuracy of the chemical catalyst composition, the cationic sources were taken from precursor solutions made from freshly opened metal nitrate salts. Regarding the main A cations investigated in this study, two precursor solutions, one of yttrium and one of bismuth were prepared by dissolving 48.94 g (0.127 mol) of $Y(NO_3)_3 \cdot 6H_2O$ or 61.99 g (0.127 mol) of $Bi(NO_3)_3 \cdot 5H_2O$ in 500 mL of an aqueous solution ($c_{Y^{3+}, Bi^{3+}} = 0.2556$ mol/L) containing 30 mL of 65% nitric acid, respectively. Addition of nitric acid was necessary for the successful solution of the nitrate salts and hinders the preferred adsorption of cations on the surface of the used PET bottles. Thus, a 25 mL of the precursor solution contains exactly 1.5 mL of 65% nitric acid and 6.39 mmol of yttrium or bismuth, respectively. For an easy handling of the preparation procedure, the needed volumes of yttrium and bismuth precursor solutions were determined to be in total 25 mL. As the cations of Cr^{3+} , Mn^{2+} and Fe^{3+} were only used as dopants of at maximum 1.00 mol-%, the precursor solutions were drastically reduced in concentration by a factor of 100 to 2.556 mmol/L. Thus, 0.205 g (0.51 mmol) of $Cr(NO_3)_3 \cdot 9H_2O$, 0.128 g (0.51 mmol) of $Mn(NO_3)_2 \cdot 4H_2O$ and 0.207 g (0.51 mmol) of $Fe(NO_3)_3 \cdot 9H_2O$ were dissolved in 200 mL of an aqueous solution containing 0.3 mL of 65% nitric acid, respectively. The approach of using precursor solutions clearly improves the reproducibility and is, moreover, inevitable because exposure to air is known to change the content of water of crystallization in nitrate salts over time.

To prepare precursor solutions of metals, which are only available as ethanlates like tantalum and tungsten or as isopropoxides like titanium, high dilution with isopropanol was performed. Prior dilution of metal ethanlates and isopropoxides in isopropanol was found to be inevitable for the successful solubility of the metal sources in the aqueous solution. For the preparation of the alcoholic precursor solutions, 10 g (35.18 mmol) of

Ti(O*i*-Pr)₄, 10 g (24.62 mmol) of Ta(OEt)₅ or 10 g (22.02 mmol) of W(OEt)₆ were diluted in isopropanol up to a total volume of 200 mL, respectively. Thus, the concentrations in Ti⁴⁺, Ta⁵⁺ and W⁶⁺ were determined to be 0.176 mol/L, 0.123 mol/L and 0.110 mol/L, respectively. These isopropanol precursor solutions had to be used up within three days after preparation, as humidity leads to the slow formation of metal hydroxides and oxides over time even if the bottles are sealed tightly. Prior to addition of the metal alkoxide solution into the aqueous medium, this already diluted solution has to be diluted by absolute ethanol again. In a typical synthesis applying about 40 mL of the isopropanol diluted metal source, an additional 100 mL of absolute ethanol is added and this alcoholic mixture is subsequently added into the aqueous solution. This loop way of repeatedly diluted precursor solutions is the only possibility of preventing the alkoxides from preterm hydrolysis in the aqueous media itself or for example in the pipette tips.

3.3.2 Preparation of Y₂Ti₂O₇ with different Ti/Y ratios (Y_{2-x}Ti₂O_{7-1.5x})

The ratio of metal cations to EDTA and citric acid was adjusted to be 1 : 1.05 : 1.5. The typical synthesis of stoichiometric Y₂Ti₂O₇ (Ti/Y ratio of 1.00) is given as follows and the used amounts of chemicals are documented in Table 3. The detailed experimental data for the preparation of the Y_{2-x}Ti₂O_{7-1.5x} series for the Ti/Y ratios of 0.95, 1.05, 1.075, 1.10 and 1.15 leading to Y₂(Y_{0.05})Ti_{1.95}O_{6.97}, Y_{1.90}Ti₂O_{6.86}, Y_{1.86}Ti₂O_{6.80}, Y_{1.82}Ti₂O_{6.73} and Y_{1.74}Ti₂O_{6.61}, respectively, are provided in the appendix in Table A3 to Table A7. To achieve different Ti/Y ratios in Y₂Ti₂O₇ the amount of yttrium is kept constant among the different batches of preparation, whereas the amounts of EDTA, citric acid and of the titanium precursor solution were readjusted appropriately.

	molar mass / g·mol ⁻¹	density / g·cm ³	mass / g	volume / mL	molar amount / mmol	eq.
Y(NO ₃) ₃ ·6H ₂ O	382.91	-	2.45	-	6.39	2
Ti(O- <i>i</i> Pr) ₄	284.23	0.955	1.82	1.90	6.39	2
EDTA	292.25	-	3.92	-	13.42	4.2
C ₆ H ₈ O ₇ ·H ₂ O	210.14	-	4.03	-	19.17	6
Y₂Ti₂O₇	385.50	-	1.23	-	3.195	1

Table 3: Synthesis of Y₂Ti₂O₇ (Ti/Y ratio of 1.00).

In the preparation of stoichiometric Y₂Ti₂O₇, 3.92 g EDTA and 4.03 g citric acid monohydrate were dissolved in a solution containing 300 mL distilled water and

9.25 mL of an aqueous 30% ammonia solution. After injection of 3.0 mL of 65% nitric acid, 25 mL of the $Y(NO_3)_3 \cdot 6H_2O$ precursor solution containing 6.39 mmol yttrium was added to the solution. About 150 mL of the titanium precursor solution containing exactly 6.39 mmol (1.82 g) of $Ti(Oi-Pr)_4$ were added to the mixture. The clear solution was evaporated at 373 K for 18 hours to ca. 50 mL of a light yellowish gel, which was transferred into a calcination basin. Complete decomposition into a black amorphous powder was achieved in a heating mantle at ca. 573 K using an evaporation basin from Haldenwanger (type 130). Finally, the as-prepared amorphous samples were calcined at 1023 K or 1173 K for 4 hours (heating ramp: 100 K/h). A scheme of the synthesis route also applied in all other sol-gel synthesis is given in Figure 13.

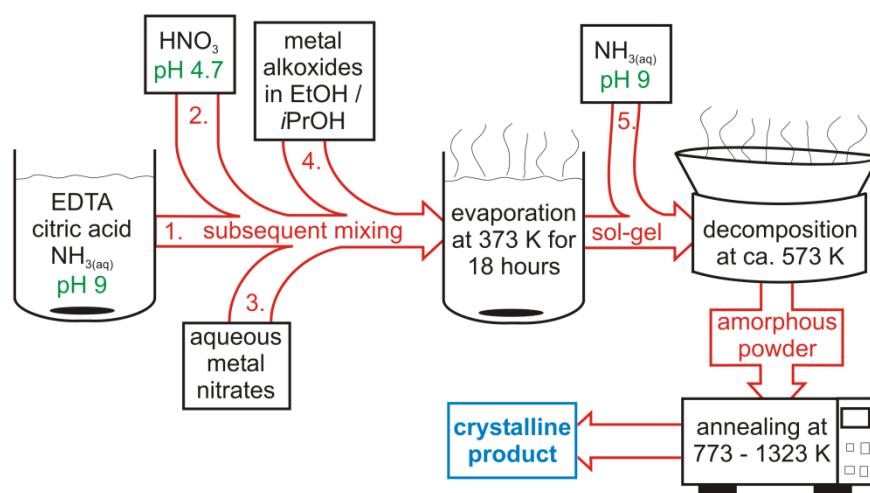


Figure 13: Preparation procedure of mixed oxide pyrochlores via the modified Pechini sol-gel method. Following the presented sequence of additions is mandatory to achieve the solubility of all compounds.

3.3.3 Preparation of $Y_{1.5}Bi_{0.5}Ti_2O_7$ with different $Ti/(Y+Bi)$ ratios $((Y_{1.5}Bi_{0.5})_{1-x}Ti_2O_{7-3x})$

Table 4 presents the typical synthesis of stoichiometric bismuth doped yttrium titanate $Y_{1.5}Bi_{0.5}Ti_2O_7$ ($Ti/(Y+Bi)$ ratio of 1.00). The detailed experimental data for the preparation of the $(Y_{1.5}Bi_{0.5})_{1-x}Ti_2O_{7-3x}$ series for $Ti/(Y+Bi)$ ratios of 0.95, 1.05, 1.10, 1.15 and 1.20 resulting in $(Y_{1.49}Bi_{0.51})(Y_{0.05}Ti_{1.95})O_{6.97}$, $Y_{1.43}Bi_{0.48}Ti_2O_{6.86}$, $Y_{1.36}Bi_{0.45}Ti_2O_{6.73}$, $Y_{1.30}Bi_{0.43}Ti_2O_{6.61}$ and $Y_{1.25}Bi_{0.42}Ti_2O_{6.50}$, respectively, are provided in the appendix in Table A8 to Table A12.

The amounts of yttrium and bismuth were maintained in all batches to obtain a constant yttrium to bismuth ratio of three to one. The different Ti/(Y+Bi) ratios in $Y_{1.5}Bi_{0.5}Ti_2O_7$ were obtained by adjusting the amounts of EDTA, citric acid and of the titanium precursor solution used in the preparation appropriately. The ratio of metal cations to EDTA and citric acid was adjusted to be 1 : 1.05 : 1.5.

	molar mass / g·mol ⁻¹	density / g·cm ⁻³	mass / g	volume / mL	molar amount / mmol	eq.
Y(NO ₃) ₃ ·6H ₂ O	382.91	-	1.84	-	4.79	1.5
Bi(NO ₃) ₃ ·5H ₂ O	485.07	-	0.77	-	1.60	0.5
Ti(O-iPr) ₄	284.23	0.955	1.82	1.90	6.39	2
EDTA	292.25	-	3.92	-	13.42	4.2
C ₆ H ₈ O ₇ ·H ₂ O	210.14	-	4.03	-	19.17	6
Y_{1.5}Bi_{0.5}Ti₂O₇	445.54	-	1.42	-	3.195	1

Table 4: Synthesis of $Y_{1.5}Bi_{0.5}Ti_2O_7$ (Ti/(Y+Bi) ratio of 1.00).

The preparation of stoichiometric $Y_{1.5}Bi_{0.5}Ti_2O_7$ is given exemplarily as follows. A 3.92 g of EDTA and a 4.03 g of citric acid monohydrate were dissolved in a solution containing 300 mL distilled water and 9.25 mL of an aqueous 30% ammonia solution. After injection of 3.0 mL of 65% nitric acid, 18.75 mL of the Y(NO₃)₃·6H₂O precursor solution containing 4.79 mmol of yttrium and 6.25 mL of the Bi(NO₃)₃·5H₂O precursor solution containing 1.60 mmol of bismuth were added to the solution. About 150 mL of the titanium precursor solution containing exactly 6.39 mmol (1.82 g) of Ti(O*i*-Pr)₄ were added to the mixture. The clear solution was evaporated at 373 K for 18 h to ca. 50 mL of a yellowish gel, which was transferred into a calcination basin. Complete decomposition into a black amorphous powder was achieved in a heating mantle at ca. 573 K using an evaporation basin from Haldenwanger (type 130). Finally, the as-prepared amorphous samples were calcined at 1023 K or 1173 K for 4 hours (heating ramp: 100 K/h).

3.3.4 Preparation of $YBiTi_2O_7$ with different Ti/(Y+Bi) ratios ($(YBi)_{1-x}Ti_2O_{7-3x}$)

Table 5 presents the typical synthesis of stoichiometric bismuth yttrium titanate $YBiTi_2O_7$ (Ti/(Y+Bi) ratio of 1.00). The increased amount of bismuth in the structure leads to the ability of tolerating a much higher amount of excess titanium in the pyrochlore. The detailed experimental data for the preparation of the series of

(YBi)_{1-x}Ti₂O_{7-3x} samples for Ti/(Y+Bi) ratios of 1.10, 1.15, 1.20, 1.25 and 1.30 resulting in stoichiometries of Y_{0.91}Bi_{0.91}Ti₂O_{6.73}, Y_{0.87}Bi_{0.87}Ti₂O_{6.61}, Y_{0.83}Bi_{0.83}Ti₂O_{6.50}, Y_{0.80}Bi_{0.80}Ti₂O_{6.40} and Y_{0.77}Bi_{0.77}Ti₂O_{6.31}, respectively, are provided in the appendix in Table A13 to Table A17.

The amounts of yttrium and bismuth were kept constant in all batches to maintain an equimolar ratio between yttrium and bismuth. The different Ti/(Y+Bi) ratios in YBiTi₂O₇ were obtained by adjusting the amounts of EDTA, citric acid and of the titanium precursor solution used in the preparation appropriately. The ratio of metal cations to EDTA and citric acid was adjusted to be 1 : 1.05 : 1.5.

	molar mass / g·mol ⁻¹	density / g·cm ⁻³	mass / g	volume / mL	molar amount / mmol	eq.
Y(NO ₃) ₃ ·6H ₂ O	382.91	-	1.22	-	3.20	1
Bi(NO ₃) ₃ ·5H ₂ O	485.07	-	1.55	-	3.20	1
Ti(O-iPr) ₄	284.23	0.955	1.82	1.90	6.39	2
EDTA	292.25	-	3.92	-	13.42	4.2
C ₆ H ₈ O ₇ ·H ₂ O	210.14	-	4.03	-	19.17	6
YBiTi₂O₇	505.58	-	1.62	-	3.195	1

Table 5: Synthesis of YBiTi₂O₇ (Ti/(Y+Bi) ratio of 1.00).

The preparation of stoichiometric YBiTi₂O₇ is given exemplarily as follows. A 3.92 g of EDTA and a 4.03 g of citric acid monohydrate were dissolved in a solution containing 300 mL distilled water and 9.25 mL of an aqueous 30% ammonia solution. After injection of 3.0 mL of 65% nitric acid, 12.5 mL of the Y(NO₃)₃·6H₂O precursor solution and 12.5 mL of the Bi(NO₃)₃·5H₂O precursor solution each containing 3.20 mmol of yttrium or bismuth, respectively, were added to the solution. About 150 mL of the titanium precursor solution containing exactly 6.39 mmol (1.82 g) of Ti(O*i*-Pr)₄ were added to the mixture. The clear solution was evaporated at 373 K for 18 h to ca. 50 mL of a yellowish gel, which was transferred into a calcination basin. Complete decomposition into a black amorphous powder was achieved in a heating mantle at ca. 573 K using an evaporation basin from Haldenwanger (type 130). Finally, the as-prepared amorphous samples were calcined at 873 K, 1023 K or 1173 K for 4 hours, respectively (heating ramp: 100 K/h).

3.3.5 Preparation of bismuth titanates with different Ti/Bi ratios ($\text{Bi}_{2-x}\text{Ti}_{0.75x}\text{Ti}_2\text{O}_7$, $\text{Bi}_4\text{Ti}_3\text{O}_{12}$ and $\text{Bi}_2\text{Ti}_4\text{O}_{11}$)

The ratio of metal cations to EDTA and citric acid was adjusted to be 1 : 1.05 : 1.5. The typical synthesis of stoichiometric $\text{Bi}_2\text{Ti}_2\text{O}_7$ (Ti/Bi ratio of 1.00) is given as follows and the used amounts of chemicals are documented in Table 6. The detailed experimental data for the preparation of the $(\text{Bi}_{2-x}\text{Ti}_{0.75x})\text{Ti}_2\text{O}_7$ series for the Ti/Bi ratios of 1.20, 1.25, 1.30, 1.35, 1.40, 1.45 and 1.50 leading to $(\text{Bi}_{1.79}\text{Ti}_{0.15})\text{Ti}_2\text{O}_7$, $(\text{Bi}_{1.75}\text{Ti}_{0.19})\text{Ti}_2\text{O}_7$, $(\text{Bi}_{1.71}\text{Ti}_{0.22})\text{Ti}_2\text{O}_7$, $(\text{Bi}_{1.67}\text{Ti}_{0.25})\text{Ti}_2\text{O}_7$, $(\text{Bi}_{1.63}\text{Ti}_{0.28})\text{Ti}_2\text{O}_7$, $(\text{Bi}_{1.59}\text{Ti}_{0.31})\text{Ti}_2\text{O}_7$ and $(\text{Bi}_{1.55}\text{Ti}_{0.33})\text{Ti}_2\text{O}_7$, respectively, are provided in the appendix in Table A18 to Table A24. To obtain different Ti/Bi ratios in the $(\text{Bi}_{2-x}\text{Ti}_{0.75x})\text{Ti}_2\text{O}_7$ series, the amount of bismuth precursor solution is kept constant among the different batches of preparation, whereas the amounts of EDTA, citric acid and of the titanium precursor solution were readjusted appropriately. The preparation of other stoichiometric bismuth titanate phases, that is $\text{Bi}_4\text{Ti}_3\text{O}_{12}$ and $\text{Bi}_2\text{Ti}_4\text{O}_{11}$, was performed by basically adopting the synthesis of the pyrochlores, but using Ti/Bi ratios of 0.75 and 2.00, respectively. The detailed experimental data are supplied in the appendix in Table A25 and Table A26.

	molar mass / $\text{g}\cdot\text{mol}^{-1}$	density / $\text{g}\cdot\text{cm}^{-3}$	mass / g	volume / mL	molar amount / mmol	eq.
$\text{Bi}(\text{NO}_3)_3\cdot 5\text{H}_2\text{O}$	485.07	-	3.10	-	6.39	2
$\text{Ti}(\text{O}-i\text{Pr})_4$	284.23	0.955	1.82	1.90	6.39	2
EDTA	292.25	-	3.92	-	13.42	4.2
$\text{C}_6\text{H}_8\text{O}_7\cdot\text{H}_2\text{O}$	210.14	-	4.03	-	19.17	6
$\text{Bi}_2\text{Ti}_2\text{O}_7$	625.65	-	2.00	-	3.195	1

Table 6: Synthesis of $\text{Bi}_2\text{Ti}_2\text{O}_7$ (Ti/Bi ratio of 1.00).

In the preparation of stoichiometric $\text{Bi}_2\text{Ti}_2\text{O}_7$, 3.92 g EDTA and 4.03 g citric acid monohydrate were dissolved in a solution containing 300 mL distilled water and 9.25 mL of an aqueous 30% ammonia solution. After injection of 3.0 mL of 65% nitric acid, 25 mL of the $\text{Bi}(\text{NO}_3)_3\cdot 5\text{H}_2\text{O}$ precursor solution containing 6.39 mmol bismuth was added to the solution. About 150 mL of the titanium precursor solution containing exactly 6.39 mmol (1.82 g) of $\text{Ti}(\text{O}-i\text{Pr})_4$ were added to the mixture. The clear solution was evaporated at 373 K for 18 h to ca. 50 mL of a yellowish gel, which was transferred into a calcination basin from Haldenwanger (type 130).

Due to the high amount of bismuth in the structure, the decomposition of the bismuth titanate gels was very challenging in preventing the formation of the $\text{Bi}_4\text{Ti}_3\text{O}_{12}$ by-phase

to obtain samples of $(\text{Bi}_{2-x}\text{Ti}_{0.75x})\text{Ti}_2\text{O}_7$ free of by-phases. The perovskite $\text{Bi}_4\text{Ti}_3\text{O}_{12}$ forms at temperatures as low as 873 K. As the decomposition of organic gels and the crystallization of bismuth titanates itself are strongly exothermic processes, a once initiated crystallization is self-amplified, cannot be stopped and has to be avoided in its origin. Thus, immediately after complete decomposition of the gel, the resulting hot black amorphous powder was quenched with distilled water. Finally, the amorphous $\text{Bi}_{2-x}\text{Ti}_2\text{O}_{7-1.5x}$ samples were calcined at 773 K and 873 K for 4, 6, 8 or 10 hours, respectively. Interestingly, the $\text{Bi}_4\text{Ti}_3\text{O}_{12}$ by-phase formation in $(\text{Bi}_{2-x}\text{Ti}_{0.75x})\text{Ti}_2\text{O}_7$ samples does not occur at 773 K or 873 K in the controlled environment of the oven. In the case of the chemical compositions of $\text{Y}_{2-x}\text{Ti}_2\text{O}_{7-1.5x}$, $(\text{Y}_{1.5}\text{Bi}_{0.5})_{1-x}\text{Ti}_2\text{O}_{7-3x}$ and $(\text{YBi})_{1-x}\text{Ti}_2\text{O}_{7-3x}$, the high fraction of yttrium of at least 50 % on the A site stabilizes the pyrochlore structure and prevents $\text{Bi}_4\text{Ti}_3\text{O}_{12}$ by-phase formation at temperatures as low as 873 K.

The sample of $\text{Bi}_4\text{Ti}_3\text{O}_{12}$ (Ti/Bi ratio of 0.75) was annealed at 773 K or 873 K for 4 hours and $\text{Bi}_2\text{Ti}_4\text{O}_{11}$ (Ti/Bi ratio of 2.00) was annealed at 873 K, 973 K, or 1073 K for 4 hours, respectively. The annealing of all samples was performed with a heating ramp of 100 K/h.

3.3.6 Preparation of $\text{Y}_{1.86}\text{Ti}_2\text{O}_{6.80}$ doped with Cr^{3+} , Mn^{3+} , Fe^{3+}

Table 7 presents the typical synthesis of stoichiometry optimized yttrium titanate $\text{Y}_{1.86}\text{Ti}_2\text{O}_{6.80}$ (Ti/Y ratio of 1.075) doped with Cr^{3+} , Mn^{3+} or Fe^{3+} . The amounts of yttrium, EDTA and citric acid monohydrate were kept constant for all batches. The amounts of the titanium precursor solution as well as of the dopants $\text{Cr}(\text{NO}_3)_3 \cdot 9\text{H}_2\text{O}$, $\text{Mn}(\text{NO}_3)_2 \cdot 4\text{H}_2\text{O}$, $\text{Fe}(\text{NO}_3)_3 \cdot 9\text{H}_2\text{O}$ and $\text{Ta}(\text{OEt})_5$ were adjusted appropriately. The ratio of overall metal cations to EDTA and citric acid was adjusted to be 1 : 1.05 : 1.5.

The preparation of $\text{Y}_{1.86}\text{Ti}_2\text{O}_{6.80}$ doped with 0.25 mol-% of Cr^{3+} is exemplarily explained as follows. A 4.07 g of EDTA and a 4.18 g of citric acid monohydrate were dissolved in a solution containing 300 mL distilled water and 9.25 mL of an aqueous 30% ammonia solution. After injection of 3.0 mL of 65% nitric acid, 25 mL of the $\text{Y}(\text{NO}_3)_3 \cdot 6\text{H}_2\text{O}$ precursor solution containing 6.39 mmol of yttrium and 6.72 mL of the $\text{Cr}(\text{NO}_3)_3 \cdot 9\text{H}_2\text{O}$ precursor solution containing 0.01717 mmol of chromium were added to the solution. About 150 mL of the titanium precursor solution containing exactly 6.852 mmol (1.948 g) of $\text{Ti}(\text{O}i\text{-Pr})_4$ were added to the mixture. The clear solution was evaporated at

373 K for 18 h to ca. 50 mL of a yellowish gel, which was transferred into a calcination basin. Complete decomposition into a black amorphous powder was achieved in a heating mantle at ca. 573 K using an evaporation basin from Haldenwanger (type 130). Finally, the as-prepared amorphous samples were calcined at 1023 K for 4 hours (heating ramp: 100 K/h).

doping	substance	molar mass / g·mol ⁻¹	density / g·cm ⁻³	mass / g	volume / mL	molar amount / mmol	eq.
0.10 % Cr ³⁺	Cr(NO ₃) ₃ ·9H ₂ O	400.19	-	0.00275	2.69*	0.00687	0.0022
	Ti(O-iPr) ₄	284.23	0.955	1.950	2.04	6.862	2.148
0.25 % Cr ³⁺	Cr(NO ₃) ₃ ·9H ₂ O	400.19	-	0.00687	6.72*	0.01717	0.00538
	Ti(O-iPr) ₄	284.23	0.955	1.948	2.04	6.852	2.145
0.50 % Cr ³⁺	Cr(NO ₃) ₃ ·9H ₂ O	400.19	-	0.01375	13.44*	0.03435	0.01075
	Ti(O-iPr) ₄	284.23	0.955	1.943	2.03	6.835	2.139
1.00 % Cr ³⁺	Cr(NO ₃) ₃ ·9H ₂ O	400.19	-	0.02749	26.88*	0.06869	0.0215
	Ti(O-iPr) ₄	284.23	0.955	1.933	2.02	6.801	2.129
0.25 % Cr ³⁺ , 0.25 % Ta ⁵⁺	Cr(NO ₃) ₃ ·9H ₂ O	400.19	-	0.00687	6.72*	0.01717	0.00538
	Ta(OEt) ₅	406.25	1.566	0.00698	0.0045	0.01717	0.00538
	Ti(O-iPr) ₄	284.23	0.955	1.943	2.03	6.835	2.139
0.25 % Mn ^{2+/3+}	Mn(NO ₃) ₂ ·4H ₂ O	251.01	-	0.00431	6.72*	0.01717	0.00538
	Ti(O-iPr) ₄	284.23	0.955	1.948	2.04	6.852	2.145
0.25 % Fe ³⁺	Fe(NO ₃) ₃ ·9H ₂ O	404.00	-	0.00694	6.72*	0.01717	0.00538
	Ti(O-iPr) ₄	284.23	0.955	1.948	2.04	6.852	2.145
	Y(NO ₃) ₃ ·6H ₂ O	382.91	-	2.45	-	6.39	2
	EDTA	292.25	-	4.07	-	13.92	4.3575
	C ₆ H ₈ O ₇ ·H ₂ O	210.14	-	4.18	-	19.89	6.225
	Y_{1.867}Ti₂O_{6.80}	369.75	-	1.27	-	3.43	1.075

Table 7: Synthesis of Y_{1.867}Ti₂O_{6.80} (Ti/Y ratio of 1.075) doped with Cr³⁺, Mn^{2+,3+}, Fe³⁺. The volumes marked with asterisk refer to the volumes of used Cr³⁺, Mn²⁺ and Fe³⁺ precursor solutions each prepared with a concentration of 2.556 mmol/L.

3.3.7 Preparation of Y_{1.86}Ti_{1.6}Ta_{0.4}O₇ and Y_{1.86}Ti_{1.8}W_{0.2}O₇

Table 8 presents the preparation of stoichiometry optimized Y_{1.86}Ti_{1.6}Ta_{0.4}O₇ and Y_{1.86}Ti_{1.8}W_{0.2}O₇ with a (Ti+Ta+W)/Y ratio of 1.075. The ratio of overall metal cations to EDTA and citric acid was adjusted to be 1 : 1.05 : 1.5.

	molar mass / g·mol ⁻¹	density / g·cm ⁻³	mass / g	volume / mL	molar amount / mmol	eq.
Y(NO ₃) ₃ ·6H ₂ O	382.91	-	2.45	-	6.39	2
Ti(O-iPr) ₄	284.23	0.955	1.56	1.64	5.50	1.72
Ta(OEt) ₅	406.25	1.566	0.56	0.36	1.37	0.43
EDTA	292.25	-	4.07	-	13.92	4.3575
C ₆ H ₈ O ₇ ·H ₂ O	210.14	-	4.18	-	19.89	6.225
Y_{1.86}Ti_{1.6}Ta_{0.4}O₇	426.13	-	1.36	-	3.195	1
Y(NO ₃) ₃ ·6H ₂ O	382.91	-	2.45	-	6.39	2
Ti(O-iPr) ₄	284.23	0.955	1.76	1.84	6.18	1.935
W(OEt) ₆	454.21	-	0.31	-	0.69	0.215
EDTA	292.25	-	4.07	-	13.92	4.3575
C ₆ H ₈ O ₇ ·H ₂ O	210.14	-	4.18	-	19.89	6.225
Y_{1.86}Ti_{1.8}W_{0.2}O₇	400.09	-	1.28	-	3.195	1

Table 8: Synthesis of Y_{1.86}Ti_{1.6}Ta_{0.4}O₇ and Y_{1.86}Ti_{1.8}W_{0.2}O₇ ((Ti+Ta+W)/Y ratio of 1.075).

In the preparation of Y_{1.86}Ti_{1.6}Ta_{0.4}O₇, 4.07 g of EDTA and a 4.18 g of citric acid monohydrate were dissolved in a solution containing 300 mL distilled water and 9.25 mL of an aqueous 30 % ammonia solution. After injection of 3.0 mL of 65 % nitric acid, 25 mL of the Y(NO₃)₃·6H₂O precursor solution were added to the solution. About 150 mL of the titanium-tantalum precursor solution containing exactly 5.50 mmol (1.56 g) of Ti(Oi-Pr)₄ and 1.37 mmol (0.56 g) of Ta(OEt)₅ were added to the mixture. For the preparation of Y_{1.86}Ti_{1.8}W_{0.2}O₇, 150 mL of an titanium-tungsten precursor solution containing exactly 6.18 mmol (1.76 g) of Ti(Oi-Pr)₄ and 0.69 mmol (0.31 g) of W(OEt)₆ were added instead.

The clear solutions were evaporated at 373 K for 18 h to ca. 50 mL of a yellowish gel, which was transferred into a calcination basin. Complete decomposition into a black amorphous powder was achieved in a heating mantle at ca. 573 K using an evaporation basin from Haldenwanger (type 130). Finally, the as-prepared amorphous samples were calcined at 1023 K, 1173 K or 1323 K for 4 hours (heating ramp: 100 K/h).

3.3.8 Preparation of Y₂Ta₂O₅N₂ via the pre-stage of M⁻YTaO₄

The ratio of metal cations to EDTA and citric acid was adjusted to be 1 : 1.05 : 1.5. The typical synthesis of M⁻YTaO₄ is given as follows and the used amounts of chemicals are documented in Table 9.

	molar mass / g·mol ⁻¹	density / g·cm ⁻³	mass / g	volume / mL	molar amount / mmol	eq.
Y(NO ₃) ₃ ·6H ₂ O	382.91	-	2.45	-	6.39	1
Ta(OEt) ₅	406.25	1.566	2.60	1.66	6.39	1
EDTA	292.25	-	3.92	-	13.42	2.1
C ₆ H ₈ O ₇ ·H ₂ O	210.14	-	4.03	-	19.17	3
YTaO₄	333.85	-	2.13	-	6.39	1

Table 9: Synthesis of M⁻-YTaO₄.

In the preparation of M⁻-YTaO₄, 3.92 g EDTA and 4.03 g citric acid monohydrate were dissolved in a solution containing 300 mL distilled water and 9.25 mL of an aqueous 30% ammonia solution. After injection of 4.5 mL of 65% nitric acid, 25 mL of the Y(NO₃)₃·6H₂O precursor solution containing 6.39 mmol yttrium was added to the solution. About 150 mL of the tantalum precursor solution containing exactly 6.39 mmol (2.60 g) of Ta(OEt)₅ were added to the mixture. The clear solution was evaporated at 373 K for 18 h to ca. 50 mL of a yellowish gel, which was transferred into a calcination basin from Haldenwanger (type 130). Finally, the amorphous sample was calcined at 1323 K for 12 hours.

The phase transition from monoclinic M⁻-YTaO₄ into pyrochlore Y₂Ta₂O₅N₂ was achieved by thermal ammonolysis. The crystalline powder of M⁻-YTaO₄ was placed in a corundum sagger, which was deposited in the middle of a quartz tube located in a tube furnace. The furnace was heated to 1223 K (heating ramp: 10 K/min) under Argon atmosphere (flow rate: 50 mL/min). By reaching the final temperature, the Argon flow rate is reduced to 10 mL/min and the ammonia gas flow is adjusted to 60 mL/min. After 15 hours the reaction is completed and the furnace is allowed to cool down under an Argon flow rate of 50 mL/min. Several fritted wash bottles filled with distilled water were used to neutralize the ammonia gas stream leaving the reactor.

4 Results and Discussion

4.1 Non-stoichiometric $Y_2Ti_2O_7$

Non-stoichiometric $Y_2Ti_2O_7$ pyrochlores featuring different Ti/Y ratios ranging from 0.95 to 1.15 were prepared by an aqueous sol-gel method and annealed at different temperatures. The thus synthesized catalysts were characterized by X-ray diffraction, UV-vis reflectance spectroscopy and electron microscopy. The samples were loaded with nanoparticles of rhodium or platinum acting as co-catalysts and tested for photocatalytic hydrogen production in the presence of methanol as sacrificial agent. Varying the annealing temperature and, more importantly, the Ti/Y ratio during the sol-gel preparation induce structural changes in non-stoichiometric pyrochlores of $Y_2Ti_2O_7$. The structural properties of the pyrochlore mixed oxides clearly correlate to the corresponding photocatalytic activities in the hydrogen producing test reaction.

4.1.1 Characterization of non-stoichiometric $Y_2Ti_2O_7$

Stoichiometric $Y_2Ti_2O_7$ crystallizes in the cubic pyrochlore structure (cf. to chapter 2.3). Figure 14 reveals the X-ray diffraction data of stoichiometric $Y_2Ti_2O_7$ calcined at 1173 K for 4h.

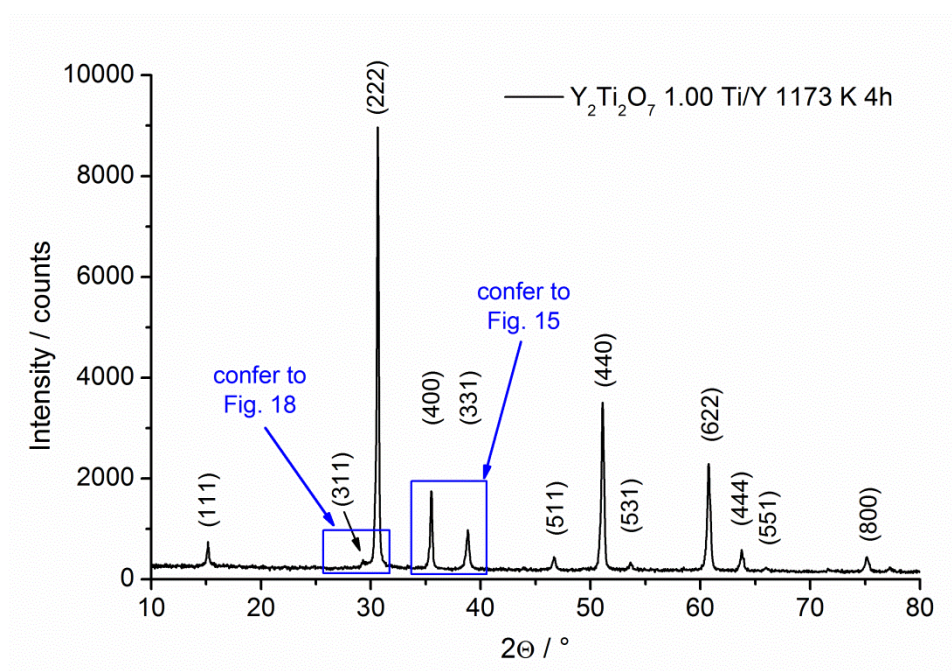


Figure 14: XRD pattern of stoichiometric $Y_2Ti_2O_7$ annealed at 1173 K for 4h.

The observed XRD pattern fits almost perfectly with the published ICSD file (No. 15633) and a lattice parameter of $a = 10.109 \text{ \AA}$ is obtained. The lattice parameter of stoichiometric $\text{Y}_2\text{Ti}_2\text{O}_7$ calcined at 1023 K amounts to 10.121 \AA , thus, undergoes a slight decrease at lower calcination temperature. All investigated samples are entirely crystallized. Changing the ratio between titanium and yttrium from $\text{Ti/Y} = 0.95$ to $\text{Ti/Y} = 1.15$ does not influence the stability of the pyrochlore phase itself, while, however, the structural composition as well as the phase purity change. Two regions of the XRD pattern are of special interest. Since small amounts of rutile are formed as a by-phase at high Ti/Y ratios, the phase purity is investigated in the 2θ region from 26° to 32° , which will be discussed below (vide infra, insets of Figure 18).

Moreover, in the ideal pyrochlore structure of $\text{Y}_2\text{Ti}_2\text{O}_7$, yttrium (A-site) and titanium (B-site) are strictly placed on different crystallographic positions. The degree of cationic disorder can be assigned to the amount of comparatively larger Y^{3+} ions occupying the B-site of the structure leading to a shift of the lattice parameter to higher values as well as to a change in the relative intensities in the X-ray diffraction pattern. Both effects are illustrated qualitatively in Figure 15, which displays the 2θ region of the XRD from 34.75° to 39.5° of $\text{Y}_2\text{Ti}_2\text{O}_7$ 1173 K 4h samples with different Ti/Y ratios in detail (cf. to Figure 14). In the case of the $\text{Y}_2\text{Ti}_2\text{O}_7$ samples calcined at 1023 K, the X-ray diffraction looks similar. The X-ray data will now be discussed in detail.

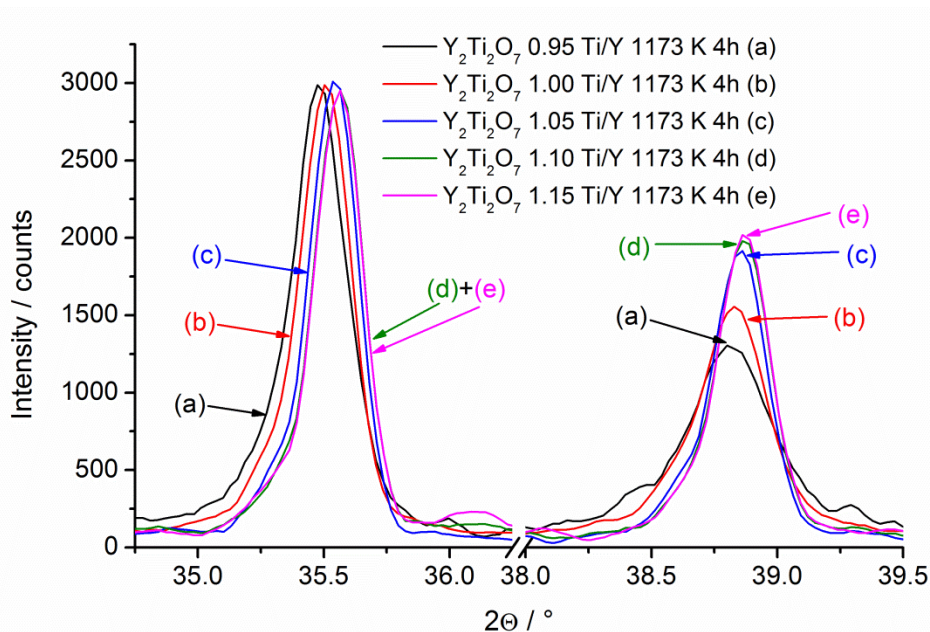


Figure 15: XRD pattern of $\text{Y}_2\text{Ti}_2\text{O}_7$ annealed at 1173 K 4h featuring different Ti/Y ratios in the angular range of $34.5\text{-}39.5^\circ 2\theta$ indicating a decrease in the $I(400)/I(331)$ ratio due to an increasing Ti/Y ratio.

Cationic disorder up to a stochastic distribution of yttrium and titanium leads to a structure transition from the pyrochlore superstructure (space group: $Fd\bar{3}m$) into a defect fluorite structure^[121, 122] (space group: $Fm\bar{3}m$). In order to estimate the degree of cation antisites, the comparison of the intensities of the (400) and (331) reflections is the most promising way^[123]. The (400) reflection is part of the pyrochlore as well as the defect fluorite pattern, whereas the (331) reflection appears in the pyrochlore pattern exclusively. Therefore, the ratio $I(400)/I(331)$ provides the extend of cationic distortion on the B-site ideally occupied by titanium cations. The lower the ratio of the X-ray intensities values, the better yttrium and titanium are separated into their intended lattice positions.

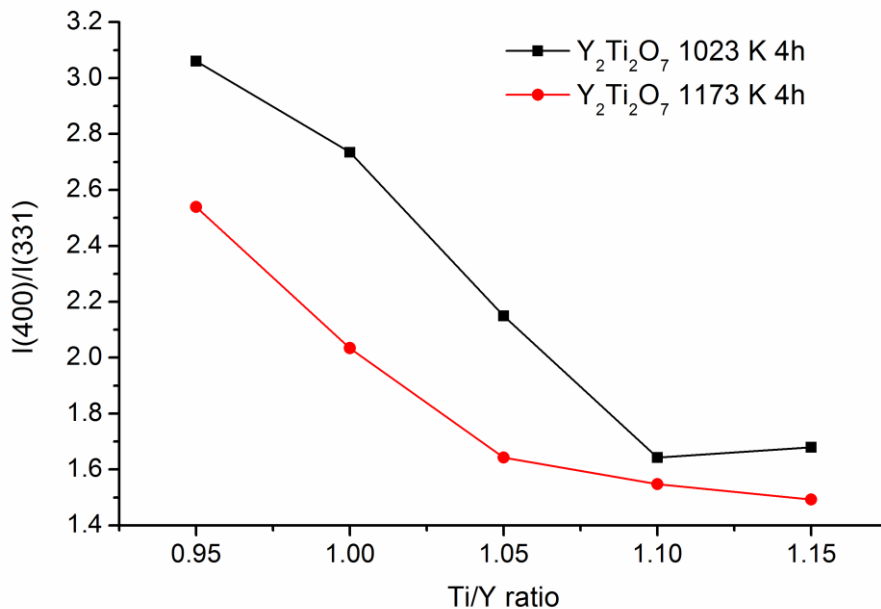


Figure 16: Quotient of the intensities of the (400) and (331) reflections as a function of the Ti/Y ratio for $Y_2Ti_2O_7$ calcined at 1023 K and 1173 K.

Figure 16 shows a plot of the $I(400)/I(331)$ ratio as a function of the Ti/Y ratio for $Y_2Ti_2O_7$ calcined at 1023 K and 1173 K, respectively. The intensity quotient $I(400)/I(331)$ decreases with increasing Ti/Y ratio evincing that cationic distortion is minimized by introducing more titanium into the structure. For the $Y_2Ti_2O_7$ samples calcined at 1023 K the $I(400)/I(331)$ ratio decreases from about 3.10 (Ti/Y = 0.95) to about 1.65 (Ti/Y = 1.10) emphasizing the eminent change in the value as well as in the lattice distortion. Furthermore, the cationic distortion is a function of the annealing temperature, i. e., the cation antisite concentration values much lower, if the calcination is performed at 1173 K. The minimization of cationic antisites requires titanium excesses of

5 % or 10 %, if $\text{Y}_2\text{Ti}_2\text{O}_7$ is annealed at 1173 K or 1023 K, respectively. Under that conditions titanium and yttrium are assumed to be completely separated into their predetermined lattice positions.

Moreover, the concept that the lattice cationic distortion is minimized by employment of a defined titanium excess is supported by analyzing the changes in the lattice parameter, as cationic distortion leads to a broadening of the lattice by “doping” the titanium B-site of the structure with larger yttrium cations. As the effective ionic radius of yttrium exceeds that of the substituted titanium, cationic distortion results in a broadening of the lattice by “doping” the B-site of the structure with yttrium cations thus increasing the lattice parameter. The changes in the values of the lattice parameter are not as significant as those obtained in the comparison of the X-ray diffraction intensities, however, they are most certainly detectable. Figure 17 shows the correlation between the Ti/Y ratio and the lattice parameter for samples calcined at 1023 K and at 1173 K, respectively, obtained by Rietveld refinement of the diffraction data based on the ideal structure of $\text{Y}_2\text{Ti}_2\text{O}_7$ including the refinement of the zero error. The decrease of the Ti/Y ratio leads to an increase of the lattice parameter. It is again found that the cationic lattice distortion is reduced by increasing the annealing temperature, as the lattice parameter values considerable lower, if the samples are annealed at a higher temperature of 1173 K. The lattice parameter reaches a constant value of 10.099 Å at titanium excesses of 5 % and 10 % for $\text{Y}_2\text{Ti}_2\text{O}_7$ annealed at 1173 K and 1023 K, respectively.

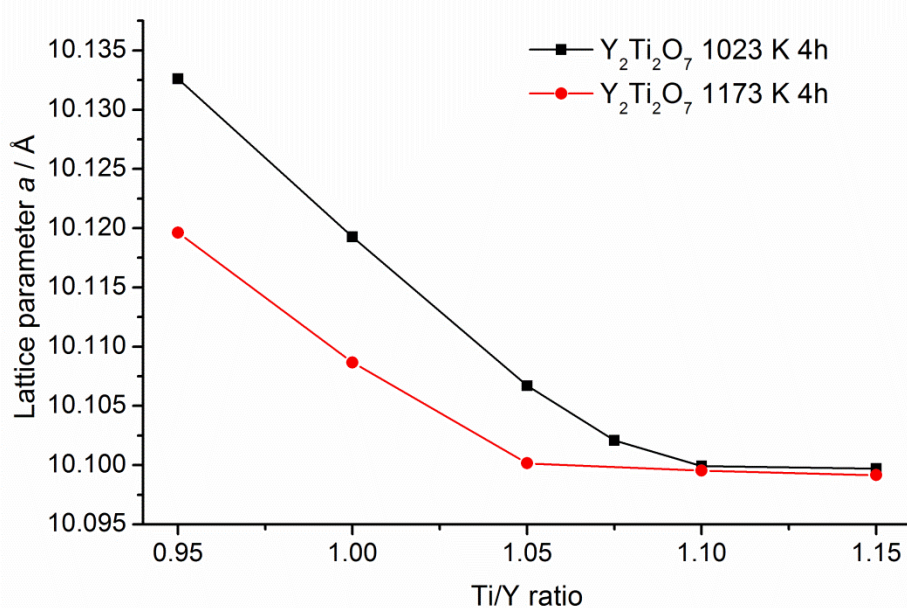


Figure 17: Lattice parameter as a function of the Ti/Y ratio for $\text{Y}_2\text{Ti}_2\text{O}_7$ calcined at 1023 K and 1173 K.

In conclusion, the employment of an yttrium excess of 5 % (Ti/Y ratio of 0.95) in the sol gel synthesis increases the cationic distortion, which can readily be explained by the population of the B-site by yttrium cations. A “stuffed” pyrochlore structure with the general formula of $Y_2(Ti_{2-x}Y_x)O_{7-0.5x}$ is formed. This formula is corroborated by Stanek et al.^[124], who conducted a model study about the defect formation in pyrochlores. It was predicted that excess yttrium in $Y_2Ti_2O_7$ leads to the formation of clustered defects composed of two yttrium cations occupying the titanium site and one oxygen vacancy.

Even the stoichiometric samples reveal a significant level of intrinsic cationic distortion caused by yttrium and titanium interchanging their intended lattice positions, as the introduction of a titanium excess of 5 % (Ti/Y ratio of 1.05) leads to further decrease of the lattice parameter and the I(400)/I(331) ratio. Therefore, the formula of the “real” stoichiometric pyrochlore structure is supposed to be $(Y_{2-x}Ti_x)(Ti_{2-x}Y_x)O_7$. Such a stoichiometry was reported by Fuentes et al.^[125] to be accessible under ball milling conditions, resulting, however, in a very high amount of cation antisites. Moreover, a significant degree of these cation antisites is found to withstand a 12 hour temperature post-treatment at 923 K and 1073 K, while the distortion was completely cured by treatment at 1473 K. This corroborates well with the presented concept that a small degree of intrinsic antisites exists in stoichiometric $Y_2Ti_2O_7$, but being a function of the annealing temperature. Thus, considering the samples with Ti/Y ratios ≤ 1.05 , the lattice parameters as well as the I(400)/I(331) ratio values are apparently higher, if the calcination is performed at a lower temperature of 1023 K assuming that a major part of the lattice defects are cured by annealing at a higher temperature of 1173 K. Atomistic simulations^[126] also confirm that cation antisites are the most probable intrinsic defects formed in stoichiometric pyrochlores.

As soon as the lattice parameter as well as the I(400)/I(331) ratio reach a constant value, yttrium and titanium are supposed to be completely separated on their specific lattice positions leading to an yttrium and oxygen deficient pyrochlore structure with a composition of $Y_{2-x}Ti_2O_{7-0.5x}$. This is achieved at Ti/Y ratios of 1.05 and 1.10 for $Y_2Ti_2O_7$ annealed at 1173 K and 1023 K, respectively. Further increase of the Ti/Y ratio does not result in the introduction of more vacancies, but in the formation of TiO_2 rutile as a by-phase.

Detection and quantification of small amounts of rutile pose a challenge. The insets of Figure 18 displays the X-ray diffraction data in the 2θ range from 26° to 32° of $Y_2Ti_2O_7$ calcined at 1173 K (part A) and 1023 K (part B), respectively, with different Ti/Y ratios.

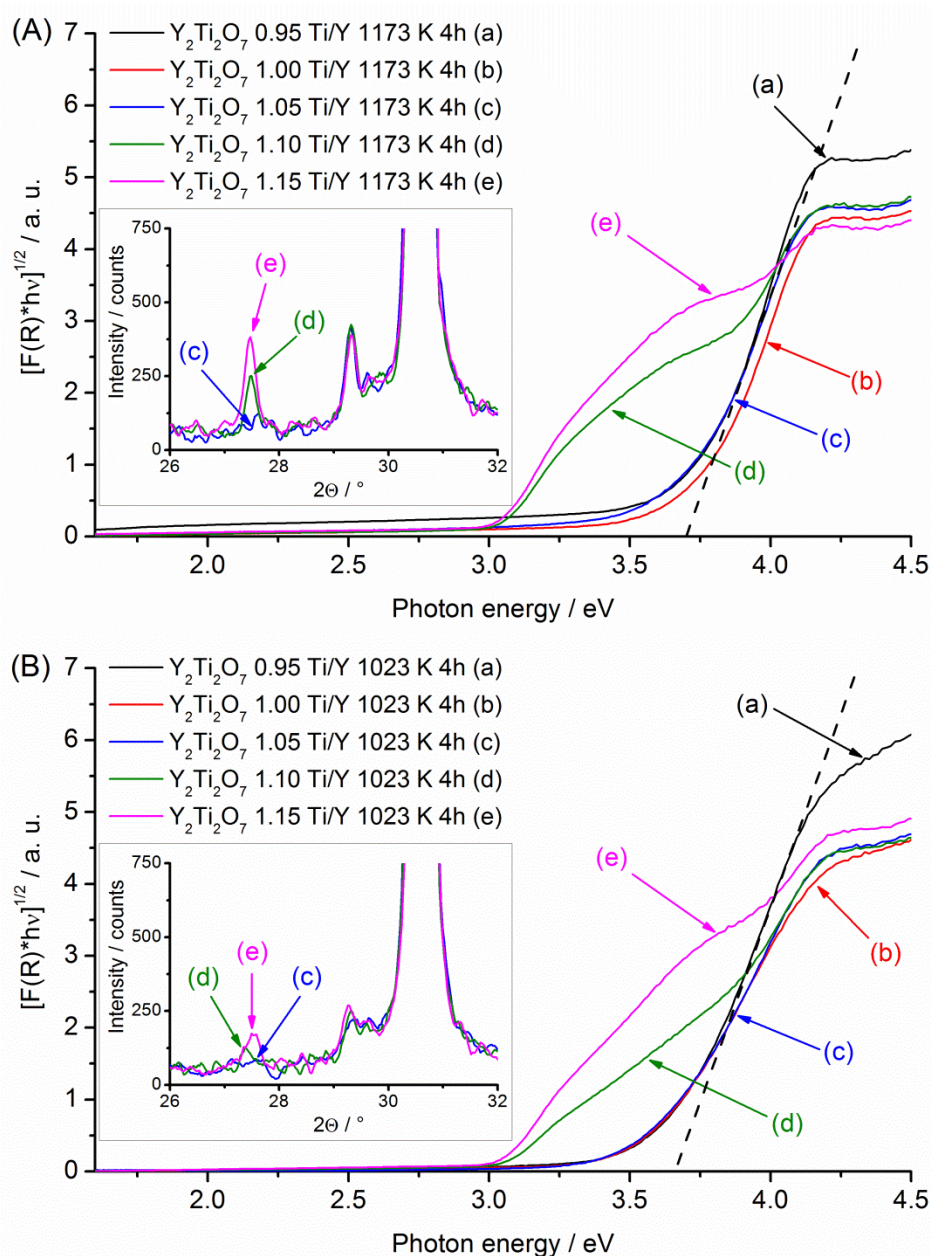


Figure 18: Tauc-plots (for indirect band gap transition) calculated from the UV-vis diffuse reflectance spectra of $\text{Y}_2\text{Ti}_2\text{O}_7$ with different Ti/Y ratios calcined at 1173 K (part A) and 1023 K (part B), respectively. Insets: Details of the X-ray diffraction data in the angular range of $26\text{--}32^\circ 2\theta$ for analysis of the by-phase TiO_2 rutile.

In the insets, the X-ray diffraction data of the samples with Ti/Y ratios of 0.95 (a), 1.00 (b) and 1.05 (c) are represented by that sample featuring a titanium excess of 5 % (c), as the data are almost identical in the focused part. There is no evidence of a TiO_2 rutile by-phase in the X-ray diffraction data up to a titanium excess of 5 %, irrespective of the annealing temperature. Switching to a Ti/Y ratio of 1.10 (d) reveals an additional reflection at an angle of $2\theta = 27.45^\circ$ assigned to the (110) reflection of the titania phase rutile only for the sample annealed at a higher temperature of 1173 K. Increasing the

titanium excess to 15 % (e) leads to an intensive (110) reflection of rutile for samples of both annealing temperatures. For comparison, the intensity of the minor (311) reflection of the yttrium titanate pyrochlore (cf. to Figure 14) is similar to that of the rutile (110) reflection being the most intensive in the rutile pattern.

The main sections of Figure 18 show the Kubelka-Munk transformation of the UV-vis diffuse reflectance spectra in order to calculate the band gap energies of the materials annealed at 1173 K (part A) and 1023 K (part B), respectively. Since stoichiometric and non-stoichiometric yttrium titanates crystallizing in the pyrochlore structure are supposed to be semi-conductors with indirect band gap transitions, band gap energies are obtained from the intersection point of the linear part of the plot $(F(R) \cdot hv)^{1/2}$ vs. hv with the energy axis. It is obvious that the Tauc-plots of the samples with Ti/Y ratios of 0.95 (a), 1.00 (b) and 1.05 (c) feature almost the same shape resulting in a band gap energy value of 3.7 eV, irrespective of the annealing temperature (cf. to the dashed lines in Figure 18). For the $Y_2Ti_2O_7$ samples with $Ti/Y \geq 1.10$ an additional absorption between 3.0 eV and 3.7 eV is visible, which becomes more intensive, if the sample is annealed at a higher temperature of 1173 K and/or features a higher titanium excess of 15 %. The additional absorption band is easily contributed to the TiO_2 phase rutile, as its band gap energy amounts to about 3.0 eV^[127]. Trusting the X-ray data solely, yttrium titanate with an excess of 10 % titanium calcined at 1023 K (d) appears to yield a pure pyrochlore phase, but the presence of rutile TiO_2 is proven by the corresponding diffuse reflectance UV-vis spectrum. To prove the surprisingly strong absorption of rutile, a physical mixture of 95 wt.-% $Y_2Ti_2O_7$ and 5 wt.-% of TiO_2 rutile was prepared. Indeed, a similar UV-vis reflectance spectrum was collected from the mixture. However, the characteristic rutile absorption of the mixture reached only about 70 % of the extent provided by the sample with a Ti/Y ratio of 1.15, which is considered to contain the same amount of rutile. This difference can be explained by insufficient dispersion in the repeatedly mechanical ground mixture, which cannot be as perfect as in the sol-gel process providing a nano-scaled distribution.

By means of the Rietveld refinement method a quantitative analysis for the calculation of the rutile content was performed. The results are presented in Figure 19 with the corresponding axis label on the right hand of the figure. Theoretically, adding an extra titanium amount of 5 % to a synthesis matrix will result in the formation of ca. 2 wt.-% of TiO_2 rutile, if additional titanium is not changing the stoichiometry but is rather completely converted into the rutile by-phase. For samples calcined at 1173 K, the

stoichiometry of $Y_2Ti_2O_7$ featuring a titanium excess of 5 % remains unchanged by introducing additional titanium, as the rutile fraction increases equally by about 2 wt-%. Annealed at 1023 K, the sample with a titanium excess of 10 % exhibits a rutile content of only 1.1 wt-% assuming that the real pyrochlore stoichiometry is changed up to a Ti/Y ratio of around 1.075, which corroborates with the fact, that the 5 % excess titanium sample still exhibits lattice distortion. Therefore, a sample with a Ti/Y ratio of 1.075 was prepared as well and found to be free of rutile impurities. The lattice distortion in this sample is clearly reduced, but it still misses the quality of the sample featuring 10 % excess titanium (cf. to Figure 17). The finding that more titanium does not change the stoichiometry anymore, but is completely converted into TiO_2 rutile, is confirmed by increasing the Ti/Y ratio from 1.10 to 1.15, by which the rutile fraction is raised by about 2.5 wt-% regardless of the annealing temperature. It is important to be aware of the possible inaccuracy appearing in the quantitative analysis by the Rietveld refinement method, particularly for the analysis of small amounts of rutile. However, since the results obtained by other measurements corroborate very well, the quantitative analysis by the Rietveld method is taken as being reliable. Mizutani et al.^[24] reported that small amounts of Y_2O_3 and TiO_2 are soluble in the pyrochlore $Y_2Ti_2O_7$ below 1723 K, whereas a significant amount of Y_2O_3 is soluble above this temperature. Interpreting their phase diagram shown for Y_2O_3 - TiO_2 identifies a stable pyrochlore phase within the Ti/Y ratios of ca. 0.91 and 1.07 below 1723 K, which corroborates very well with the results presented herein.

Besides the phase analysis, the average crystallite sizes are provided by the Rietveld refinement as well. Figure 19 shows the average crystallite sizes of the $Y_2Ti_2O_7$ samples as a function of the Ti/Y ratio with the corresponding axis label on the left hand of the figure. Up to a Ti/Y ratio of 1.05, the increase of the Ti/Y ratio results in the formation of crystallites with slightly higher average sizes. On the other hand, the increase of the calcination temperature leads to significantly larger crystallite sizes due to sintering effects. Average crystallite sizes range from 30 nm to 50 nm or from 50 nm to 90 nm for samples annealed at 1023 K or 1173 K, respectively. The increase in average crystallite sizes due to the increase of the Ti/Y ratio is significantly more pronounced for $Y_2Ti_2O_7$ samples annealed at a higher temperature of 1173 K. Exceeding the Ti/Y ratios of 1.075 (1023 K) or 1.05 (1173 K) does not change the crystallite size and the stoichiometry of the pyrochlore phase anymore, while the rutile by-phase starts to form.

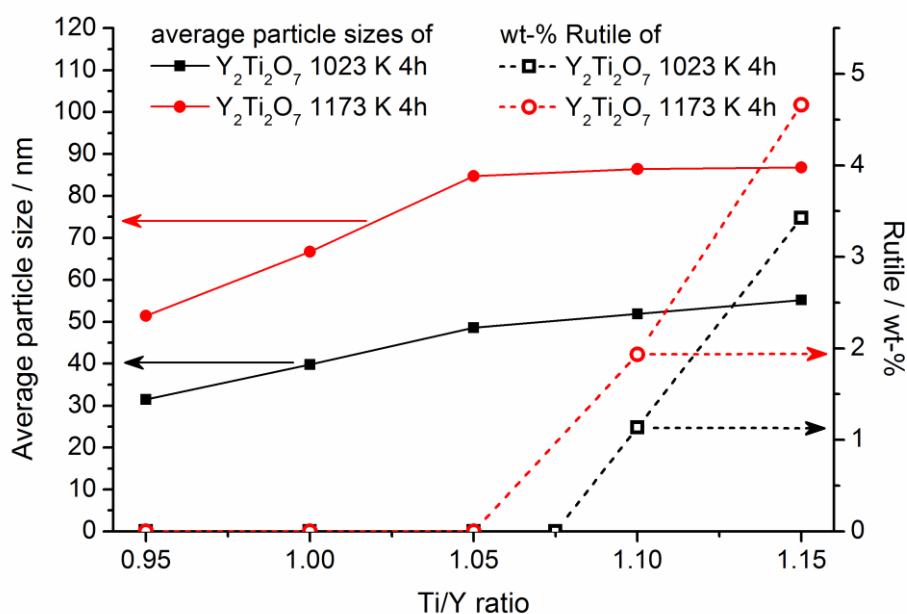


Figure 19: Average crystallite sizes and TiO_2 rutile fractions obtained by Rietveld refinement of the X-ray diffraction data of $\text{Y}_2\text{Ti}_2\text{O}_7$ samples as a function of the Ti/Y ratio.

Figure 20(a) displays a TEM micrograph of $\text{Y}_2\text{Ti}_2\text{O}_7$ Ti/Y 1.00 calcined at 1023 K for 4h in dark field mode showing the strong agglomeration of the yttrium titanate particles. The cavities and calderas are supposed to be formed by gas bubbles evaporating during the sol-gel decomposition process. Part (b) of Figure 20 represents the lower right corner of part (a) in a higher magnification. A broad crystallite size distribution ranging from 10 to 100 nm is observed. The particles are loosely connected to each other forming a sponge-like system with irregular pores. In Figure 20(c) the distribution of rhodium nanoparticles on the $\text{Y}_2\text{Ti}_2\text{O}_7$ photocatalyst is presented. The bright particles in the micrograph are assigned to rhodium. The rhodium nanoparticles being of 2-3 nm in size are homogeneously distributed on the surface of the catalyst, but tend to aggregate into clusters with diameters ranging from 10 nm to 30 nm. Similar characteristics regarding particle size and distribution are found for photodeposited platinum as well.

In summary, optimum conditions regarding minimization of lattice distortion and phase purity of $\text{Y}_2\text{Ti}_2\text{O}_7$ are reached at a titanium excess of 5 % for an annealing temperature of 1173 K. At 1023 K annealing, the sample with a Ti/Y ratio of 1.075 is free of rutile, but not entirely free of lattice distortion, while the Ti/Y 1.10 sample exhibits the inverted characteristics. Therefore, an optimum Ti/Y ratio is supposed to lie in between these two values.

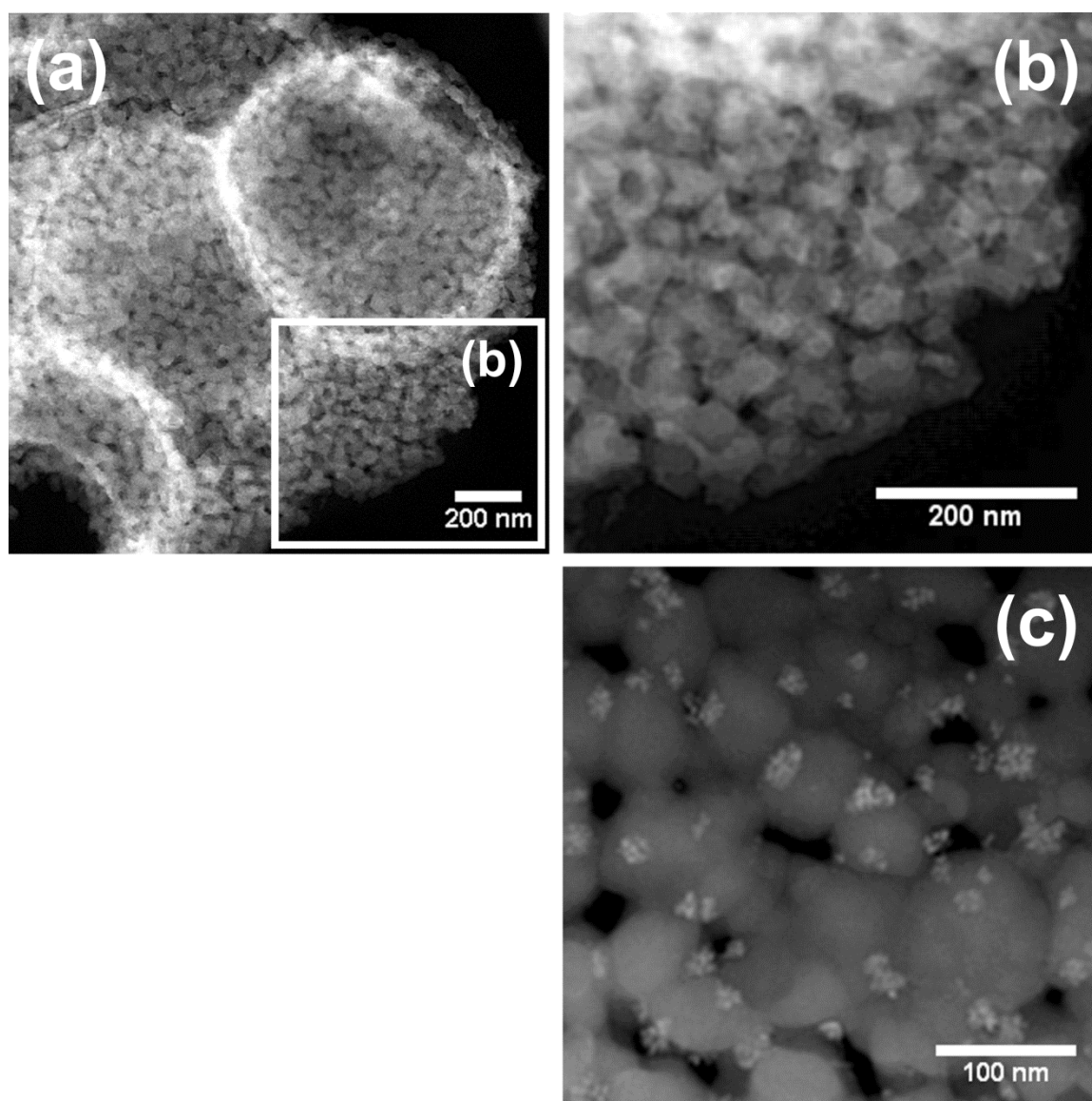


Figure 20: TEM micrographs in dark field mode of (a) $Y_2Ti_2O_7$ Ti/Y 1.00 calcined at 1023 K for 4h and part (b) being a detail of part (a) with higher magnification. Part (c) shows the TEM micrograph in dark field mode of the same material, but after photodeposition of 0.75 wt.-% of rhodium.

4.1.2 Photocatalytic hydrogen production with $Y_{2-x}Ti_2O_{7-1.5x}$

The photocatalytic activities of the $Y_2Ti_2O_7$ samples were investigated by detecting the hydrogen production from aqueous solutions containing 10 vol.-% of methanol. In contrast to the overall water splitting reaction, organic sacrificial reagents like methanol are widely-used to determine the activity in the photocatalytic hydrogen production, because organic alcohols are significantly easier oxidizable than water being a 4-hole oxidation process^[50]. Platinum^[128] and Rhodium^[93] were chosen as co-catalysts, well-known for being efficient hydrogen evolution sites. The metals were produced in the initial phase of illumination by insitu photodeposition. The hydrogen production rate in

the first 30 min period is always lower than that in the second or third period, as photogenerated electron-hole pairs are consumed competitively by the process of photodeposition, which is supposed to be completed after at least 60 minutes of irradiation when reaching stable activity. To evaluate the photocatalytic role of yttrium titanate, a measurement without photocatalyst was performed, in which no hydrogen production was detected. Moreover, a measurement without co-catalyst over $\text{Y}_2\text{Ti}_2\text{O}_7$ Ti/Y 1.05 1023 K being free of rutile impurities also yielded no hydrogen at all. As hydrogen evolution sites are not provided by yttrium titanate itself, loading with a co-catalyst is a prerequisite for the photocatalytic hydrogen formation even in the presence of a sacrificial reagent. The experimental detection limit of the gas chromatograph was found to be around $3 \mu\text{mol H}_2/\text{h}$.

Figure 21 shows the photocatalytic activities regarding hydrogen production as a function of the Ti/Y ratio for $\text{Y}_2\text{Ti}_2\text{O}_7$ samples calcined at 1023 K and loaded by photodeposition with 0.75 wt.-% of platinum. The activity is enhanced impressively from $9 \mu\text{mol H}_2/\text{h}$ for the sample featuring an yttrium excess of 5 % to a maximum of $71 \mu\text{mol H}_2/\text{h}$ obtained by the sample with a Ti/Y ratio of 1.10, while remaining in the same pyrochlore structure type. By proceeding to a titanium excess of 15 %, the photocatalytic activity is decreased to $61 \mu\text{mol H}_2/\text{h}$.

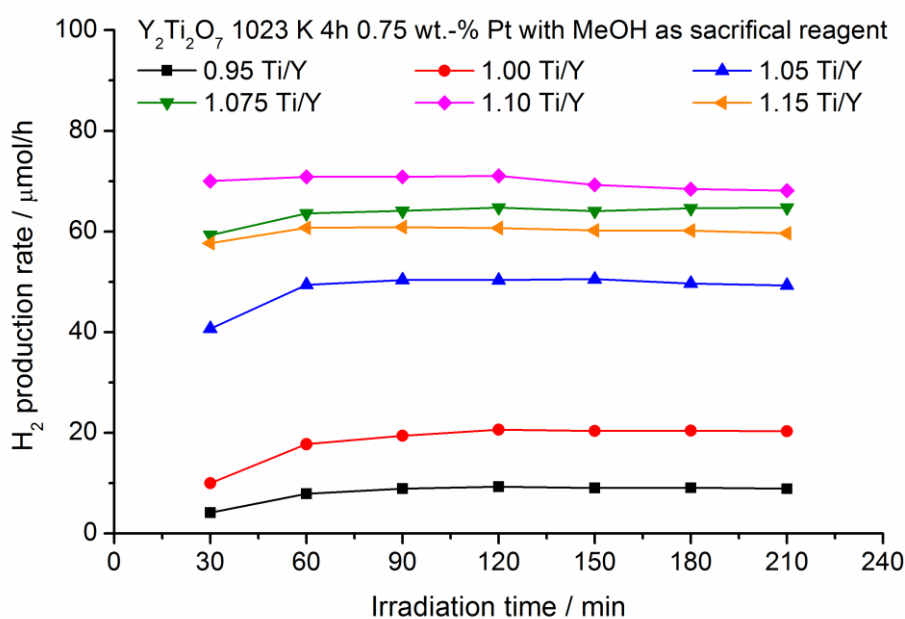


Figure 21: Photocatalytic activity regarding hydrogen production over $\text{Y}_2\text{Ti}_2\text{O}_7$ calcined at 1023 K for 4h with 0.75 wt.-% platinum as co-catalyst and in the presence of 10 vol.-% methanol as sacrificial reagent.

The activities obtained by samples annealed at 1023 K corroborate very well with the previously mentioned structural findings of cationic lattice distortion in the yttrium titanate pyrochlores. As the lattice distortion is reduced by increasing the Ti/Y ratio, the photocatalytic activity is enhanced concomitantly. The Ti/Y 1.10 sample provides slightly higher activities than the most active pure pyrochlore sample (Ti/Y ratio of 1.075), although it contains a small rutile fraction. This superior activity does not derive from the rutile by-phase, as changing to a titanium excess of 15 % considerably extends the rutile fraction, but lowers the activity. Compared to the titania modification anatase, the rutile phase is known to be less active for photocatalytic hydrogen production, as the flatband potential coincides almost exactly with the redox potential of the $H^+ / \frac{1}{2}H_2$ couple only resulting in a small driving force for proton reduction^[129]. Scaife^[79] proposed the valence band edge of an oxide semi-conductor to be about +3.0 eV (vs. NHE), if it only contains transition metal ions with empty d-orbitals and the valence band is formed of O2p orbitals solely. Considering the energy band gap of 3.7 eV obtained for $Y_2Ti_2O_7$, the conduction band edge should be located at about -0.7 eV (vs. NHE), which should, in principle, provide a high driving force for proton reduction.

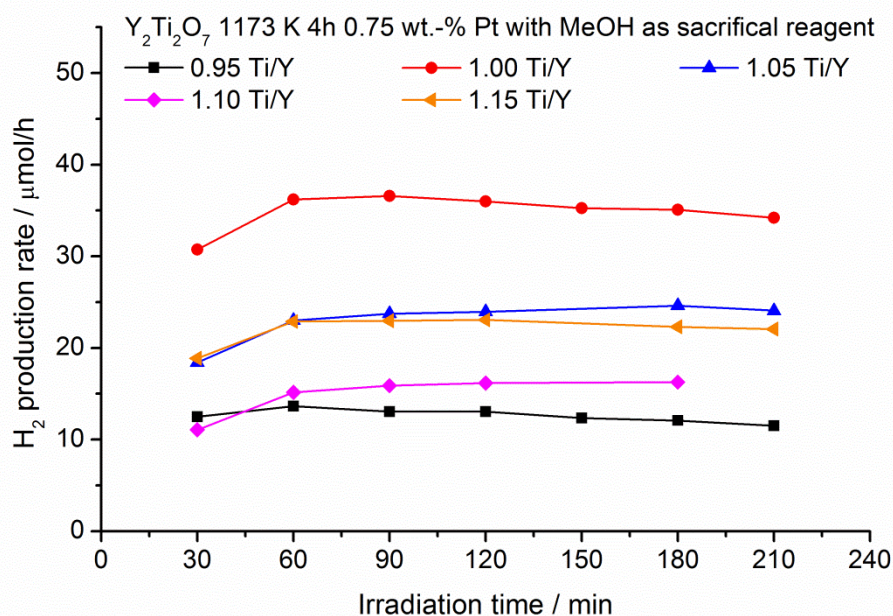


Figure 22: Photocatalytic activity regarding hydrogen production over $Y_2Ti_2O_7$ calcined at 1173 K for 4h with 0.75 wt.-% platinum as co-catalyst and in the presence of 10 vol.-% methanol as sacrificial reagent.

Figure 22 presents the photocatalytic activities of platinum loaded $Y_2Ti_2O_7$ samples calcined at 1173 K. The stuffed pyrochlore with 5 % excess yttrium again states the sample with the lowest activity of 14 $\mu\text{mol } H_2/\text{h}$. In contrast to the annealing at 1023 K,

at a higher temperature of 1173 K the activity increases considerably to its highest value for the stoichiometric sample ($Ti/Y = 1.00$, $37 \mu\text{mol H}_2/\text{h}$), but subsequently decreases markedly to values of $16\text{-}25 \mu\text{mol H}_2/\text{h}$, once excess titanium is introduced into the structure. The negative role of rutile is not as apparent as in the sample series annealed at 1023 K. As the Ti/Y 1.10 sample at 1023 K is highly active, the rutile fraction reduces the overall photocatalytic activity. At 1173 K annealing, very large crystallite sizes are the determining factor for significantly reduced activities of the pyrochlore samples at $Ti/Y \geq 1.05$. Rutile is less active than the structure-optimized $Y_2Ti_2O_7$ at 1023 K, but its activity is comparable to these 1173 K pyrochlore samples. This leads to almost the same activities for samples with $Ti/Y \geq 1.05$ at 1173 K annealing. The slightly higher activity of the sample featuring a Ti/Y ratio of 1.15 is explained by the experimental error.

As photocatalytic measurements were performed in a flow-through reactor system, they are not obscured by a pressure build up. Furthermore, every point of measurement can be analyzed independently from the others, which is not the case for a closed gas-circulation system. Therefore, the applied system is particularly suitable for determining even small variations in the steadiness of the hydrogen production rate. As can be depicted from Figure 21 and Figure 22, activities are usually perfectly constant for samples loaded with platinum, however, a few samples calcined at 1173 K suffer from a minor loss in the hydrogen production rate of 2-4 % per hour.

Rhodium as an alternative co-catalyst was also photodeposited on the various yttrium titanates, which were subsequently tested in the photocatalytic hydrogen production. In general, the strong influence of different Ti/Y ratios on the photocatalytic activity was exactly reproduced, as illustrated in Figure 24 (vide infra). The detailed results of the photocatalytic hydrogen production in the presence of rhodium are provided in the appendix as Figure A1 and Figure A2. A comparison of rhodium and platinum acting as co-catalysts on the most active $Y_2Ti_2O_7$ samples is given in Figure 23. Both platinum loaded samples yield stable photocatalytic activities over time. Employment of rhodium leads to a prolonged decrease in activity of approximately 10 % per hour. This instability of the hydrogen production rate occurs independently of the annealing temperature and the stoichiometry of the catalyst (cf. to Figure A1 and Figure A2). The decrease in activity may be attributed to a lower oxidation stability of rhodium ($E_0(Rh^{3+}|Rh) = +0.76 V$) compared to that of platinum ($E_0(Pt^{2+}|Pt) = +1.18 V$) being a more precious metal^[52]. Applying a wide band gap material like $Y_2Ti_2O_7$ as photocatalyst results in a strong oxidation potential of photogenerated holes. Therefore,

platinum seems to be more suitable as co-catalyst for $Y_2Ti_2O_7$ and rhodium should be coupled to photocatalysts featuring a valence band situated at a more negative potential vs. NHE.

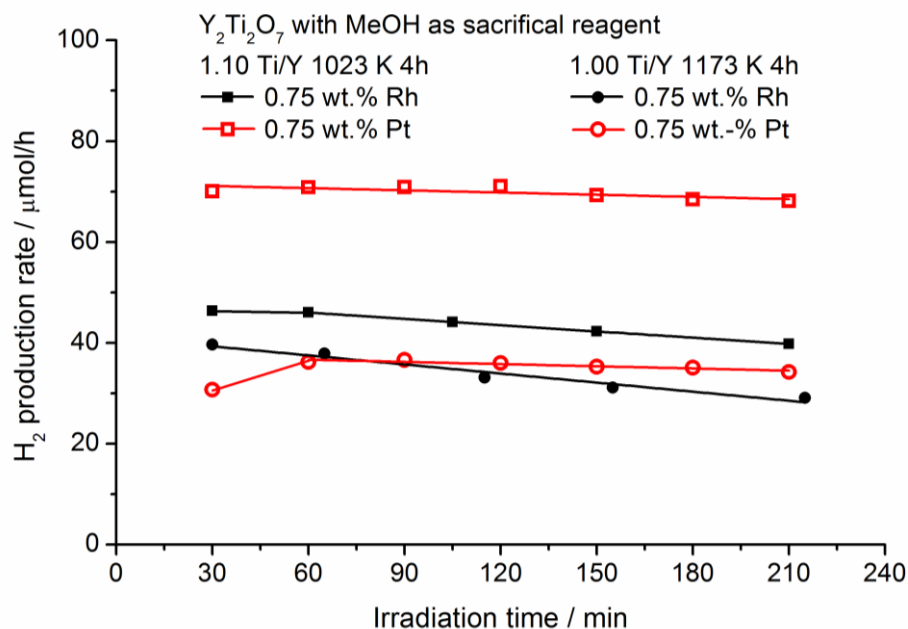


Figure 23: Steadiness of photocatalytic hydrogen production over $Y_2Ti_2O_7$ 1.10 Ti/Y 1023 K 4h and $Y_2Ti_2O_7$ 1.00 Ti/Y 1173 K 4h loaded with 0.75 wt.-% rhodium or 0.75 wt.-% platinum as co-catalyst and in the presence of 10 vol.-% methanol as sacrificial reagent.

4.1.3 Structure related photocatalysis in $Y_{2-x}Ti_xO_{7-1.5x}$

A summary of the photocatalytic hydrogen production rates and the corresponding photonic efficiencies under full arc irradiation are given in Figure 24. The hydrogen production rates of samples annealed at 1023 K are significantly enhanced, if platinum is applied as co-catalyst. A maximum photonic efficiency of ca. 1.4 % is obtained for the most active photocatalyst, that is, $Y_2Ti_2O_7$ 1.10 Ti/Y annealed at 1023 K and loaded with 0.75 wt.-% of platinum. As this sample still contains a small rutile fraction being unfavourable for the photocatalytic activity, further optimization of the Ti/Y ratio between 1.075 and 1.10 is considered to provide even better photocatalytic activities, if the sample hits the spot of phase purity and minimized lattice distortion.

To estimate the quantum efficiency in the spectral region $Y_2Ti_2O_7$ is able to absorb, a ferrioxalate actinometry was performed using a Schott WG360 cut off filter, which is opaque for photons with wavelength below 360 nm. Applying a WG360 cut off filter reduces the photon flux to $1.09 \cdot 10^{-6}$ mol/s. Subtracting this value from the photon flux

under full arc irradiation leads to a photon flux of $3.90 \cdot 10^{-7}$ mol/s for the spectral region ranging from 200 nm to 360 nm. Although this value is a very rough estimate, it should be higher than the real value of the photon flux in this region, as this cut off filter does not only cut wavelength below 360 nm, but also reduces the transmission at higher wavelengths. Finally, an overestimated photon flux results in underestimated values for the photonic efficiencies. A photonic efficiency in the spectral region ranging from 200 nm to 360 nm of ca. 5 % is obtained for $Y_2Ti_2O_7$ Ti/Y 1.10 1023 K loaded with 0.75 wt.-% of platinum.

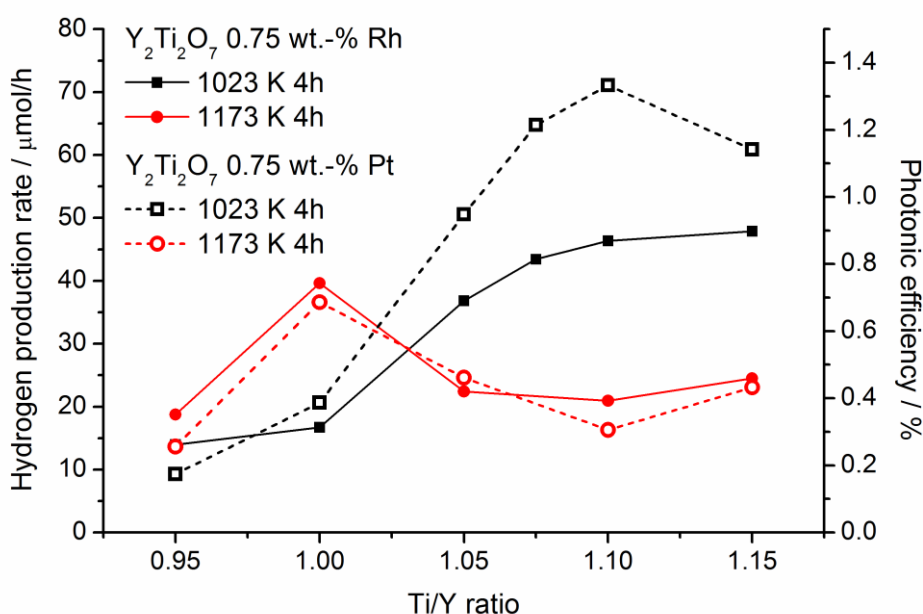


Figure 24: Photocatalytic activities and photonic efficiencies regarding hydrogen production over $Y_2Ti_2O_7$ calcined at 1023 K or 1173 K for 4h with 0.75 wt.-% of rhodium or platinum as co-catalyst and in the presence of 10 vol.-% methanol as sacrificial reagent.

However, an explanation is needed for the fact that different optimum Ti/Y ratios of 1.10 and 1.00 are found for different annealing temperatures of 1023 K and 1173 K, respectively. As presented in Figure 25, the variations in the photocatalytic activities can be perfectly attributed to the average crystallite sizes and the cationic lattice distortion, while considering the unfavorable presence of rutile. The factors are classified and subsequently rated by quality marks. The BET surface areas are provided as well being in good accordance with the calculated crystallite sizes. The fact that low temperature annealing at 1023 K results in considerable higher activities leads to the conclusion that smaller crystallite sizes must have a beneficial effect on the herein investigated photocatalytic reaction. Although the average crystallite size of samples annealed at

1023 K is slightly increased with increasing Ti/Y ratio, the photocatalytic activity is enhanced tremendously, which can only be explained by the minimization of the cationic lattice distortion. The sample featuring a Ti/Y ratio of 1.075 (1023 K) is not included in this Figure, but is in principle equal to the sample with Ti/Y of 1.05 (1023 K). The mean value of the photocatalytic activity in hydrogen production achieved with rhodium and platinum as co-catalysts amounts to 54.1 $\mu\text{mol H}_2/\text{h}$, which is in good accordance to the triple plus rating.

At 1173 K, the increase in average crystallite sizes is more and the distortion is less pronounced at low Ti/Y ratios. The positive effect of decreasing distortion is traded against the negative effect of increasing crystallite sizes leading to a maximum activity of the stoichiometric sample, if annealed at 1173 K.

		Ti/Y ratio			
		0.95	1.00	1.05	1.10
1023 K 4h	highest distortion	⊖ ⊖	high distortion ⊖	low distortion ⊕	no distortion ⊕ ⊕
	small particles	⊕ ⊕	small particles BET: 16.7 m ² /g ⊕ ⊕	small particles BET: 13.1 m ² /g ⊕ ⊕	small particles rutile ⊖ ⊖
	11.6 $\mu\text{mol/h}$ →	⊖	18.7 $\mu\text{mol/h}$ →	43.7 $\mu\text{mol/h}$ →	58.7 $\mu\text{mol/h}$ →
1173 K 4h	high distortion	⊖	low distortion ⊕	no distortion ⊕ ⊕	no distortion ⊕ ⊕
	small particles	⊕ ⊕	medium particles BET: 8.9 m ² /g ⊕	large particles BET: 4.1 m ² /g ⊖	large particles rutile ⊖ ⊖
	16.2 $\mu\text{mol/h}$ →	⊕	38.1 $\mu\text{mol/h}$ →	23.5 $\mu\text{mol/h}$ →	18.6 $\mu\text{mol/h}$ →

Particle sizes:	Cationic distortion (via lattice parameter):
small: 30 - 55 nm ⊕⊕	highest: 10.1275 - 10.1400 Å ⊖⊖
medium: 55 - 80 nm ⊕	high: 10.1150 - 10.1275 Å ⊖
large: 80 - 105 nm ⊖	low: 10.1025 - 10.1150 Å ⊕
	no: 10.0900 - 10.1025 Å ⊕⊕

Figure 25: Cationic lattice distortion and average particle sizes of the catalysts are classified and rated by quality marks considering a negative effect of the rutile by-phase. The overall ratings are in very good accordance with the mean values of the photocatalytic activities, thus explaining the optimum Ti/Y ratios obtained for different annealing temperatures.

Higashi et al.^[130] reported improved photocatalytic activities by introducing an excess of 5% yttrium into stoichiometric $\text{Y}_2\text{Ti}_2\text{O}_7$, which was explained by a reduced formation of TiO_2 rutile as by-phase formed in their synthesis at very high annealing temperatures

above 1273 K. This finding is in good agreement with the herein presented results demonstrating a negative effect of the by-phase rutile, in particular at higher annealing temperatures. Moreover, strong evidence is provided by Higashi's work that the optimum Ti/Y ratio decreases by increasing the calcination temperature with an ideal Ti/Y ratio of 0.95 being considered possible for an annealing temperature above 1273 K. However, the present work clearly demonstrates the advantage of low temperature annealing leading to smaller crystallite sizes and thus, higher activities.

A lot of work has been published correlating the photocatalytic activity to various kinds of lattice distortion. Mixed oxides containing p-block elements with d^{10} configuration like In^[131] or Sb^[132] were found to yield good activities if these ions are displaced out of the gravity centre in the highly distorted MO₆ octahedra leading to an induced dipole moment improving the charge separation. The herein reported lattice distortion in Y₂Ti₂O₇ is characterized by a sort of chemical distortion leading to the formation of cationic antisites in the lattice. The titanium cations on the B position are restricted to highly symmetrical positions in the lattice of the cubic pyrochlore structure. Although the surrounding six oxygen ions do have one positional parameter influencing the octahedral geometry, the titanium ions cannot be displaced out of the gravity centre and all the six Ti-O distances have to be equal. Thus, the purity of the TiO₆ octahedral network in d^0 transition metal oxides like titanates is supposed to be the crucial criterion for good photocatalytic activity.

The photocatalytic activity of pyrochlore Y₂Ti₂O₇ is determined by cationic lattice distortion, average crystallite sizes and the presence of rutile. These factors are controlled by the Ti/Y ratio and the annealing temperature. The degree of cationic lattice distortion in pyrochlore Y₂Ti₂O₇ with different Ti/Y ratios has been determined by the analysis of variations in the lattice parameter and in the I(400)/I(331) ratio. Lattice distortion being also a function of the annealing temperature is successfully minimized by increasing the Ti/Y ratio. The chemical composition changes from the "stuffed" pyrochlore Y₂(Ti_{2-x}Y_x)O_{7-0.5x} via (Y_{2-x}Ti_x)(Ti_{2-x}Y_x)O₇ for the stoichiometric sample even possessing a marked degree of intrinsic cationic distortion, to a non-stoichiometric composition of Y_{2-x}Ti₂O_{7-1.5x}.

Probing Y₂Ti₂O₇ prepared with different Ti/Y ratios in the hydrogen producing photocatalytic test reaction provides clear evidence that reduced cationic lattice distortion leads to greatly increased photocatalytic activities. Especially at an annealing temperature of 1023 K, only the minimization of cationic distortion is responsible for an increase in

photocatalytic activity from 9 $\mu\text{mol H}_2/\text{h}$ to 71 $\mu\text{mol H}_2/\text{h}$, while even a negative effect of slightly increasing crystallite sizes is overwhelmed. Figure 26 illustrates the correlation between changes in the $\text{Y}_{2-x}\text{Ti}_2\text{O}_{7-1.5x}$ structure at 1023 K annealing and the photocatalytic activity induced by variations in the Ti/Y ratio. By increasing the Ti/Y ratio, the B-site of the structure is subsequently purified from yttrium acting as defect site leading to enhanced charge carrier separation and, thus to improved photocatalytic activity until TiO_2 rutile is formed as by-phase.

A maximum photonic efficiency of 1.4 % is achieved. Hydrogen production rates remain constant over time, if platinum is used as co-catalyst. Applying rhodium as co-catalyst on a high band-gap material like $\text{Y}_2\text{Ti}_2\text{O}_7$ results in decreasing activities attributed to the oxidation of rhodium by photogenerated holes.

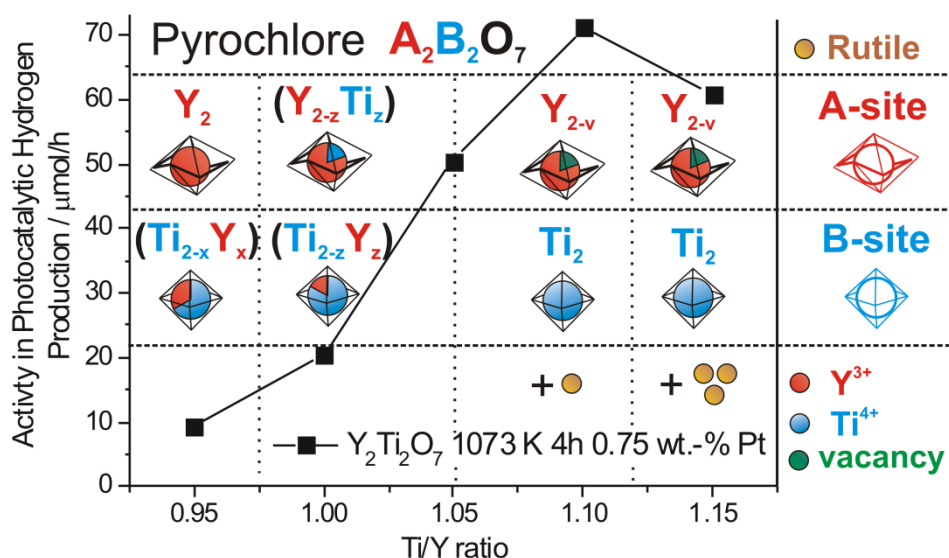


Figure 26: Correlation between the cationic lattice distortion in the $\text{Y}_{2-x}\text{Ti}_2\text{O}_{7-1.5x}$ structure at 1023 K annealing and the photocatalytic activity as a function of the Ti/Y ratio. An increase in the Ti/Y ratio leads to the purification of the B-site of the structure from yttrium acting as defect site. The photocatalytic activity is improved until TiO_2 rutile is formed as by-phase.

4.1.4 Optimum co-catalyst loading and stability of $\text{Y}_{1.867}\text{Ti}_2\text{O}_{6.80}$

It was shown that increasing the Ti/Y ratio in $\text{Y}_{2-x}\text{Ti}_2\text{O}_{7-1.5x}$ leads to a significant improvement of the photocatalytic activity in hydrogen production due to optimizations in the pyrochlore lattice. However, at a pre-determined co-catalyst loading of 0.75 wt.-%, it was observed that applying platinum as co-catalyst yields significantly higher hydrogen production rates than using rhodium. This behavior was found true for all samples of yttrium titanate irrespective of the Ti/Y ratio. Consequently, the optimum co-catalyst

loadings of platinum as well as rhodium were determined using the most active sample of the series, $Y_{1.867}Ti_2O_{6.80}$ (Ti/Y ratio of 1.075) annealed at 1023 K for 4 hours.

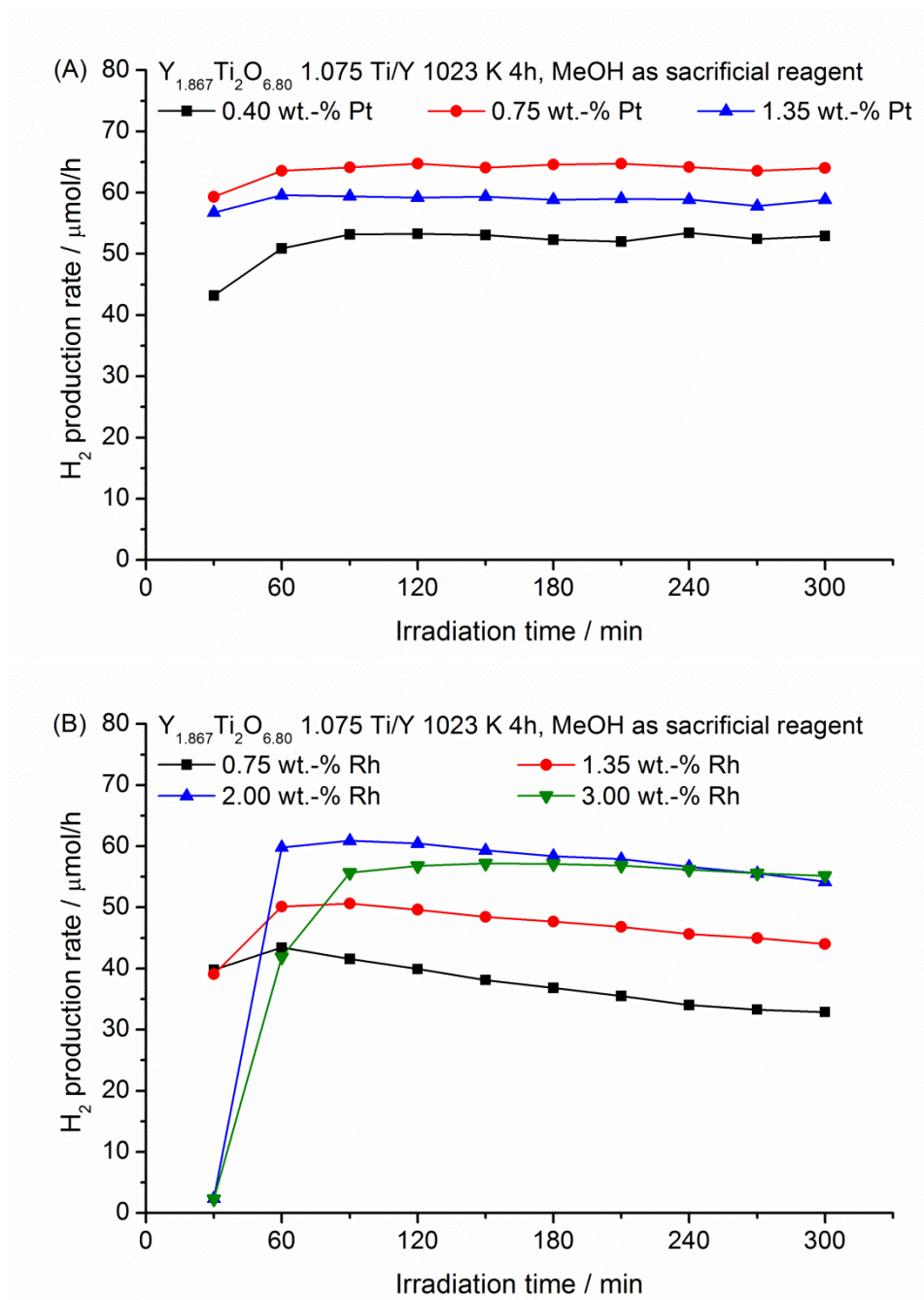


Figure 27: Photocatalytic activity regarding hydrogen production over $Y_{1.867}Ti_2O_{6.80}$ (Ti/Y=1.075) calcined at 1023 K for 4h in the presence of 10 vol.-% methanol as sacrificial reagent as a function of the co-catalyst loading of platinum (A) and rhodium (B).

Figure 27(A) shows that a platinum loading of 0.75 wt.-% like previously applied indeed states the optimum co-catalyst loading. Part (B) of Figure 27 demonstrates that using rhodium as co-catalyst leads to completely different results, as a loading of 0.75 wt.-% is clearly too low. The highest temporary hydrogen production rate of 61.0 $\mu\text{mol H}_2/\text{h}$ is

obtained with a rhodium loading of 2.00 wt.-%, which is very close to that value achieved by applying an optimum platinum loading of 0.75 wt.-%. Thus, choosing appropriate co-catalyst loadings should in principle lead to the same photocatalytic activities, irrespective of the co-catalysts itself. The extend of the previously mentioned decline in activity occurring over time under co-catalysis of rhodium depends on the co-catalyst loading. A higher rhodium loading leads to more stable hydrogen production rates. Even no significant decrease in activity is observed within 300 minutes of irradiation at 3.0 wt.-% Rh. However, this stabilizing effect is supposed to be a simple function of the deposited rhodium amount and should result in the same, but delayed decline of activity, as a higher loading should not inhibit the fundamental process of rhodium photo-oxidation.

4.2 Non-stoichiometric $Y_{1.5}Bi_{0.5}Ti_2O_7$ and $YBiTi_2O_7$

By adjusting the Ti/(Y+Bi) ratios during synthesis, non-stoichiometric pyrochlores of $(Y_{1.5}Bi_{0.5})_{1-x}Ti_2O_{7-3x}$ and $(YBi)_{1-x}Ti_2O_{7-3x}$ were prepared by an aqueous sol-gel method and annealed at different temperatures. The materials were characterized by X-ray diffraction and UV-vis reflectance spectroscopy. The samples were tested for photocatalytic hydrogen production in the presence of methanol as sacrificial agent after being loaded with nanoparticles of rhodium or platinum acting as co-catalysts. The stepwise substitution of yttrium by bismuth in $Y_2Ti_2O_7$ forms $(Y_{1.5}Bi_{0.5})_{1-x}Ti_2O_{7-3x}$ and $(YBi)_{1-x}Ti_2O_{7-3x}$ for shifting the band gap energy towards the visible light region. For these materials, non-stoichiometric chemical compositions are obtained by the variation of the Ti/(Y+Bi) ratio. The samples are tested for activity and stability in the photocatalytic hydrogen producing test reaction. Moreover, special attention is paid to the stability of the bismuth containing titanates during photocatalysis.

4.2.1 Characterization of non-stoichiometric yttrium bismuth titanates

The yttrium bismuth titanates $(Y_{1.5}Bi_{0.5})_{1-x}Ti_2O_{7-3x}$ and $(YBi)_{1-x}Ti_2O_{7-3x}$ crystallize in the cubic pyrochlore structure of $A_2B_2O_6O'$ (cf. to chapter 2.3). Yttrium and bismuth are placed on the A-site and titanium ions on the B-site. Vacancy (\square) formation has not been found on the B-site and is only rarely possible on the O-site^[133]. Contrarily, the A- and O'-sites can accommodate a high degree of vacancies up to zero occupation^[133]. To incorporate excess BO_2 in the pyrochlore structure, in general, two vacancy models are

possible: either the vacancies are exclusively formed on the A site or additionally on the O` site. Therefore, structures of $(Y_{0.85}Bi_{0.85}Ti_{0.22}\square_{0.07})Ti_2O_6[O]`$ or $(Y_{0.77}Bi_{0.77}\square_{0.46})Ti_2O_6[O_{0.31}\square_{0.69}]`$ are obtained by a Ti/(Y+Bi) ratio of 1.30 for $YBiTi_2O_7$, respectively. As the simultaneous formation of vacancies on the A- and O`-sites is clearly favored in literature^[134, 135], this model is used herein as well.

Many reports deal with the stoichiometry in the pyrochlore $Bi_2Ti_2O_7$. Often, large amounts of $Bi_4Ti_3O_{12}$ are found as by-phase. Thus, a high stability of $Bi, O`$ -vacant structures of $Bi_{2-x}Ti_2O_{7-1.5x}$ has to be considered. The phase diagram of the Y_2O_3 - TiO_2 system published by Mizutani et al.^[24] describes a small stability field for non-stoichiometric $Y_2Ti_2O_7$ within the Ti/Y ratios of approximately 0.9 to 1.07. Previously we demonstrated for $Y_2Ti_2O_7$ that a pure pyrochlore phase can be successfully synthesized with a titanium excess of up to 7.5 % leading to a tremendous increase in photocatalytic activity (cf. to chapter 4.1.1). Further increase in the Ti/Y ratio led to the formation of TiO_2 rutile as an unwanted by-phase.

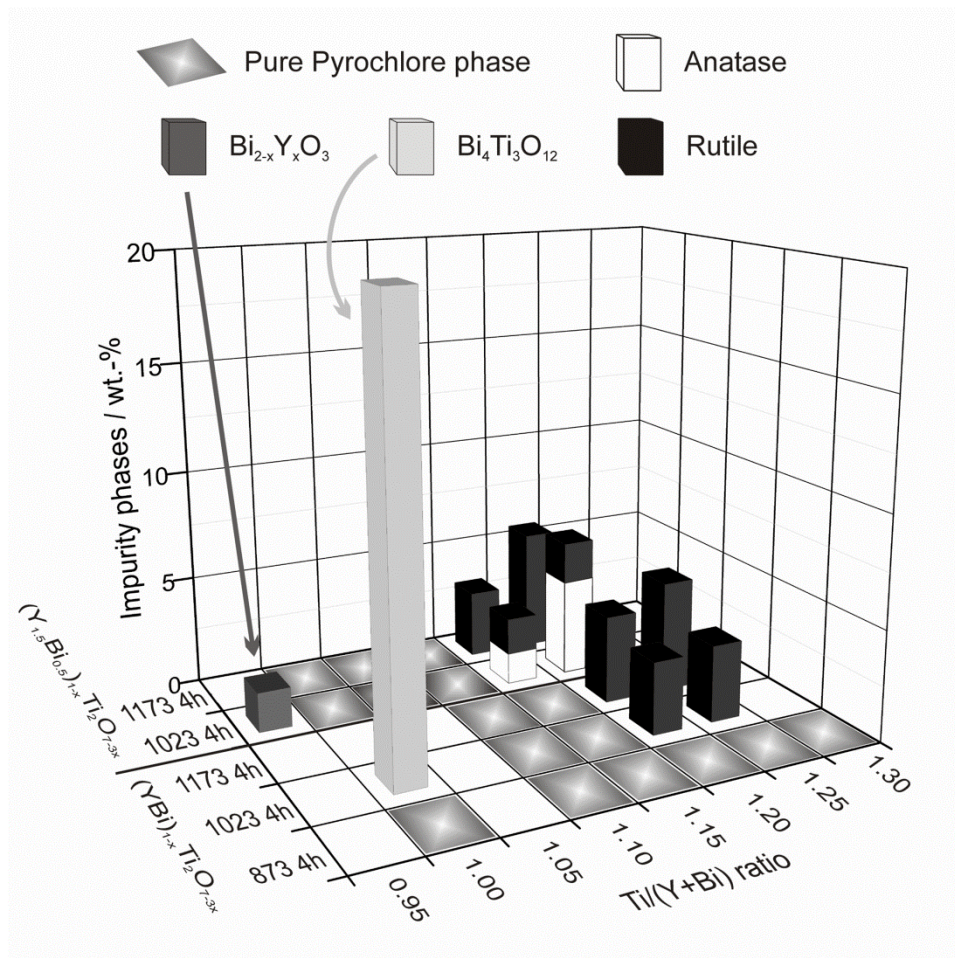


Figure 28: Phase analysis of $(Y_{1.5}Bi_{0.5})_{1-x}Ti_2O_{7-3x}$ and $(YBi)_{1-x}Ti_2O_{7-3x}$ samples annealed at 873 K, 1023 K or 1173 K for 4h as a function of the Ti/(Y+Bi) ratio.

Figure 28 shows that the stability range of the pyrochlore structure for higher titanium excess is extended considerably by partial replacement of yttrium by bismuth. At annealing temperatures of 1023 K and 1173 K, a pure pyrochlore phase is obtained from stoichiometric $Y_{1.5}Bi_{0.5}Ti_2O_7$ up to a composition of $Y_{1.36}Bi_{0.45}Ti_2O_{6.73}$ ($Ti/(Y+Bi)=1.10$). Passing to an even higher $Ti/(Y+Bi)$ ratio results in the formation of TiO_2 both as rutile and anatase as unwanted additional phases. A stoichiometric composition of $YBiTi_2O_7$ is only accessible at 873 K. At that annealing temperature, a pure pyrochlore phase can be formed up to a titanium excess of 30 %. At temperatures as high as 1023 K, a pure pyrochlore phase of $(YBi)_{1-x}Ti_2O_{7-3x}$ is only obtained, if a moderate titanium excess of 10 % or 15 % is introduced. At higher titanium excess rutile is formed as the only by-phase.

Doping of yttrium titanate by bismuth results in a lower band gap energy due to the hybridization of fully occupied Bi 6s and O 2p orbitals^[136] shifting the top of the valence band to more negative values (vs. NHE). Figure 29 shows the Tauc-plot^[112-114] of the UV-vis diffuse reflectance spectra in order to determine the effect of bismuth doping on the band gap energy.

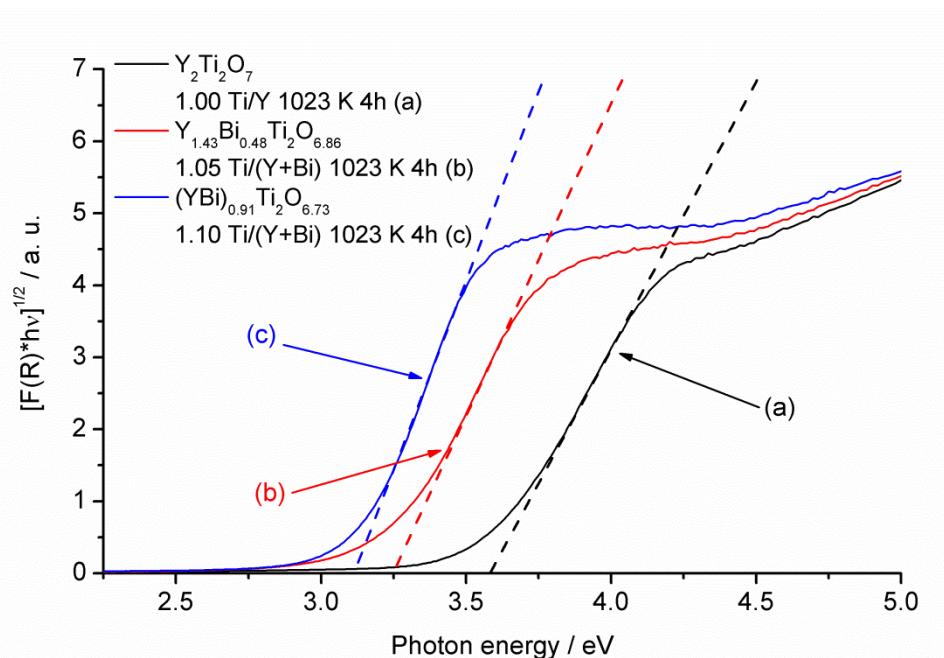


Figure 29: Tauc-plots (for indirect band gap transition) calculated from the UV-vis diffuse reflectance spectra of $Y_2Ti_2O_7$ (a), $Y_{1.43}Bi_{0.48}Ti_2O_{6.86}$ (b) and $(YBi)_{0.91}Ti_2O_{6.73}$ (c) annealed at 1023 K 4h exhibiting $Ti/(Y+Bi)$ ratios of 1.00, 1.05 and 1.10, respectively.

As band gap energies are not a function of the $Ti/(Y+Bi)$ but only of the Bi/Y ratio in the pure pyrochlore structure, the different series of samples are exemplified by

$\text{Y}_{1.43}\text{Bi}_{0.48}\text{Ti}_2\text{O}_{6.86}$ and $(\text{YBi})_{0.91}\text{Ti}_2\text{O}_{6.73}$. For comparison, stoichiometric $\text{Y}_2\text{Ti}_2\text{O}_7$ is listed as well. All samples were annealed at 1023 K for 4 hours. Band gap energies are obtained from the intersection point of the linear part of the plot $(F(R)\cdot hv)^{1/2}$ vs. hv with the energy axis, as stoichiometric as well as non-stoichiometric yttrium bismuth titanate pyrochlores are supposed to be semi-conductors revealing indirect band gap transitions. The replacement of 25 % of yttrium in $\text{Y}_2\text{Ti}_2\text{O}_7$ by bismuth leads to a shift in the band gap energy from 3.7 eV (cf. to chapter 4.1.1) to 3.3 eV. Samples of $(\text{YBi})_{1-x}\text{Ti}_2\text{O}_{7-3x}$ exhibit band gap energies of 3.1 eV.

As also found for $\text{Y}_2\text{Ti}_2\text{O}_7$ before (cf. to chapter 4.1.1), small amounts of rutile impurities can be detected very precisely by diffuse reflectance UV-vis spectroscopy. Figure 30 demonstrates that this is again true for $(\text{Y}_{1.5}\text{Bi}_{0.5})_{1-x}\text{Ti}_2\text{O}_{7-3x}$, but not for $(\text{YBi})_{1-x}\text{Ti}_2\text{O}_{7-3x}$ samples, as its band gap energy matches almost perfectly with that of rutile (3.0 eV^[127]).

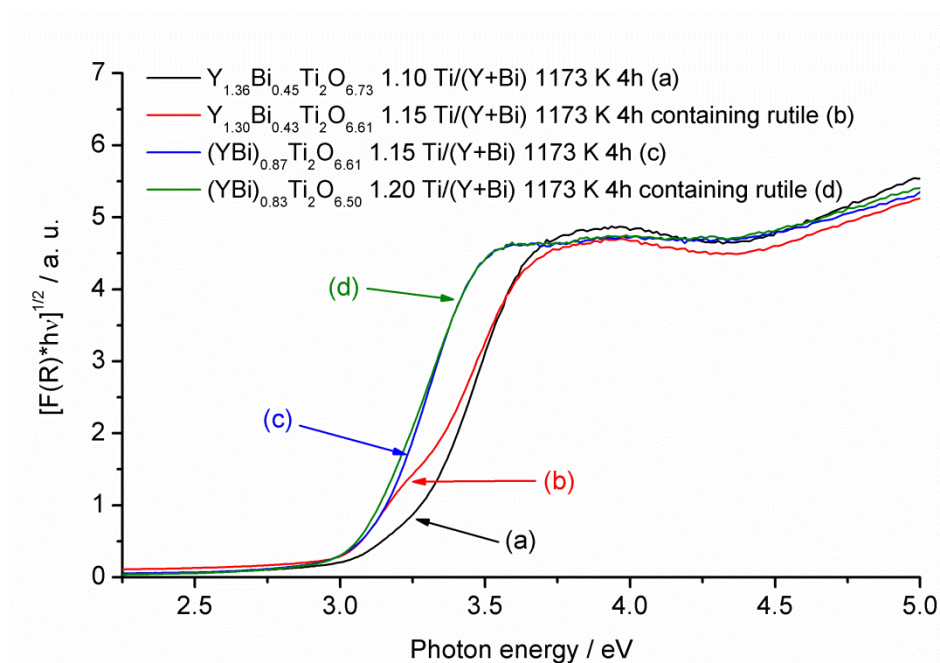


Figure 30: Tauc-plots (for indirect band gap transition) calculated from the UV-vis diffuse reflectance spectra of $(\text{Y}_{1.5}\text{Bi}_{0.5})_{1-x}\text{Ti}_2\text{O}_{7-3x}$ and $(\text{YBi})_{1-x}\text{Ti}_2\text{O}_{7-3x}$ samples annealed at 1173 K for band gap energy calculation and the analysis of the titania by-phase rutile.

The stability limit of the pyrochlore structure was determined by the stepwise increase of the titanium content in yttrium bismuth titanates. Figure 31 shows the X-ray diffraction data of pure pyrochlore phases exemplarily for $\text{Y}_{1.36}\text{Bi}_{0.45}\text{Ti}_2\text{O}_{6.73}$ (part A) and $(\text{YBi})_{0.87}\text{Ti}_2\text{O}_{6.61}$ (part B). In the 2θ range from 24.5 to 31.5 °, the formation of the TiO_2 by-phase rutile is confirmed by the presence of the (110) reflection (vide infra Figure 32).

Additional X-ray diffraction data of stoichiometric samples of YBiTi_2O_7 (873 K) and $\text{Y}_{1.5}\text{Bi}_{0.5}\text{Ti}_2\text{O}_7$ (1023 K and 1173 K) are provided as supporting information in Figure A3.

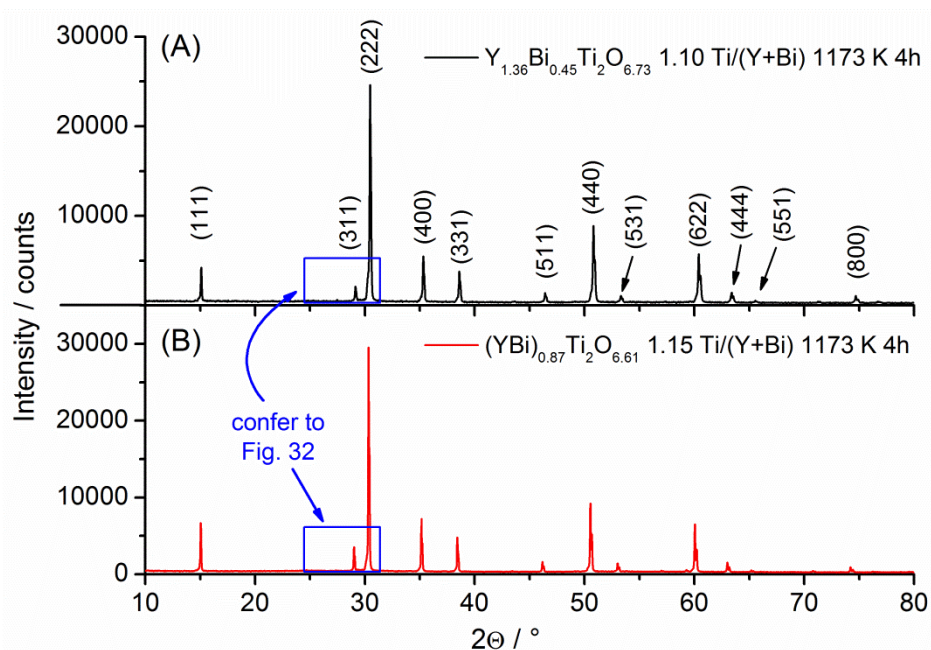


Figure 31: XRD pattern of $\text{Y}_{1.36}\text{Bi}_{0.45}\text{Ti}_2\text{O}_{6.73}$ (part A) and $(\text{YBi})_{0.87}\text{Ti}_2\text{O}_{6.61}$ (part B) annealed at 1173 K for 4h featuring Ti/(Y+Bi) ratios of 1.10 and 1.15, respectively.

The average crystallite sizes calculated by the Rietveld refinement method were found to be rather a function of the annealing temperature and the bismuth content in the structure than of the Ti/(Y+Bi) ratio. For $(\text{Y}_{1.5}\text{Bi}_{0.5})_{1-x}\text{Ti}_2\text{O}_{7-3x}$, average crystallite sizes of about 70 nm and 150 nm are calculated for samples annealed at 1023 K and 1173 K, respectively. Featuring higher bismuth content, samples of $(\text{YBi})_{1-x}\text{Ti}_2\text{O}_{7-3x}$ calcined at temperatures as high as 1023 K exhibit considerable enlarged average crystallite sizes of more than 200 nm. But, low temperature annealing at 873 K leads to very small average crystallite sizes of 70 nm for $(\text{YBi})_{1-x}\text{Ti}_2\text{O}_{7-3x}$ as well.

Figure 32 shows the analysis of titania by-phases in $(\text{Y}_{1.5}\text{Bi}_{0.5})_{1-x}\text{Ti}_2\text{O}_{7-3x}$ (part A: 1023 K, part B: 1173 K) and $(\text{YBi})_{1-x}\text{Ti}_2\text{O}_{7-3x}$ (part C: 1023 K, part D: 1173 K). Surprisingly, anatase is solely formed in presence of $(\text{Y}_{1.5}\text{Bi}_{0.5})_{1-x}\text{Ti}_2\text{O}_{7-3x}$, but not of $\text{Y}_2\text{Ti}_2\text{O}_7$ or $(\text{YBi})_{1-x}\text{Ti}_2\text{O}_{7-3x}$. As all samples were completely amorphous prior to annealing at 1023 K, we do not have an explanation for this behavior yet.

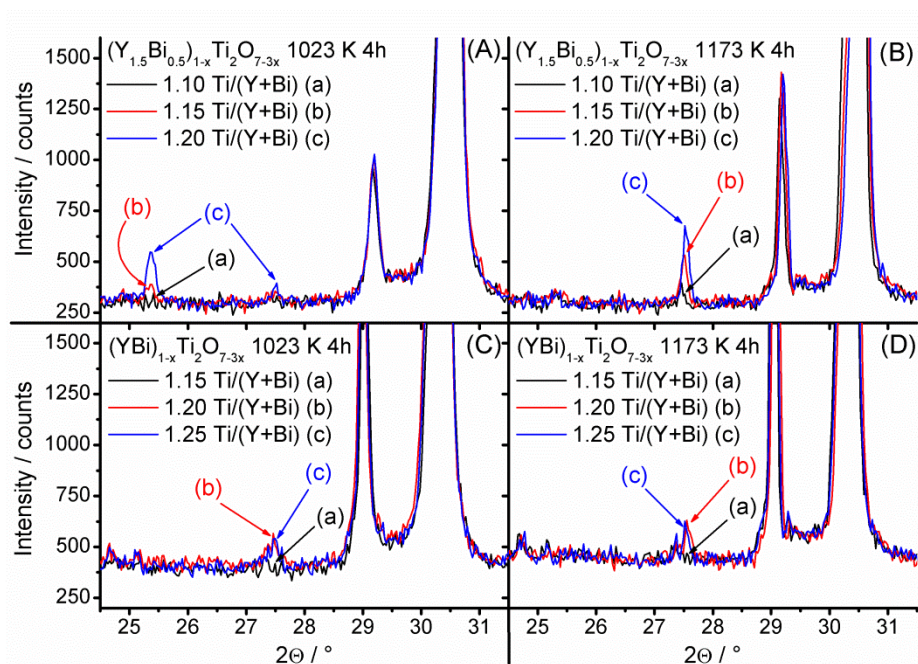


Figure 32: Detail of the X-ray diffraction data in the angular range of 24.5 to 31.5 ° 2θ for analysis of the titania by-phases rutile and anatase of $(Y_{1.5}Bi_{0.5})_{1-x}Ti_2O_{7-3x}$ and $(YBi)_{1-x}Ti_2O_{7-3x}$ samples annealed at 1023 K or 1173 K as a function of the Ti/(Y+Bi) ratio.

Pyrochlore stuffing is characterized by cation antisite formation, i. e., cations typically on the A position are placed at the B position. In the herein investigated materials this would lead to the doping of the TiO_6 octahedral network with yttrium and/or bismuth ions, which is considered unfavorable for photocatalytic activity. In case of $Y_2Ti_2O_7$, an excess of yttrium lead to the formation of a “stuffed” pyrochlore $Y_2(Ti_{2-x}Y_x)O_{7-0.5x}$ exhibiting a high degree of cationic lattice distortion, which was reduced by increasing the Ti/Y ratio up to a chemical composition of $Y_{2-x}Ti_2O_{7-1.5x}$ containing vacancies on the A-site of the structure (cf. to chapter 4.1.3). Due to the complete separation of yttrium and titanium on their specific lattice positions the activity in photocatalytic hydrogen production was enhanced from 9 $\mu\text{mol H}_2/\text{h}$ to 71 $\mu\text{mol H}_2/\text{h}$.

The degree of cation antisites can be estimated^[123] by the X-ray intensity ratios of the I(400)/I(331) reflections. The lower the ratio of the X-ray intensities, the better yttrium, bismuth and titanium are separated into their intended lattice positions.

Figure 33 shows a plot of the ratio I(400)/I(331) as a function of the Ti/(Y+Bi) ratio for $(Y_{1.5}Bi_{0.5})_{1-x}Ti_2O_{7-3x}$ and $(YBi)_{1-x}Ti_2O_{7-3x}$ samples annealed at 873 K, 1023 K and 1173 K, respectively. For comparison, the values for $Y_2Ti_2O_7$ calcined at 1023 K and 1173 K are presented as well. Surprisingly, the pyrochlore stuffing seems to be possible only in the case of bismuth free yttrium titanate. Here the increase of the Ti/Y ratio

resulted in a significant decrease of the I(400)/I(331) ratio from 3.1 to 1.6 due to the “destuffing” of the structure. As soon as bismuth ions are present, the I(400)/I(331) ratio values to about 1.6 being considered as the ideal value for a completely destuffed pyrochlore structure.

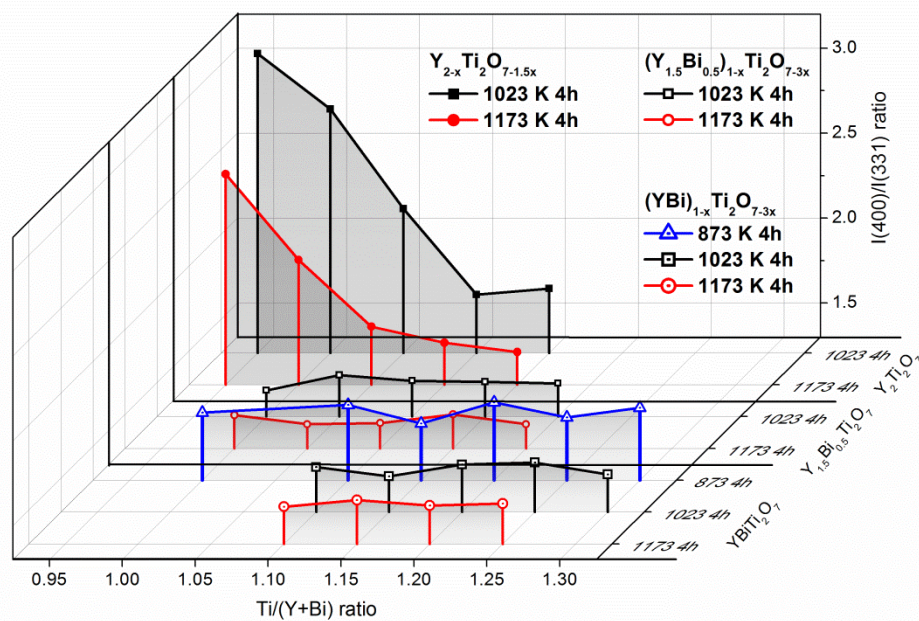


Figure 33: Quotients of the intensities of the (400) and (331) reflections as a function of the Ti/(Y+Bi) ratio for $(Y_{1.5}Bi_{0.5})_{1-x}Ti_2O_{7-3x}$, $(YBi)_{1-x}Ti_2O_{7-3x}$ and $Y_{2-x}Ti_2O_{7-1.5x}$ calcined at 873 K, 1023 K and 1173 K.

The cationic lattice distortion in a stuffed pyrochlore structure can be determined by the variation in the lattice parameter as well. As the effective ionic radii of yttrium and especially of bismuth exceed that of the substituted titanium, cationic distortion results in an expansion of the lattice, that is, an increase of the lattice parameter, by “doping” the B-site. Figure 34 shows the correlation between the Ti/(Y+Bi) ratio and the lattice parameter for samples of $(YBi)_{1-x}Ti_2O_{7-3x}$ (part A) and $(Y_{1.5}Bi_{0.5})_{1-x}Ti_2O_{7-3x}$ (part B) annealed at 873 K, 1023 K and 1173 K, respectively. For comparison, the change in the lattice parameter for different Ti/Y ratios in the Bi-free pyrochlore calcined at 1023 K and 1173 K is displayed as well (part C). Lattice parameters are calculated by the Rietveld refinement method of the diffraction data based on ideal pyrochlore structures of yttrium bismuth titanates including the refinement of the zero error. Only for the pure Bi-free material, the decrease of the Ti/Y ratio leads to an increase in the lattice parameter due to the stuffing of the B-site by larger yttrium ions; the lattice parameters of most bismuth containing yttrium titanates are not changed significantly by variation of the Ti/(Y+Bi) ratio. Only for $(YBi)_{1-x}Ti_2O_{7-3x}$ samples annealed at 873 K, a slight

decrease in the lattice parameter from 10.233 Å to 10.222 Å is observed by passing from the stoichiometric composition to a titanium excess of 15 %, which may derive from destuffing of the pyrochlore structure. Indeed, the substitution of yttrium by larger bismuth ions leads to a lattice broadening ideally corroborating with Vegard's law^[137, 138]. The lattice parameter of $\text{Y}_2\text{Ti}_2\text{O}_7$ was determined to be $a = 10.095$ Å (cf. to chapter 4.1.1), those of $(\text{Y}_{1.5}\text{Bi}_{0.5})_{1-x}\text{Ti}_2\text{O}_{7-3x}$ and $(\text{YBi})_{1-x}\text{Ti}_2\text{O}_{7-3x}$ are found to be $a = 10.162$ Å and 10.228 Å, respectively. Garbout et al.^[139] reported about the sol-gel synthesis of YBiTi_2O_7 using triethanolamine/diethanolamine as ligands, but a pure pyrochlore phase could only be obtained at very high annealing temperatures of at least 1273 K. A lattice parameter of $a = 10.199$ Å was found.

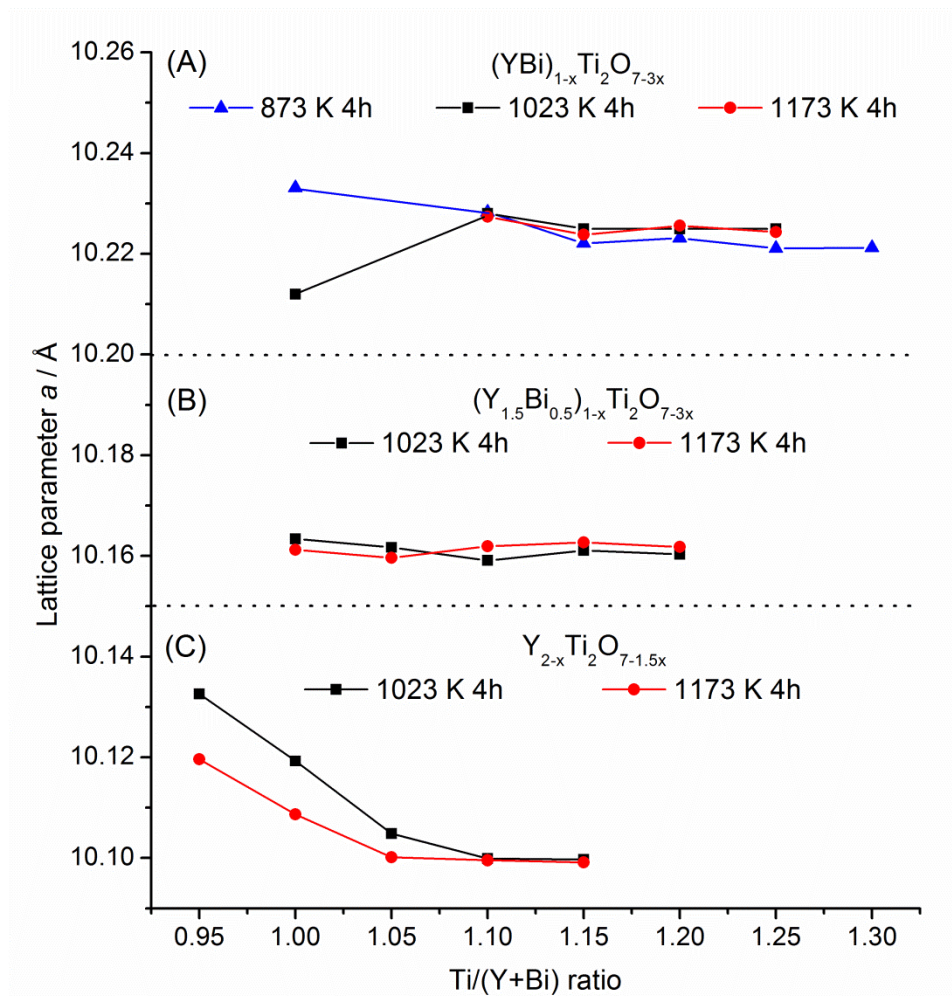


Figure 34: The lattice parameters as a function of the Ti/(Y+Bi) ratio for $(\text{YBi})_{1-x}\text{Ti}_2\text{O}_{7-3x}$ (A), $(\text{Y}_{1.5}\text{Bi}_{0.5})_{1-x}\text{Ti}_2\text{O}_{7-3x}$ (B) and $\text{Y}_{2-x}\text{Ti}_2\text{O}_{7-1.5x}$ (C) calcined at 873 K, 1023 K and 1173 K.

At an annealing temperature of 1023 K, the lattice parameter of stoichiometric YBiTi_2O_7 amounts to a remarkable low value of 10.212 Å. As can be depicted from the

corresponding X-ray diffraction data presented in Figure 35(A), the sample contains a large amount (ca. 20 wt.-%) of the by-phase $\text{Bi}_4\text{Ti}_3\text{O}_{12}$ (cf. to Figure 28 as well), by what the remaining pyrochlore structure is highly depleted in bismuth. The chemical composition of “ YBiTi_2O_7 ” annealed at 1023 K was determined by the Rietveld refinement to be rather $\text{Y}_{1.15}\text{Bi}_{0.75}\text{Ti}_2\text{O}_{6.85}$ than stoichiometric. Since the lattice expansion is mainly determined by the ratio between yttrium and bismuth, the lattice parameter of $\text{Y}_{1.15}\text{Bi}_{0.75}\text{Ti}_2\text{O}_{6.85}$ fits nicely between those of $\text{Y}_{1.5}\text{Bi}_{0.5}\text{Ti}_2\text{O}_7$ and YBiTi_2O_7 .

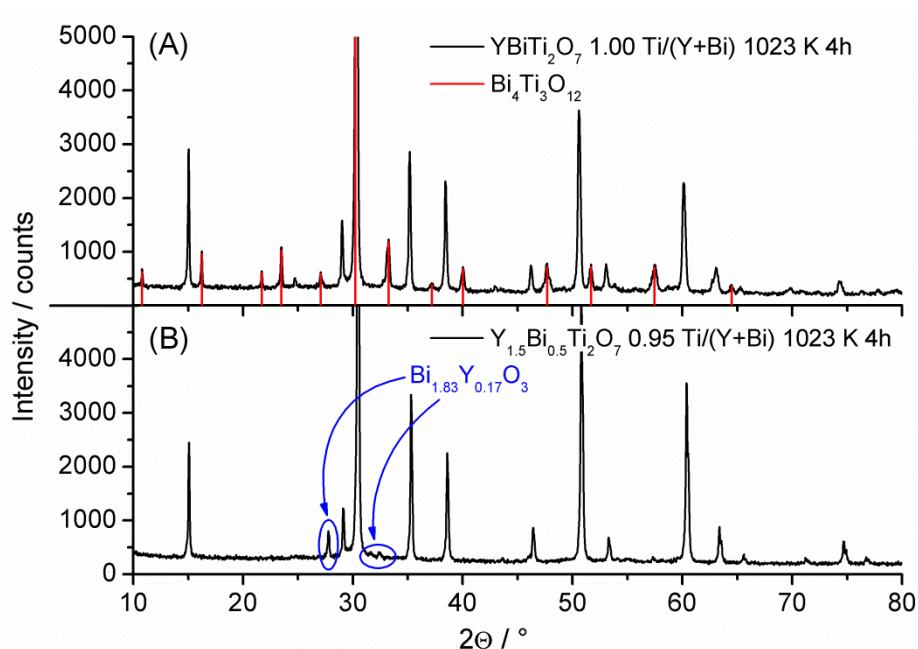


Figure 35: XRD pattern of YBiTi_2O_7 (part A) and $\text{Y}_{1.5}\text{Bi}_{0.5}\text{Ti}_2\text{O}_7$ (part B) annealed at 1023 K 4h and featuring $\text{Ti}/(\text{Y}+\text{Bi})$ ratios of 1.00 and 0.95, respectively, for analysis of the by-phases $\text{Bi}_4\text{Ti}_3\text{O}_{12}$ and $\text{Bi}_{1.83}\text{Y}_{0.17}\text{O}_3$. Perovskite $\text{Bi}_4\text{Ti}_3\text{O}_{12}$ is referenced by the PDF-file 01-089-7503.^[140]

To investigate the possibility of stuffed bismuth containing pyrochlores, a sample with an excess of yttrium and bismuth was prepared, that is, $\text{Y}_{1.5}\text{Bi}_{0.5}\text{Ti}_2\text{O}_7$ 0.95 $\text{Ti}/(\text{Y}+\text{Bi})$ 1023 K 4h. Although forced stuffing is easily achieved in the case of $\text{Y}_2(\text{Ti}_{2-x}\text{Y}_x)\text{O}_{7-0.5x}$ (cf. to chapter 4.1.1), Figure 35(B) shows that this attempt failed due to the formation of the strongly bismuth enriched by-phase of $\text{Bi}_{1.83}\text{Y}_{0.17}\text{O}_3$. The very large bismuth ions (eff. ionic radius: 117 pm for 8-fold coordination)^[141] cannot be placed on the B-site of the structure. Pyrochlore stuffing of lanthanide titanates is known to be only possible with lutetium to terbium ions^[121] possessing smaller effective ionic radii^[141] ranging from 97.7 pm to 104 pm, respectively. Yttrium featuring an effective ionic radius of 101.9 pm^[141] fits into this scheme. Moreover, the size of bismuth ions seems to be too large to form pyrochlores free of vacancies, because there are only a few reports^[142]

about stoichiometric $\text{Bi}_2\text{Ti}_2\text{O}_7$ in the literature. In contrast, a stable pyrochlore phase is often suggested to exhibit a bismuth content not exceeding that of $\text{Bi}_{1.74}\text{Ti}_2\text{O}_{6.62}$ ^[143]. Therefore, the fact that bismuth stuffing is impossible does not necessarily implicate the absence of yttrium stuffing, which may be masked in some way.

Figure 36 shows the TEM micrographs in darkfield mode of $\text{Y}_{1.36}\text{Bi}_{0.45}\text{Ti}_2\text{O}_{6.73}$ (Ti/(Y+Bi) ratio of 1.10) and $(\text{YBi})_{0.77}\text{Ti}_2\text{O}_{6.31}$ (Ti/(Y+Bi) ratio of 1.30) loaded with 1.35 wt.-% of rhodium and 3.0 wt.-% of platinum, respectively. The bright areas are assigned to photodeposited co-catalyst nanoparticles. A broad particle size distribution is found for the catalysts itself ranging from 20 to 100 nm, which is in good agreement with the average crystallite sizes calculated by X-ray diffraction (40 nm in average for both samples).

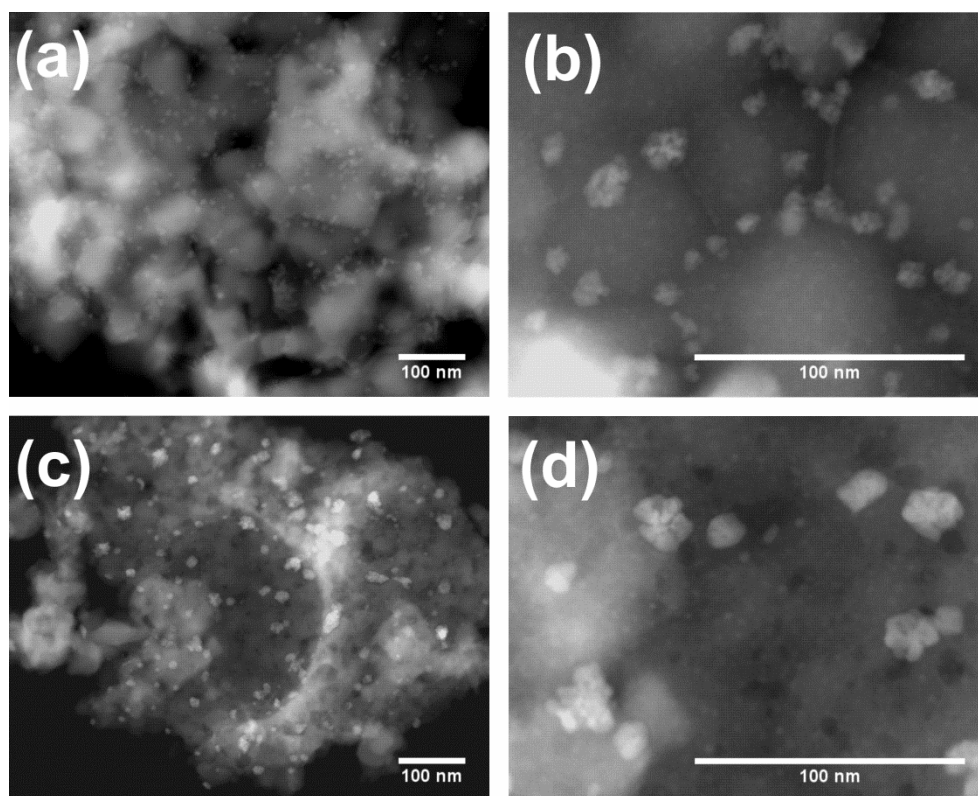


Figure 36: TEM micrographs in dark field mode of $\text{Y}_{1.36}\text{Bi}_{0.45}\text{Ti}_2\text{O}_{6.73}$ Ti/(Y+Bi) 1.10 calcined at 1023 K for 4h [parts (a) and (b)] and $(\text{YBi})_{0.77}\text{Ti}_2\text{O}_{6.31}$ Ti/(Y+Bi) 1.30 annealed at 873 K for 4h [parts (c) and (d)]. The samples were loaded by photodeposition with 1.35 wt.-% of rhodium and 3.0 wt.-% of platinum, respectively.

Both rhodium and platinum were photodeposited with a primary crystallite size of about 3 nm, which tend to agglomerate forming small co-catalyst islands. The diameter of these islands depends on the applied co-catalyst loading. A small loading of 1.35 wt.-% leads to a diameter of about 15 nm and a loading of 3.0 wt.-% results in 30 nm co-catalyst

islands. Although the co-catalysts are indeed mainly deposited in these characteristic clusters, parts (b) and (d) of Figure 36 made in a higher magnification (1000000x) indicate that co-catalyst primary particles being 1-2 nm in size are also finely dispersed on the surface of the catalysts.

By means of *energy-dispersive X-ray spectroscopy* (EDXS) the bright areas in the micrographs made in darkfield mode are assigned to the co-catalyst nanoparticles. This method was only applicable to samples, which were loaded with a high co-catalyst loading of at least 3.0 wt.-%. Thus, the $(\text{YBi})_{0.77}\text{Ti}_2\text{O}_{6.31}$ (Ti/(Y+Bi) ratio of 1.30) sample providing 3.0 wt.-% of platinum was chosen. The platinum mapping is presented in Figure 37(b) indicating that platinum is mainly located at the bright areas of the darkfield TEM micrograph in part (a) correctly assigned to platinum. In part (c) of Figure 37 the color-coded combination of the original micrograph and the Pt mapping is shown, in which blue areas are assigned to platinum. The EDXS mapping of yttrium, bismuth and titanium is given in the appendix in Figure A4 proving that all cations are homogeneously distributed, which was expected for a single phase mixed oxide.

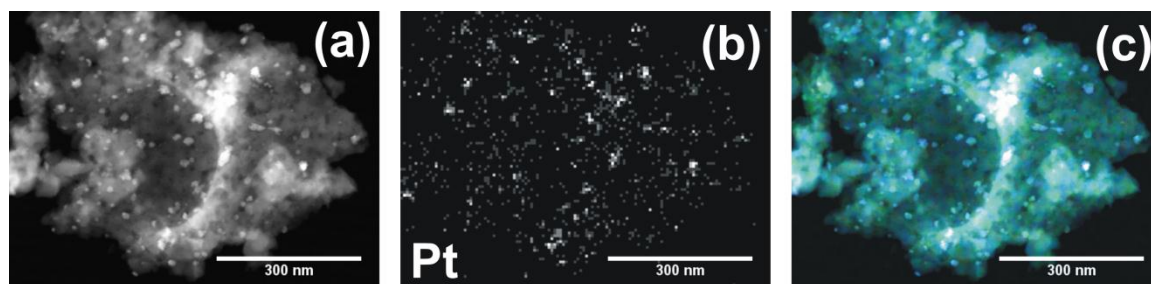


Figure 37: TEM micrograph in dark field mode (a) and EDXS analysis of $(\text{YBi})_{0.77}\text{Ti}_2\text{O}_{6.31}$ Ti/(Y+Bi) 1.30 annealed at 873 K for 4h and loaded with 3.0 wt.-% of platinum. Part (b) shows the platinum mapping after 40 minutes and part (c) the color-coded transformation, in which blue areas are assigned to platinum.

4.2.2 Photocatalytic hydrogen production with $(\text{Y}_{1.5}\text{Bi}_{0.5})_{1-x}\text{Ti}_2\text{O}_{7-3x}$

Figure 38 shows the photocatalytic hydrogen production as a function of the Ti/(Y+Bi) ratio for samples calcined at 1023 K and loaded by photodeposition with 0.75 wt.-% of platinum. Whereas stoichiometric $\text{Y}_{1.5}\text{Bi}_{0.5}\text{Ti}_2\text{O}_7$ as well as $\text{Y}_{1.43}\text{Bi}_{0.48}\text{Ti}_2\text{O}_{6.86}$ are almost inactive, the hydrogen production rate increases significantly from below 2 $\mu\text{mol H}_2/\text{h}$ to about 8.5 $\mu\text{mol H}_2/\text{h}$ by passing to $\text{Y}_{1.36}\text{Bi}_{0.45}\text{Ti}_2\text{O}_{6.73}$ (Ti/(Y+Bi)=1.10) still stating a pure pyrochlore phase. By further increase of the titanium content in the structure anatase and rutile are formed as by-phases, but the hydrogen production rates stay almost constant between 8 and 9 $\mu\text{mol H}_2/\text{h}$. An increase of the annealing temperature to 1173 K leads to

significantly enlarged average crystallite sizes decreasing the photocatalytic activity markedly (cf. to the appendix in Figure A5). Platinum loading of $(Y_{1.5}Bi_{0.5})_{1-x}Ti_2O_{7-3x}$ leads to almost steady hydrogen production rates.

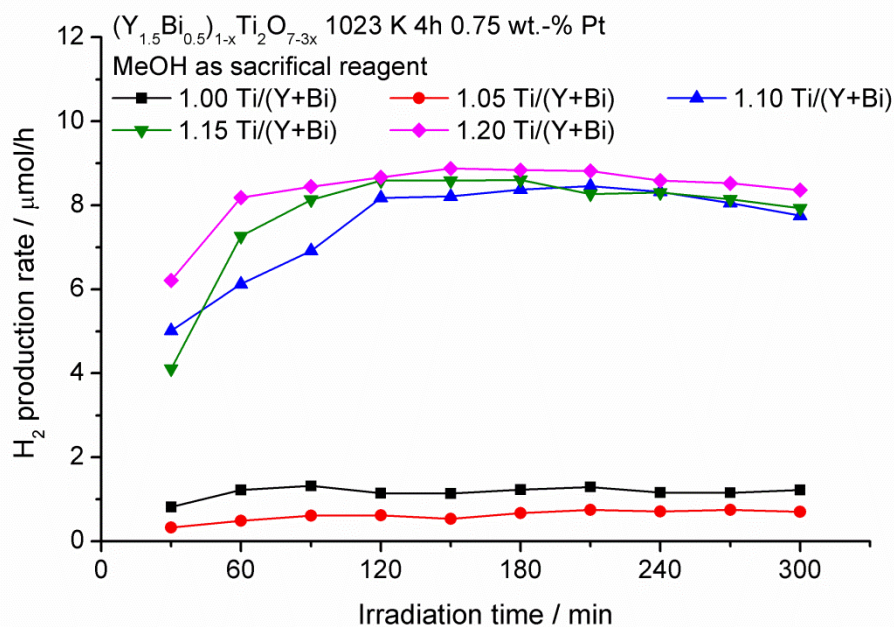


Figure 38: Photocatalytic activity regarding hydrogen production over $(Y_{1.5}Bi_{0.5})_{1-x}Ti_2O_{7-3x}$ calcined at 1023 K for 4h with 0.75 wt.-% platinum as co-catalyst and in the presence of 10 vol.-% methanol as sacrificial reagent.

The photocatalytic activity in hydrogen production of $(Y_{1.5}Bi_{0.5})_{1-x}Ti_2O_{7-3x}$ samples loaded with 0.75 wt.-% of rhodium and annealed at 1023 K and 1173 K are presented as additional information in Figure A6 and Figure A7, respectively. Also with rhodium as co-catalyst, a Ti/(Y+Bi) ratio of 1.10 is optimum, but in general higher activities are achieved than by platinum loaded samples. However, rhodium loaded samples suffer from decreasing hydrogen production rates. A similar behavior was found for rhodium loaded samples of $Y_{2-x}Ti_2O_{7-1.5x}$ (cf. to chapter 4.1.2), which is assigned to the less precious character of the rhodium metal ($E_0(Rh^{3+}|Rh) = +0.76 V$) compared to that of platinum ($E_0(Pt^{2+}|Pt) = +1.18 V$) leading to a lower oxidation stability^[52].

Figure 39 summarizes the maximum measured hydrogen production rates achieved by $(Y_{1.5}Bi_{0.5})_{1-x}Ti_2O_{7-3x}$ samples. The photocatalytic activity is clearly enhanced by increasing the Ti/(Y+Bi) ratio up to 1.10. The hydrogen production rate is reduced, if a small amount of rutile is formed as by-phase (samples annealed at 1173 K), but is not influenced significantly in presence of a mixture of anatase and rutile by-phases (samples annealed at 1023 K). In the latter case, the more photocatalytically active anatase phase

compensates the negative effect of rutile. The titania phase rutile is considered to be less active for photocatalytic hydrogen production than the anatase modification, as the flatband potential of anatase coincides almost exactly with the redox potential of the $H^+ / \frac{1}{2}H_2$ couple resulting in a smaller driving force for proton reduction^[129]. Thus, even in anatase containing samples the photocatalytic activity is assumed to derive mainly from the pyrochlore phase.

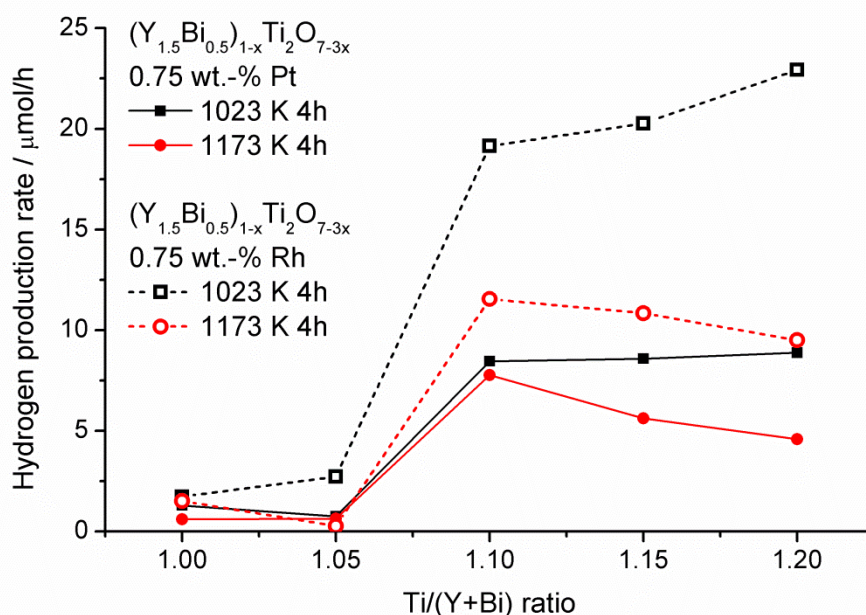


Figure 39: Maximum photocatalytic activities in hydrogen production over $(Y_{1.5}Bi_{0.5})_{1-x}Ti_2O_{7-3x}$ calcined at 1023 K or 1173 K for 4h with 0.75 wt.-% of rhodium or platinum as co-catalyst and in the presence of 10 vol.-% methanol as sacrificial reagent.

4.2.3 Photocatalytic hydrogen production with $(YBi)_{1-x}Ti_2O_{7-3x}$

Figure 40 shows the photocatalytic hydrogen production of Pt-loaded samples calcined at 873 K as a function of the Ti/(Y+Bi) ratio. In contrast to $(Y_{1.5}Bi_{0.5})_{1-x}Ti_2O_{7-3x}$ samples, almost no activities are achieved at a low co-catalyst loading of 0.75 wt.-% of rhodium or platinum (vide infra, Figure 43(A)). Therefore, measurements had to be performed under a quite high co-catalyst loading of 2.00 wt.-%. Again, the stoichiometric sample is almost inactive and a reasonable hydrogen production rate is not obtained until a Ti/(Y+Bi) ratio of at least 1.15 is realized corresponding to $(YBi)_{0.87}Ti_2O_{6.61}$. Increase of the titanium excess to 30 % leads to an improvement of the hydrogen production rate from 2 $\mu\text{mol H}_2/\text{h}$ to about 15 $\mu\text{mol H}_2/\text{h}$ by $(YBi)_{0.77}Ti_2O_{6.31}$ still consisting of a pure pyrochlore phase. Nevertheless, Figure 40 also demonstrates that for $(YBi)_{1-x}Ti_2O_{7-3x}$ samples, the

issue of decreasing activities becomes highly serious, as most samples suffer from decreasing hydrogen formation rates with time. The hydrogen production rate of the most active sample is decreased by about one-third within five hours of illumination giving rise to the assumption that decreasing activities do not only arise from the co-catalyst, but being also a function of the bismuth content in the structure.

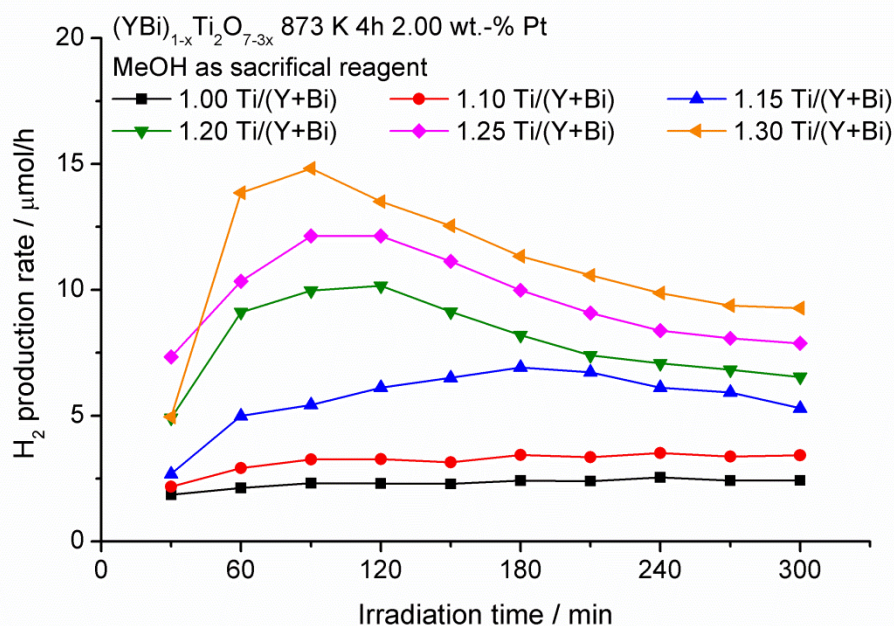


Figure 40: Photocatalytic activity regarding hydrogen production over $(\text{YBi})_{1-x}\text{Ti}_2\text{O}_{7-3x}$ calcined at 873 K for 4h with 2.00 wt.-% platinum as co-catalyst and in the presence of 10 vol.-% methanol as sacrificial reagent.

A summary of obtained maximum hydrogen production rates for $(\text{YBi})_{1-x}\text{Ti}_2\text{O}_{7-3x}$ samples is given in Figure 41 also providing the data for samples annealed at 1023 K and 1173 K. The detailed measurements of 1023 K samples are shown as additional information in Figure A8. A similar behaviour is found for $(\text{YBi})_{1-x}\text{Ti}_2\text{O}_{7-3x}$ samples annealed at 1023 K, as the activity is improved up to $(\text{YBi})_{0.83}\text{Ti}_2\text{O}_{6.5}$ ($\text{Ti}/(\text{Y}+\text{Bi})=1.20$). As expected, the hydrogen production rate decreases by further titanium addition due to a higher rutile content. The unexpected quite high activity of the stoichiometric sample is explained easily by the presence of about 20 wt.-% of $\text{Bi}_4\text{Ti}_3\text{O}_{12}$. Indeed, this perovskite itself is considered as poorly active, but goes along with the formation of $\text{Y}_{1.15}\text{Bi}_{0.75}\text{Ti}_2\text{O}_{6.85}$ featuring a higher Y/Bi ratio and a significant amount of vacancies on the A,O`-sites. Both characteristics were proven to be beneficial for photocatalytic hydrogen production. The hydrogen production rates obtained with samples annealed at 1173 K are almost insignificant. However, by far the best activities are obtained with

samples annealed at 873 K. Smaller average crystallite sizes of 70 nm are responsible for better performance. Furthermore, at this low temperature, a higher titanium excess is introducible into the structure resulting in a higher degree of A,O`-site vacancies and maybe in less cationic distortion, but not in the formation of TiO₂ by-phases.

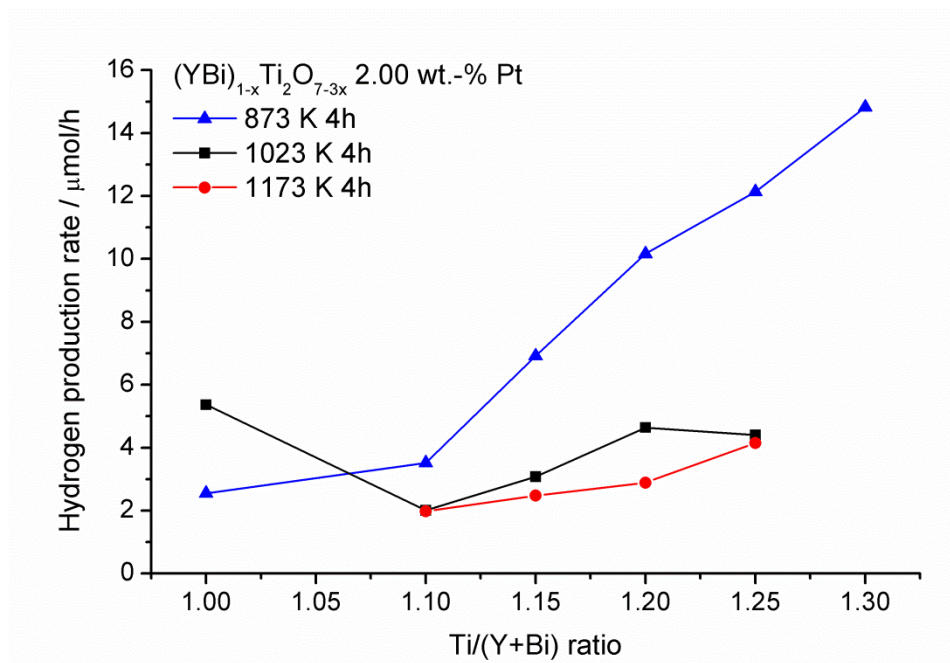


Figure 41: Maximum photocatalytic activities in hydrogen production over (YBi)_{1-x}Ti₂O_{7-3x} calcined at 873 K, 1023 K or 1173 K for 4h with 2.00 wt.-% platinum as co-catalyst and in the presence of 10 vol.-% methanol as sacrificial reagent.

4.2.4 Optimum co-catalyst loading and stability of non-stoichiometric yttrium bismuth titanates

Figure 42 shows the photocatalytic hydrogen production of Y_{1.36}Bi_{0.45}Ti₂O_{6.73} (Ti/(Y+Bi)=1.10) annealed at 1023 K being the most active sample in this series as a function of the co-catalyst loading of platinum (part (A)) and rhodium (part (B)). For both co-catalysts, an optimum loading of 1.35 wt.-% is found. The maximum hydrogen production rate amounts to 27.2 μmol H₂/h for the rhodium loaded sample. In contrast to other platinum loaded samples in its series, Y_{1.36}Bi_{0.45}Ti₂O_{6.73} loaded with 1.35 wt.-% of platinum reveals a considerable loss in activity with time. The amount of loaded co-catalyst clearly influences the extent of activity loss, as further increase of the platinum loading to 2.00 wt.-% results indeed in a lower hydrogen production rate, but being stable over time. Nevertheless, for rhodium loaded samples, the decrease in activity can only be reduced by supplying a rhodium loading of 2.00 wt.-%, but cannot be eliminated entirely.

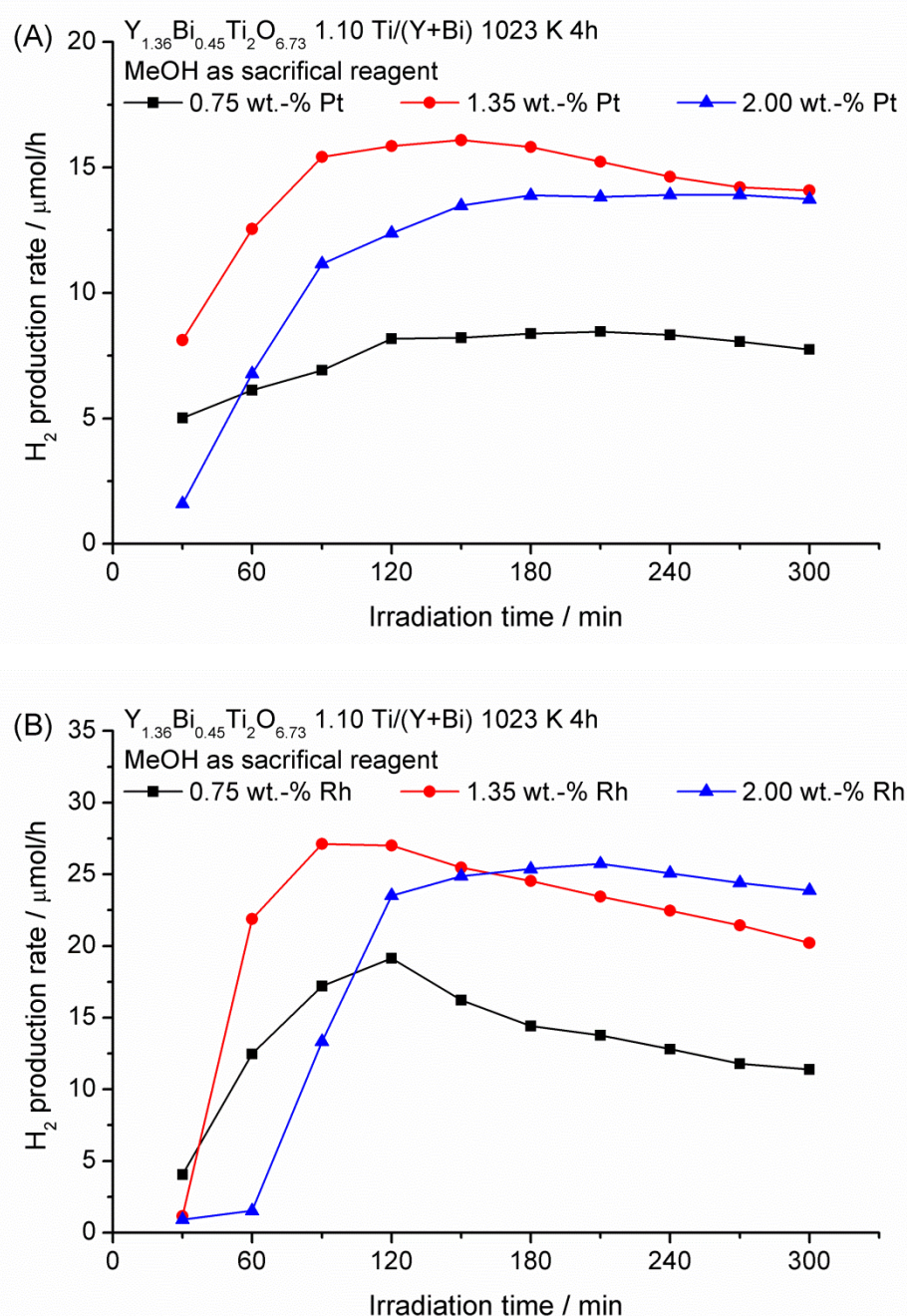


Figure 42: Photocatalytic activity regarding hydrogen production over $\text{Y}_{1.36}\text{Bi}_{0.45}\text{Ti}_2\text{O}_{6.73}$ (Ti/(Y+Bi)=1.10) calcined at 1023 K for 4h in the presence of 10 vol.-% methanol as sacrificial reagent as a function of the co-catalyst loading of platinum (A) and rhodium (B).

Figure 43 presents the evolution of the hydrogen production rates of $(\text{YBi})_{0.77}\text{Ti}_2\text{O}_{6.31}$ (Ti/(Y+Bi)=1.30) annealed at 873 K 4h stating the most active sample in that test series as a function of the co-catalyst loading of platinum (part (A)) as well as rhodium (part (B)). The highest temporary hydrogen production rate of 17.5 $\mu\text{mol H}_2/\text{h}$ is obtained by $(\text{YBi})_{0.77}\text{Ti}_2\text{O}_{6.31}$ loaded with 3.00 wt.-% of platinum, an optimum rhodium loading of 2.00 wt.-% leads to a slightly lower value. The optimum co-catalyst loading is clearly

increased by higher bismuth content in the pyrochlore structure. The intrinsic capability of charge separation seems to be reduced, which has to be compensated by an increasing amount of co-catalyst. The decline in charge separation may not only derive from the reduction of the band gap energy making charge recombination thermodynamically more probable, but also from distortion in the TiO_6 -octahedral geometry, which is conceivable in a pyrochlore structure possessing yttrium as well as bismuth on the same lattice site.

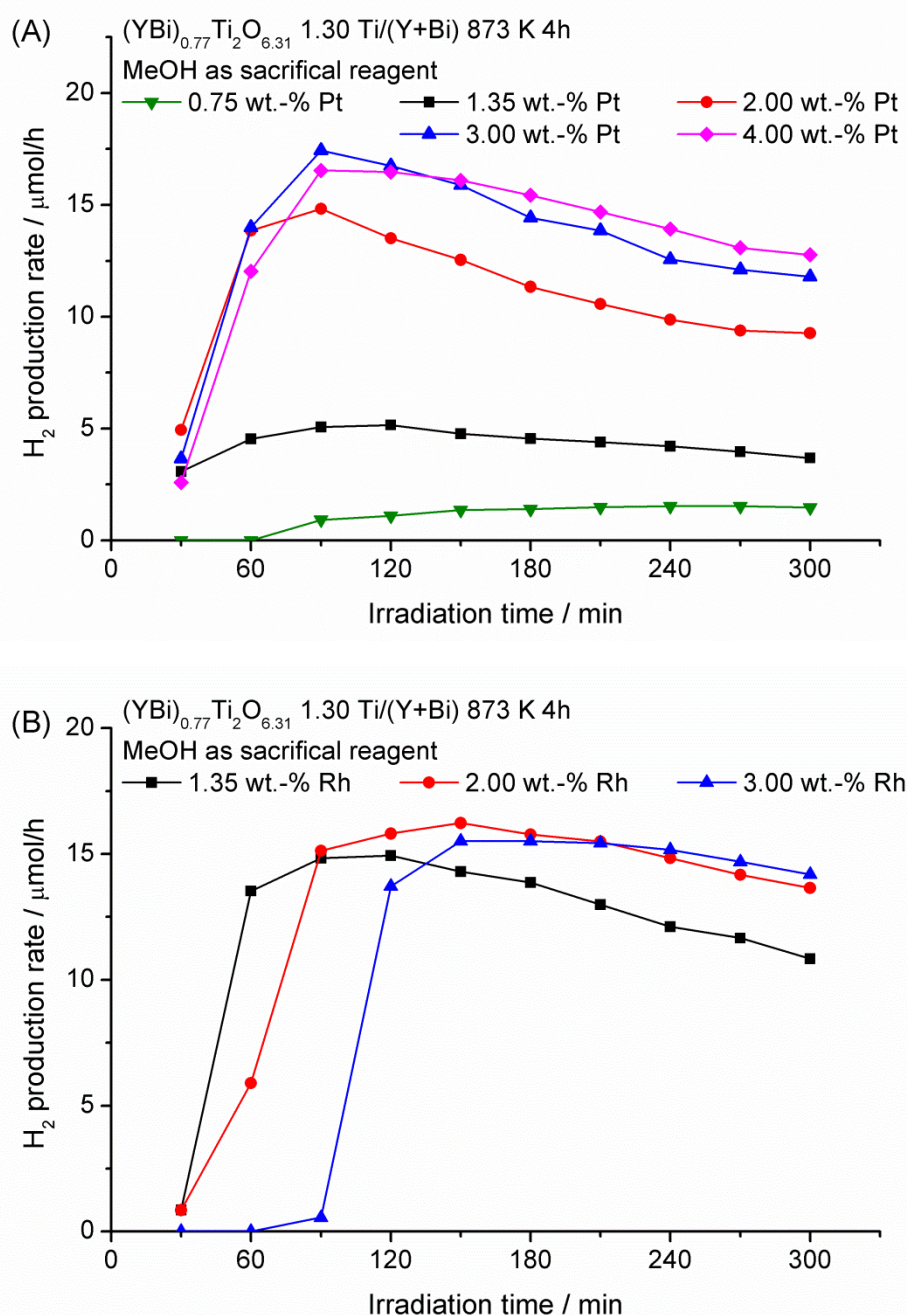


Figure 43: Photocatalytic activity regarding hydrogen production over $(\text{YBi})_{0.77}\text{Ti}_2\text{O}_{6.31}$ (Ti/(Y+Bi)=1.30) calcined at 873 K for 4h in the presence of 10 vol.-% methanol as sacrificial reagent as a function of the co-catalyst loading of platinum (A) and rhodium (B).

Although the stability of hydrogen production is enhanced by raising the co-catalyst loading, a perfectly stable activity has not been achieved for $(\text{YBi})_{0.77}\text{Ti}_2\text{O}_{6.31}$ even with high loadings of up to 4.00 wt.-%. In a long term run over a period of 18 hours utilizing $(\text{YBi})_{0.77}\text{Ti}_2\text{O}_{6.31}$ loaded with 3 wt.-% of Pt, the hydrogen production rate decreased from 17.5 $\mu\text{mol H}_2/\text{h}$ to 7.5 $\mu\text{mol H}_2/\text{h}$. It is supposed that elemental bismuth or bismuth suboxides are formed by photoreduction. However, no additional phases could be detected in the long term measurement sample by X-ray diffraction.

To gather information about the photocatalytic stability of bismuth containing titanates is difficult, as these materials are most often used in photocatalytic dye-degradation reactions^[32, 144]. Usually, only a very small dye concentration is applied leading to pseudo-first order reaction kinetics. The rate of the reaction is a function of the relative degree of dye degradation (Abs/Abs_0) and both are decreasing with time. Thus, stability issues of a photocatalyst will probably be masked. The reaction type of photocatalytic hydrogen production is qualified in particular for validation of catalyst stability, as it is characterized by pseudo-zero order kinetics due to the high amount of methanol applied. Kudo and Hiji^[35] reported about photocatalytic hydrogen production with the pyrochlore $\text{Bi}_2\text{Ti}_2\text{O}_7$ and the Aurivillius perovskite phase $\text{Bi}_4\text{Ti}_3\text{O}_{12}$ under similar conditions as applied in this work but could not discuss stabilities, since both stoichiometric catalysts did not show any photocatalytic activity in presence of methanol, which is in agreement with our results.

4.2.5 Photonic efficiencies of non-stoichiometric yttrium bismuth titanates

Figure 44 summarizes the maximum photocatalytic hydrogen production rates taken from measurements presented in Figure 42 and Figure 43. The right axis is assigned to the corresponding photonic efficiencies. For $\text{Y}_{1.36}\text{Bi}_{0.45}\text{Ti}_2\text{O}_{6.73}$ ($\text{Ti}/(\text{Y}+\text{Bi}) = 1.10$), a maximum photonic efficiency of about 0.55 % is obtained by loading 1.35 wt.-% of rhodium. Whereas the optimization of the co-catalyst loading for $(\text{YBi})_{0.77}\text{Ti}_2\text{O}_{6.31}$ ($\text{Ti}/(\text{Y}+\text{Bi})=1.30$) leads to approximately the same hydrogen production rates for platinum as well as rhodium acting as co-catalyst, the loading of $\text{Y}_{1.36}\text{Bi}_{0.45}\text{Ti}_2\text{O}_{6.73}$ with rhodium seems to be beneficial, which, however, needs further investigation. For $(\text{YBi})_{0.77}\text{Ti}_2\text{O}_{6.31}$ a maximum photonic efficiency of about 0.35 % is obtained. It should be noted that the calculation of photonic efficiencies is based on the ferrioxalate

actinometry quantifying the amount of photons in the spectral region ranging from 200 nm to 485 nm, whereas $Y_{1.36}Bi_{0.45}Ti_2O_{6.73}$ and $(YBi)_{0.77}Ti_2O_{6.31}$ are only able to absorb photons up to wavelengths of about 380 nm and 400 nm, respectively. Hence, the values given here can be regarded as lower limits of the actual photonic efficiencies. Nevertheless, photonic efficiencies of photocatalysts exhibiting different band gap energies are better comparable this way. After optimization of the Ti/(Y+Bi) ratio, the annealing temperature and the co-catalyst loading for all samples, it is evident that the substitution of yttrium by bismuth clearly decreases the photocatalytic activity of $Y_{2-x}Ti_2O_{7-1.5x}$. The maximum achieved photonic efficiency is reduced from 1.4 % to 0.55 % to 0.35 % by passing from $Y_{1.82}Ti_2O_{6.73}$ (Ti/Y = 1.10) 1023 K 4h (cf. to chapter 4.1.2) to $Y_{1.36}Bi_{0.45}Ti_2O_{6.73}$ 1023 K to $(YBi)_{0.77}Ti_2O_{6.31}$ 873 K, respectively.

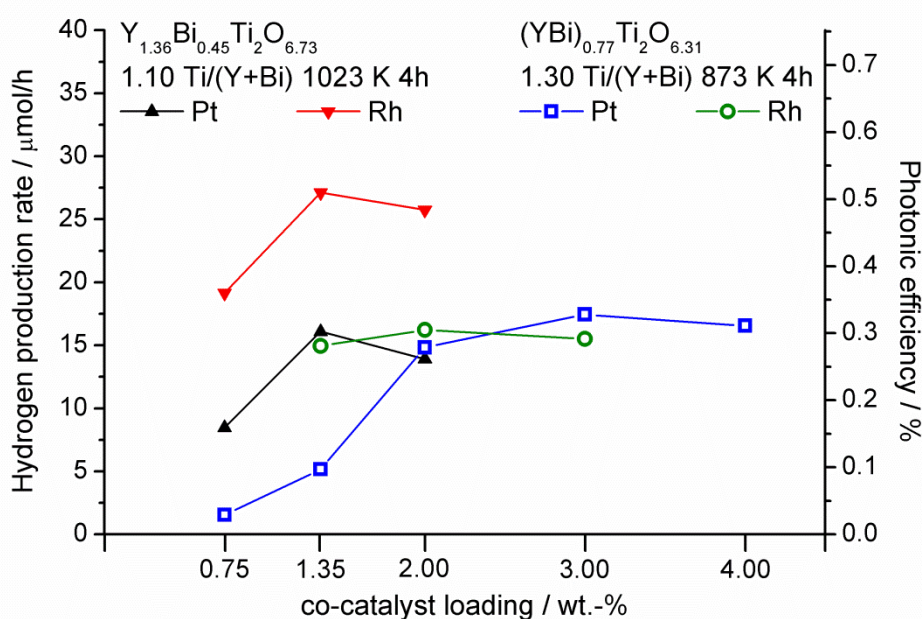


Figure 44: Photocatalytic activities and photonic efficiencies regarding hydrogen production over $(Y_{1.5}Bi_{0.5})_{1-x}Ti_2O_{7-3x}$ 1.10 Ti/(Y+Bi) annealed at 1023 K for 4h and $(YBi)_{1-x}Ti_2O_{7-3x}$ 1.30 Ti/(Y+Bi) annealed at 873 K for 4h as a function of the co-catalyst loading. Measurements were performed in the presence of 10 vol.-% methanol acting as sacrificial reagent.

The stability range of the $Y_{2-x}Ti_2O_{7-1.5x}$ pyrochlore structure for higher titanium excess is significantly extended by partial substitution of yttrium by larger bismuth ions. Bismuth ions are found to stabilize a high degree of vacancies on the A, O⁻-sites of yttrium bismuth titanate pyrochlores, which results in an extended stability range of structures featuring excess titanium stoichiometries. Pure pyrochlores of $Y_{1.36}Bi_{0.45}Ti_2O_{6.73}$ and $(YBi)_{0.77}Ti_2O_{6.31}$ were obtained with corresponding titanium excesses of 10 % and 30 %, respectively.

respectively. Increasing the bismuth content in $Y_{2-x}Ti_2O_{7-1.5x}$ via $(Y_{1.5}Bi_{0.5})_{1-x}Ti_2O_{7-3x}$ to $(YBi)_{1-x}Ti_2O_{7-3x}$ results in the reduction of the band gap energy from 3.7 eV via 3.3 eV to 3.1 eV and in the decrease of the temperature of crystallization from 1023 K to 873 K, respectively. A stringent structural tune-up is indispensable to achieve good photocatalytic properties for bismuth containing yttrium titanate pyrochlores, which are almost inactive in photocatalytic hydrogen production, if prepared in stoichiometric composition. The annealing temperature should be chosen as low as possible, but providing a complete crystallization. The titanium excess should be adjusted as high as the formation of the rutile by-phase is still avoided. Maximum hydrogen production rates of 27.2 $\mu\text{mol H}_2/\text{h}$ and 17.5 $\mu\text{mol H}_2/\text{h}$ were achieved by $Y_{1.36}Bi_{0.45}Ti_2O_{6.73}$ and $(YBi)_{0.77}Ti_2O_{6.31}$ corresponding to photonic efficiencies of 0.55 % and 0.35 %, respectively. Nevertheless, bismuth doping decreases the photonic efficiency of structure optimized yttrium titanate (PE: 1.4 %) considerably, although the band gap energy is kindly reduced.

However, the reason for the strong improvement of the photocatalytic activity due to the increase of the titanium excess in the structure has still to be clarified. Although there is a lack of typical evidence for the pyrochlore de-stuffing mechanism proven for yttrium and lanthanide titanates, it might be an explanation, if the titanium-yttrium lattice interchange is masked. Moreover, large bismuth cations are expected to change or distort the TiO_6 -octahedral geometry. The formation of $Bi, O^{\cdot-}$ -site vacancies due to a higher titanium excess has a reverse effect improving the charge carrier separation and thus, the photocatalytic activity.

Moreover, the bismuth content in the structure clearly determines the stability during photocatalysis. Applied as co-catalyst on a wide band gap semi-conductor, rhodium being a less precious metal compared to platinum suffers from the disadvantage of photo-oxidation. As already seen for samples of $Y_{2-x}Ti_2O_{7-1.5x}$, most of the $(Y_{1.5}Bi_{0.5})_{1-x}Ti_2O_{7-3x}$ samples loaded with platinum provide steady activities. At higher bismuth content, the instability of the pyrochlore $(YBi)_{1-x}Ti_2O_{7-3x}$ itself, but not of the co-catalyst is responsible for activities being never perfectly stable. By increasing the co-catalyst loading on $(YBi)_{1-x}Ti_2O_{7-3x}$ samples, the decrease in activity can be weakened, but cannot be entirely eliminated.

4.3 Non-stoichiometric $\text{Bi}_2\text{Ti}_2\text{O}_7$ and other bismuth titanates

Pyrochlore bismuth titanate ($\text{Bi}_{2-x}\text{Ti}_{0.75x}$) Ti_2O_7 was prepared by an aqueous sol-gel method and annealed at different temperatures. Non-stoichiometry was obtained by adjusting the Ti/Bi ratio during synthesis. Additionally the two bismuth titanate phases $\text{Bi}_4\text{Ti}_3\text{O}_{12}$ and $\text{Bi}_2\text{Ti}_4\text{O}_{11}$ were synthesized. The materials were characterized by X-ray diffraction and UV-vis reflectance spectroscopy. Photocatalytic hydrogen production was tested in the presence of methanol as sacrificial agent after loading the bismuth titanates with nanoparticles of platinum acting as co-catalysts. Non-stoichiometric chemical compositions are obtained by the variation of the Ti/Bi ratio in the preparation process. Bismuth depleted bismuth titanates are found to provide a special vacancy structure in the cationic sub-lattice. Although the samples are depleted in bismuth, the band gap energy is situated appropriately to absorb in the visible light region. The vacancy structure in non-stoichiometric “ $\text{Bi}_2\text{Ti}_2\text{O}_7$ ” is analyzed by Rietveld refinement. The samples are tested for activity and stability in the photocatalytic hydrogen producing test reaction. The two bismuth titanate phases $\text{Bi}_4\text{Ti}_3\text{O}_{12}$ and $\text{Bi}_2\text{Ti}_4\text{O}_{11}$ providing Ti/Bi ratios, which are not obtainable as pyrochlore structure, were tested for comparison as well.

4.3.1 Characterization of non-stoichiometric bismuth titanate

Several phases of bismuth titanate with different Ti/Bi ratios were synthesized. A Ti/Bi ratio of 0.75 and annealing at 873 K led to the perovskite structure of $\text{Bi}_4\text{Ti}_3\text{O}_{12}$. The corresponding X-ray diffraction pattern is shown in Figure 45(a). However, the paraelectric tetragonal phase (SG: $I4/mmm$) and the ferroelectric orthorhombic phase (SG: $B2cb$) of $\text{Bi}_4\text{Ti}_3\text{O}_{12}$ ^[145] generate almost the same X-ray pattern making a decision about the present modification difficult. Figure 45(c) shows the diffraction pattern of $\text{Bi}_2\text{Ti}_4\text{O}_{11}$, which is obtained by adjusting the Ti/Bi ratio to 2.00 at annealing temperatures as high as 1073 K. At lower temperatures a mixture of phases is obtained as shown in the additional information (Figure A9). At 873 K, non-stoichiometric pyrochlore “ $\text{Bi}_2\text{Ti}_2\text{O}_7$ ” is formed together with TiO_2 rutile, and at 973 K the $\text{Bi}_2\text{Ti}_4\text{O}_{11}$ phase is spiked with a small amount of the pyrochlore phase. A similar behavior for the evolution of $\text{Bi}_2\text{Ti}_4\text{O}_{11}$ was found by Kidchob et al.^[34], although the same phase compositions were already formed at temperatures being 100 K lower, which may derive as a consequence of thin film preparation. Lattice parameters of $a = 14.61 \text{ \AA}$, $b = 3.81 \text{ \AA}$,

$c = 14.96 \text{ \AA}$ and $\beta = 93.18^\circ$ were found for monoclinic $\alpha\text{-Bi}_2\text{Ti}_4\text{O}_{11}$ (SG: C2/c), which are in good accordance to the literature^[28].

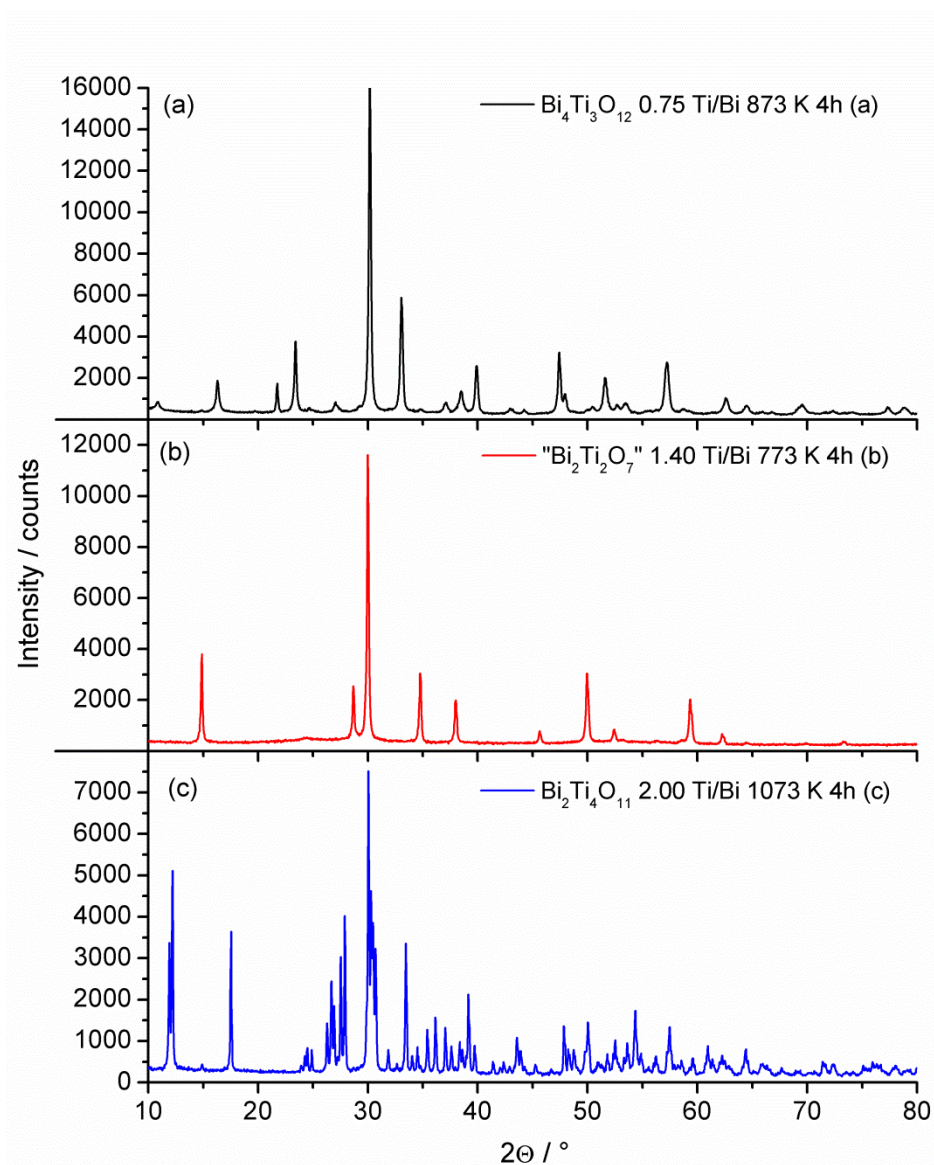


Figure 45: XRD patterns of various bismuth titanates $\text{Bi}_4\text{Ti}_3\text{O}_{12}$ (a), “ $\text{Bi}_2\text{Ti}_2\text{O}_7$ ” (Ti/Bi = 1.40) (b) and $\text{Bi}_2\text{Ti}_4\text{O}_{11}$ (c) annealed at 873 K, 773 K and 1073 K for 4 hours, respectively.

According to literature^[29], a pure pyrochlore phase of $\text{Bi}_2\text{Ti}_2\text{O}_7$ is difficult to achieve at a Ti/Bi ratio of 1.00. Actually, we also did not succeed in preparing stoichiometric $\text{Bi}_2\text{Ti}_2\text{O}_7$. The sample was largely amorphous at an annealing temperature of 673 K, and at higher temperatures of 773 K and 873 K the by-phase $\text{Bi}_4\text{Ti}_3\text{O}_{12}$ appeared, as shown in the additional information in Figure A10. Nevertheless, non-stoichiometric pure pyrochlore phases were found to form in a wide range of Ti/Bi ratios from 1.20 to 1.50. The cubic pyrochlore structure has the ideal composition of $\text{A}_2\text{B}_2\text{O}_6\text{O}^\cdot$. Bismuth is placed

on the A-site and titanium ions occupy the B-site. Due to the titanium excess, vacancies are formed at the Bi-site and potentially at the O`-site, which may have a stabilizing effect on the structure. Exemplarily for the non-stoichiometric “ $\text{Bi}_2\text{Ti}_2\text{O}_7$ ” series, the X-ray diffraction pattern of the “ $\text{Bi}_2\text{Ti}_2\text{O}_7$ ” (Ti/Bi = 1.40) sample annealed at 773 K for 4 hours is shown in Figure 45(b).

An annealing time of 4 hours leads to a complete crystallization of non-stoichiometric “ $\text{Bi}_2\text{Ti}_2\text{O}_7$ ” samples featuring Ti/Bi ratios of up to 1.40. Higher titanium excesses of 45 % or 50 % results in partially amorphous samples. Figure 46 displays the diffraction data of the Ti/Bi 1.50 sample of “ $\text{Bi}_2\text{Ti}_2\text{O}_7$ ” annealed for different periods of time. An increased background is obvious, if annealing is conducted for only 4 hours. A period of 8 hours is needed for entire crystallization. The UV-vis diffuse reflectance spectra presented in the inset of Figure 46 show a slight shift of the band gap energy into the visible region, if the sample is annealed for only 4 hours. Such a pale yellow color was also obtained for largely amorphous samples calcined at only 673 K. In conclusion, a phase of $\text{Bi}_2\text{Ti}_3\text{O}_9$ as predicted by Yordanov et al.^[30] for a Ti/Bi ratio of 1.50 was not found for annealing temperatures ranging from 673 K to 873 K. In fact, a pure pyrochlore phase of non-stoichiometric “ $\text{Bi}_2\text{Ti}_2\text{O}_7$ ” is obtained after specific heat treatment at 773 K for 8 hours.

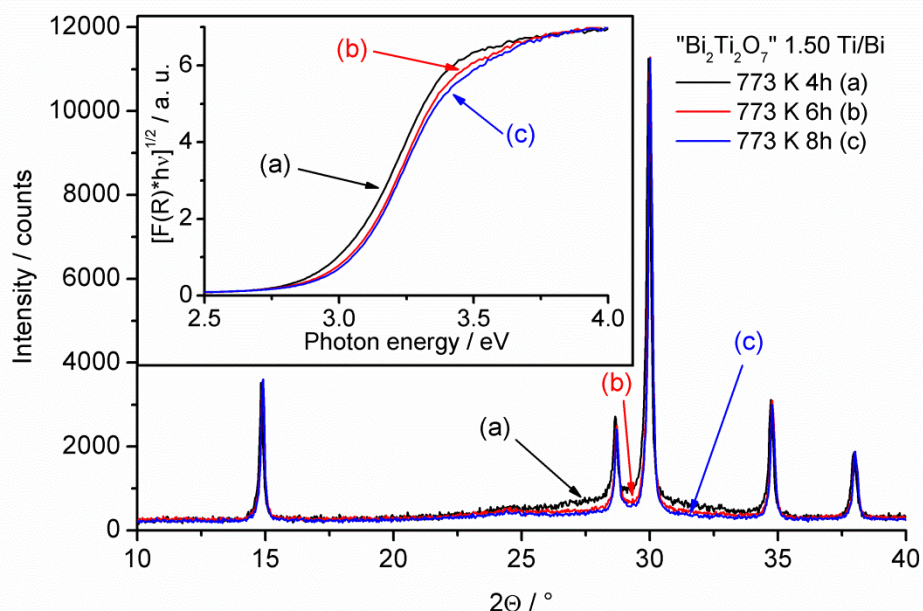


Figure 46: XRD patterns and UV-vis diffuse reflectance spectra (inset) of “ $\text{Bi}_2\text{Ti}_2\text{O}_7$ ” samples (Ti/Bi = 1.50) annealed at 773 K for 4 hours (a), 6 hours (b) and 8 hours (c). The degree of crystallinity is improved with prolonged annealing.

The lattice parameter of non-stoichiometric “ $\text{Bi}_2\text{Ti}_2\text{O}_7$ ” is found to be a function of the Ti/Bi ratio. As shown for the series of samples annealed at 773 K for 4 hours the lattice parameter is reduced from 10.37 Å for a stoichiometric composition to 10.33 Å for “ $\text{Bi}_2\text{Ti}_2\text{O}_7$ ” featuring a Ti/Bi ratio of 1.50 (cf. to Figure 47). The increasing degree of vacancies is considered to be responsible for the lattice contraction. This behavior is found for samples annealed at a higher temperature of 873 K only up to a Ti/Bi ratio of 1.30. A higher titanium excess leads to the formation of a TiO_2 rutile by-phase, but not to a pyrochlore being more enriched in titanium and vacancies. The lattice parameters of the “stoichiometric” $\text{Bi}_2\text{Ti}_2\text{O}_7$ samples are lower than expected, which might be explained by the presence of a $\text{Bi}_4\text{Ti}_3\text{O}_{12}$ by-phase (as shown in Figure A10), so that the pyrochlore structure is in fact not stoichiometric, but depleted for sure in bismuth and potentially in oxygen. Interestingly, the high amount of $\text{Bi}_4\text{Ti}_3\text{O}_{12}$ in the stoichiometric composition annealed at 873 K leads to a pyrochlore being more depleted in bismuth than the sample with 20 % excess titanium is.

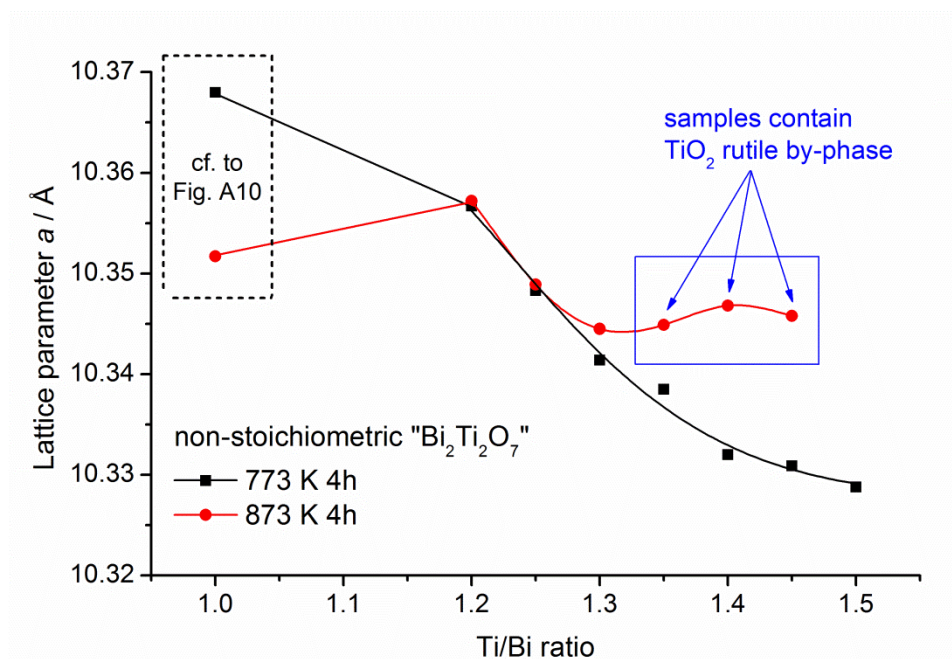


Figure 47: The lattice parameter of non-stoichiometric “ $\text{Bi}_2\text{Ti}_2\text{O}_7$ ” samples annealed at 773 K and 873 K as a function of the Ti/Bi ratio.

Incorporation of bismuth in mixed oxide photocatalysts is a promising way to achieve visible light response. The hybridization of fully occupied Bi 6s and O 2p orbitals^[136] is known to shift the top of the valence band to more negative values (vs. NHE) lowering the band gap energy in comparison to yttrium titanate (cf. to chapter 4.1.1). The conduction band is built up from Ti 3d orbitals. Figure 48 shows the Kubelka-Munk

transformation of the UV-vis diffuse reflectance spectra of the herein investigated bismuth titanates.

Samples of $\text{Bi}_2\text{Ti}_4\text{O}_{11}$ and non-stoichiometric “ $\text{Bi}_2\text{Ti}_2\text{O}_7$ ” are supposed to reveal indirect band gap transitions. The tetragonal phase of $\text{Bi}_4\text{Ti}_3\text{O}_{12}$ shows an indirect transition, while the orthorhombic phase was calculated to yield a direct band gap transition.^[145] As both phases are difficult to differentiate, band gap transitions were assumed to be indirect for all samples. Thus, the band gap energies are obtained from the intersection point of the linear part of the plot $(F(R)\cdot hv)^{1/2}$ vs. hv with the energy axis.

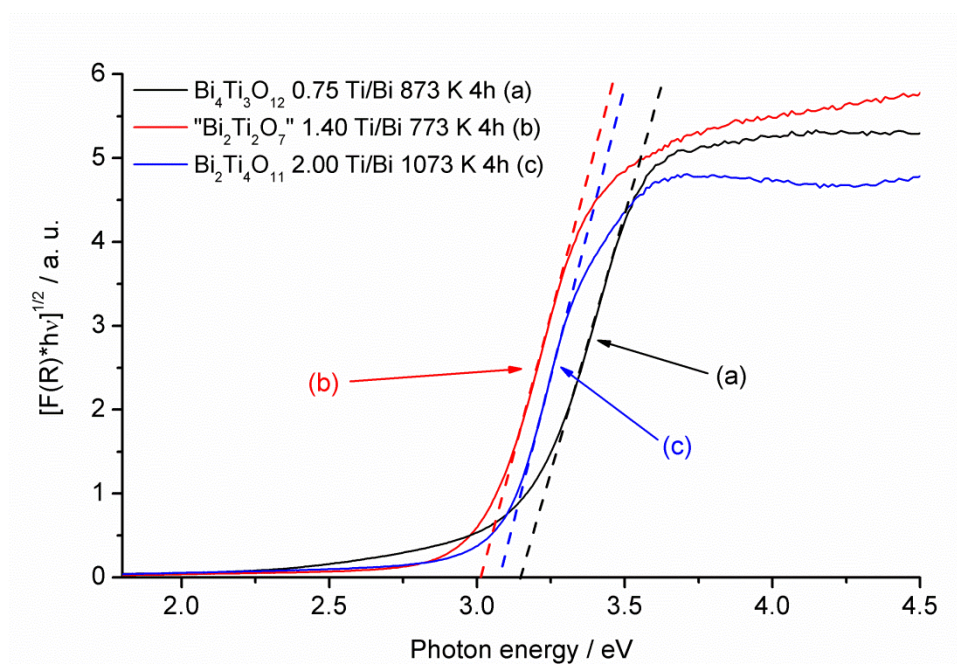


Figure 48: Tauc-plots (for indirect band gap transition) calculated from the UV-vis diffuse reflectance spectra for band gap energy calculations of $\text{Bi}_4\text{Ti}_3\text{O}_{12}$ (a), “ $\text{Bi}_2\text{Ti}_2\text{O}_7$ ” (Ti/Bi = 1.40) (b) and $\text{Bi}_2\text{Ti}_4\text{O}_{11}$ (c) annealed at 873 K, 773 K and 1073 K for 4 hours, respectively.

The non-stoichiometric “ $\text{Bi}_2\text{Ti}_2\text{O}_7$ ” samples feature almost the same band gap energies if entirely crystallized. Energy band gaps of 3.2 eV, 3.0 eV and 3.1 eV were obtained for $\text{Bi}_4\text{Ti}_3\text{O}_{12}$, “ $\text{Bi}_2\text{Ti}_2\text{O}_7$ ” and $\text{Bi}_2\text{Ti}_4\text{O}_{11}$ featuring Ti/Bi ratios of 0.75, 1.00 - 1.50 and 2.00, respectively. A clear dependency between the Ti/Bi ratio and the band gap energy is not found. It is known that beside the chemical composition also the crystal structure determines the band structure and thus, the band gap energy.

4.3.2 The vacancy structure in non-stoichiometric “Bi₂Ti₂O₇”

It was previously shown that it is not possible for bismuth to interchange its lattice position with titanium in the pyrochlore structure, as an excess of yttrium and bismuth (Ti/(Y+Bi) ratio of 0.95) in Y_{1.5}Bi_{0.5}Ti₂O₇ leads to the by-phase evolution of Bi_{1.83}Y_{0.17}O₃ (cf. to Figure 35(B)). Therefore, the pyrochlore stuffing mechanism cannot be responsible for changes in the photocatalytic activity of non-stoichiometric “Bi₂Ti₂O₇” samples of different Ti/Bi ratios. To prove the possibility that the variation in the Ti/Bi ratio may have another influence on structural properties and thus, on the photocatalytic activity, a Rietveld refinement including the refinement of atomic positions was conducted on the non-stoichiometric series of “Bi₂Ti₂O₇” samples annealed at 773 K. The Rietveld refinement unveils the location of vacancies in the structure, which have to emerge as a consequence of non-stoichiometry. Moreover, an increasing amount of vacancies in the structure is supposed to change atomic distances and angles. As long as the location of vacancies is questionable, the chemical structure of non-stoichiometric bismuth titanate is given as “Bi₂Ti₂O₇” with no relation between possible vacancies on the Bi and O` sites.

In undistorted pyrochlores like Y₂Ti₂O₇, the A cations are placed on the *16c* site (0, 0, 0), the B cations on *16d* (1/2, 1/2, 1/2) and the O` anion on *8a* (1/8, 1/8, 1/8). All of these Wyckoff sites are highly symmetric, as they do not have any positional parameters. Only the O anions occupy a positional site, namely *48f* (*x*, 1/8, 1/8).^[25] Considering the facts that titanium ions are rigid in the lattice and that the TiO₆ octahedral network is built up only from O and not from O` anions, a change in the *x* positional parameter of the O anion will change the octahedral geometry. Four structural models for non-stoichiometric “Bi₂Ti₂O₇” are suggested and refined by the Rietveld method. The models differ in terms of vacancy structure and atomistic distortion caused by bismuth cations as shown in Table 10.

No.	stoichiom.	vacancies (□)	A site			B site	O site	O` site		Ti/Bi ratio of 1.50
			Bi	□	Ti	Ti	O	O	□	
1	stoichiom.	No	<i>16c</i>	no	-	<i>16d</i>	<i>48f</i>	<i>8a</i>	no	Bi ₂ Ti ₂ O ₇
2	non-stoichiom.	A and O`	<i>16c</i>	yes	-	<i>16d</i>	<i>48f</i>	<i>8a</i>	yes	(Bi _{1.33} □ _{0.67})Ti ₂ O ₆ □ ₁
3	non-stoichiom.	A and O`	<i>96g</i>	yes	-	<i>16d</i>	<i>48f</i>	<i>48f</i>	yes	(Bi _{1.33} □ _{0.67})Ti ₂ O ₆ □ ₁
4	non-stoichiom.	A	<i>96g</i>	yes	<i>16c</i>	<i>16d</i>	<i>48f</i>	<i>8a, 48f</i>	no	(Bi _{1.55} Ti _{0.33} □ _{0.11})Ti ₂ O ₇

Table 10: Structure models for the Rietveld refinement of the “Bi₂Ti₂O₇” series annealed at 773 K. The structures are different in the predicted stoichiometry and vacancy distribution. The Wyckoff positions are characterized by the following coordinates: *16c* (0, 0, 0), *16d* (1/2, 1/2, 1/2), *48f* (*x*, 1/8, 1/8), *8a* (1/8, 1/8, 1/8) and *96g* (*x*, *x*, *z*).

In the first structure suggestion (structure 1) an undistorted structure model that fits for $\text{Y}_2\text{Ti}_2\text{O}_7$ was utilized for the bismuth titanate series. Moreover, the different occupation numbers for bismuth and the O` oxygen in non-stoichiometric compositions were not taken into account, i. e., the structures are pretended to be free of vacancies. This structure model was chosen as an initial approach, although the disregard of non-stoichiometry cannot lead to realistic results.

The second suggestion (structure 2) considers the stoichiometry changes due to different Ti/Bi ratios. This model predicts the generation of vacancies at the A site combined with vacancies at the O` site due to charge neutrality. The chemical composition is $(\text{Bi}_{2-x}\square_x)\text{Ti}_2\text{O}_{7-1.5x}\square_{1.5x}$ ranging up to $(\text{Bi}_{1.33}\square_{0.67})\text{Ti}_2\text{O}_6\square_1$ for a Ti/Bi ratio of 1.50. Such a stoichiometry is often proposed for non-stoichiometric pyrochlores featuring an A-cation with inert electron pair.^[134, 143] All ions are placed on the highly symmetric atomic positions used in structure 1 as well.

In structure suggestion 3, the vacancy model was kept as it is in structure 2, i. e. showing A,O`-site vacancies, but bismuth as well as O` oxygen are symmetrically displaced from their ideal positions. Large bismuth ions providing an inert lone electron pair are well known to displace off high symmetry positions. Esquivel-Elizondo et al.^[29] performed DFT calculations on $\text{Bi}_2\text{Ti}_2\text{O}_7$ predicting the ideal displacement of bismuth on the $96g$ site to be (0.015, 0.015, 0.964). As the multiplicity of the $96g$ site is six times higher than that of the former $16c$ site, each bismuth ion is located at one of six possible equivalent positions around the $16c$ site. In the same way the occupancy is reduced from 1 to 1/6. As a consequence of bismuth displacement the O` anions are distorted as well. The multiplicity is again increased by a factor of 6 by changing the site from $8a$ to $48f$, which leads to an occupancy of 1/6 and to 6 possible positions around the $8a$ site. Coordinates of (0.136, 1/8, 1/8) are utilized.^[29] The possible displacements of bismuth and O` oxygen in the O`Bi₄ tetrahedra are shown in Figure 49. The chemical structure stays the same as in structure 2, i. e., $(\text{Bi}_{2-x}\square_x)\text{Ti}_2\text{O}_{7-1.5x}\square_{1.5x}$.

In structure suggestion 4 the distorted sites for bismuth and O` oxygen are used, but it is predicted that the charge neutralization due to the bismuth depletion is ensured by titanium partially occupying the bismuth position. Finally, vacancies are only formed on the A-site, but no longer on the O` site, which leads to a significantly reduced amount of overall vacancies. The general chemical structure is $(\text{Bi}_{2-x}\text{Ti}_{0.75x}\square_{0.25x})\text{Ti}_2\text{O}_7$. By DFT calculations Stanek et al. proposed such a vacancy structure as being energetically favoured for pyrochlores with BO_2 excess.^[124] The A-site titanium is placed on the

$16c$ site and the corresponding degree of O' oxygen occupies the undistorted $8a$ site, as no distortion is expected for titanium being a very small cation. The occupancies used in the refinements for the structure suggestions 2-4 are determined in order to fulfil the aforementioned restrictions in non-stoichiometric bismuth titanate and are provided in Table A27 to Table A29 in the appendix. For the refinement of structure 1, all occupancies were set to one.

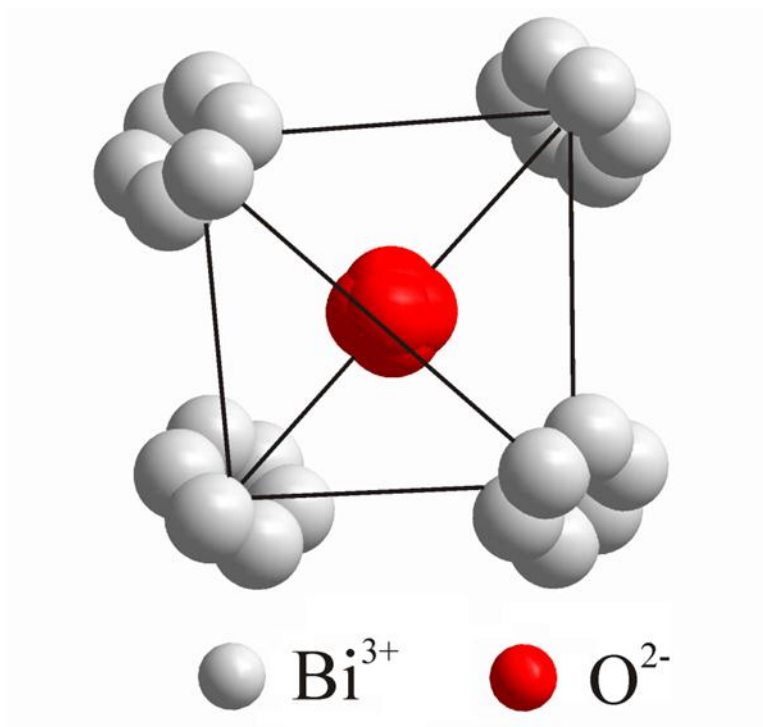


Figure 49: Displacements in the $O'Bi_4$ tetrahedron in non-stoichiometric “ $Bi_2Ti_2O_7$ ” samples predicting six possible positions for bismuth and O' oxygen. Bismuth is placed at $96g$ (0.015, 0.015, 0.964) and O' at $48f$ (0.136, 1/8, 1/8). The distorted Wyckoff sites $96g$ and $48f$ are centred around the ideal pyrochlore sites of $16c$ and $8a$, respectively.

The Rietveld refinement provides the evolution of the x positional parameter of oxygen as a function of the Ti/Bi ratio for each structure suggestion. The x positional parameter is responsible for changes in the geometry of the TiO_6 octahedra. The results are summarized in Table 11 also showing the corresponding goodness of fit (GOF). The GOF value is given as the quotient of the weighted profile R-factor R_{wp} and the expected R-factor R_{exp} and values to 1, if the applied model is in complete accordance with the measured X-ray diffraction pattern. Measurement parameters like step size and time per step may have a significant influence on the R_{exp} .

No.	Structure		Ti/Bi ratio							
			1.00	1.20	1.25	1.30	1.35	1.40	1.45*	1.50*
1	Bi ₂ Ti ₂ O ₇	<i>x</i>	0.4692	0.4520	0.4462	0.4502	0.4350	0.4290	0.4260	0.4262
		<i>GOF</i>	2.58	3.20	3.51	3.31	3.92	2.90	2.89	2.84
2	(Bi _{2-x} □ _x)Ti ₂ O ₆ □ _{1-1.5x}	<i>x</i>	0.4692	0.4254	0.4173	0.4168	0.4005	0.3901	0.3813	0.3719
		<i>GOF</i>	2.58	2.97	3.31	2.95	3.84	2.95	3.00	3.03
3	(Bi _{2-x} □ _x)Ti ₂ O ₆ □ _{1-1.5x}	<i>x</i>	0.4621	0.4336	0.4291	0.4279	0.4210	0.4157	0.4142	0.4131
		<i>GOF</i>	2.77	2.15	2.08	2.12	2.51	2.20	2.38	2.56
4	(Bi _{2-x} Ti _{0.75x} □ _{0.25x})Ti ₂ O ₇	<i>x</i>	0.4689	0.4499	0.4444	0.4416	0.4363	0.4325	0.4305	0.4296
		<i>GOF</i>	2.56	2.19	2.10	2.08	1.89	1.60	1.58	1.62

Table 11: Results of the Rietveld refinement for structures 1-4 each describing a slightly different structure of “Bi₂Ti₂O₇” by systematically combining non-stoichiometry (structures 1-3), atomistic distortion of bismuth and O` oxygen (structures 3-4), and different vacancy distributions (structures 2-4). The *x* stands for the *x* positional parameter of O oxygen and *GOF* for the goodness of fit. Samples with Ti/Bi ratios ≤ 1.40 were annealed at 773 K for 4h, the samples with Ti/Bi ratios of 1.45* and 1.50* at 773 K for 6h and 8h, respectively.

In general, it can be seen that the *x* positional parameter of oxygen decreases with increasing Ti/Bi ratio. This trend maintains irrespectively of the applied structure model. By means of the high *GOF* values it is obvious that structure 1 is as expected not an applicable approach for describing non-stoichiometric bismuth titanate. However, the results obtained for structure 2 do not lead to a much better fit, although the non-stoichiometry is considered. The decrease in the *x* positional parameter is much too high leading to virtually impossible geometries for the TiO₆ octahedra. The structure is not sufficiently described by simply including the non-stoichiometry, but atomistic distortions of bismuth and O` oxygen have to be taken into consideration, what can be seen in the results for structure 3 indicating a significantly improved fit. Actually, the values of the oxygen *x* positional parameter are returned into a more realistic range between 0.42 and 0.45. Finally, the vacancy structure in non-stoichiometric pyrochlores is analyzed. Structures 3 and 4 differentiate between the compositions of (Bi_{2-x}□_x)Ti₂O_{7-1.5x}□_{1.5x} and (Bi_{2-x}Ti_{0.75x}□_{0.25x})Ti₂O₇ with vacancies in the Bi,O`-sites or solely in the Bi site, respectively. As the *GOF* values obtained for structure 4 are significantly lower than those for structure 3, vacancies only at the A site are clearly favoured. Especially at high Ti/Bi ratios of ≥ 1.35 corresponding to samples possessing a high amount of vacancies, the *GOF* values are greatly improved. One should not pay too much attention to the poor *GOF* values obtained for the Bi₂Ti₂O₇ sample with a Ti/Bi ratio of 1.00, as this sample is not really stoichiometric, but contaminated with a significant amount of Bi₄Ti₃O₁₂ by-phase making the fitting more difficult. Exemplarily, the data of the Rietveld refinement of non-stoichiometric “Bi₂Ti₂O₇” featuring a Ti/Bi

ratio of 1.50 annealed at 773 K for 8 hours is shown in Figure 50. The raw data as well as the calculated fit for structure 4 are shown in the main part. The corresponding difference plots for all four structures are presented in the bottom of Figure 50. By means of the difference plots it is obvious that the fits are quite poor for structures 1 and 2, but the fit is significantly improved for structure 3 and especially for structure 4. The Rietveld data and difference plots of other “ $\text{Bi}_2\text{Ti}_2\text{O}_7$ ” samples with selected Ti/Bi ratios of 1.00, 1.20, 1.30 and 1.40 are provided in Figure A11 to Figure A14 as additional information.

In conclusion, the structure of non-stoichiometric pyrochlore bismuth titanate is described in the best way by considering atomistic distortions of bismuth and O` oxygen and vacancies solely on the A site leading to a composition of $(\text{Bi}_{2-x}\text{Ti}_{0.75x}\square_{0.25x})\text{Ti}_2\text{O}_7$.

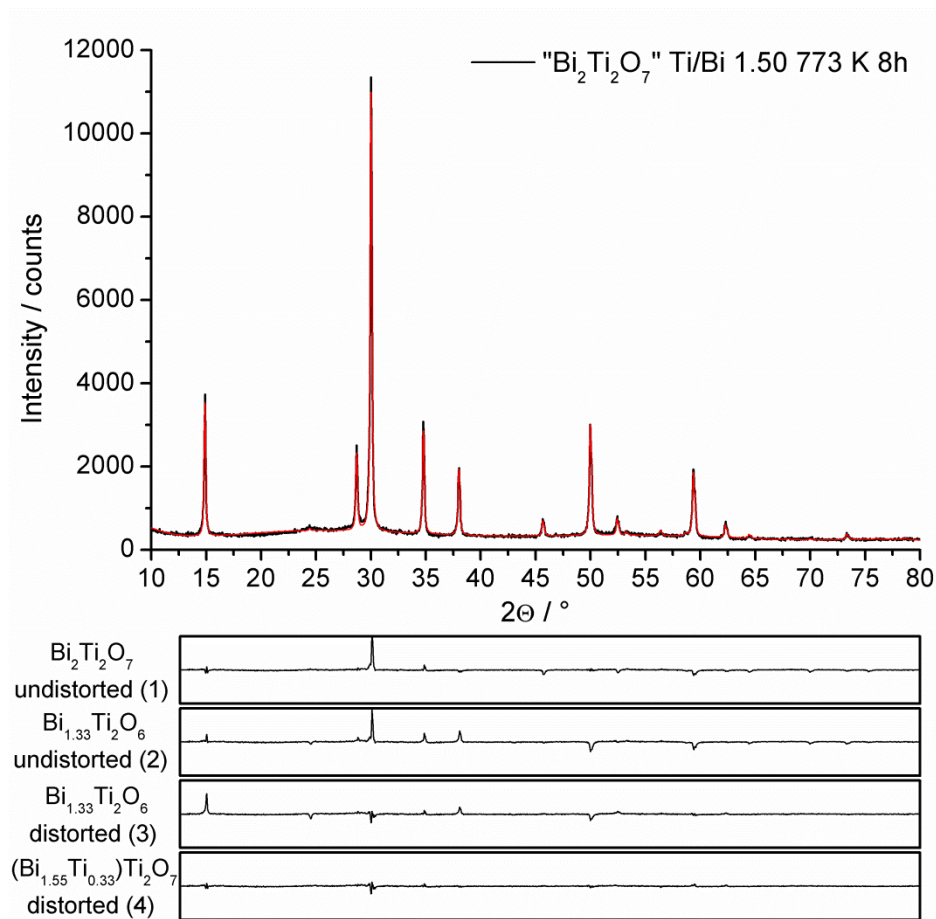


Figure 50: Rietveld refinement of non-stoichiometric “ $\text{Bi}_2\text{Ti}_2\text{O}_7$ ” featuring a Ti/Bi ratio of 1.50 annealed at 773 K for 8 hours. The main part shows the raw data and the calculated fit for structure 4. The difference plots for all four structures are given in the bottom each providing the same scale ranging from -3000 to +3000 counts.

4.3.3 Photocatalytic hydrogen production

The samples were tested in photocatalytic hydrogen production with methanol as sacrificial reagent involving the in-situ photodeposition of 3.0 wt.-% of platinum. The photocatalytic activities of $(\text{Bi}_{2-x}\text{Ti}_{0.75x})\text{Ti}_2\text{O}_7$ samples annealed at 773 K for 4 hours in the Ti/Bi range of 1.00 to 1.50 are presented in Figure 51.

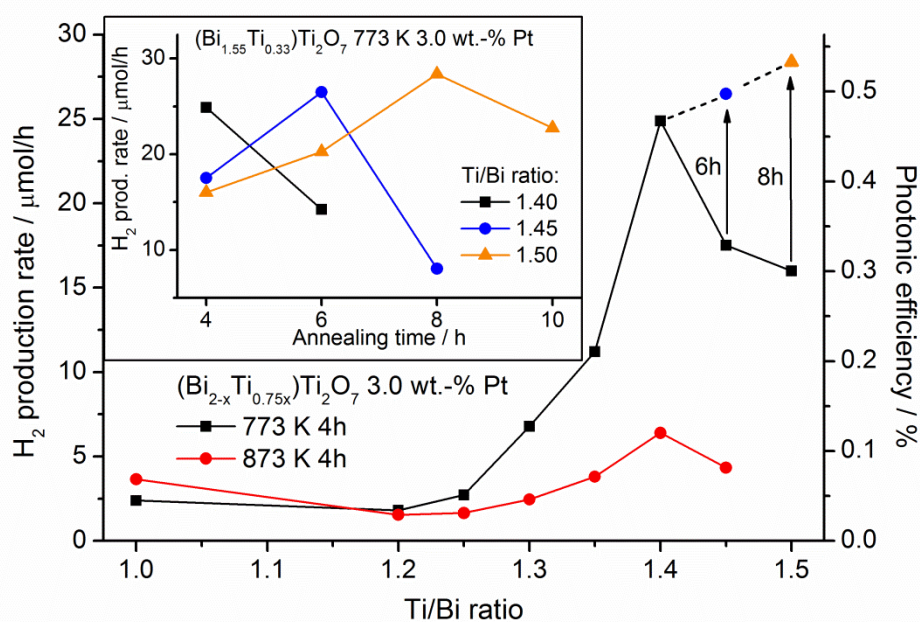


Figure 51: Maximum photocatalytic activities and photonic efficiencies regarding hydrogen production over $(\text{Bi}_{2-x}\text{Ti}_{0.75x})\text{Ti}_2\text{O}_7$ annealed at 773 K for 4h as a function of the Ti/Bi ratio. The inset shows the maximum hydrogen production rates over $(\text{Bi}_{2-x}\text{Ti}_{0.75x})\text{Ti}_2\text{O}_7$ with Ti/Bi ratios of 1.40 - 1.50 annealed at 773 K as a function of the annealing time. All measurements were performed in the presence of 10 vol.-% of methanol acting as sacrificial reagent and involved the in-situ photodeposition of 3.00 wt.-% of platinum.

The stoichiometric composition consisting of $(\text{Bi}_{2-x}\text{Ti}_{0.75x})\text{Ti}_2\text{O}_7$ with a small amount of $\text{Bi}_4\text{Ti}_3\text{O}_{12}$ by-phase was found to be completely inactive. The same counts for samples up to a Ti/Bi ratio of 1.25. Initially, the pure pyrochlore phase of $(\text{Bi}_{1.71}\text{Ti}_{0.22})\text{Ti}_2\text{O}_7$ (Ti/Bi of 1.30) shows a measurable hydrogen production rate. The hydrogen production rate is enhanced considerably by stepwise increase of the Ti/Bi ratio to 1.40 yielding $25 \mu\text{mol H}_2/\text{h}$ in maximum. Interestingly, further increase of the titanium content to Ti/Bi ratios of 1.45 and 1.50 leads to pure pyrochlore phases, but decreases the photocatalytic activity, if annealed for only 4 hours. Both samples were proven to be partially amorphous (cf. to Figure 46). A complete crystallization was not achieved for $(\text{Bi}_{1.59}\text{Ti}_{0.31})\text{Ti}_2\text{O}_7$ and $(\text{Bi}_{1.55}\text{Ti}_{0.33})\text{Ti}_2\text{O}_7$ featuring Ti/Bi ratios of 1.45 and 1.50 until the annealing was conducted for 6 and 8 hours, respectively. The influence of the annealing

time on the photocatalytic activity of $(\text{Bi}_{1.55}\text{Ti}_{0.33})\text{Ti}_2\text{O}_7$ is presented as additional information in Figure A15. The photocatalytic activity is improved with increasing degree of crystallinity. Optimum heating spans of 6 and 8 hours were found for $(\text{Bi}_{1.59}\text{Ti}_{0.31})\text{Ti}_2\text{O}_7$ and $(\text{Bi}_{1.55}\text{Ti}_{0.33})\text{Ti}_2\text{O}_7$ featuring Ti/Bi ratios of 1.45 and 1.50, respectively, as the activity is reduced at even longer thermal treatments.

The right axis of Figure 51 is assigned to the corresponding photonic efficiencies. A maximum hydrogen production rate of $28.4 \mu\text{mol H}_2/\text{h}$ and a photonic efficiency of about 0.55 % are obtained for $(\text{Bi}_{1.55}\text{Ti}_{0.33})\text{Ti}_2\text{O}_7$ (Ti/Bi = 1.50) after heat treatment at 773 K for 8 hours. Furthermore, the results for samples annealed at a higher temperature of 873 K for 4 hours are also included in Figure 51. The corresponding hydrogen production measurements are shown in the additional information in Figure A16 in detail. The higher annealing temperature of 873 K results in reduced photocatalytic activities for all samples. A maximum hydrogen production rate of only $6.4 \mu\text{mol H}_2/\text{h}$ is obtained. The activity of the pyrochlore is that low that even a rutile contamination (present at Ti/Bi ratios of 1.35-1.45, cf. to Figure 47) seems to be beneficial.

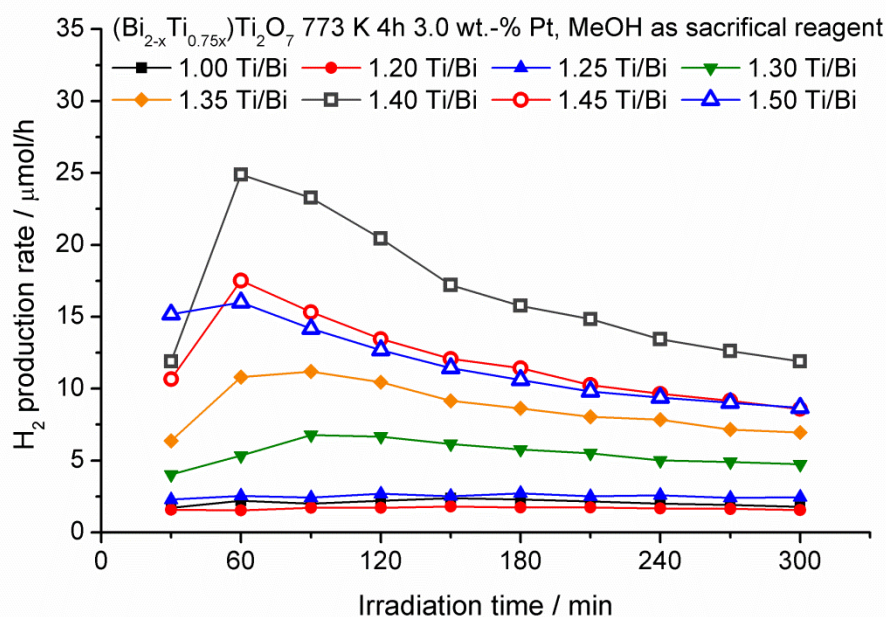


Figure 52: Photocatalytic activity regarding hydrogen production over $(\text{Bi}_{2-x}\text{Ti}_{0.75x})\text{Ti}_2\text{O}_7$ calcined at 773 K for 4 hours with 3.0 wt.-% of platinum as co-catalyst and in the presence of 10 vol.-% methanol as sacrificial reagent.

As can be deduced from Figure 52 and Figure A15, the hydrogen production rates of $(\text{Bi}_{2-x}\text{Ti}_{0.75x})\text{Ti}_2\text{O}_7$ samples are decreasing with time. The most active sample of $(\text{Bi}_{1.55}\text{Ti}_{0.33})\text{Ti}_2\text{O}_7$ (Ti/Bi of 1.50) lost around 50 % of its initial activity within

300 minutes of irradiation, although a high co-catalyst loading of 3.0 wt.-% was applied. Bismuth rich catalysts are supposed to be highly instable towards photoreduction, which may lead to elemental bismuth or bismuth suboxides. However, crystalline by-phases could not be detected by X-ray diffraction even after 24 hours of illumination.

To check whether stability issues are restricted to pyrochlore $(\text{Bi}_{2-x}\text{Ti}_{0.75x})\text{Ti}_2\text{O}_7$ samples, bismuth titanate structures with other Ti/Bi ratios of 0.75 ($\text{Bi}_4\text{Ti}_3\text{O}_{12}$) and 2.00 ($\text{Bi}_2\text{Ti}_4\text{O}_{11}$) were synthesized and tested in photocatalytic hydrogen production as well. The results are presented in Figure 53. A clear correlation is found between the stability during photocatalysis and the Ti/Bi ratio. Very low activities were provided by samples of perovskite $\text{Bi}_4\text{Ti}_3\text{O}_{12}$ (Ti/Bi of 0.75), which were also highly instable losing almost their entire activity within 3 hours of illumination. In the test series with a Ti/Bi ratio of 2.00, the $\text{Bi}_2\text{Ti}_4\text{O}_{11}$ 973 K sample containing a small amount of pyrochlore $(\text{Bi}_{2-x}\text{Ti}_{0.75x})\text{Ti}_2\text{O}_7$ yielded the highest activity of 23 $\mu\text{mol H}_2/\text{h}$. Nevertheless, the highest overall peak performance in the hydrogen production rate is still achieved by the non-stoichiometric pyrochlore $(\text{Bi}_{1.55}\text{Ti}_{0.33})\text{Ti}_2\text{O}_7$ (Ti/Bi of 1.50), but the stability during photocatalysis is enhanced considerably by a higher titanium content leading to a higher activity at longer irradiation times.

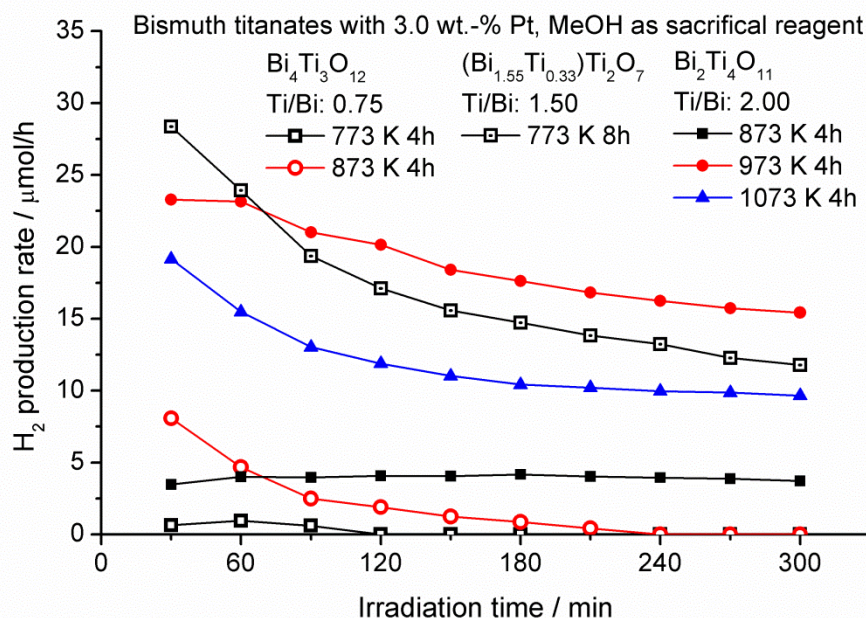


Figure 53: Photocatalytic activity regarding hydrogen production over $\text{Bi}_4\text{Ti}_3\text{O}_{12}$ (Ti/Bi = 0.75) annealed at 773 K and 873 K for 4 hours, $(\text{Bi}_{1.55}\text{Ti}_{0.33})\text{Ti}_2\text{O}_7$ (Ti/Bi = 1.50) calcined at 773 K for 8 hours, and $\text{Bi}_2\text{Ti}_4\text{O}_{11}$ (Ti/Bi = 2.00) annealed at 873 K, 973 K and 1073 K for 4 hours. All measurements were performed in the presence of 10 vol.-% of methanol acting as sacrificial reagent and involved the in-situ photodeposition of 3.00 wt.-% of platinum.

4.3.4 Structure-photocatalysis relation

In order to correlate the photocatalytic activities of the $(\text{Bi}_{2-x}\text{Ti}_{0.75x})\text{Ti}_2\text{O}_7$ series with structural properties, the TiO_6 octahedral geometry is taken into consideration. The geometry of the TiO_6 octahedra is determined by the x positional parameter of O oxygen and the lattice parameter a , while the position of titanium cations is rigidly given by the high symmetry of the Wyckoff site $16d$ ($1/2, 1/2, 1/2$). Figure 54 shows that the x positional parameter decreases with increasing Ti/Bi ratio by using structure 4. Knop et al.^[25] claimed an x positional parameter of 0.4201 and a lattice parameter of 10.095 Å for $\text{Y}_2\text{Ti}_2\text{O}_7$ being the most active material in the group of pyrochlores, which yielded a hydrogen production rate of 71 $\mu\text{mol H}_2/\text{h}$ (cf. to chapter 4.1.3) under the same experimental conditions. Increasing the Ti/Bi ratio in $(\text{Bi}_{2-x}\text{Ti}_{0.75x})\text{Ti}_2\text{O}_7$ leads to a convergence of the x positional parameter towards the value given for $\text{Y}_2\text{Ti}_2\text{O}_7$. As those samples featuring a high Ti/Bi ratio are also highly active in photocatalysis, a correlation between activity and changes in the TiO_6 octahedral geometry is suggested.

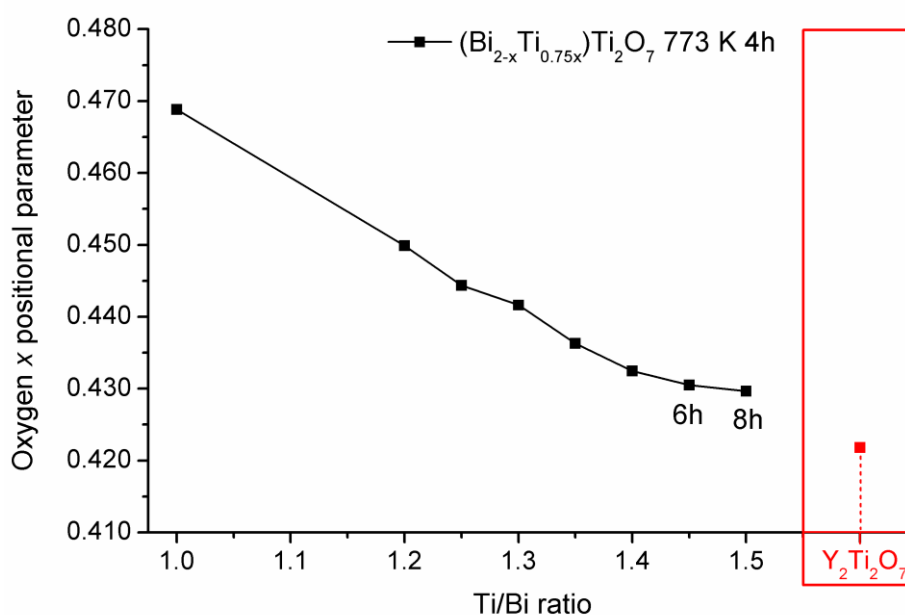


Figure 54: The x positional parameter of O oxygen obtained from Rietveld refinement as a function of the Ti/Bi ratio in $(\text{Bi}_{2-x}\text{Ti}_{0.75x}\square_{0.25x})\text{Ti}_2\text{O}_7$. Samples with Ti/Bi ratios ≤ 1.40 were annealed at 773 K for 4h, the samples with Ti/Bi of 1.45* and 1.50* at 773 K for 6h and 8h, respectively. The value of highly active $\text{Y}_2\text{Ti}_2\text{O}_7$ is given for comparison.

The change in the x positional parameter presented in Figure 54 leads to the following changes in the octahedral geometry for non-stoichiometric $(\text{Bi}_{2-x}\text{Ti}_{0.75x})\text{Ti}_2\text{O}_7$ with selected Ti/Bi ratios of 1.00, 1.20, 1.35 and 1.50.

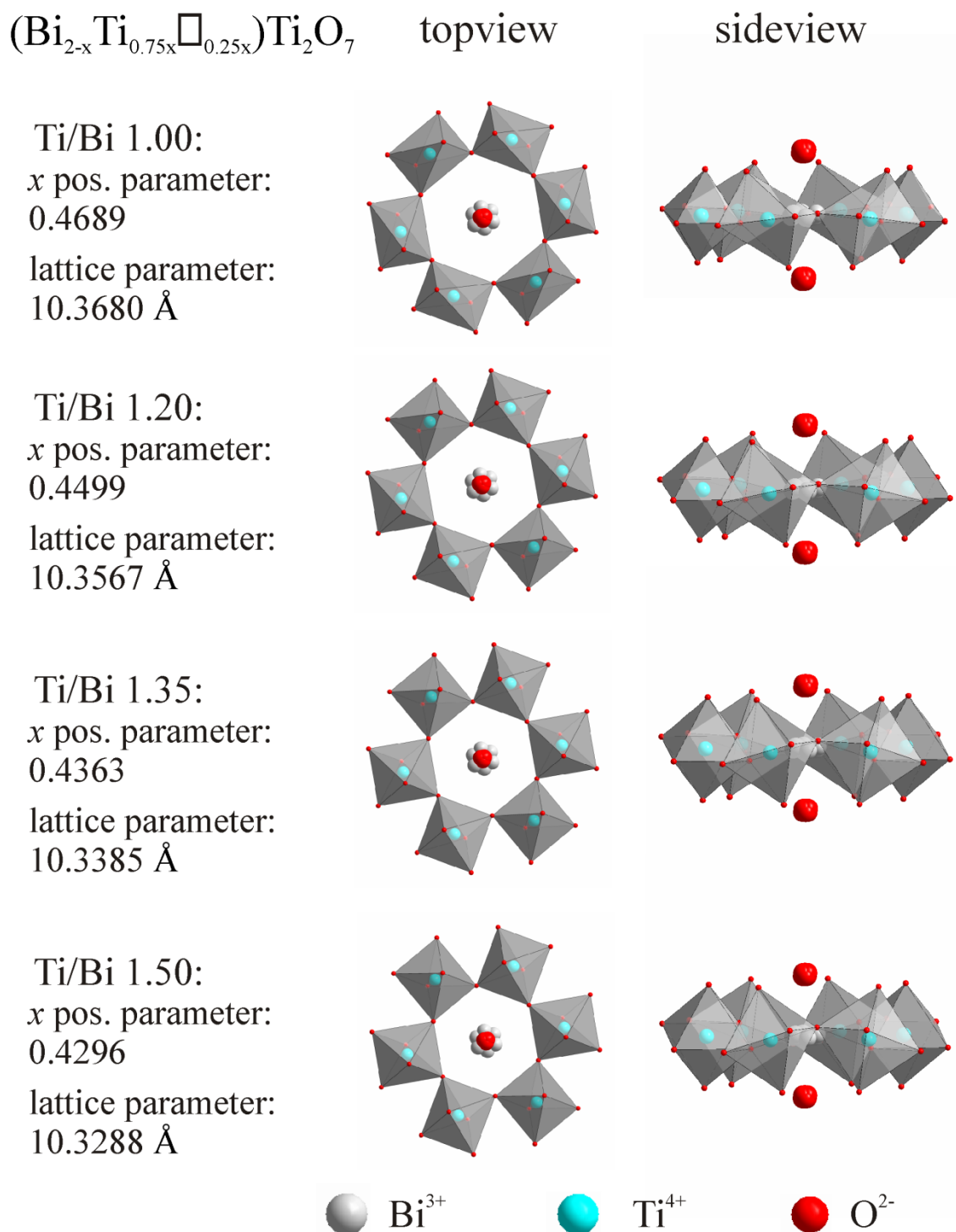


Figure 55: Change of the geometry in the TiO_6 octahedra as a function of the Ti/Bi ratio in $(\text{Bi}_{2-x}\text{Ti}_{0.75x}\square_{0.25x})\text{Ti}_2\text{O}_7$. The crystallographic position of bismuth is surrounded by six TiO_6 octahedra. The samples with Ti/Bi ratios of 1.00, 1.20 and 1.35 were annealed at 773 K for 4h, the sample with a Ti/Bi ratio of 1.50 at 773 K for 8h. The value of highly active $\text{Y}_2\text{Ti}_2\text{O}_7$ is given for comparison.

Figure 55 shows that the TiO_6 octahedra are highly distorted in the stoichiometric sample (Ti/Bi of 1.00). In general, a total of 15 O-Ti-O angles are provided in the structure. Three of them are predetermined to be 180° . The other six pairs of O-Ti-O angles have

the same value with each pair adding up to a sum of 180° . As the first characteristic of the TiO_6 octahedral geometry, Figure 56 presents the O-Ti-O angle as a function of the Ti/Bi ratio in $(\text{Bi}_{2-x}\text{Ti}_{0.75x})\text{Ti}_2\text{O}_7$.

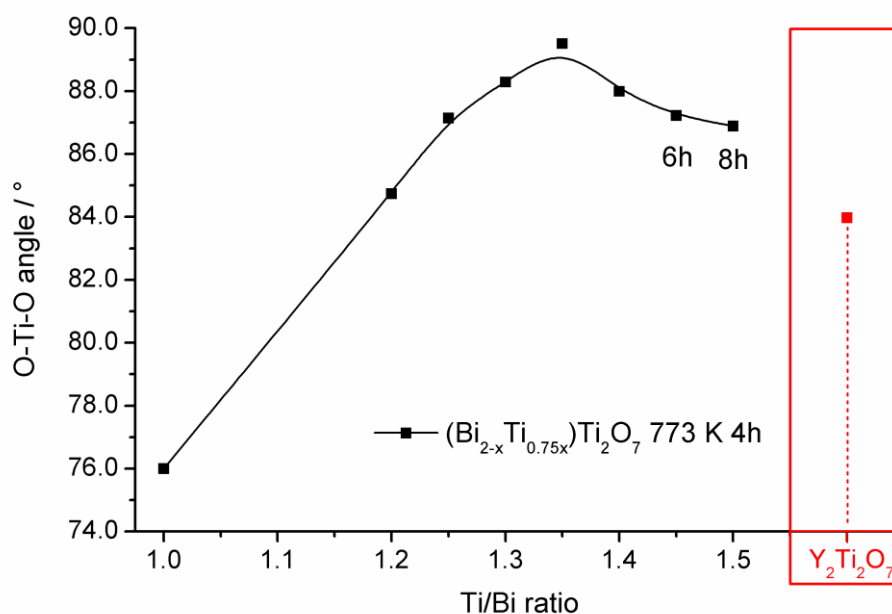


Figure 56: Evolution of the O-Ti-O angle in the TiO_6 octahedra obtained from Rietveld refinement as a function of the Ti/Bi ratio in $(\text{Bi}_{2-x}\text{Ti}_{0.75x}\square_{0.25x})\text{Ti}_2\text{O}_7$. Samples with Ti/Bi ratios ≤ 1.40 were annealed at 773 K for 4h, the samples with Ti/Bi of 1.45* and 1.50* at 773 K for 6h and 8h, respectively. The value of highly active $\text{Y}_2\text{Ti}_2\text{O}_7$ is given for comparison.

The stoichiometric sample possesses the highest octahedral distortion with O-Ti-O angles of $76.0^\circ/104.0^\circ$. For the sample featuring a Ti/Bi ratio of 1.35 an almost perfect octahedral geometry with angles of $89.5^\circ/90.5^\circ$ is obtained. Interestingly, by further increase of the Ti/Bi ratio the O-Ti-O angles depart again from that value considered as perfect. But it is questionable, if values of $90^\circ/90^\circ$ for the O-Ti-O angles are ideal, as the O-Ti-O angles in the very active $\text{Y}_2\text{Ti}_2\text{O}_7$ material amount to $83^\circ/97^\circ$. On the other hand, the O-Ti-O angles cannot be solely responsible for a high photocatalytic activity, as the sample with a Ti/Bi ratio of 1.20 featuring similar O-Ti-O angles of $85^\circ/95^\circ$ should have a good activity as well. But, this sample was completely inactive. Therefore, attention must also be paid to the Ti-O-Ti angle in the TiO_6 octahedral network, whose evolution is shown in Figure 57 as a function of the Ti/Bi ratio in the $(\text{Bi}_{2-x}\text{Ti}_{0.75x})\text{Ti}_2\text{O}_7$ series.

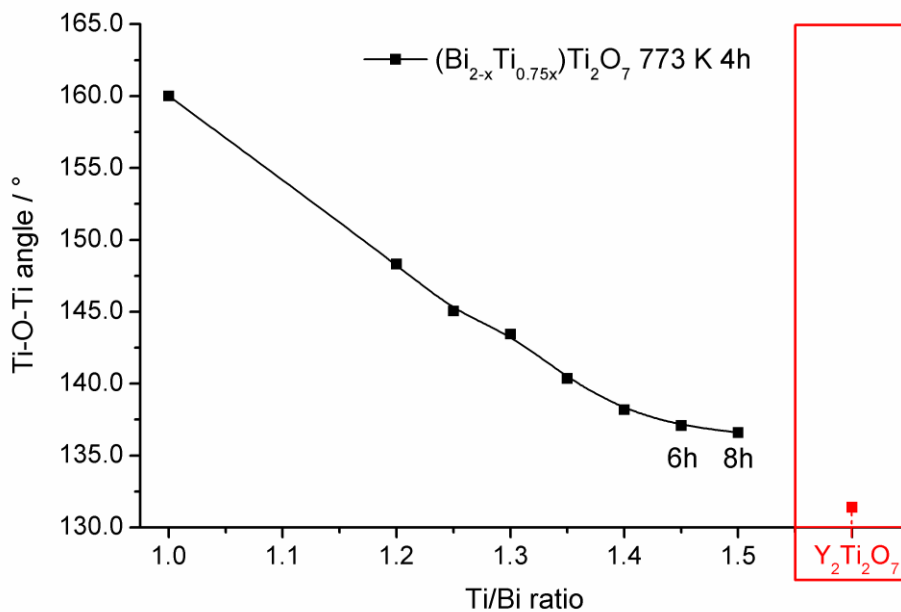


Figure 57: Evolution of the Ti-O-Ti angle in the TiO_6 octahedral network obtained from Rietveld refinement as a function of the Ti/Bi ratio in $(\text{Bi}_{2-x}\text{Ti}_{0.75x})\text{Ti}_2\text{O}_7$. Samples with Ti/Bi ratios ≤ 1.40 were annealed at 773 K for 4h, the samples with Ti/Bi of 1.45* and 1.50* at 773 K for 6h and 8h, respectively. The value of highly active $\text{Y}_2\text{Ti}_2\text{O}_7$ is given for comparison.

The Ti-O-Ti angle in $(\text{Bi}_{2-x}\text{Ti}_{0.75x})\text{Ti}_2\text{O}_7$ decreases continuously by increasing the Ti/Bi ratio. The overall change ranging from 160° to 135° is significant. As $\text{Y}_2\text{Ti}_2\text{O}_7$ has an even lower Ti-O-Ti angle of 131.4° , the reduced angle is supposed to be an important criterion for enhanced photocatalytic activity. Beside the octahedral angles also the Ti-O distance influencing the orbital overlap is examined. The Ti-O distance derives not only from the O oxygen x positional parameter, but also from the lattice parameter a . Due to an increasing degree of vacancies in the structure, the lattice parameter a was found to decrease as a function of the Ti/Bi ratio (cf. to Figure 47), which should lead to a decrease of the Ti-O distance. However, despite this lattice shrinkage, the Ti-O distance is actually even increased as shown in Figure 58. Additional space provided by the progressive generation of vacancies in the structure is effectively used by oxygen moving slightly away from titanium cations and thus, leading to an increase in the Ti-O distance from 1.861 \AA to 1.965 \AA . The Ti-O distance (1.960 \AA) of active $\text{Y}_2\text{Ti}_2\text{O}_7$ is again very close to those distances obtained for highly active $(\text{Bi}_{2-x}\text{Ti}_{0.75x})\text{Ti}_2\text{O}_7$ samples. In titanate pyrochlores empty Ti 3d orbitals are available for π -bonding with filled O 2p orbitals of 48f oxygen.^[146] A larger distance between titanium and oxygen usually leads to a decrease in the orbital overlap in the TiO_6 octahedra reducing the charge delocalization. The reasons why this should be advantageous for photocatalysis are not clear yet.

In conclusion, the O oxygen x positional parameter has been found to determine the geometry of the TiO_6 octahedra. Due to the augmented vacancy generation at higher Ti/Bi ratios, the oxygen ions undergo a slight change in their lattice position leading to an enlarged Ti-O distance of 1.965 Å and a reduced Ti-O-Ti angle of 135° . These structural changes in the geometry of TiO_6 octahedra are considered responsible for the significant improve in photocatalytic activities of $(\text{Bi}_{2-x}\text{Ti}_{0.75x})\text{Ti}_2\text{O}_7$ samples at higher Ti/Bi ratios, as very similar values for these structural characteristics were found for highly active $\text{Y}_2\text{Ti}_2\text{O}_7$ as well.

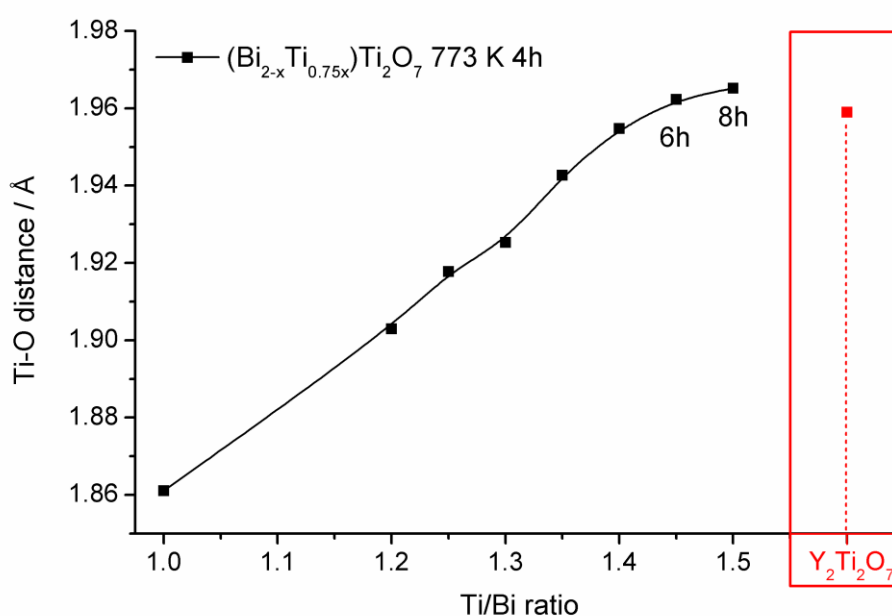


Figure 58: Evolution of the Ti-O distance in the TiO_6 octahedra obtained from Rietveld refinement as a function of the Ti/Bi ratio in $(\text{Bi}_{2-x}\text{Ti}_{0.75x}\square_{0.25x})\text{Ti}_2\text{O}_7$. Samples with Ti/Bi ratios ≤ 1.40 were annealed at 773 K for 4h, the samples with Ti/Bi of 1.45* and 1.50* at 773 K for 6h and 8h, respectively. The value of highly active $\text{Y}_2\text{Ti}_2\text{O}_7$ is given for comparison.

4.3.5 Pt/ Cr_2O_3 core-shell co-catalyst

Although a high photocatalytic activity is obtained for pyrochlore $(\text{Bi}_{1.55}\text{Ti}_{0.33})\text{Ti}_2\text{O}_7$ (Ti/Bi = 1.50) in the initial phase of irradiation, the decrease in activity over time is a major drawback. Usually, the co-catalyst/chromium core-shell system is effectively used in the process of photocatalytic overall water splitting to inhibit the back reaction between just formed hydrogen and oxygen to water, which is thermodynamically favored on the surface of blank precious metals like platinum or rhodium. The most prominent system reported by Yoshida et al.^[95] consists of a rhodium core and a Cr_2O_3 shell, which

is permeable for protons and hydrogen, but not for oxygen. The reduction process of protons to molecular hydrogen is still supposed to take place on the surface of the Rh particles.

After achieving promising results in hydrogen production in presence of methanol, $(\text{Bi}_{1.55}\text{Ti}_{0.33})\text{Ti}_2\text{O}_7$ 773 K 8h was tested in the overall water splitting reaction as well applying a Pt/ Cr_2O_3 core-shell structure. The photodeposition process of the Pt/ Cr_2O_3 core-shell structure was performed in presence of methanol, but was difficult to control, as the hydrogen production rate was found to decrease markedly with prolonging irradiation time, if blank Pt acts as co-catalyst. Thus, a Cr(VI) solution was added already after 30 minutes of irradiation to reduce the period of platinum core deposition as much as possible even if the Pt deposition might not be completed.

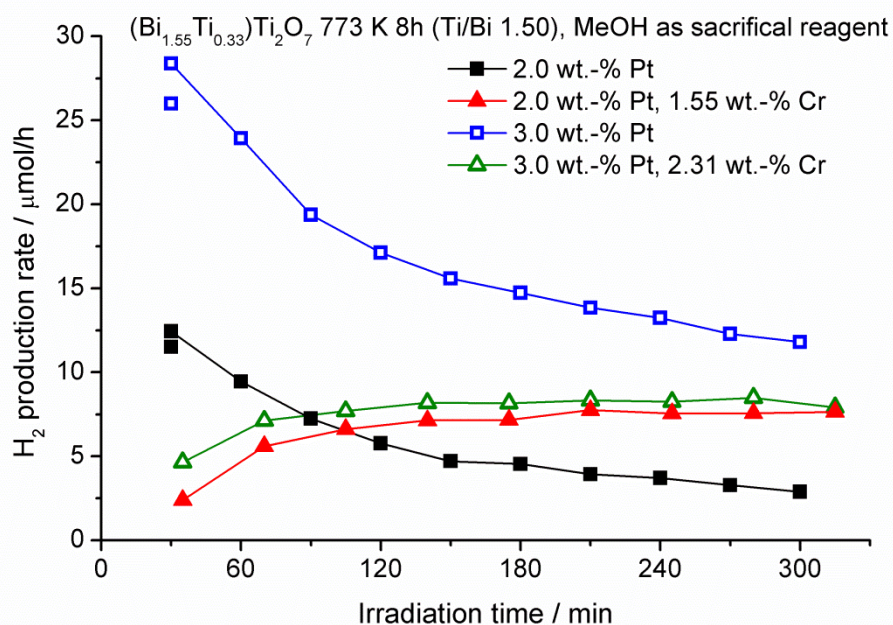


Figure 59: Activity and stability of photocatalytic hydrogen production over $(\text{Bi}_{1.55}\text{Ti}_{0.33})\text{Ti}_2\text{O}_7$ (Ti/Bi = 1.50) annealed at 773 K for 8 hours loaded with bare Pt or core-shell Pt/ Cr_2O_3 as a function of the co-catalyst loading. All measurements were performed in the presence of 10 vol.-% of methanol acting as sacrificial reagent.

The two single data points in Figure 59 are obtained after 30 minutes of irradiation prior to addition of the chromium source and are referred to as a test of reproducibility, which is quite good as being closely to the data points achieved in the normal test runs applying blank Pt, which are displayed in Figure 59 as well. After addition of the Cr(VI) solution, the hydrogen production rate decreased to zero and hydrogen could not be detected anymore within the 300 minutes of Cr_2O_3 photodeposition. The actual Cr loading was

determined by UV-vis spectroscopy to be 1.55 wt.-% and 2.31 wt.-%, respectively. Since residual Cr^{6+} in solution inhibits any hydrogen formation, filtration was performed before starting the test in overall water splitting.

As only about 1-2 $\mu\text{mol H}_2/\text{h}$ were detected, which is close to the detection limit of the gas chromatograph, the catalyst was found to be little active in overall water splitting. Additionally, O_2 has not been detected. This was expected, as Argon was used as carrier gas in the GC system optimized for H_2 analysis while considering the comparable small difference in thermal conductivity between O_2 and Ar in combination with the very low oxygen production rate. Additionally, O_2 is known to be much better soluble in water than H_2 .^[147] However, due to the stability issues it was expected that the low initial hydrogen production rate would decrease quickly. But in contrast, this activity persisted over the whole irradiation period of 5 hours. Thus, the $(\text{Bi}_{1.55}\text{Ti}_{0.33})\text{Ti}_2\text{O}_7$ 773 K 8h loaded with 2.0 wt.-% Pt/1.55 wt.-% Cr (in Cr_2O_3) was centrifuged, re-dispersed in an aqueous solution containing 10 vol.-% of methanol and tested for photocatalytic hydrogen production. The results are shown in Figure 59. Indeed, the catalyst provides a stable hydrogen production rate of 8 $\mu\text{mol H}_2/\text{h}$, if a Cr_2O_3 shell is additionally deposited. The photocatalytic activity becomes superior after 2 hours of irradiation compared to the sample loaded with 2.0 wt.-% of blank Pt suffering from a decreasing hydrogen production rate. Additionally, a second Pt/ Cr_2O_3 loading of 3.0 wt.-% Pt/2.31 wt.-% Cr (in Cr_2O_3) was tested, as 3.0 wt.-% was found to be the optimum Pt loading, if blank platinum is applied. A significant improvement in activity is obtained for the blank Pt sample, whereas the Pt/ Cr_2O_3 loaded sample does not benefit from a higher co-catalyst loading. However, the activities of both samples converge with time. A Pt/Cr ratio of 1.5 was chosen, as Maeda et al.^[148] reported this value to blend well with the $(\text{Ga}_{1-x}\text{Zn}_x)(\text{N}_{1-x}\text{O}_x)$ system, which indeed might not be applicable to the bismuth titanate system.

The formation of molecular hydrogen is characterized by a 2 electron reduction step, in which the electrons have to be close to each other. Precious metals like platinum are good hydrogen evolution sites, because they act as electron sinks and accumulate photogenerated electrons at their surface sites. The loss in activity occurring for samples loaded with blank Pt is attributed to the photo-reduction of Bi^{3+} forming bismuth suboxides or elemental bismuth in a multi-electron reduction process. As this photodecomposition is prevented by the Cr_2O_3 shell, it is supposed that photogenerated

electrons migrate selectively to the interface of platinum and Cr_2O_3 , which inhibits the electron transfer to bismuth ions in the lattice effectively (cf. to Figure 60).

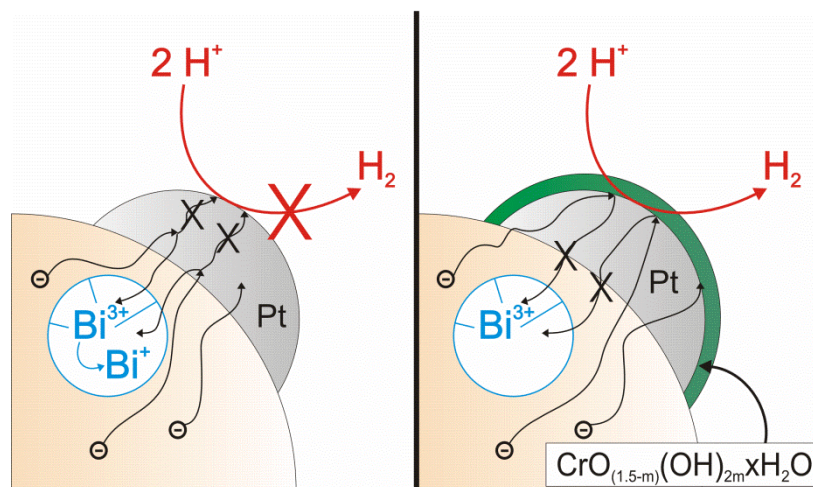


Figure 60: Proposed scheme of how the Cr_2O_3 shell inhibits the photoreduction of Bi^{3+} in the $(\text{Bi}_{1.55}\text{Ti}_{0.33})\text{Ti}_2\text{O}_7$ photocatalyst occurring under illumination, if bare Pt acts as co-catalyst.

4.4 Ti-site doping in structure-optimized $\text{Y}_{1.867}\text{Ti}_2\text{O}_{6.80}$

In chapters 4.2 and 4.3, it was shown that the band gap energy of $\text{Y}_2\text{Ti}_2\text{O}_7$ is effectively reduced by partial or complete substitution of yttrium ions by isoelectric bismuth ions on the A site of the structure. In chapter 4.1, a titanium excess of 7.5 % in $\text{Y}_2\text{Ti}_2\text{O}_7$ (Ti/Y ratio of 1.075) was found to be the optimum stoichiometry at an annealing temperature of 1023 K, as it hits the spot of minimized cationic lattice distortion while being free of rutile impurities. Consequently, this sample provided the highest activity in photocatalytic hydrogen production. Based on this highly active sample of $\text{Y}_{1.867}\text{Ti}_2\text{O}_{6.80}$, another attempt was made to reduce the band gap energy in order to achieve activity in the visible light region.

4.4.1 B-site doping of $\text{Y}_{1.867}\text{Ti}_2\text{O}_{6.80}$ with Cr^{3+} , Mn^{3+} and Fe^{3+}

The B site of the pyrochlore structure typically occupied by titanium is doped with transition metals featuring partially filled d orbitals. The cations of Cr^{3+} , Mn^{3+} and Fe^{3+} were chosen providing a variation in the number of d electrons ranging from d^3 to d^5 , respectively. As those cations are incorporated into the B site of the structure, an octahedral coordination is predetermined. According to the crystal field theory for octahedral coordination, the three d orbitals of d_{xy} , d_{xz} and d_{yz} are lower in energy and the

two d orbitals of d_{z^2} and $d_{x^2-y^2}$ are higher in energy compared to the barycenter in a spherical field, because the former orbitals are more far away from the ligands than the latter orbitals. Based on symmetry operations the lower energy orbitals are referred to as t_{2g} and the higher energy orbitals as e_g . In the Cr^{3+} cation featuring an electron configuration of $[\text{Ar}]d^3$, only each of the low energy d orbitals is occupied by one electron. The Mn^{3+}O_6 octahedral unit with $[\text{Ar}]d^4$ is exclusively available in *high spin*^[149] configuration describing that the fourth d electron is located in one of the high energy d orbitals. For the Fe^{3+} cation featuring an electronic configuration of $[\text{Ar}]d^5$, again *high spin* configuration is proposed, as half occupation of d orbitals is usually preferred. The consequential energy-level diagram is presented in Figure 61.

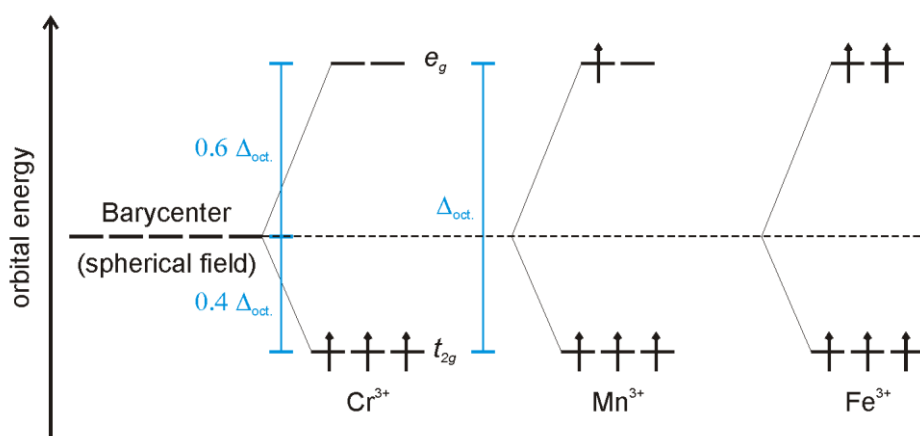


Figure 61: Crystal field splitting in the MO_6 octahedra with $\text{M}^{3+} = \text{Cr}^{3+}$, Mn^{3+} and Fe^{3+} providing *high spin* configuration.

Being dependent on the scale of the d orbital splitting ($\Delta_{\text{okt.}}$), partially occupied or empty d orbitals might be located within the energy band gap. If located in the band gap, a partially occupied d orbital serves as donor level and an empty d orbital as acceptor level. Accordingly, the photon energy needed to excite an electron from the valence band into an acceptor level or an electron from a donor level into the conduction band is lower than the photon energy needed for the direct transition from the valence band into the conduction band. Therefore, the energy band gap of $\text{Y}_2\text{Ti}_2\text{O}_7$ is reduced by doping transition metals with partially filled d orbitals. To refill the donor level or to lift an electron trapped in an acceptor level into the conduction band, usually, a second photon is needed, if $\Delta E > kT$. A photogenerated electron trapped in an acceptor level may itself contribute to the activity in photocatalytic hydrogen production, if the acceptor level is located at energies sufficient for proton reduction, that is, more negative

than 0 V vs. NHE. The potential modes of excitation in Cr,Mn,Fe-doped $Y_2Ti_2O_7$ are presented in Figure 62.

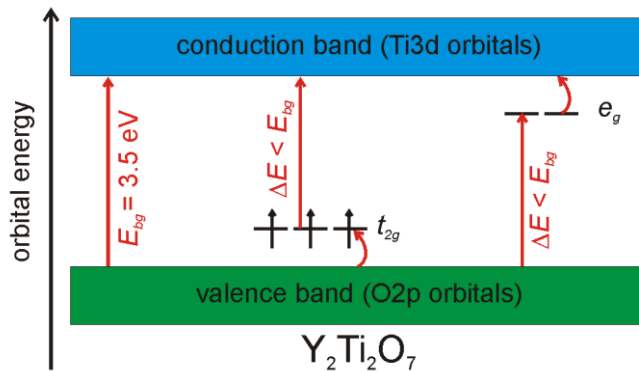


Figure 62: Potential modes of excitation in M^{3+} -doped $Y_2Ti_2O_7$ with $M^{3+} = Cr^{3+}, Mn^{3+}$ and Fe^{3+} . The excitation with $\Delta E < E_{bg}$ is enabled by the generation of acceptor and donor energy levels within the band gap.

However, doping the lattice with foreign cations is supposed to generate defects in the lattice acting as recombination centres, especially, if the substitution of Ti^{4+} is performed with non-isoelectric cations of M^{3+} . This might additionally lead to the formation of vacancy related defects in the anion sublattice due to charge balance.

In octahedral coordination (coordination number c. n. of 6) and in *high spin* configuration, the effective ionic radii of Cr^{3+} , Mn^{3+} and Fe^{3+} were reported to be 61.5 pm, 64.5 pm and 64.5 pm, respectively^[141]. As the effective ionic radius of Ti^{4+} with a c. n. of 6 amounts to 60.5 pm^[141], an exclusive substitution on the B site should be secured. For comparison, eight-fold coordinated Y^{3+} exhibits an effective ionic radius of 101.9 pm^[141] being sufficiently larger.

Whereas the trivalent ions of chromium and iron, namely Cr^{3+} and Fe^{3+} , present the most stable oxidation states, the trivalent form of manganese Mn^{3+} is rather uncommon. Although other highly stable manganese cations of Mn^{2+} ($[Ar]d^5$) and Mn^{4+} ($[Ar]d^3$) are indeed comfortable with the octahedral coordination, these cations possess effective ionic radii of 83 pm and 53 pm^[141] in *high spin* configuration, respectively. Based on the effective ionic radius, possible Mn^{4+} cations would be incorporated on the B site replacing titanium exclusively. If manganese is present in a divalent state, the significant increase in the effective ionic radius might also lead to the incorporation on the A site of the structure substituting yttrium cations. It is known^[149] that divalent MnO is oxidized to trivalent Mn_2O_3 between 743 K and 873 K and Mn_2O_3 is not further oxidized to tetravalent MnO_2 until a high temperature of 1273 K is reached. This behaviour of the

valence state in manganese oxides under heat treatment supports the assumption that manganese exists at a trivalent state of Mn^{3+} in the $\text{Y}_{1.867}\text{Ti}_2\text{O}_{6.80}$ pyrochlore at 1023 K.

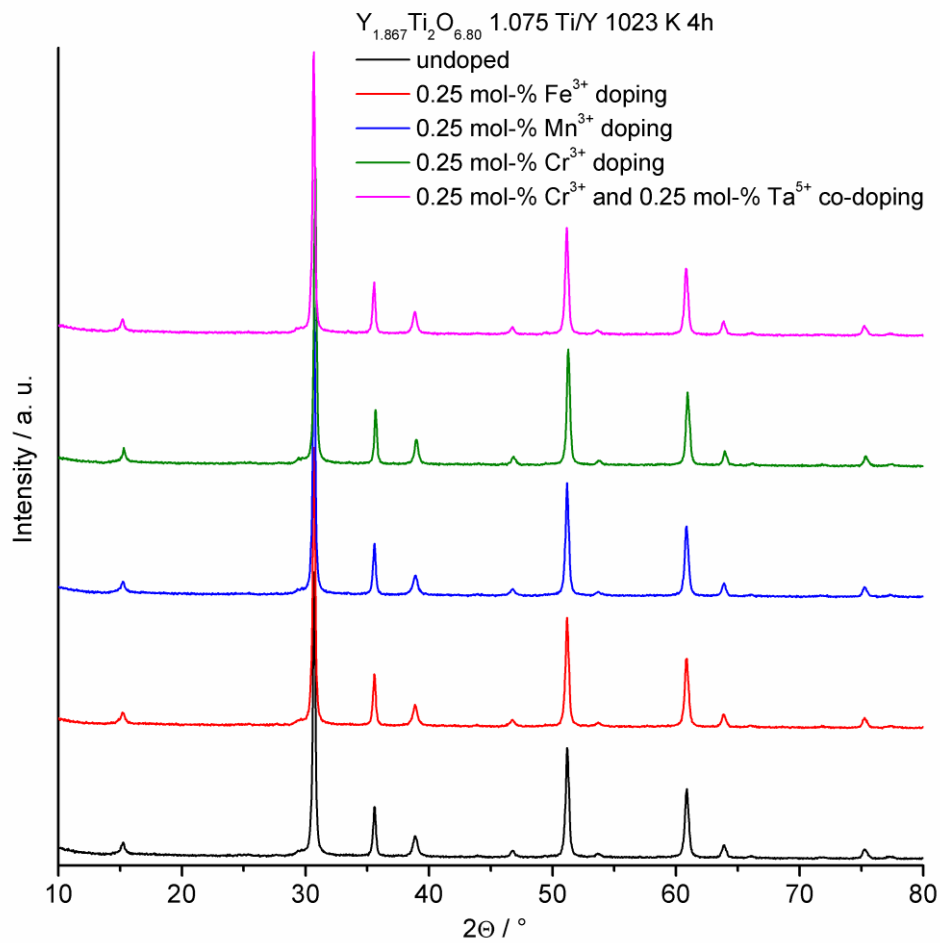


Figure 63: XRD pattern of $\text{Y}_{1.867}\text{Ti}_2\text{O}_{6.80}$ doped with 0.25 mol-% of Cr^{3+} , Mn^{3+} or Fe^{3+} . Additionally, a co-doped sample with 0.25 mol-% of each Cr^{3+} and Ta^{5+} , and the undoped sample are included. Annealing was performed at 1023 K for 4h and all samples feature a Ti/Y ratio of 1.075.

Figure 63 shows the XRD data of stoichiometry optimized $\text{Y}_{1.867}\text{Ti}_2\text{O}_{6.80}$ samples doped with 0.25 mol-% of Cr^{3+} , Mn^{3+} or Fe^{3+} . Additionally, a sample co-doped with 0.25 mol-% of Cr^{3+} and 0.25 mol-% of Ta^{5+} was prepared to prove the influence of charge balance. All of the samples were prepared with a titanium excess of 7.5 %. The annealing was performed at 1023 K for 4 hours. Therefore, the undoped $\text{Y}_{1.867}\text{Ti}_2\text{O}_{6.80}$ sample is presented as reference. In the XRD pattern, neither the formation of a by-phase nor a variation in the lattice parameter could be identified. The lattice parameter a of Cr^{3+} , Mn^{3+} , Fe^{3+} -doped $\text{Y}_{1.867}\text{Ti}_2\text{O}_{6.80}$ with a doping level of 0.25 mol-% ranges between 10.1030 Å and 10.1050 Å. For comparison, the undoped $\text{Y}_{1.867}\text{Ti}_2\text{O}_{6.80}$ (Ti/Y ratio of 1.075) exhibits a lattice parameter a of 10.1037 Å. These variations in the lattice

parameter are negligible in comparison to the variations caused by the lattice distortion of yttrium and titanium cations interchanging their intended lattice positions (cf. to chapter 4.1.1). For a doping level of only 0.25 mol-% such a result was expected. However, the samples indeed exhibit different colours. The Kubelka-Munk transformations of the diffuse reflectance UV-vis spectra are presented in Figure 64.

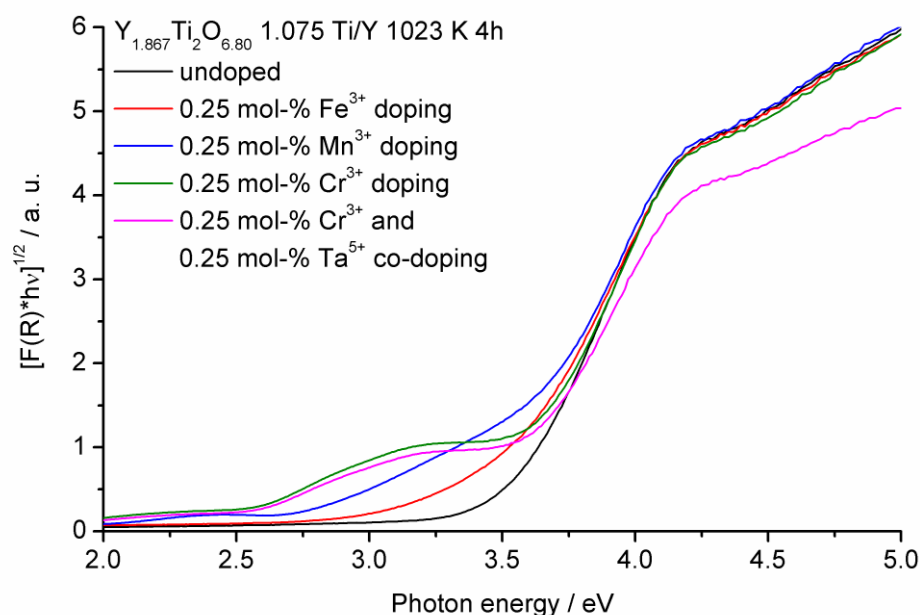


Figure 64: Tauc-plots (for indirect band gap transition) calculated from the UV-vis diffuse reflectance spectra of $Y_{1.867}Ti_2O_{6.80}$ doped with 0.25 mol-% of Cr^{3+} , Mn^{3+} or Fe^{3+} . Additionally, a co-doped sample with 0.25 mol-% of each Cr^{3+} and Ta^{5+} , and the undoped sample are included. Annealing was performed at 1023 K for 4h and all samples feature a Ti/Y ratio of 1.075.

The optical properties are significantly changed even at small doping levels. Interestingly, the absorption edge is not uniformly shifted to lower energies. Depending on the dopant cation, new absorption bands are formed. For the cations of Cr^{3+} , Mn^{3+} and Fe^{3+} , these additional absorptions edge at ca. 2.5 eV, 2.7 eV and 3.0 eV, respectively. However, the Ta^{5+} co-doping of chromium doped $Y_{1.867}Ti_2O_{6.80}$ has no significant influence on the optical properties.

The Cr^{3+} , Mn^{3+} and Fe^{3+} doped $Y_{1.867}Ti_2O_{6.80}$ samples were subsequently tested in photocatalytic hydrogen production in presence of methanol acting as sacrificial reagent to determine the influence of the dopant on the photocatalytic activity. Two different co-catalysts, platinum and rhodium, were chosen. As a platinum loading of 0.75 wt.-% were found to be the optimum for undoped $Y_{1.867}Ti_2O_{6.80}$ (Ti/Y ratio of 1.075) annealed at

1023 K, the same amount of platinum was also applied on the doped samples. The results in photocatalysis are presented in Figure 65.

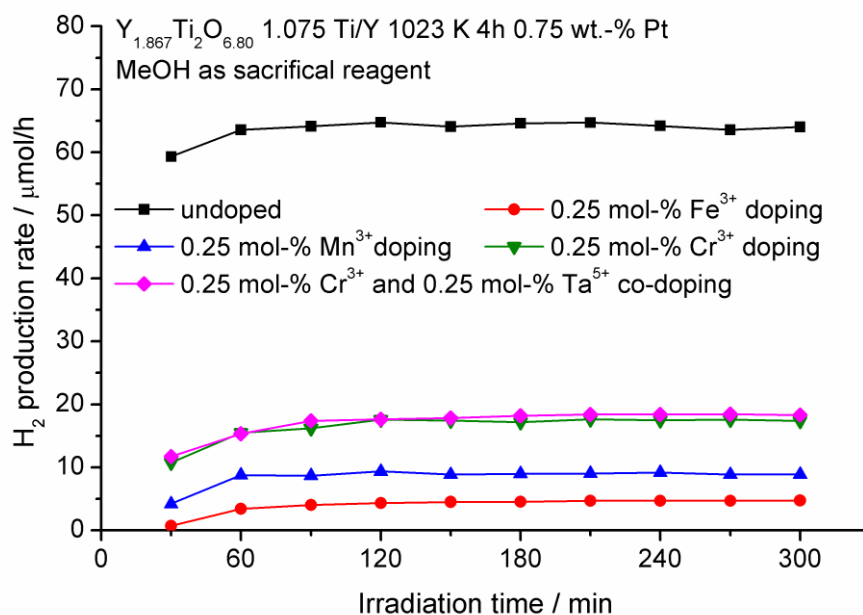


Figure 65: Photocatalytic activity regarding hydrogen production over $Y_{1.867}Ti_2O_{6.80}$ (Ti/Y ratio of 1.075) doped with 0.25 mol-% of Cr^{3+} , Mn^{3+} or Fe^{3+} calcined at 1023 K for 4h in the presence of 10 vol.-% methanol as sacrificial reagent. Additionally, a co-doped sample with 0.25 mol-% of each Cr^{3+} and Ta^{5+} , and the undoped sample are included. All samples were loaded with 0.75 wt.-% of platinum by in-situ photodeposition.

The lowest activity is achieved with the Fe^{3+} doped sample featuring hydrogen production rates below 5 $\mu\text{mol H}_2/\text{h}$. By doping 0.25 mol-% of Mn^{3+} , the activity is increased to about 9 $\mu\text{mol H}_2/\text{h}$. The highest activity is obtained with 0.25 mol-% Cr^{3+} -doped $Y_{1.867}Ti_2O_{6.80}$ reaching 18 $\mu\text{mol H}_2/\text{h}$. The photocatalytic activity seems to increase with the absorption in the visible light region, which increases in the manner $Fe^{3+} < Mn^{3+} < Cr^{3+}$. Therefore, decreasing the band gap energy within the series of doped samples from 3.0 eV to 2.5 eV improves the photocatalytic activity. Doping improves the photocatalysts` ability of absorbing a higher fraction of incident photons leading to a higher hydrogen production rate. Unfortunately, this only fits within the series of doped samples of $Y_{1.867}Ti_2O_{6.80}$, as undoped and structure optimized $Y_{1.867}Ti_2O_{6.80}$ with a Ti/Y ratio of 1.075 provides a significantly higher photocatalytic activity of 65 $\mu\text{mol H}_2/\text{h}$ under similar conditions of full arc irradiation. In general, the lower activities of doped samples are attributed to a higher concentration of recombination centers referred to defects. Interestingly, the additional co-doping of 0.25 mol-% Cr^{3+} -doped $Y_{1.867}Ti_2O_{6.80}$

with the same mol fraction of Ta^{5+} provides the same photocatalytic activity. Thus, the improvement of the charge balance induced by the Tantalum co-doping has no influence on photocatalysis. This result indicates that vacancies in the oxygen sublattice are not the type of defects being critical for photocatalytic applications, which is corroborated by the fact that structure optimized $\text{Y}_{1.867}\text{Ti}_2\text{O}_{6.80}$ is highly active, although it incorporates a significant amount of vacancies in the anion sublattice. The substitution of tetravalent titanium by trivalent cations leads to a slightly higher degree of oxygen vacancies, which is easily compensable by the pyrochlore structure. Therefore, the M^{3+} cation doping contaminates the TiO_6 octahedral network by creating defect sites. A similar mechanism was found in “stuffed” $\text{Y}_2(\text{Ti}_{2-x}\text{Y}_x)\text{O}_{7-1.5x}$, in which yttrium self-doping leads to a significantly reduced photocatalytic activity by influencing the mobility and separation of charge carriers (cf. to chapter 4.1.3). The photocatalytic hydrogen production with rhodium is presented in Figure 66.

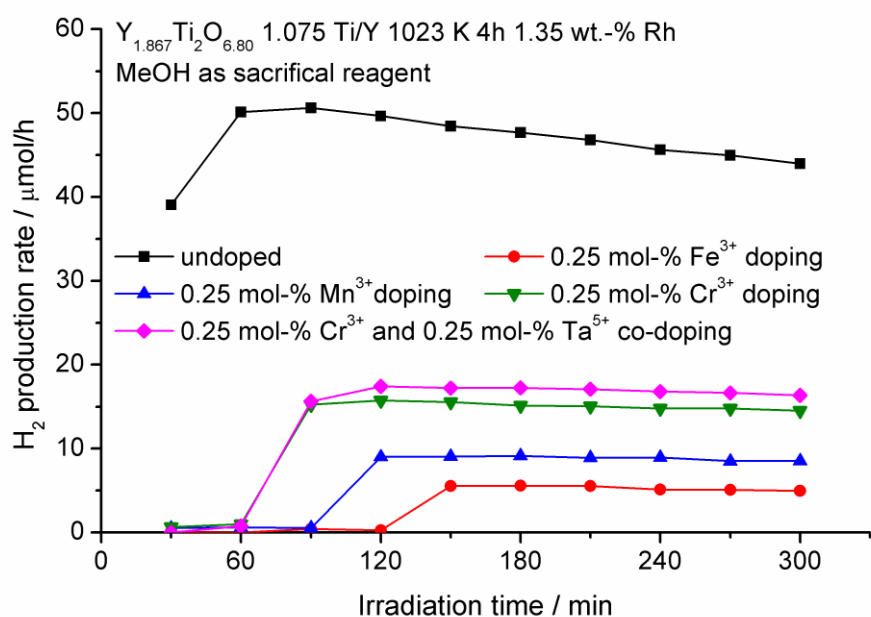


Figure 66: Photocatalytic activity regarding hydrogen production over $\text{Y}_{1.867}\text{Ti}_2\text{O}_{6.80}$ (Ti/Y ratio of 1.075) doped with 0.25 mol-% of Cr^{3+} , Mn^{3+} or Fe^{3+} calcined at 1023 K for 4h in the presence of 10 vol.-% methanol as sacrificial reagent. Additionally, a co-doped sample with 0.25 mol-% of each Cr^{3+} and Ta^{5+} , and the undoped sample are included. All samples were loaded with 0.75 wt.-% of platinum by in-situ photodeposition.

A co-catalyst loading of 1.35 wt.-% was found as optimum in tests with undoped $\text{Y}_{1.867}\text{Ti}_2\text{O}_{6.80}$ and this loading is applied on the doped samples as well. In principle, the results obtained with platinum as co-catalyst are confirmed. The Cr^{3+} doping yields

superior activity compared to the doping with Mn^{3+} and Fe^{3+} . The platinum in-situ photodeposition was completed after at least 60 minutes, even in the case of samples featuring very low activities. If rhodium is applied as co-catalyst, the initial period of in-situ photodeposition correlates very well with the photocatalytic activity. In expression, the lower the activity, the longer the time needed for photodeposition and for reaching stable activities. Undoped $\text{Y}_{2-x}\text{Ti}_2\text{O}_{7-1.5x}$ pyrochlores were found to suffer from a loss in activity of about 10 %/h, if rhodium is applied as co-catalyst (cf. to chapter 4.1.2). The results in Figure 66 indicate that this loss in activity can be almost completely inhibited by doping $\text{Y}_{1.867}\text{Ti}_2\text{O}_{6.80}$ with Cr^{3+} , Mn^{3+} or Fe^{3+} .

Table 12 summarizes the lattice parameters, average crystallite sizes, optical band edges and photocatalytic activities regarding hydrogen production of 0.25 mol-% Cr^{3+} , Mn^{3+} and Fe^{3+} doped $\text{Y}_{1.867}\text{Ti}_2\text{O}_{6.80}$. The average crystallite sizes calculated by the Scherrer equation within the Rietveld refinement are not much affected by doping. Whereas the samples doped with 0.25 mol-% of Mn^{3+} and Fe^{3+} feature almost the same crystallite size of about 50 nm as the undoped sample, doping with 0.25 mol-% of Cr^{3+} slightly increases the crystallite size to 56.1 nm. In conclusion the Cr^{3+} doping yielded the best results regarding optical properties and photocatalytic activity, even though undoped and structure optimized $\text{Y}_{1.867}\text{Ti}_2\text{O}_{6.80}$ provides the clearly superior activity.

$\text{Y}_{1.867}\text{Ti}_2\text{O}_{6.80}$ 1023 K 4h	lattice parameter $a / \text{\AA}$	aver. crystal size / nm	band edge energies / eV	hydrogen production / $\mu\text{mol H}_2/\text{h}$	
				Pt	Rh
undoped	10.1037	50.3	3.7	64.8	50.6
0.25 mol-% Fe^{3+}	10.1034	49.6	3.0, 3.7	4.8	5.6
0.25 mol-% Mn^{3+}	10.1048	50.2	2.7, 3.7	9.4	9.2
0.25 mol-% Cr^{3+}	10.1044	56.1	2.5, 3.7	17.7	15.8
0.25 mol-% Cr^{3+} 0.25 mol-% Ta^{5+}	10.1041	53.9	2.5, 3.7	18.5	17.4

Table 12: Summary of the lattice parameters, the average crystallite sizes, the optical band edge energies and photocatalytic activities regarding hydrogen production of 0.25 mol-% Cr^{3+} , Mn^{3+} and Fe^{3+} doped $\text{Y}_{1.867}\text{Ti}_2\text{O}_{6.80}$ (Ti/Y ratio of 1.075).

4.4.2 Optimum dopant level in Cr^{3+} doped $\text{Y}_{1.867}\text{Ti}_2\text{O}_{6.80}$

The fact that the incorporation of Cr^{3+} cations leads to a markedly strong absorption and yielded the highest photocatalytic activity among the series of dopants was encouraging to prepare chromium doped $\text{Y}_{1.867}\text{Ti}_2\text{O}_{6.80}$ with different doping levels. The additional doping levels were chosen to be 0.10 mol-%, 0.50 mol-% and 1.00 mol-%. The

corresponding X-ray diffraction data are again completely unspectacular, but they prove that a pyrochlore structure is obtained up to a Cr^{3+} doping level of 1.00 mol-% while by-phases are not formed. The XRD data of chromium doped samples are presented in Figure A17 in the appendix. The lattice parameter a was found to vary between 10.1030 Å and 10.1055 Å and thus, to be not much affected by the chromium doping level of up to 1.00 mol-%.

The Kubelka-Munk transformations of the diffuse reflectance UV-vis spectra are indeed of higher importance and are shown in Figure 67. Obviously, the strongest gain in additional visible light absorptivity is achieved up to a chromium doping level of 0.25 mol-%. Further increase of the doping level only marginally raises the absorptivity at 2.5 eV. However, at these high doping levels, an additional absorption at approximately 2.0 eV arises, which is attributed to another trap level in the band gap.

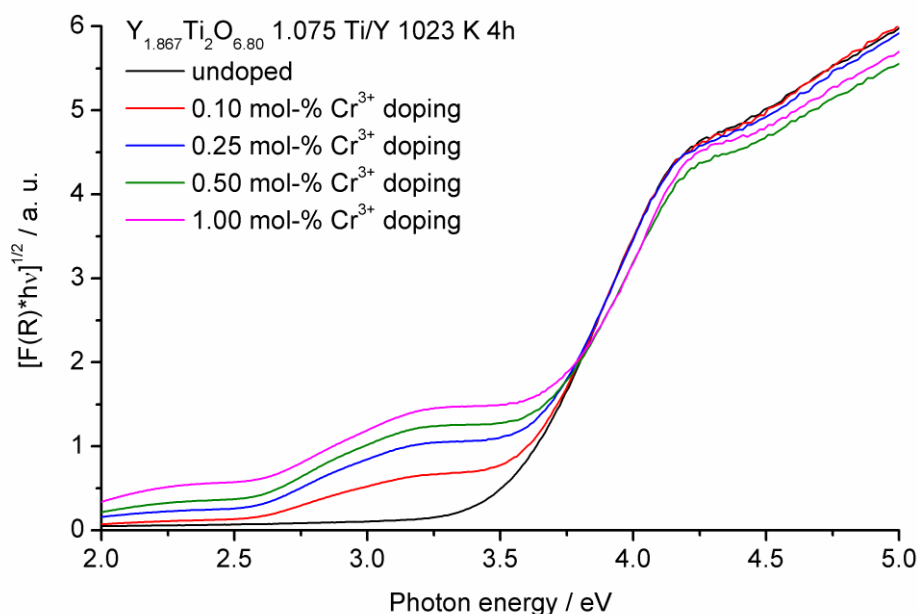


Figure 67: Tauc-plots (for indirect band gap transition) calculated from the UV-vis diffuse reflectance spectra of $\text{Y}_{1.867}\text{Ti}_2\text{O}_{6.80}$ doped with 0.10, 0.25, 0.50 or 1.00 mol-% of Cr^{3+} . The data for the undoped sample is included as well. Annealing was performed at 1023 K for 4h and all samples feature a Ti/Y ratio of 1.075.

The sample featuring different chromium dopant levels were tested in photocatalytic hydrogen production with methanol acting as sacrificial agent. Again, platinum and rhodium were chosen as co-catalysts. For the platinum aided photocatalysis, a 0.75 wt.-% loading of platinum was applied. The results are presented in Figure 68. The samples doped with 0.10, 0.25, 0.50 and 1.00 mol-% of chromium provide hydrogen production

rates of 26.6, 17.7, 5.4 and 1.0 $\mu\text{mol H}_2/\text{h}$, respectively, if 0.75 wt.-% of platinum are applied. By means of the additional doping levels it is clearly demonstrated that even chromium doping leads to significantly reduced photocatalytic activities at all, if compared to the undoped sample. The photocatalytic activity concomitantly decreases with increasing dopant level, as the negative effect of additional recombination centers exceeds the positive effect of additional absorption.

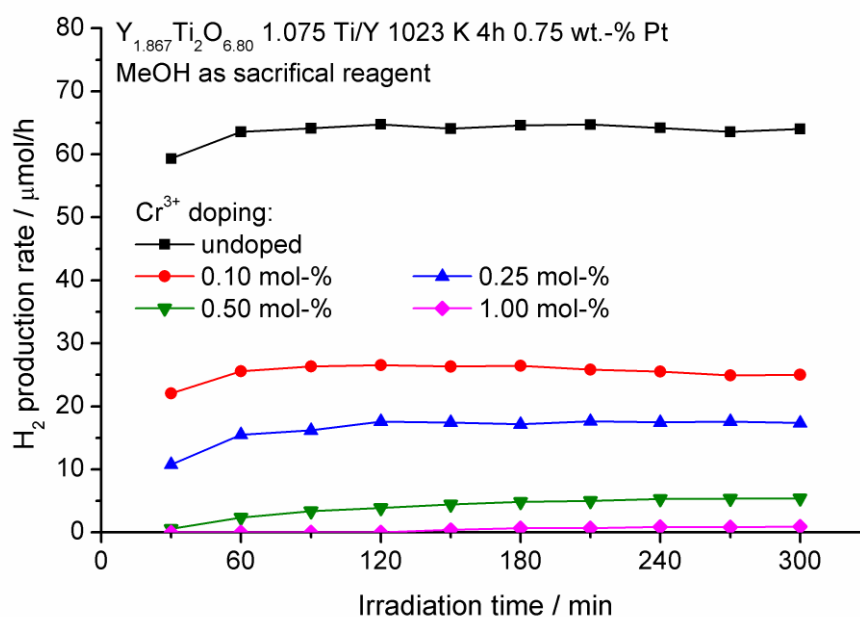


Figure 68: Photocatalytic activity regarding hydrogen production over $\text{Y}_{1.867}\text{Ti}_2\text{O}_{6.80}$ (Ti/Y ratio of 1.075) doped with 0.10, 0.25, 0.50 or 1.00 mol-% of Cr^{3+} in the presence of 10 vol.-% methanol as sacrificial reagent. The data for the undoped sample is included as well. Annealing was performed at 1023 K for 4h and all samples feature a Ti/Y ratio of 1.075. All samples were loaded with 0.75 wt.-% of platinum by in-situ photodeposition.

The test of photocatalytic hydrogen production was also performed under aid of 1.35 wt.-% of rhodium. Although these results corroborate very well with those obtained for platinum, the measurements provide some interesting details as shown in Figure 69. Hydrogen production rates of 27.5, 15.8, 5.1 and 0.0 $\mu\text{mol H}_2/\text{h}$ were obtained for samples doped with 0.10, 0.25, 0.50 and 1.00 mol-% of chromium, respectively, if 0.75 wt.-% of rhodium are applied. The rhodium photodeposition on the sample featuring a chromium doping level of 0.50 mol-% needed at least 240 minutes of irradiation until being completed and some activity is obtained. If 1.00 mol-% of chromium is doped, the photodeposition could not have been accomplished within the limits of the measurements.

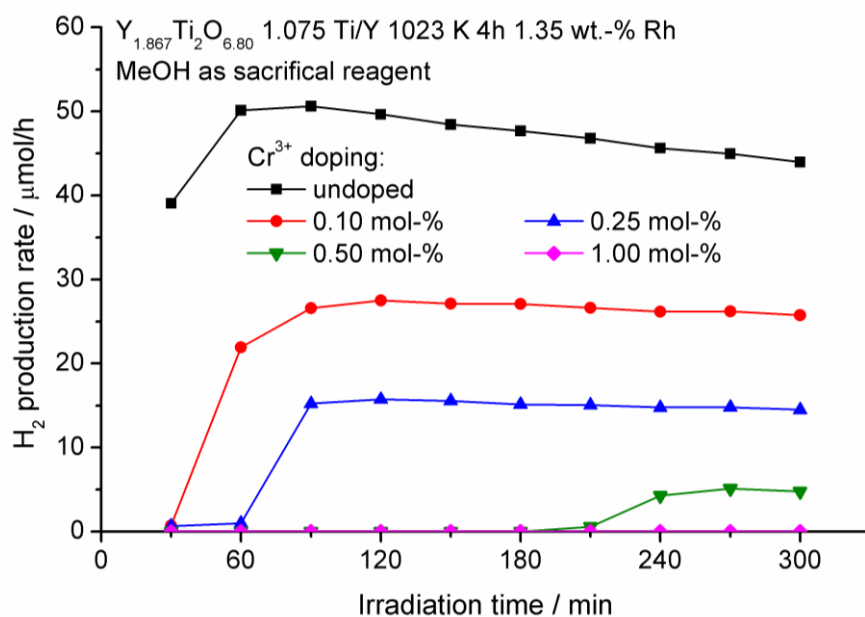


Figure 69: Photocatalytic activity regarding hydrogen production over $Y_{1.867}Ti_2O_{6.80}$ (Ti/Y ratio of 1.075) doped with 0.10, 0.25, 0.50 or 1.00 mol-% of Cr^{3+} in the presence of 10 vol.-% methanol as sacrificial reagent. The data for the undoped sample is included as well. Annealing was performed at 1023 K for 4h and all samples feature a Ti/Y ratio of 1.075. All samples were loaded with 0.75 wt.-% of rhodium by in-situ photodeposition.

But the most interesting detail in the rhodium assisted photocatalysis refers to the stability of the photocatalytic process and the photocatalyst itself. If $Y_{1.867}Ti_2O_{6.80}$ is doped with chromium cations, the hydrogen production rate is almost ideally stabilized over time irrespective of the dopant level applied. As the photocatalytic activity is significantly decreased with increasing chromium dopant level, a very low dopant concentration of Cr^{3+} in the range of 10^{-2} to 10^{-5} mol-% is considered to reduce the activity only very slightly, while stabilizing the hydrogen production rate substantially. The photooxidation of rhodium is supposed to be the reason for the loss in photocatalytic activity over rhodium loaded wide band gap semi-conductors like $Y_{2-x}Ti_2O_{7-1.5x}$. The photogenerated holes are assumed to exhibit very high oxidation potentials. As the oxidation stability of rhodium is lower ($E_0(Rh^{3+}|Rh) = +0.76 V$) compared to that of platinum^[52] ($E_0(Pt^{2+}|Pt) = +1.18 V$), the addressed loss in stability only occurs, if rhodium is applied as co-catalyst while platinum assisted samples yield perfectly stable hydrogen production rates. The doping of $Y_{2-x}Ti_2O_{7-1.5x}$ with cations featuring partially filled d orbitals leads to additional donor and/or acceptor energy levels within the energy band gap (cf. to Figure 62). If additional donor levels are created, the photoexcitation of therein located electrons will generate a hole of a lower oxidation potential compared to

holes photogenerated under band gap irradiation. These holes may no longer possess the suitable oxidation potential to oxidize rhodium. The formation of a Rh/Cr₂O₃ core-shell co-catalyst system (cf. to chapter 4.3.5) during illumination is not expected, as Cr³⁺ is supposed to be incorporated in the bulk material like a “real” dopant, but not only as a surface state.

The lattice parameters a , the average crystallite sizes, the band edge energies and the hydrogen production rates of Y_{1.867}Ti₂O_{6.80} doped with 0.10, 0.25, 0.50 and 1.00 mol-% of Cr³⁺ are summarized in Table 13. The average crystallite sizes were found to increase with increasing dopant level. Irrespective of the co-catalyst applied, already a doping level of as low as 1.00 mol-% results in the almost complete inhibition of any photocatalytic processes. Thus, doping Y_{1.867}Ti₂O_{6.80} with trivalent cations featuring partially filled d orbitals seems to be not suitable to improve the photocatalytic activity at all. This again highlights the outstanding influence that the purity of the TiO₆ octahedral network exerts on the photocatalytic activity. In this context, it does not play a role if the chemical impurity in the TiO₆ octahedral network derives from a kind of yttrium self-doping like described for cationic lattice distortion, or from forced cation doping performed in this chapter. In conclusion, high purity in the TiO₆ octahedra leads to high photocatalytic activity.

Y _{1.867} Ti ₂ O _{6.80} 1023 K 4h	lattice parameter a / Å	aver. crystal. size / nm	band edge energies / eV	hydrogen production / μmol H ₂ /h	
				Pt	Rh
undoped	10.1037	50.3	3.7	64.8	50.6
0.10 mol-% Cr ³⁺	10.1055	50.4	2.5, 3.7	26.6	27.5
0.25 mol-% Cr ³⁺	10.1044	56.1	2.5, 3.7	17.7	15.8
0.50 mol-% Cr ³⁺	10.1030	57.0	2.0, 2.5, 3.7	5.4	5.1
1.00 mol-% Cr ³⁺	10.1041	57.0	2.0, 2.5, 3.7	1.0	0.0

Table 13: Summary of the lattice parameters, the average crystallite sizes, the optical band edge energies and photocatalytic activities regarding hydrogen production of Y_{1.867}Ti₂O_{6.80} (Ti/Y ratio of 1.075) samples doped with 0.10, 0.25, 0.50 and 1.00 mol-% of Cr³⁺.

4.4.3 B-site doping of Y_{1.867}Ti₂O_{6.80} with Ta⁵⁺ and W⁶⁺

As the doping of Y_{1.867}Ti₂O_{6.80} with transition metals featuring partially filled d orbitals had not succeeded in improving the photocatalytic activity, the B site of structure optimized Y_{1.867}Ti₂O_{6.80} (Ti/Y ratio of 1.075) was highly doped with other d^0 transition metal cations. A non-isoelectric substitution also gave the opportunity to investigate the influence of vacancies in the lattice possibly acting as defects. In order to eliminate the

vacancies in the oxygen sublattice completely, non-isoelectric substitution of Ti^{4+} by Ta^{5+} and W^{6+} was performed. Due to the higher valence states of Ta^{5+} and W^{6+} , the charge balance may lead to a complete refill of the seventh oxygen O^7 located in the Wyckoff position $8a$ ($1/8, 1/8, 1/8$) in $\text{Y}_{2-x}\text{B}_2\text{O}_6\text{O}^7$, if the stoichiometry is adjusted appropriately. As the amount of oxygen vacancies in $\text{Y}_{1.867}\text{Ti}_2\text{O}_{6.80}$ is known to be 0.20 per formula unit, a 20 mol-% of tantalum or a 10 mol-% of tungsten had to be applied as the correct doping level. The cations of tantalum and tungsten, Ta^{5+} and W^{6+} , possess effective ionic radii of 64 pm and 60 pm in octahedral coordination (c. n. of 6). Due to the effective ionic radii of Ti^{4+} and Y^{3+} , which are 60.5 pm (c. n. of 6) and 101.9 pm (c. n. of 8), respectively, an exclusive substitution for titanium on the B site is most likely. New pyrochlore oxides of $\text{Y}_{1.867}\text{Ti}_{1.6}\text{Ta}_{0.4}\text{O}_7$ and $\text{Y}_{1.867}\text{Ti}_{1.8}\text{W}_{0.2}\text{O}_7$ are predicted.

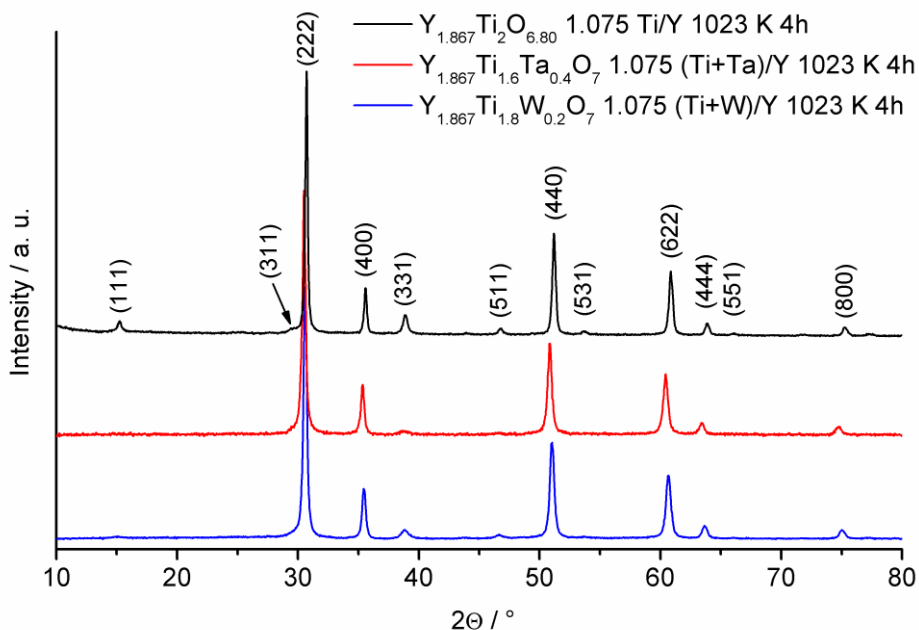


Figure 70: XRD pattern of $\text{Y}_{1.867}\text{Ti}_2\text{O}_{6.80}$, $\text{Y}_{1.867}\text{Ti}_{1.6}\text{Ta}_{0.4}\text{O}_7$ and $\text{Y}_{1.867}\text{Ti}_{1.8}\text{W}_{0.2}\text{O}_7$ featuring $(\text{Ti}+\text{Ta}+\text{W})/\text{Y}$ ratios of 1.075. Annealing was performed at 1023 K for 4h.

The X-ray diffraction data of $\text{Y}_{1.867}\text{Ti}_2\text{O}_{6.80}$, $\text{Y}_{1.867}\text{Ti}_{1.6}\text{Ta}_{0.4}\text{O}_7$ and $\text{Y}_{1.867}\text{Ti}_{1.8}\text{W}_{0.2}\text{O}_7$ annealed at 1023 K are presented in Figure 70. The ratio of the sum of the moles of B cations ($\text{Ti}+\text{Ta}+\text{W}$) to moles of yttrium cations is maintained at 1.075 for all samples. Interestingly, the doping with tantalum and tungsten has significant influence on the pyrochlore structure. First, a lot of reflections usually present in the pattern of a pyrochlore structure like $\text{Y}_{1.867}\text{Ti}_2\text{O}_{6.80}$ are missing in the case of $\text{Y}_{1.867}\text{Ti}_{1.6}\text{Ta}_{0.4}\text{O}_7$ annealed at 1023 K. A closer look reveals that the pattern lacks almost all reflections providing an odd index, namely, the reflections with indices of (111), (311), (531) and

(551). Only the reflections with the indices of (331) and (511) are present, even though they are very much weakened in intensity compared to the reflections featuring only even indices. However, these two reflections are very important, because by them $Y_{1.867}Ti_{1.6}Ta_{0.4}O_7$ is defined to be a pyrochlore structure. If those reflections were absent as well, the structure would be referred to as defect fluorite, a parental structure to the pyrochlore which is reached by reducing the crystal symmetry. The A and B cations, which are strictly separated on different positions in the pyrochlore structure, are placed on the same crystallographic lattice position in the defect fluorite structure of A_4O_6X (SG: $Fm\bar{3}m$)^[150]. The reason for the lattice transformation in $Y_{1.867}Ti_{1.6}Ta_{0.4}O_7$ is again the mechanism of lattice cationic distortion as previously described in chapter 4.1. In the case of $Y_2Ti_2O_7$, self-induced cationic interchange leads to $(Y_{2-x}Ti_x)(Ti_{2-x}Y_x)O_7$. This cationic interchange is supposed to be a function of the difference in effective ionic radii of the A and B cations. The more the effective ionic radii differ, the better the cationic antisite formation is inhibited. Compared to the radius of Ti^{4+} (60.5 pm), the effective ionic radius of Ta^{5+} (64 pm) is closer to that of Y^{3+} , which facilitates the formation of cation antisites in $Y_{1.867}Ti_{1.6}Ta_{0.4}O_7$. As the effective ionic radius of W^{6+} (60 pm) almost matches the radius of Ti^{4+} , the cation antisite formation in $Y_{1.867}Ti_{1.8}W_{0.2}O_7$ is expected to be reduced. The X-ray diffraction pattern of $Y_{1.867}Ti_{1.8}W_{0.2}O_7$ annealed at 1023 K corroborates with this thesis, as all important reflections are present, even though the intensities of those reflections featuring odd indices are weakened, if compared to $Y_{1.867}Ti_2O_{6.80}$. In chapter 4.1.1 the $I(400)/(331)$ ratio was found to be a half-quantitative indicator for cationic lattice distortion. For $Y_{1.867}Ti_{1.8}W_{0.2}O_7$ annealed at 1023 K, this ratio amounts to 5.94, which is significantly higher compared to all investigated samples of $Y_{2-x}Ti_2O_{7-1.5x}$ indicating a high cationic lattice distortion. However, changing the chemical composition will for sure have a different influence on each lattice plane making a direct comparison difficult. Whereas the tungsten doping in $Y_{1.867}Ti_{1.8}W_{0.2}O_7$ increases the lattice parameter a of $Y_{1.867}Ti_2O_{6.80}$ only slightly from 10.1075 Å to 10.1272 Å, it is increased stronger by the tantalum doping in $Y_{1.867}Ti_{1.6}Ta_{0.4}O_7$ amounting to 10.1667 Å. Although W^{6+} has almost the same size as Ti^{4+} , the increase in the lattice parameter can be explained by increasing cationic lattice distortion in $Y_{1.867}Ti_{1.8}W_{0.2}O_7$. The significant lattice expansion in $Y_{1.867}Ti_{1.6}Ta_{0.4}O_7$ is not only due to even higher lattice distortion, but as well due to the larger effective ionic radius of Ta^{5+} compared to Ti^{4+} . Compared to $Y_{1.867}Ti_2O_{6.80}$, the average crystallite sizes of tantalum and tungsten doped samples annealed at 1023 K were found to be much smaller in the range of 31 nm.

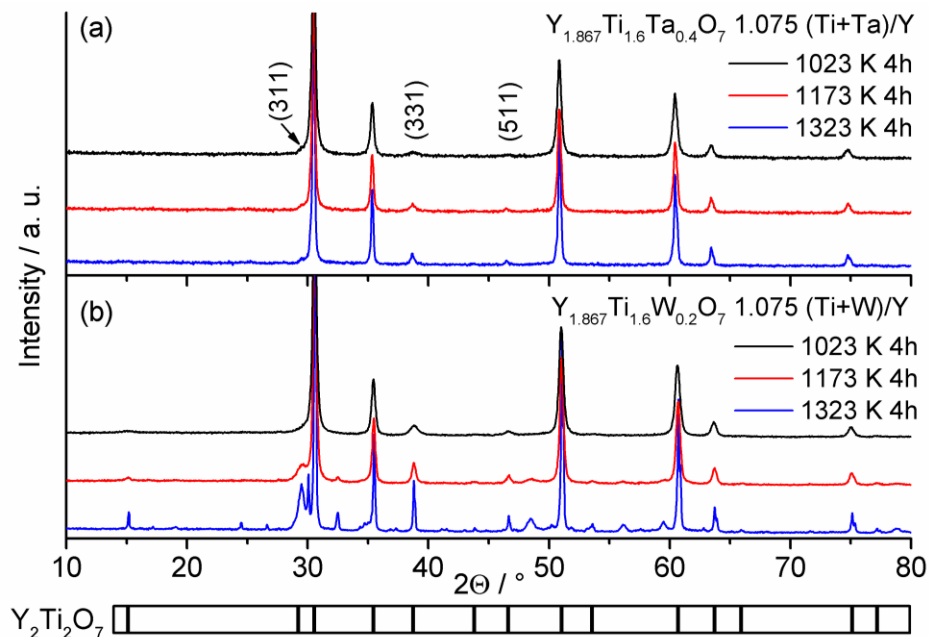


Figure 71: XRD pattern of $Y_{1.867}Ti_{1.6}Ta_{0.4}O_7$ (part (a)) and $Y_{1.867}Ti_{1.8}W_{0.2}O_7$ (part (b)) featuring (Ti+Ta+W)/Y ratios of 1.075 and annealed at 1023 K, 1273 K and 1323 K for 4h.

The samples of $Y_{1.867}Ti_{1.6}Ta_{0.4}O_7$ and $Y_{1.867}Ti_{1.8}W_{0.2}O_7$ were also annealed at higher temperatures of 1173 K and 1323 K each for four hours. The development of the X-ray pattern of $Y_{1.867}Ti_{1.6}Ta_{0.4}O_7$ as a function of the annealing temperature is presented in Figure 71(a). The high intensity of the (222) reflection was cut to focus on the important part of the data, namely, the development of reflections featuring the odd indices of (311), (331) and (511). By increasing the annealing temperature these reflections become more and more apparent. This trend is connected to a reduction in cationic lattice distortion. This finding that the increase in the annealing temperature leads to the curing of lattice antisite defects was already observed for $Y_{2-x}Ti_2O_{7-1.5x}$ before (cf. to chapter 4.1). Reduced cationic lattice distortion is also evinced by the development of the lattice parameter a , which is consecutively decreased with increasing annealing temperature to a value of 10.1517 Å for 1323 K. However, the $I(400)/(331)$ ratio amounts to a very high value of 6.73 even after 1323 K annealing predicting high cationic lattice distortion in $Y_{1.867}Ti_{1.6}Ta_{0.4}O_7$ at all annealing temperatures, although these values are hard to compare to those of $Y_{2-x}Ti_2O_{7-1.5x}$ as stated above. The average crystallite size of $Y_{1.867}Ti_{1.6}Ta_{0.4}O_7$ is found to increase from 30.3 nm via 44.7 nm to 115.2 nm at annealing temperatures of 1023 K, 1173 K and 1323 K, respectively. By phases like TiO_2 rutile found in the synthesis of $Y_{2-x}Ti_2O_{7-1.5x}$ at temperatures as high as 1173 K are not formed. Part (b) of Figure 71 presents the development of the XRD pattern of $Y_{1.867}Ti_{1.8}W_{0.2}O_7$ as a function of the annealing temperature. All the reflections with odd indices missed at 1023 K are

apparent at 1173 K annealing and indeed of a significant intensity. As found for $Y_{1.867}Ti_{1.6}Ta_{0.4}O_7$ and $Y_{2-x}Ti_2O_{7-1.5x}$, the cationic lattice distortion is also reduced for $Y_{1.867}Ti_{1.8}W_{0.2}O_7$ by raising the annealing temperature. An $I(400)/(331)$ ratio of 1.89 is obtained for 1323 K annealing reaching almost the value considered for pyrochlores being free of cationic antisites. Concomitantly, the lattice parameter a is reduced to a value of 10.1094 Å after heat treatment at 1323 K, which is very close to the value of $Y_{1.867}Ti_2O_{6.80}$ being free of cationic distortion. As the effective ionic radii of W^{6+} and Ti^{4+} are very similar, no influence of the tungsten doping on the lattice parameter is expected. However, the X-ray pattern at 1173 K shows two additional reflections at 2θ angles of 32.53° and 48.52° being very weak in intensity, but definitely belonging to a by-phase. By further increase of the annealing temperature to 1323 K, these reflections become abundantly clear and at least 20 more reflections appear, but being very weak in intensity compared to the reflections deriving from the pyrochlore structure. Unfortunately, we were unable to determine the lattice system, not to mention the space group, of the additional phase or phases. Only the formation of TiO_2 by-phases is excluded. In conclusion, it is demonstrated that the pyrochlores of $Y_{1.867}Ti_{1.6}Ta_{0.4}O_7$ and $Y_{1.867}Ti_{1.8}W_{0.2}O_7$ can be successfully prepared without impurity phases up to annealing temperatures of 1323 K and 1173 K, respectively.

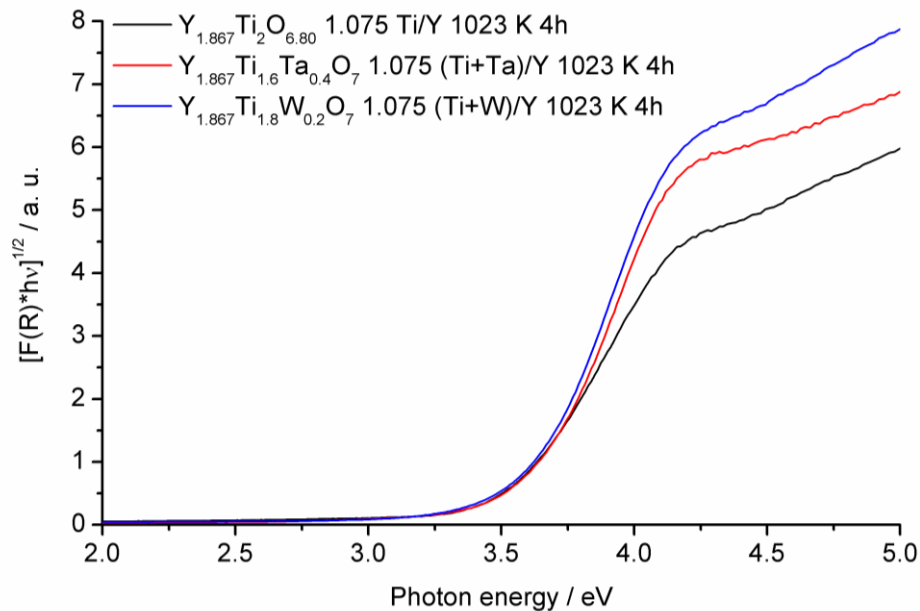


Figure 72: Tauc-plots (for indirect bad gap transition) calculated from the UV-vis diffuse reflectance spectra of $Y_{1.867}Ti_2O_{6.80}$, $Y_{1.867}Ti_{1.6}Ta_{0.4}O_7$ and $Y_{1.867}Ti_{1.8}W_{0.2}O_7$ annealed at 1023 K for 4h and featuring (Ti+Ta+W)/Y ratios of 1.075.

The Kubelka-Munk transformation of the diffuse reflectance UV-vis spectra of $Y_{1.867}Ti_2O_{6.80}$, $Y_{1.867}Ti_{1.6}Ta_{0.4}O_7$ and $Y_{1.867}Ti_{1.8}W_{0.2}O_7$ each annealed at 1023 K are presented in Figure 72. It is obvious that the band gap energy of $Y_{1.867}Ti_2O_{6.80}$ is not changed by tantalum or tungsten doping, as all three samples exhibit the same E_{bg} of 3.7 eV. Indeed, the B site doping of $Y_{1.867}Ti_2O_{6.80}$ with tantalum or tungsten has an influence on the band structure, as empty orbitals of Ta5d and W5d are supposed to hybridize with the Ti3d orbitals and thus, contribute to the conduction band. However, the Ta5d as well as the W5d orbitals are supposed to be located at energies being more negative vs. NHE compared to the Ti3d orbitals. Thus, doping with Ta^{5+} or W^{6+} will not affect the lower edge of the conduction band and the band gap energy is not changed.

As shown in Figure 73 again presenting Kubelka-Munk transformations of the diffuse reflectance UV-vis spectra, applying higher annealing temperatures of 1173 K or 1323 K for $Y_{1.867}Ti_{1.6}Ta_{0.4}O_7$ and $Y_{1.867}Ti_{1.8}W_{0.2}O_7$ leads to a slight shift of the absorption edge to higher energies by about 0.05 - 0.10 eV. Moreover, compared to the tungsten doped sample, the tantalum doped material exhibits slightly increased band gap energies at identical annealing temperatures.

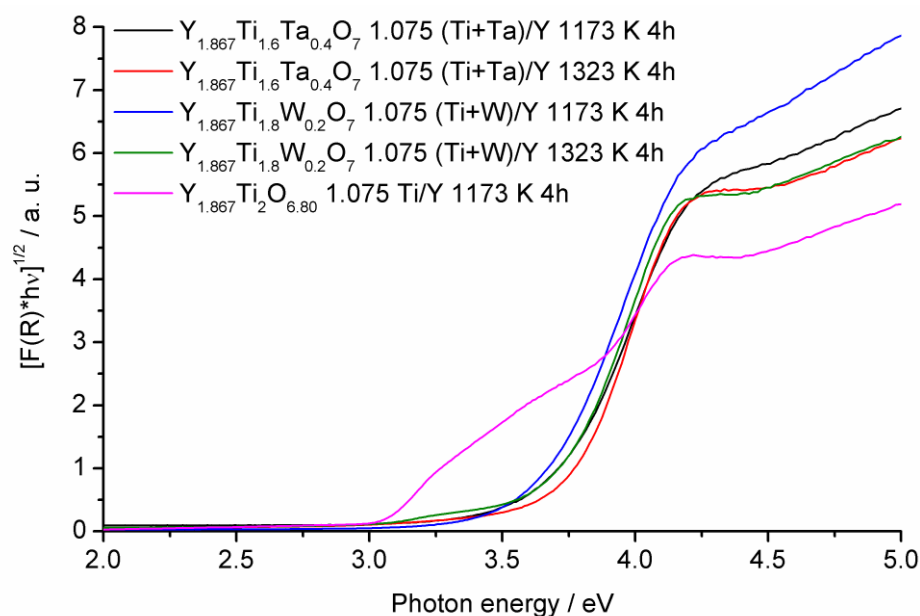


Figure 73: Tauc-plots (for indirect band gap transition) calculated from the UV-vis diffuse reflectance spectra of $Y_{1.867}Ti_2O_{6.80}$, $Y_{1.867}Ti_{1.6}Ta_{0.4}O_7$ and $Y_{1.867}Ti_{1.8}W_{0.2}O_7$ annealed at 1173 K and 1323 K for 4h and featuring (Ti+Ta+W)/Y ratios of 1.075.

The sample of $Y_{1.867}Ti_{1.8}W_{0.2}O_7$ annealed at 1323 K, which was proven by XRD to contain an impurity phase, provides an additional absorption band edging to about 3 eV.

Maybe, this sample is also contaminated with a very small fraction of rutile being invisible towards the X-ray diffraction method. For comparison, the $Y_{1.867}Ti_2O_{6.80}$ (Ti/Y ratio of 1.075) sample annealed at 1173 K is presented as well containing a very large fraction of TiO_2 rutile, which is evinced by the very strong additional absorption between 3.0 eV and 3.7 eV. Doping of tantalum and tungsten greatly enhance the ability of the $Y_{1.867}Ti_2O_{6.80}$ pyrochlore to withstand the rutile by-phase formation at temperatures as high as 1173 K.

The samples of tantalum and tungsten doped $Y_{1.867}Ti_2O_{6.80}$ annealed between 1023 K and 1323 K were tested in photocatalytic hydrogen production with 10 vol.-% of methanol acting as sacrificial reagent. As an optimum platinum co-catalyst loading of 0.75 wt.-% was found for $Y_{1.867}Ti_2O_{6.80}$ (Ti/Y ratio of 1.075), this loading was also applied for the tantalum and tungsten doped samples.

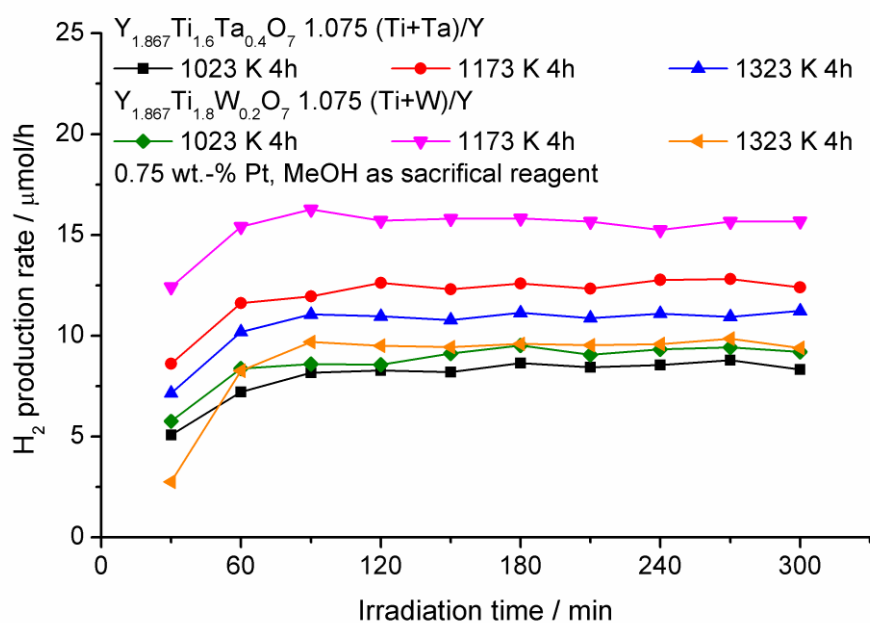


Figure 74: Photocatalytic activity regarding hydrogen production over $Y_{1.867}Ti_{1.6}Ta_{0.4}O_7$ and $Y_{1.867}Ti_{1.8}W_{0.2}O_7$ featuring a (Ti+W+Ta)/Y ratio of 1.075 as function of the annealing temperature (1023 K, 1173 K and 1323 K). The samples were loaded with 0.75 wt.-% of platinum by in-situ photodeposition. The measurements were performed in the presence of 10 vol.-% methanol as sacrificial reagent.

Figure 74 presents the photocatalytic measurements of $Y_{1.867}Ti_{1.6}Ta_{0.4}O_7$ and $Y_{1.867}Ti_{1.8}W_{0.2}O_7$ samples annealed at 1023 K, 1173 K and 1323 K, respectively. All samples yield stable activities over time, what was expected by applying platinum as co-catalyst. Interestingly, the tantalum as well as tungsten doped samples provide the highest activity at a higher annealing temperature of 1173 K. This annealing temperature states

the optimum, as hydrogen production rates were found to be lower at temperatures of 1023 K and 1323 K. For undoped $Y_{1.867}Ti_2O_{6.80}$, the optimum thermal treatment was 1023 K and a decrease in activity with increasing annealing temperature was found.

Table 14 summarizes the physicochemical properties and the photocatalytic activities regarding hydrogen production of $Y_{1.867}Ti_{1.6}Ta_{0.4}O_7$ and $Y_{1.867}Ti_{1.8}W_{0.2}O_7$ samples annealed between 1023 K and 1323 K. It seems that cationic lattice distortion and the average crystallite size influence the photocatalytic activity. This behaviour was already found in the case of undoped $Y_{2-x}Ti_2O_{7-1.5x}$ where optimizations in the Ti/Y ratio (1.075) and in the annealing temperature (1023 K) lead to a great improvement in photocatalytic activity (cf. to chapter 4.1.3). For tantalum and tungsten doped $Y_{1.867}Ti_2O_{6.80}$, the best compromise of minimized cationic lattice distortion and high active surface area provided by small crystallite sizes is found at an annealing temperature of 1173 K. However, the comparison to undoped $Y_{1.867}Ti_2O_{6.80}$ yielding up to 65 $\mu\text{mol H}_2/\text{h}$ under full arc irradiation shows that the 12.8 $\mu\text{mol H}_2/\text{h}$ and 16.3 $\mu\text{mol H}_2/\text{h}$ provided by samples doped with tantalum and tungsten, respectively, are rather disappointing.

(Ti+Ta+W) ratio of 1.075	lattice parameter a / Å	I(400)/I(331) ratio	aver. crystal. size / nm	band gap energy / eV	hydrogen prod. rate / $\mu\text{mol H}_2/\text{h}$	
$Y_{1.867}Ti_{1.6}Ta_{0.4}O_7$	1023 K 4h	10.1668	13.97	30.3	3.70	8.8
	1173 K 4h	10.1556	7.61	44.7	3.75	12.8
	1323 K 4h	10.1517	6.73	68.7	3.75	11.2
$Y_{1.867}Ti_{1.8}W_{0.2}O_7$	1023 K 4h	10.1272	5.94	30.8	3.70	9.5
	1173 K 4h	10.1198	3.22	40.9	3.75	16.3
	1323 K 4h	10.1094	1.89	115.2	3.75	9.9

Table 14: Summary of the lattice parameters, the I(400)/I(331) ratios, the average crystallite sizes, the band gap energies and the photocatalytic activities regarding hydrogen production of samples of $Y_{1.867}Ti_{1.6}Ta_{0.4}O_7$ and $Y_{1.867}Ti_{1.8}W_{0.2}O_7$ ((Ti+Ta+W)/Y ratio of 1.075) annealed at temperatures of 1023 K, 1173 K and 1323 K for 4 hours, respectively.

4.5 Nitrogen doped $Y_2Ta_2O_5N_2$

Two different concepts of reducing the band gap energy in pyrochlore mixed oxides were successfully applied so far. In the first concept, the substitution of yttrium ions by isoelectric bismuth ions on the A site of the structure leads to a shift of the band gap energy from 3.6 eV up to 2.8 eV (cf. to chapters 4.2 and 4.3). In the second concept, the band gap energy is reduced by the B-site doping with transition metal cations of Cr^{3+} , Mn^{3+} and Fe^{3+} featuring partially filled *d* orbitals (cf. to chapter 4.4). In the third concept, visible light absorption is achieved by anion doping. As the photocorrosive oxidation forming sulfur^[151] still marks a major drawback of sulfide photocatalysts, the nitrogen doping is supposed to be the most promising type of anion doping. Unfortunately, the nitrogen doping can only be achieved by high temperature treatment with ammonia gas, which is not compatible with most of the applied cations. A high process temperature of 1223 K is needed, because NH_3 has to dissociate to form reactive intermediates of NH_2 and NH .^[152, 153] Both bismuth and titanium were found to be reduced by ammonia at a temperature of 1223 K forming elemental bismuth and titanium(III)nitride (TiN),^[154] whereas tantalum and yttrium maintain their oxidation states. Thus, the mixed metal oxynitride of $Y_2Ta_2O_5N_2$ is prepared via the crystalline pre-stage of $YTaO_4$.^[155] Figure 75(a) shows the X-ray diffraction data of the high temperature monoclinic M' - $YTaO_4$ phase^[156] prepared by the sol-gel method after annealing at 1323 K for 12 hours. A reference pattern of M' - $YTaO_4$ made by Wolten^[157] is given as well. Although a low temperature tetragonal T' - $YTaO_4$ phase is known,^[156] it could not be obtained in pure state.

In order to obtain phase pure $Y_2Ta_2O_5N_2$, the ammonolysis of M' - $YTaO_4$ was optimized. The process temperature was altered between 1123 and 1273 K, the process time between 7.5 and 20 hours, and the ammonia flow rate between 40 and 80 mL/min. The best results were obtained at 1223 K and with an ammonia flow rate of 60 mL/min over a period of 15 hours. Figure 75(b) shows the X-ray diffraction data of this sample. The ammonolysis of M' - $YTaO_4$ was successful, as the low symmetric monoclinic phase of M' - $YTaO_4$ is almost completely transformed into the highly symmetrical pyrochlore phase. However, the Ta_3N_5 by-phase formation could not be avoided, although many attempts were made. A phase analysis conducted by Rietveld refinement yielded weight fractions of 82 wt.-% and 18 wt.-% for the pyrochlore “ $Y_2Ta_2O_5N_2$ ” and the by-phase Ta_3N_5 , respectively. Under consideration of this composition, the nitrogen content of the pyrochlore phase was determined by CHN elemental analysis to be 2.10 nitrogen ions per formula unit

leading to $\text{Y}_2\text{Ta}_2\text{O}_{4.85}\text{N}_{2.10}$. However, the presence of a large amount of Ta_3N_5 alters the chemical composition of the pyrochlore to $\text{Y}_2(\text{Ta}_{2-x}\text{Y}_x)\text{O}_{4.85-x}\text{N}_{2.10}$. This yttrium self-doping was already found to be the reason for significantly decreased photocatalytic activities in the “stuffed” pyrochlore of $\text{Y}_2(\text{Ti}_{2-x}\text{Y}_x)\text{O}_{7-0.5x}$ (cf. to chapter 4.1). Thereby, it was found that yttrium stuffing in pyrochlores increases the intensity ratio of the I(400)/I(331) reflections due to a partial phase transition towards the defect fluorite structure.

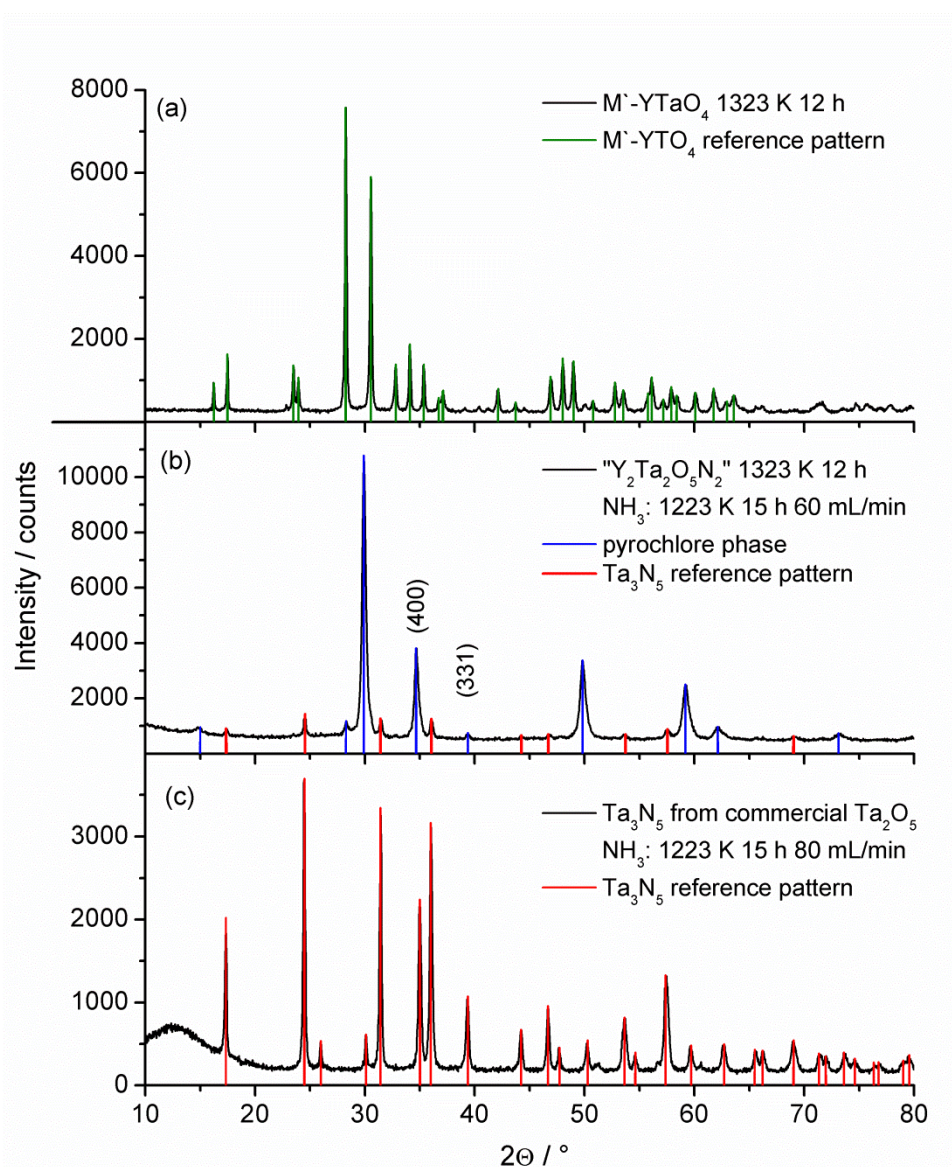


Figure 75: X-ray diffraction data of the monoclinic $\text{M}'\text{-YTaO}_4$ phase (a), the pyrochlore “ $\text{Y}_2\text{Ta}_2\text{O}_5\text{N}_2$ ” contaminated with Ta_3N_5 (b), and pure Ta_3N_5 obtained by ammonolysis of commercial Ta_2O_5 (c). The annealing temperatures and the conditions of the ammonia treatment are described in the legend. Reference patterns of $\text{M}'\text{-YTaO}_4$ ^[157] and Ta_3N_5 ^[158] are given as well.

An I(400)/I(331) ratio of about 15 found in the contaminated $Y_2(Ta_{2-x}Y_x)O_{4.85-x}N_{2.10}$ sample corroborates the assumption of yttrium self-doping, i. e. cationic distortion, when considering an I(400)/I(331) ratio of about 1.6 for destuffed pyrochlores. The lattice parameter of $Y_2(Ta_{2-x}Y_x)O_{4.85-x}N_{2.10}$ is calculated to be 10.36 Å, which differs considerably from the value given by literature (10.30 Å).^[155] As the tantalum nitride by-phase is known to be a suitable photocatalyst in dye degradation reactions,^[159] phase pure Ta_3N_5 was prepared by ammonolysis of commercial Ta_2O_5 . The corresponding X-ray diffraction pattern is given in part (c) of Figure 75.

The Kubelka-Munk transformations of the diffuse reflectance UV-vis spectra of phase pure Ta_3N_5 and the $Y_2(Ta_{2-x}Y_x)O_{4.85-x}N_{2.10} / Ta_3N_5$ mixture are given in Figure 76. Both samples provide almost the same band gap energy of about 2.05 eV. This value is in good agreement with the value given in literature for pure Ta_3N_5 .^[160] Thus, the true absorption edge of $Y_2(Ta_{2-x}Y_x)O_{4.85-x}N_{2.10}$ might be hidden by the strong absorbance of Ta_3N_5 . However, $Y_2(Ta_{2-x}Y_x)O_{4.85-x}N_{2.10}$ is expected to be excitable by visible light irradiation.

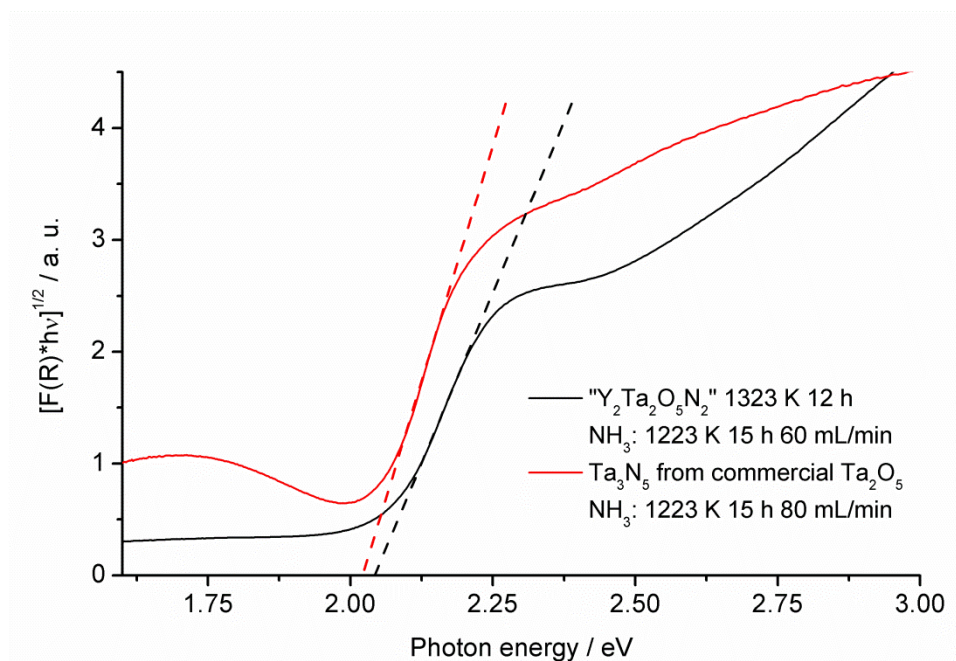


Figure 76: Tauc-plots (for indirect band gap transition) calculated from the UV-vis diffuse reflectance spectra of pyrochlore “ $Y_2Ta_2O_5N_2$ ” contaminated with Ta_3N_5 , and pure Ta_3N_5 obtained by ammonolysis of commercial Ta_2O_5 . The annealing temperatures and the conditions of the ammonia treatment are given in the legend.

The physicochemical data of band gap energies, average crystallite sizes and BET surface area are summarized in Table 15 and completed by activities achieved in photocatalytic hydrogen production. Interestingly, the process of ammonolysis reduces the average

crystallite size, as $Y_2(Ta_{2-x}Y_x)O_{4.85-x}N_{2.10}$ provides smaller crystallites than the starting material of $M'-YTaO_4$. However, besides the samples of Ta_3N_5 and $M'-YTaO_4$, the pyrochlore $Y_2(Ta_{2-x}Y_x)O_{4.85-x}N_{2.10}$ is almost inactive in photocatalytic hydrogen production as well. On the other hand, the low activity of the pyrochlore $Y_2(Ta_{2-x}Y_x)O_{4.85-x}N_{2.10}$ can be easily explained by yttrium stuffing, which reduces the activity considerably. The stuffing level in the oxynitride is much higher than in the stuffed samples of $Y_2(Ti_{2-x}Y_x)O_{7-0.5x}$ (cf. to chapter 4.1).

sample	band gap energy / eV	BET surface area / m ² /g	average crystallite size / nm	hydrogen production rate / μmol H ₂ /h
$M'-YTaO_4$	3.63	8.52	45.7	0.0
Ta_3N_5	2.05	-	40.2	1.0
$Y_2(Ta_{2-x}Y_x)O_{4.85-x}N_{2.10}$	-	-	18.1	0.6

Table 15: Summary of the band gap energies, the BET surface areas, the average crystallite sizes and the photocatalytic activities regarding hydrogen production of $M'-YTaO_4$, Ta_3N_5 and $Y_2(Ta_{2-x}Y_x)O_{4.85-x}N_{2.10}$.

5 Conclusion and outlook

Within this thesis it is shown that pyrochlore mixed oxides represent very effective and promising materials for photocatalysis even succeeding the challenging process of hydrogen production, if precisely and carefully tuned. In general, the pyrochlore structure of $A_2B_2O_6O'$ provides a tremendous capability of tolerating stoichiometry changes without undergoing a phase transition. The non-stoichiometry of A_2O_3 rich samples is compensated by cationic lattice distortion and interchange, if the difference in the effective ionic radii of the two involved cations (A and B) is comparably small. If this difference becomes larger, A_2O_3 rich compositions form a secondary phase and cationic interchange is no longer possible. For BO_2 rich compositions, the non-stoichiometry leads to vacancies in the A cation site and optionally in the O' anion site depending on the A cation species.

Increase of the TiO_2 excess leads to greatly improved photocatalytic activities for non-stoichiometric $Y_2Ti_2O_7$ as well as $Bi_2Ti_2O_7$, but the reasons for this improvement are completely different. In $Y_2Ti_2O_7$, the minimization of the cationic lattice distortion leading to $Y_{2-x}Ti_2O_{7-1.5x}$ was found to purify the TiO_6 octahedral network from yttrium cations increasing the photocatalytic activity. In $Bi_2Ti_2O_7$, The formation of a special vacancy structure leading to $(Bi_{2-x}Ti_{0.75x})Ti_2O_7$ is accompanied by the rearrangement of the oxygen sub-lattice, by which the TiO_6 octahedral geometry is optimized. The thereby improved charge carrier separation leads to a strong increase in photocatalytic activity.

The $Y_2Ti_2O_7$ material reported in literature to be the only pyrochlore compound being active in photocatalytic hydrogen production was chosen as the origin of investigations in this work. It is demonstrated for the first time that the photocatalytic activity of $Y_2Ti_2O_7$ is not only determined by the crystallite size and the presence of rutile, but mainly by a phenomena called cationic lattice distortion. These factors are controlled by the Ti/Y ratio and the annealing temperature. The degree of cationic lattice distortion in pyrochlore $Y_2Ti_2O_7$ with different Ti/Y ratios has been determined by the analysis of variations in the lattice parameter and in the I(400)/I(331) ratio. Lattice distortion is successfully minimized by increasing the Ti/Y ratio. The chemical composition changes from the “stuffed” pyrochlore $Y_2(Ti_{2-x}Y_x)O_{7-0.5x}$ via $(Y_{2-x}Ti_x)(Ti_{2-x}Y_x)O_7$ for the stoichiometric sample even possessing a marked degree of intrinsic cationic distortion, to a non-stoichiometric composition of $Y_{2-x}Ti_2O_{7-1.5x}$.

Probing $\text{Y}_2\text{Ti}_2\text{O}_7$ prepared with different Ti/Y ratios in the hydrogen producing photocatalytic test reaction provides clear evidence that reduced cationic lattice distortion leads to greatly increased photocatalytic activities. Especially at an annealing temperature of 1023 K, only the minimization of cationic distortion is responsible for an increase in photocatalytic activity from 9 $\mu\text{mol H}_2/\text{h}$ to 71 $\mu\text{mol H}_2/\text{h}$, while even a negative effect of slightly increasing crystallite sizes is overcompensated. A maximum photonic efficiency of 1.4 % is achieved. Hydrogen production rates remain constant over time, if platinum is used as co-catalyst. Applying rhodium as co-catalyst on a high band-gap material like $\text{Y}_2\text{Ti}_2\text{O}_7$ results in decreasing activities attributed to the oxidation of rhodium by photogenerated holes.

The yttrium titanate of $\text{Y}_{1.867}\text{Ti}_2\text{O}_{6.80}$ (Ti/Y ratio of 1.075) being the most active pure pyrochlore sample was doped by a variety of transition metal cations in order to achieve visible light activity. The cations of Cr^{3+} , Mn^{3+} and Fe^{3+} providing partially filled *d* orbitals were found to dope the titanium position and to be responsible for additional absorption in the visible. Even small doping levels of only 0.1 mol-% of Cr^{3+} results in an additional absorption up to 500 nm (2.5 eV). Unfortunately, even a small dopant level of only 0.25 mol-% led to a marked decrease in the high photocatalytic activity of $\text{Y}_{1.867}\text{Ti}_2\text{O}_{6.80}$ in hydrogen production for all applied dopant cations, while Cr^{3+} yielded the highest activity. The increase of the doping level lowered the photocatalytic activity even more. The attempt of doping with higher valent Ta^{5+} and W^{6+} cations led to pure pyrochlore structures of $\text{Y}_{1.867}\text{Ti}_{1.6}\text{Ta}_{0.4}\text{O}_7$ and $\text{Y}_{1.867}\text{Ti}_{1.8}\text{W}_{0.2}\text{O}_7$, by which the combined Y,O` vacancy structure in $\text{Y}_{1.867}\text{Ti}_2\text{O}_{6.80}$ is proven. However, this kind of titanium site doping also results in a marked decrease in photocatalytic activity. Although these results are quite disappointing at the first view, they corroborate greatly with the finding that yttrium self-doping of the TiO_6 octahedral network in the “stuffed” pyrochlore $\text{Y}_2(\text{Ti}_{2-x}\text{Y}_x)\text{O}_{7-0.5x}$ also reduces the photocatalytic activity significantly. Thus, a pure TiO_6 octahedral network is considered as a precondition for achieving maximum photocatalytic activity.

Considering the importance of a pure TiO_6 octahedral network, the yttrium site of the highly active yttrium titanate pyrochlore was partially doped by bismuth in order to achieve a shift of the absorption edge into the visible region of the solar spectrum without influencing the titanium site. Increasing the bismuth content in $\text{Y}_{2-x}\text{Ti}_2\text{O}_{7-1.5x}$ via

$(Y_{1.5}Bi_{0.5})_{1-x}Ti_2O_{7-3x}$ to $(YBi)_{1-x}Ti_2O_{7-3x}$ results in the reduction of the band gap energy from 3.7 eV via 3.3 eV to 3.1 eV and in the decrease of the temperature of crystallization from 1023 K to 873 K, respectively. The stability range of the $Y_{2-x}Ti_2O_{7-1.5x}$ pyrochlore structure for higher titanium excess is significantly extended by partial substitution of yttrium by larger bismuth ions, as bismuth ions are found to stabilize a high degree of vacancies on the A,O`-sites of yttrium bismuth titanate pyrochlores. Pure pyrochlores of $Y_{1.36}Bi_{0.45}Ti_2O_{6.73}$ and $(YBi)_{0.77}Ti_2O_{6.31}$ were obtained with corresponding titanium excesses of 10 % and 30 %, respectively. A stringent structural tune-up is indispensable to achieve good photocatalytic activities for bismuth containing yttrium titanate pyrochlores, which are almost inactive in photocatalytic hydrogen production, if prepared in stoichiometric composition. The annealing temperature should be chosen as low as possible, but providing a complete crystallization. The titanium excess should be adjusted as high as the formation of the rutile by-phase is still avoided. Maximum hydrogen production rates of 27.2 $\mu\text{mol H}_2/\text{h}$ and 17.5 $\mu\text{mol H}_2/\text{h}$ were achieved by $Y_{1.36}Bi_{0.45}Ti_2O_{6.73}$ and $(YBi)_{0.77}Ti_2O_{6.31}$ corresponding to photonic efficiencies of 0.55 % and 0.35 %, respectively. Nevertheless, bismuth doping decreases the photonic efficiency of structure optimized yttrium titanate (PE: 1.4 %) considerably, although the band gap energy is kindly reduced.

However, the reason for the strong improvement of the photocatalytic activity due to the increase of the titanium excess in the structure has still to be clarified. Although there is a lack of typical evidence for the pyrochlore de-stuffing mechanism proven for yttrium and lanthanide titanates, the titanium-yttrium lattice interchange might be masked. Moreover, large bismuth cations are expected to change or distort the TiO_6 octahedral geometry. The formation of Bi,O`-site vacancies due to a higher titanium excess has a reverse effect improving the charge carrier separation and thus, the photocatalytic activity.

The bismuth content in the structure clearly determines the stability during photocatalysis. Applied as co-catalyst on a wide band gap semi-conductor, rhodium being a less precious metal compared to platinum suffers from the disadvantage of photo-oxidation. As already seen for samples of $Y_{2-x}Ti_2O_{7-1.5x}$, the $(Y_{1.5}Bi_{0.5})_{1-x}Ti_2O_{7-3x}$ samples loaded with platinum provide steady activities as well. Increasing the bismuth content to $(YBi)_{1-x}Ti_2O_{7-3x}$ leads to decreasing activities over time even for the platinum loaded samples. This instability is attributed to the high bismuth content in the structure, but not to the co-catalyst. By increasing the co-catalyst loading on $(YBi)_{1-x}Ti_2O_{7-3x}$ samples the decrease in activity can be weakened, but cannot be entirely eliminated.

It was shown that the yttrium-free bismuth titanate pyrochlore $(\text{Bi}_{2-x}\text{Ti}_{0.75x})\text{Ti}_2\text{O}_7$ is a promising candidate for photocatalysis, if a stringent structural tune-up is performed. The very large effective ionic radius of bismuth makes it hard to achieve stoichiometric $\text{Bi}_2\text{Ti}_2\text{O}_7$, but enables the formation of a very high degree of Bi-vacancies in the lattice. A largely extended stability range of titanium rich stoichiometries is proven for non-stoichiometric $(\text{Bi}_{2-x}\text{Ti}_{0.75x})\text{Ti}_2\text{O}_7$ ranging at least up to a Ti/Bi ratio of 1.50, which corresponds to a chemical composition of $(\text{Bi}_{1.55}\text{Ti}_{0.33})\text{Ti}_2\text{O}_7$. This large stability range of pyrochlore bismuth titanate enabled us to analyze the cation distribution and the associated vacancy structure in the lattice systematically. It was found that the vacancy generation in the Bi-site is accompanied by the simultaneous transposition of titanium cations into the vacant lattice sites. The vacancy generation is limited to the Bi site, while the O` site is completely occupied by oxygen. However, the selective vacancy generation is supposed to be required for high photocatalytic activity reducing stress in the TiO_6 octahedral geometry in $(\text{Bi}_{2-x}\text{Ti}_{0.75x})\text{Ti}_2\text{O}_7$, which leads to an improved charge carrier mobility and thus, to a better charge separation. Therefore, the structure optimized sample of $(\text{Bi}_{2-x}\text{Ti}_{0.75x})\text{Ti}_2\text{O}_7$ Ti/Bi 1.50 provides a high photocatalytic activity in hydrogen production of $28.4 \mu\text{mol H}_2/\text{h}$, although “ $\text{Bi}_2\text{Ti}_2\text{O}_7$ ” is completely inactive, if prepared in a stoichiometric composition. Significant photocatalytic activities were only provided, if the $(\text{Bi}_{2-x}\text{Ti}_{0.75x})\text{Ti}_2\text{O}_7$ samples are annealed slightly above their temperature of crystallization at 773 K pointing out the importance of small crystallite sizes for the process of photocatalysis. The other prominent bismuth titanate phases of $\text{Bi}_4\text{Ti}_3\text{O}_{12}$ and $\text{Bi}_2\text{Ti}_4\text{O}_{11}$ were found to be less active compared to the stoichiometry optimized pyrochlore $(\text{Bi}_{1.55}\text{Ti}_{0.33})\text{Ti}_2\text{O}_7$. Due to the augmented vacancy generation at higher Ti/Bi ratios in $(\text{Bi}_{2-x}\text{Ti}_{0.75x})\text{Ti}_2\text{O}_7$, the oxygen ions undergo a slight change in their lattice position leading to an enlarged Ti-O distance and a reduced Ti-O-Ti angle. These structural changes in the TiO_6 octahedral geometry are considered responsible for the significant improve in photocatalytic activity.

As the A site in $(\text{Bi}_{2-x}\text{Ti}_{0.75x})\text{Ti}_2\text{O}_7$ is exclusively occupied by bismuth, all samples of bismuth titanate were found to be instable within the process of photocatalytic hydrogen production leading to decreasing activities with time. The most probable reason is the formation of bismuth suboxides. However, this major drawback can be compensated by coating the blank platinum co-catalyst particles with a Cr_2O_3 shell, which is supposed to inhibit the electron transfer from platinum particles to bismuth ions in the lattice.

The preparation of pyrochlore oxynitrides absorbing visible light irradiation was successful. By ammonolysis a phase transition from monoclinic M' - $YTaO_4$ into the cubic pyrochlore structure of “ $Y_2Ta_2O_5N_2$ ” was achieved. Unfortunately, the not avoidable by-phase formation of Ta_3N_5 leads to a pyrochlore being depleted in tantalum and thus, to a real composition of $Y_2(Ta_{2-x}Y_x)O_{4.85-x}N_{2.10}$. Herein, the TaO_6 octahedral network is contaminated by yttrium corresponding to the well-known mechanism of cationic lattice distortion, which decreases the photocatalytic activity significantly.

Although this work demonstrates that materials of the pyrochlore structure type can be tuned to highly active photocatalysts, the new insights in non-stoichiometric pyrochlores lead to prospective challenges in the future.

The maximum titanium excess in $(Bi_{2-x}Ti_{0.75x})Ti_2O_7$ is supposed to be higher than 50 %, because the structural composition was revised from $(Bi_{2-x}\square_x)Ti_2O_6O_{1-1.5x}\square_{1.5x}$ with a Ti excess limit of 50 % to $(Bi_{2-x}Ti_{0.75x}\square_{0.25x})Ti_2O_7$ being free of a theoretical limit. However, the movement of the oxygen in $(Bi_{2-x}Ti_{0.75x})Ti_2O_7$ with increasing Ti/Bi ratio, which is determined by X-ray diffraction, should be additionally corroborated by neutron diffraction.

Whereas the bismuth incorporation on the yttrium site of $Y_2Ti_2O_7$ yielded good results, the various doping of the titanium position led to poor activities. Thus, further attempts of doping the Ti position contaminating the TiO_6 octahedral network should not be considered.

The photocatalytic activities of the Ta^{5+} and W^{6+} doped samples ($Y_{1.867}Ti_{1.6}Ta_{0.4}O_7$ and $Y_{1.867}Ti_{1.8}W_{0.2}O_7$) were rather low, but are expected to be improvable. As a quite high annealing temperature optimum of 1173 K is observed and by-phase rutile is not formed up to an annealing temperature of at least 1323 K, the supposed optimum $(Ti+Ta+W)/Y$ ratio of 1.075 should be reinvestigated. The doping with tantalum or tungsten inhibits the rutile by-phase formation occurring in $Y_{1.867}Ti_2O_{6.80}$ at high temperatures. Thus, these doped pyrochlores should be prepared with a much higher titanium excess than the applied 7.5 mol-%. The presented results show impressively that a higher excess of titanium leads to a higher photocatalytic activity.

The compositional possibilities of $A^{3+}-B^{4+}$ pyrochlores were almost completely exhausted in this work, as the attempts of preparing other feasible pyrochlore structures like $Y_2Zr_2O_7$, $Bi_2Zr_2O_7$ and $In_2Ti_2O_7$ failed. For $Y_2Zr_2O_7$, a single phase was formed, but of defect fluorite, because the difference in the effective ionic radii of yttrium and

zirconium is not large enough to stabilize a pyrochlore phase. Usually, only the pyrochlores of A^+-B^{6+} and $A^{2+}-B^{5+}$ are taken into consideration as other possible compositions. However, new information regarding the tremendous capability of compensating a high titanium excess of at least 50 % in $Bi_2Ti_2O_7$ by the formation of vacancies in the A site leads to the possibility of realizing visible light active $A^{3+}-B^{5+}$ pyrochlores by applying special B/A ratios. Naturally, stoichiometric compositions of these elements do not form a pyrochlore structure. Indeed, a pure pyrochlore structure of $Bi_{1.33}Ta_2O_7$ was successfully prepared, which has not been reported in literature so far. Although this sample was found to be almost inactive in photocatalytic hydrogen production, it may show better results in other fields of application. Another interesting composition of $Bi_{1.33}Nb_2O_7$ is supposed as well.

Although the prepared oxynitride of $Y_2(Ta_{2-x}Y_x)O_{4.85-x}N_{2.10}$ was almost inactive in photocatalytic hydrogen production, a high potential is assigned to this structure. It is supposed that preparing this sample with a significant excess of tantalum will lead to a TaO_6 octahedral network free of yttrium.

In this thesis, the process of co-catalyst deposition was not the main topic. It is expected that optimization of the process variables or the utilization of a chemical deposition method like the $NaBH_4$ reduction will lead to a better distribution of co-catalyst nanoparticles on the surface of the catalyst, which may improve the activity at all.

6 References

- [1] J. M. Monro, *Nature* **1993**, *363*, 215-216.
- [2] M. Hoel, S. Kverndokk, *Resour. Energy Econ.* **1996**, *18*, 115-136.
- [3] A. Hepbasli, *Renew. Sust. Energy Rev.* **2008**, *12*, 593-661.
- [4] K. T. Fung, R. L. Scheffler, J. Stolpe, *IEEE T. Power Ap. Syst.* **1981**, *100*, 1176-1182.
- [5] E. Barbier, *Renew. Sust. Energy Rev.* **2002**, *6*, 3-65.
- [6] A. J. Nozik, *Annu. Rev. Phys. Chem.* **1978**, *29*, 189-222.
- [7] R. B. Bergmann, *Appl. Phys. A-Mater.* **1999**, *69*, 187-194.
- [8] M. R. Hoffmann, S. T. Martin, W. Choi, D. W. Bahnemann, *Chem. Rev.* **1995**, *95*, 69-96.
- [9] J. H. Zhao, A. H. Wang, M. A. Green, F. Ferrazza, *Appl. Phys. Lett.* **1998**, *73*, 1991-1993.
- [10] T. Maggos, A. Plassais, J. G. Bartzis, Ch. Vasilakos, N. Moussiopoulos, L. Bonafous, *Environ. Monit. Assess.* **2008**, *136*, 35-44.
- [11] Z. C. Shan, W. D. Wang, X. P. Lin, H. M. Ding, F. Q. Huang, *J. Solid State Chem.* **2008**, *181*, 1361-1366.
- [12] Q. Wang, C. C. Chen, D. Zhao, W. H. Ma, J. C. Zhao, *Langmuir* **2008**, *24*, 7338-7345.
- [13] D. W. Bahnemann, *Sol. Energy* **2004**, *77*, 445-459.
- [14] J. M. Herrmann, *Catal. Today* **1999**, *53*, 115-129.
- [15] M. Ni, M. K. H. Leung, D. Y. C. Leung, K. Sumathy, *Renew. Sust. Energy Rev.* **2007**, *11*, 401-425.
- [16] A. J. Bard, M. A. Fox, *Accounts Chem. Res.* **1995**, *28*, 141-145.
- [17] A. Currao, *Chimia* **2007**, *61*, 815-819.
- [18] J. R. Bolton, *Sol. Energy* **1996**, *57*, 37-50.
- [19] R. D. Cortright, R. R. Davda, J. A. Dumesic, *Nature* **2002**, *418*, 964-967.
- [20] M. Woodhouse, B. A. Parkinson, *Chem. Soc. Rev.* **2009**, *38*, 197-210.
- [21] R. I. Bickley, F. S. Stone, *J. Catal.* **1973**, *31*, 389-397.
- [22] R. Abe, M. Higashi, K. Sayama, Y. Abe, H. Sugihara, *J. Phys. Chem. B* **2006**, *110*, 2219-2226.
- [23] Z. G. Zou, H. Arakawa, *J. Photochem. Photobiol. A-Chem.* **2003**, *158*, 145-162.
- [24] N. Mizutani, Y. Tajima, M. Kato, *J. Am. Ceram. Soc.* **1976**, *59*, 168-168.

- [25] O. Knop, F. Brisse, L. Castelliz, *Can. J. Chemistry* **1969**, *47*, 971-990.
- [26] S. Kunej, D. Suvorov, *J. Am. Ceram. Soc.* **2008**, *91*, 3472-3475.
- [27] S. Y. Wu, W. J. Takei, M. H. Francombe, *Ferroelectrics* **1976**, *10*, 209-213.
- [28] V. Kahlenberg, H. Bohm, *Acta Crystallogr. B-Stru.* **1995**, *51*, 11-18.
- [29] J. R. Esquivel-Elizondo, B. B. Hinojosa, J. C. Nino, *Chem. Mater.* **2011**, *23*, 4965-4974.
- [30] S. P. Yordanov, C. P. Carapanov, I. S. Ivanov, P. T. Cholakov, *Ferroelectrics* **1998**, *209*, 541-552.
- [31] T. Zaremba, *J. Therm. Anal. Calorim.* **2008**, *93*, 829-832.
- [32] W. F. Yao, X. H. Xu, H. Wang, J. T. Zhou, X. N. Yang, Y. Zhang, S. X. Shang, B. B. Huang, *Appl. Cat. B-Environ.* **2004**, *52*, 109-116.
- [33] X. H. Xu, W. F. Yao, Y. Zhang, A. Q. Zhou, Y. Hou, M. Wang, *Acta Chim. Sinica* **2005**, *63*, 5-10.
- [34] T. Kidchob, L. Malfatti, D. Marongiu, S. Enzo, P. Innocenzi, *J. Am. Ceram. Soc.* **2010**, *93*, 2897-2902.
- [35] A. Kudo, S. Hijii, *Chem. Lett.* **1999**, *28*, 1103-1104.
- [36] S. Murugesan, M. N. Huda, Y. F. Yan, M. M. Al-Jassim, V. Subramanian, *J. Phys. Chem. C* **2010**, *114*, 10598-10605.
- [37] E. A. Boettner, L. J. Miedler, *Appl. Optics* **1963**, *2*, 105-108.
- [38] A. Galinska, J. Walendziewski, *Energy Fuels* **2005**, *19*, 1143-1147.
- [39] U. Müller, *Anorganische Strukturchemie*, 4. Auflage, Teubner, **2004**.
- [40] T. X. Wu, G. M. Liu, J. C. Zhao, H. Hidaka, N. Serpone, *J. Phys. Chem. B* **1998**, *102*, 5845-5851.
- [41] K. Iwata, T. Takaya, H. Hamaguchi, A. Yamakata, T. A. Ishibashi, H. Onishi, H. Kuroda, *J. Phys. Chem. B* **2004**, *108*, 20233-20239.
- [42] D. P. Colombo, R. M. Bowman, *J. Phys. Chem.* **1996**, *100*, 18445-18449.
- [43] G. F. Novikov, N. A. Radychev, *Russian Chem. Bul.* **2007**, *56*, 890-894.
- [44] N. L. Sermakasheva, G. F. Novikov, Y. M. Shul'ga, V. N. Semenov, *Semiconductors* **2004**, *38*, 380-386.
- [45] Y. Tamaki, K. Hara, R. Katoh, M. Tachiya, A. Furube, *J. Phys. Chem. C* **2009**, *113*, 11741-11746.
- [46] N. Serpone, D. Lawless, R. Khairutdinov, E. Pelizzetti, *J. Phys. Chem.* **1995**, *99*, 16655-16661.
- [47] A. Kubacka, M. Fernandez-Garcia, G. Colon, *Chem. Rev.* **2012**, *112*, 1555-1614.

- [48] V. I. Klimov, *J. Phys. Chem. B* **2000**, *104*, 6112-6123.
- [49] G. Morello, M. De Giorgi, S. Kudera, L. Manna, R. Cingolani, M. Anni, *J. Phys. Chem. C* **2007**, *111*, 5846-5849.
- [50] J. W. Tang, J. R. Durrant, D. R. Klug, *J. Am. Chem. Soc.* **2008**, *130*, 13885-13891.
- [51] K. Domen, A. Kudo, T. Onishi, N. Kosugi, H. Kuroda, *J. Phys. Chem.* **1986**, *90*, 292-295.
- [52] S. G. Bratsch, *J. Phys. Chem. Ref. Data* **1989**, *18*, 1-21.
- [53] K. Sayama, A. Tanaka, K. Domen, K. Maruya, T. Onishi, *Catal. Lett.* **1990**, *4*, 217-222.
- [54] K. Sayama, A. Tanaka, K. Domen, K. Maruya, T. Onishi, *J. Phys. Chem.* **1991**, *95*, 1345-1348.
- [55] K. Shimizu, S. Itoh, T. Hatamachi, T. Kodama, M. Sato, K. Toda, *Chem. Mater.* **2005**, *17*, 5161-5166.
- [56] A. Kudo, H. Kato, *Chem. Phys. Lett.* **2000**, *331*, 373-377.
- [57] H. Kato, K. Asakura, A. Kudo, *J. Am. Chem. Soc.* **2003**, *125*, 3082-3089.
- [58] M. A. Subramanian, G. Aravamudan, G. V. Subba Rao, *Prog. Solid State Chem.* **1983**, *15*, 55-143.
- [59] H. Nyman, S. Andersson, B. G. Hyde, M. Okeeffe, *J. Solid State Chem.* **1978**, *26*, 123-131.
- [60] P. F. Bongers, E. R. van Meurs, *J. Appl. Phys.* **1967**, *38*, 944-945.
- [61] R. Mazelsky, R. Ward, *J. Inorg. Nucl. Chem.* **1961**, *20*, 39-44.
- [62] D. J. Kim, *J. Am. Ceram. Soc.* **1989**, *72*, 1415-1421.
- [63] M. Ando, I. Oikawa, Y. Noda, S. Ohki, M. Tansho, T. Shimizu, H. Kiyono, H. Maekawa, *Solid State Ion.* **2011**, *192*, 576-579.
- [64] M. Glerup, O. F. Nielsen, F. W. Poulsen, *J. Solid State Chem.* **2001**, *160*, 25-32.
- [65] C. A. Gueymard, D. Myers, K. Emery, *Sol. Energy* **2002**, *73*, 443-467.
- [66] H. Kato, A. Kudo, *Catal. Lett.* **1999**, *58*, 153-155.
- [67] S. D. Mo, W. Y. Ching, *Phys. Rev. B* **1995**, *51*, 13023-13032.
- [68] A. J. Frank, K. Honda, *J. Phys. Chem.* **1982**, *86*, 1933-1935.
- [69] A. Kudo, H. Kato, S. Nakagawa, *J. Phys. Chem. B* **2000**, *104*, 571-575.
- [70] K. Domen, S. Naito, M. Soma, T. Onishi, K. Tamaru, *J. Chem. Soc. Chem. Comm.* **1980**, *12*, 543-544.
- [71] K. Domen, S. Naito, T. Onishi, K. Tamaru, *Chem. Phys. Lett.* **1982**, *92*, 433-434.

- [72] C. C. Hu, H. Teng, *Appl. Cat. A-Gen.* **2007**, *331*, 44-50.
- [73] C. C. Hu, C. C. Tsai, H. Teng, *J. Am. Ceram. Soc.* **2009**, *92*, 460-466.
- [74] H. Kato, H. Kobayashi, A. Kudo, *J. Phys. Chem. B* **2002**, *106*, 12441-12447.
- [75] A. Fujishima, K. Honda, *Nature* **1972**, *238*, 37.
- [76] T. A. Kandiel, A. Feldhoff, L. Robben, R. Dillert, D. W. Bahnemann, *Chem. Mater.* **2010**, *22*, 2050-2060.
- [77] D. Reyes-Coronado, G. Rodriguez-Gattorno, M. E. Espinosa-Pesqueira, C. Cab, R. de Coss, G. Oskam, *Nanotechnology* **2008**, *19*, 145605.
- [78] X. K. Li, T. Kako, J. H. Ye, *Appl. Cat. A-Gen.* **2007**, *326*, 1-7.
- [79] D. E. Scaife, *Sol. Energy* **1980**, *25*, 41-54.
- [80] A. Kudo, Y. Miseki, *Chem. Soc. Rev.* **2009**, *38*, 253-278.
- [81] M. A. Malik, N. Revaprasadu, P. O'Brien, *Chem. Mater.* **2001**, *13*, 913-920.
- [82] L. S. Zhang, W. Z. Wang, J. O. Yang, Z. G. Chen, W. Q. Zhang, L. Zhou, S. W. Liu, *Appl. Cat. A-Gen.* **2006**, *308*, 105-110.
- [83] H. G. Kim, D. W. Hwang, J. S. Lee, *J. Am. Chem. Soc.* **2004**, *126*, 8912-8913.
- [84] X. Li, J. H. Ye, *J. Phys. Chem. C* **2007**, *111*, 13109-13116.
- [85] A. Kudo, K. Omori, H. Kato, *J. Am. Chem. Soc.* **1999**, *121*, 11459-11467.
- [86] S. Cabuk, S. Simsek, *Cent. Eur. J. Phys.* **2008**, *6*, 730-736.
- [87] I. Tsuji, H. Kato, A. Kudo, *Angew. Chem. Int. Edit.* **2005**, *44*, 3565-3568.
- [88] Z. Zhao, Q. Liu, *J. Phys. D: Appl. Phys.* **2008**, *41*, 1-10.
- [89] F. Tian, C. Liu, *J. Phys. Chem. B* **2006**, *110*, 17866-17871.
- [90] K. Mizushima, M. Tanaka, A. Asai, S. Iida, J. B. Goodenough, *J. Phys. Chem. Solids* **1979**, *40*, 1129-1140.
- [91] W. Y. Choi, A. Termin, M. R. Hoffmann, *J. Phys. Chem.* **1994**, *98*, 13669-13679.
- [92] H. Y. Lin, Y. F. Chen, Y. W. Chen, *Int. J. Hydrogen Energy* **2007**, *32*, 86-92.
- [93] K. Maeda, K. Teramura, D. Lu, N. Saito, Y. Inoue, K. Domen, *Angew. Chem. Int. Edit.* **2006**, *45*, 7806-7809.
- [94] K. Maeda, K. Teramura, D. L. Lu, T. Takata, N. Saito, Y. Inoue, K. Domen, *Nature* **2006**, *440*, 295.
- [95] M. Yoshida, K. Takanabe, K. Maeda, A. Ishikawa, J. Kubota, Y. Sakata, Y. Ikezawa, K. Domen, *J. Phys. Chem. C* **2009**, *113*, 10151-10157.
- [96] M. R. Dhananjeyan, R. Annapoorani, S. Lakshmi, R. Renganathan, *J. Photochem. Photobiol. A-Chem.* **1996**, *96*, 187-191.
- [97] L. C. Chen, T. C. Chou, *Ind. Eng. Chem. Res.* **1993**, *32*, 1520-1527.

- [98] R. P. S. Suri, J. Liu, D. W. Hand, J. C. Crittenden, D. L. Perram, M. E. Mullins, *Water Environ. Res.* **1993**, *65*, 665-673.
- [99] M. Abdullah, G. K. C. Low, R. W. Matthews, *J. Phys. Chem.* **1990**, *94*, 6820-6825.
- [100] T. Y. Wei, C. C. Wan, *Ind. Eng. Chem. Res.* **1991**, *30*, 1293-1300.
- [101] N. Serpone, *J. Photochem. Photobiol. A-Chem.* **1997**, *104*, 1-12.
- [102] T. Torimoto, N. Nakamura, S. Ikeda, B. Ohtani, *Phys. Chem. Chem. Phys.* **2002**, *4*, 5910-5914.
- [103] C. G. Hatchard, C. A. Parker, *Proc. R. Soc. London Ser. A* **1956**, *235*, 518-536.
- [104] C. Y. Wang, R. Pagel, D. W. Bahnemann, J. K. Dohrmann, *J. Phys. Chem. B* **2004**, *108*, 14082-14092.
- [105] T. A. Kandiel, R. Dillert, D. W. Bahnemann, *Photochem. Photobiol. Sci.* **2009**, *8*, 683-690.
- [106] Y. Maeda, A. Fujishima, K. Honda, *J. Electrochem. Soc.* **1981**, *128*, 1731-1734.
- [107] T. L. Villarreal, R. Gomez, M. Neumann-Spallart, N. Alonso-Vante, P. Salvador, *J. Phys. Chem. B* **2004**, *108*, 15172-15181.
- [108] K. Kaneko, *J. Membrane Sci.* **1994**, *96*, 59-89.
- [109] K. S. W. Sing, D. H. Everett, R. A. W. Haul, L. Moscou, R. A. Pierotti, J. Rouquerol, T. Siemieniowska, *Pure Appl. Chem.* **1985**, *57*, 603-619.
- [110] S. Brunauer, P. H. Emmett, E. Teller, *J. Am. Chem. Soc.* **1938**, *60*, 309-319.
- [111] K. S. W. Sing, *Particle Size Analysis* **1992**, *102*, 13-32.
- [112] J. Tauc, Grigorov, R. A. Vancu, *Phys. Stat. Sol.* **1966**, *15*, 627-637.
- [113] L. Bi, J. Y. Feng, *J. Lumin.* **2006**, *121*, 95-101.
- [114] M. K. Jayaraj, A. Antony, M. Ramachandran, *Bull. Mater. Sci.* **2002**, *25*, 227-230.
- [115] A. Beer, *Ann. Phys. Chem.* **1852**, *86*, 78-88.
- [116] E. Plisko, *Spectrochim. Acta B* **1968**, *B23*, 455-464.
- [117] P. W. Atkins, *Physikalische Chemie*, 3. Auflage, Wiley-VCH, **2001**.
- [118] D. T. Cromer, J. B. Mann, *Acta Crystallogr. A* **1968**, *A24*, 321-324.
- [119] J. I. Langford, A. J. C. Wilson, *J. Appl. Cryst.* **1978**, *11*, 102-113.
- [120] Z. P. Shao, W. S. Yang, Y. Cong, H. Dong, J. H. Tong, G. X. Xiong, *J. Membrane Sci.* **2000**, *172*, 177-188.
- [121] G. C. Lau, B. D. Muegge, T. M. McQueen, E. L. Duncan, R. J. Cava, *J. Solid State Chem.* **2006**, *179*, 3126-3135.

- [122] A. V. Shlyakhtina, J. C. C. Abrantes, A. V. Levchenko, A. V. Knot'ko, O. K. Karyagina, L. G. Shcherbakova, *Solid State Ion.* **2006**, *177*, 1149-1155.
- [123] Y. H. Li, Y. Q. Wang, M. Zhou, C. P. Xu, J. A. Valdez, K. E. Sickafus, *Nucl. Instrum. Meth. B* **2011**, *269*, 2001-2005.
- [124] C. R. Stanek, L. Minervini, R. W. Grimes, *J. Am. Ceram. Soc.* **2002**, *85*, 2792-2798.
- [125] A. F. Fuentes, K. Boulallya, M. Maczka, J. Hanuza, U. Amador, *Solid State Sci.* **2005**, *7*, 343-353.
- [126] L. Minervini, R. W. Grimes, K. E. Sickafus, *J. Am. Ceram. Soc.* **2000**, *83*, 1873-1878.
- [127] L. G. J. Dehaart, A. J. Devries, G. Blasse, *J. Solid State Chem.* **1985**, *59*, 291-300.
- [128] A. Sobczynski, A. J. Bard, A. Campion, M. A. Fox, T. Mallouk, S. E. Webber, J. M. White, *J. Phys. Chem.* **1987**, *91*, 3316-3320.
- [129] M. V. Rao, K. Rajeshwar, V. R. Pai Verneker, J. DuBow, *J. Phys. Chem.* **1980**, *84*, 1987-1991.
- [130] M. Higashi, R. Abe, K. Sayama, H. Sugihara, Y. Abe, *Chem. Lett.* **2005**, *34*, 1122-1123.
- [131] J. Sato, H. Kobayashi, Y. Inoue, *J. Phys. Chem. B* **2003**, *107*, 7970-7975.
- [132] J. Sato, N. Saito, H. Nishiyama, Y. Inoue, *J. Photochem. Photobiol. A-Chem.* **2002**, *148*, 85-89.
- [133] D. Atencio, M. B. Andrade, A. G. Christy, R. Giere, P. M. Kartashov, *Can. Mineral.* **2010**, *48*, 673-698.
- [134] O. Merka, V. Yarovy, D. W. Bahnemann, M. Wark, *J. Phys. Chem. C* **2011**, *115*, 8014-8023.
- [135] F. Beech, W. M. Jordan, C. R. A. Catlow, A. Santoro, B. C. H. Steele, *J. Solid State Chem.* **1988**, *77*, 322-335.
- [136] J. Zhou, Z. Zou, A. K. Ray, X. S. Zhao, *Ind. Eng. Chem. Res.* **2007**, *46*, 745-749.
- [137] L. Vegard, *Z. Phys. A* **1921**, *5*, 17-26.
- [138] A. R. Denton, N. W. Ashcroft, *Phys. Rev. A* **1991**, *43*, 3161-3164.
- [139] A. Garbout, A. Rubbens, R. N. Vannier, S. Bouattourl, A. W. Kolsil, *J. Raman Spectrosc.* **2008**, *39*, 1469-1474.
- [140] C. H. Hervoches, P. Lightfoot, *Chem. Mater.* **1999**, *11*, 3359-3364.
- [141] R. D. Shannon, *Acta Crystallogr. A.* **1976**, *32*, 751-767.
- [142] A. L. Hector, S. B. Wiggin, *J. Solid State Chem.* **2004**, *177*, 139-145.

- [143] I. Radosavljevic, J. S. O. Evans, A. W. Sleight, *J. Solid State Chem.* **1998**, *136*, 63-66.
- [144] H. Zhang, M. Lue, S. Liu, X. Song, Y. Zhou, Z. Xiu, Z. Qiu, A. Zhang, Q. Ma, *Thin Solid Films* **2008**, *517*, 764-768.
- [145] T. Goto, Y. Noguchi, M. Soga, M. Miyayama, *Mater. Res. Bull.* **2005**, *40*, 1044-1051.
- [146] A. M. Srivastava, *J. Lumin.* **2009**, *129*, 1000-1002.
- [147] E. Wilhelm, R. Battino, R. J. Wilcock, *Chem. Rev.* **1977**, *77*, 219-262.
- [148] K. Maeda, K. Teramura, D. Lu, N. Saito, Y. Inoue, K. Domen, *J. Phys. Chem. C* **2007**, *111*, 7554-7560.
- [149] E. Riedel, *Anorganische Chemie*, 5. Auflage, deGruyter, **2002**.
- [150] F. X. Zhang, B. Manoun, S. K. Saxena, *Mat. Let.* **2006**, *60*, 2773-2776.
- [151] H. Gerischer, *J. Electroanal. Chem.* **1975**, *58*, 263-274.
- [152] E. Hulthen, S. Nakamura, *Nature* **1927**, *119*, 235-236.
- [153] A. B. F. Duncan, D. A. Wilson, *J. Am. Chem. Soc.* **1932**, *54*, 401-402.
- [154] D. M. Hoffman, *Polyhedron* **1994**, *13*, 1169-1179.
- [155] P. Maillard, F. Tessier, E. Orhan, F. Chevire, R. Marchand, *Chem. Mater.* **2005**, *17*, 152-156.
- [156] S. A. Mather, P. K. Davies, *J. Am. Ceram. Soc.* **1995**, *78*, 2737-2745.
- [157] G. M. Wolten, *Acta Crystallogr.* **1967**, *23*, 939-944.
- [158] N. Terao, *C. R. Acad. Sci. B* **1977**, *285*, 17-20.
- [159] M. Hara, G. Hitoki, T. Takata, J. N. Kondo, H. Kobayashi, K. Domen, *Catal. Today* **2003**, *78*, 555-560.
- [160] Q. H. Zhang, L. Gao, *Langmuir* **2004**, *20*, 9821-9827.

7 Appendix

7.1 Additional information

7.1.1 Additional Figures

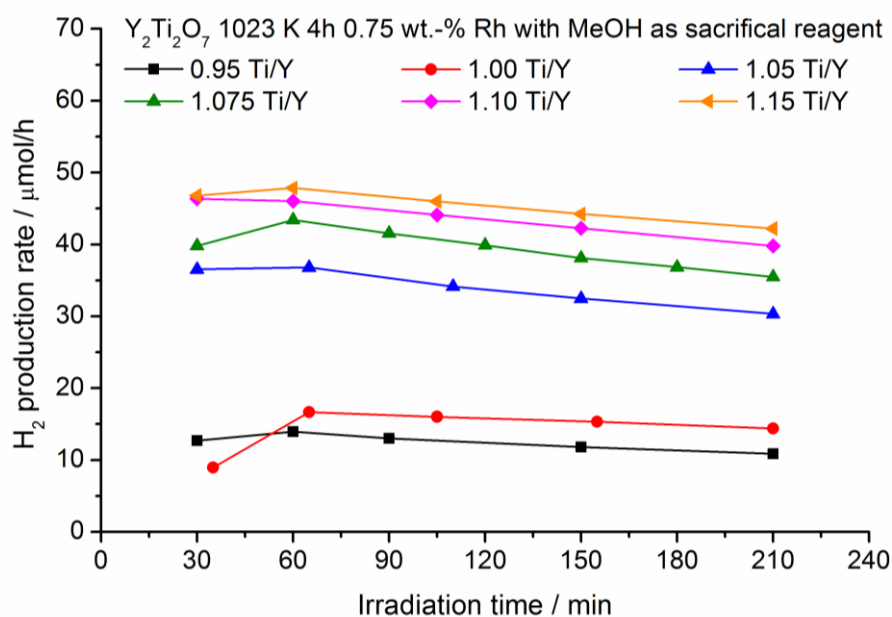


Figure A1: Photocatalytic activity regarding hydrogen production over Y₂Ti₂O₇ calcined at 1023 K for 4h with 0.75 wt.-% rhodium as co-catalyst in the presence of 10 vol.-% methanol as sacrificial reagent.

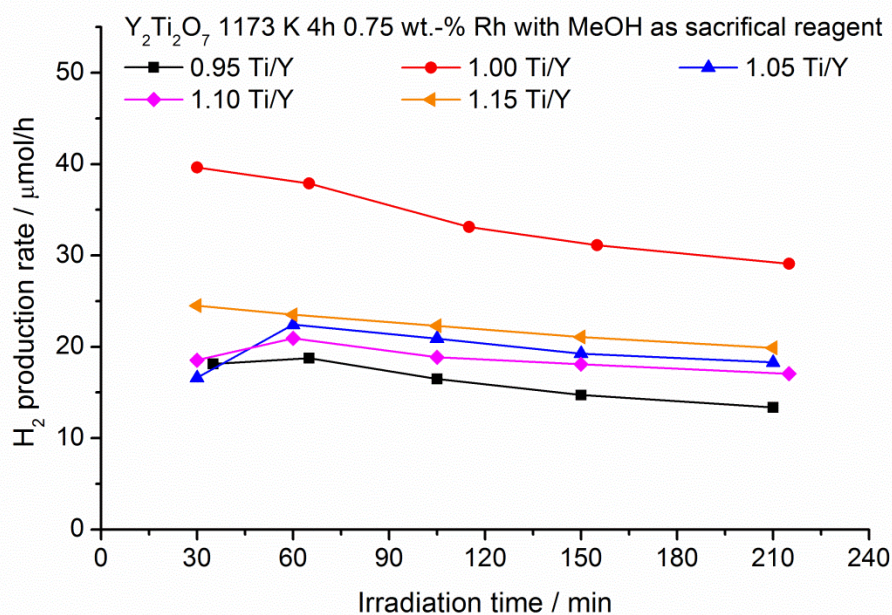


Figure A2: Photocatalytic activity regarding hydrogen production over Y₂Ti₂O₇ calcined at 1173 K for 4h with 0.75 wt.-% rhodium as co-catalyst in the presence of 10 vol.-% methanol as sacrificial reagent.

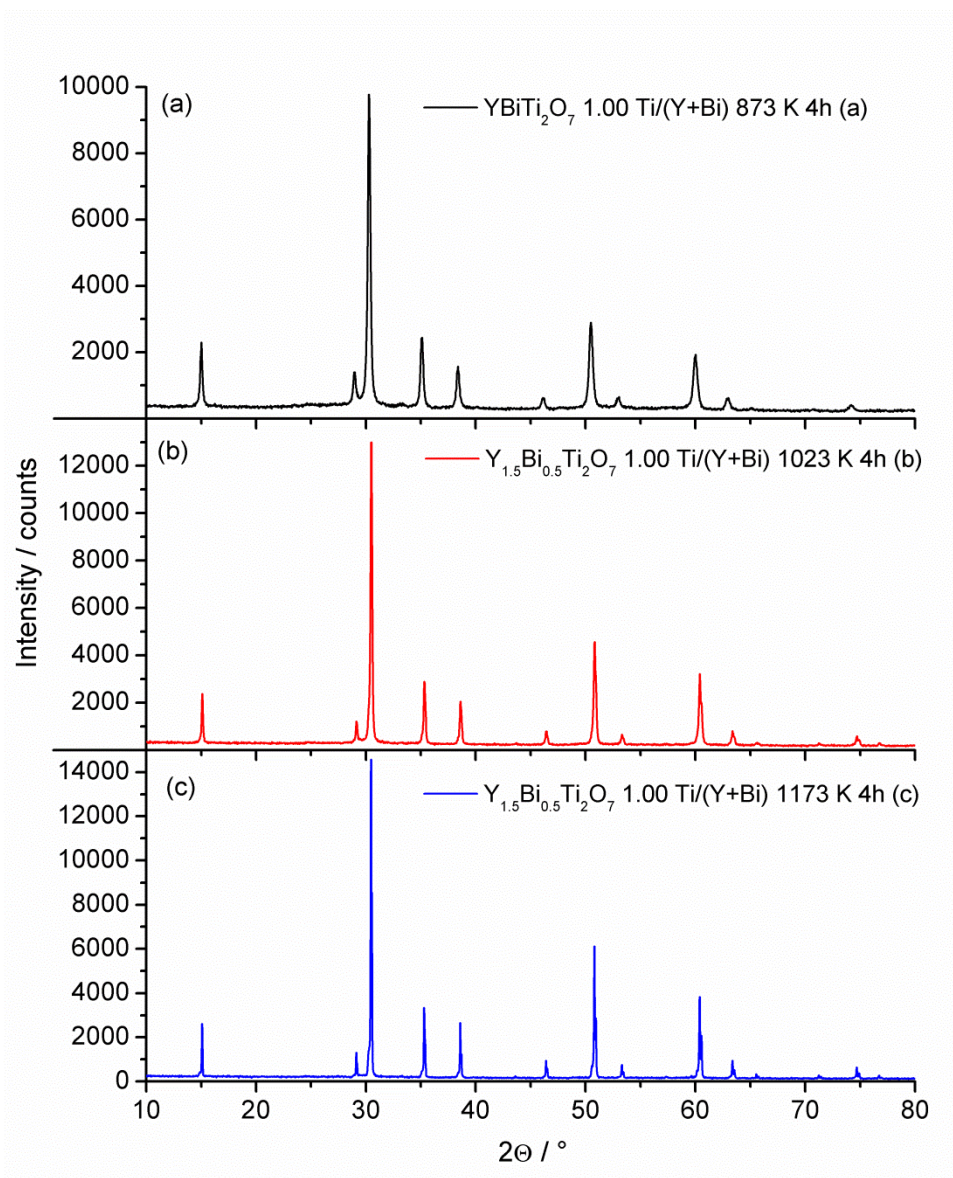


Figure A3: X-ray diffraction data of YBiTi_2O_7 annealed at 873 K for 4h (part A) and $\text{Y}_{1.5}\text{Bi}_{0.5}\text{Ti}_2\text{O}_7$ annealed at 1023 K for 4h (part B) and 1173 K for 4h (part C).

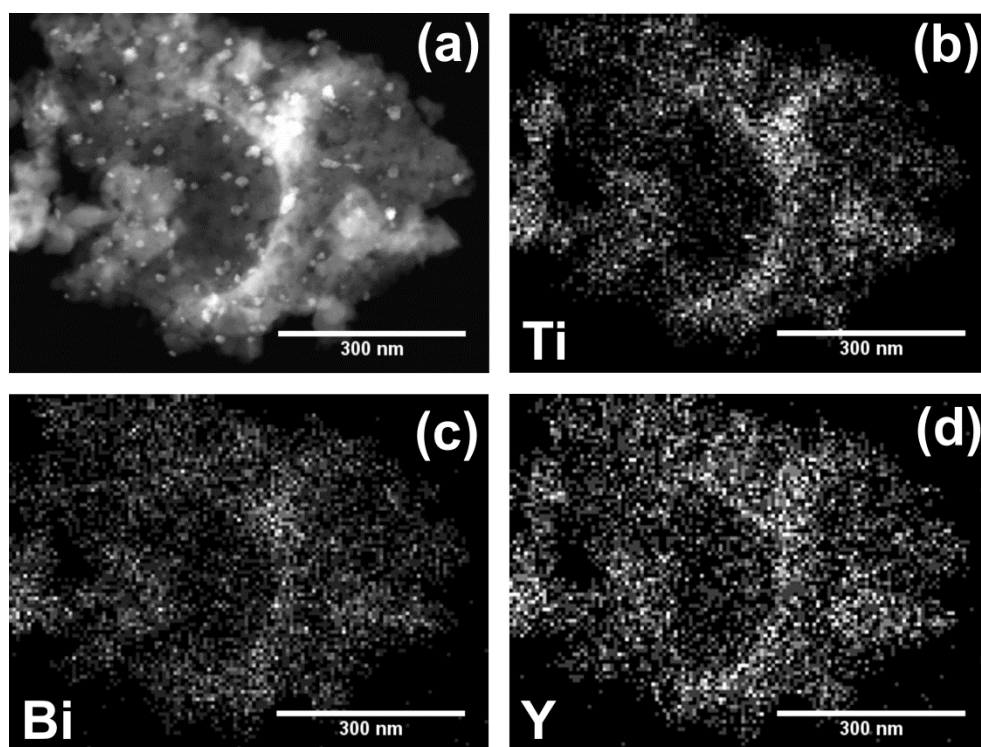


Figure A4: TEM micrograph in dark field mode (a) and EDXS analysis of $(\text{YBi})_{0.77}\text{Ti}_2\text{O}_{6.31}$ $\text{Ti}/(\text{Y+Bi})$ 1.30 annealed at 873 K for 4h and loaded with 3.0 wt.-% of platinum. The mappings of titanium, bismuth and yttrium are shown in parts (b), (c) and (d), respectively.

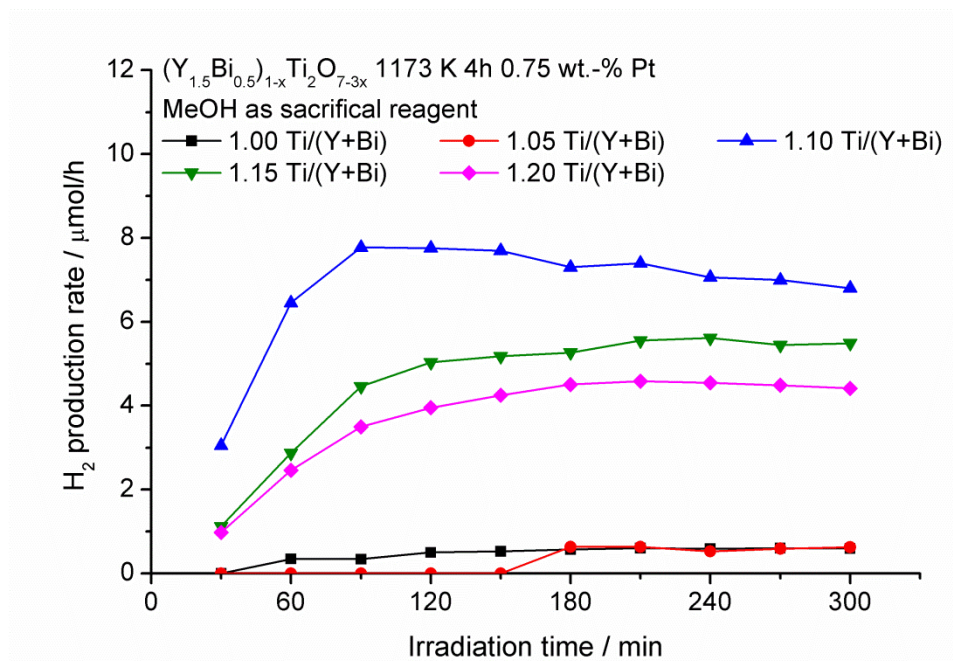


Figure A5: Photocatalytic activity regarding hydrogen production over $(\text{Y}_{1.5}\text{Bi}_{0.5})_{1-x}\text{Ti}_2\text{O}_{7-3x}$ calcined at 1173 K for 4h with 0.75 wt.-% platinum as co-catalysts in the presence of 10 vol.-% methanol as sacrificial reagent.

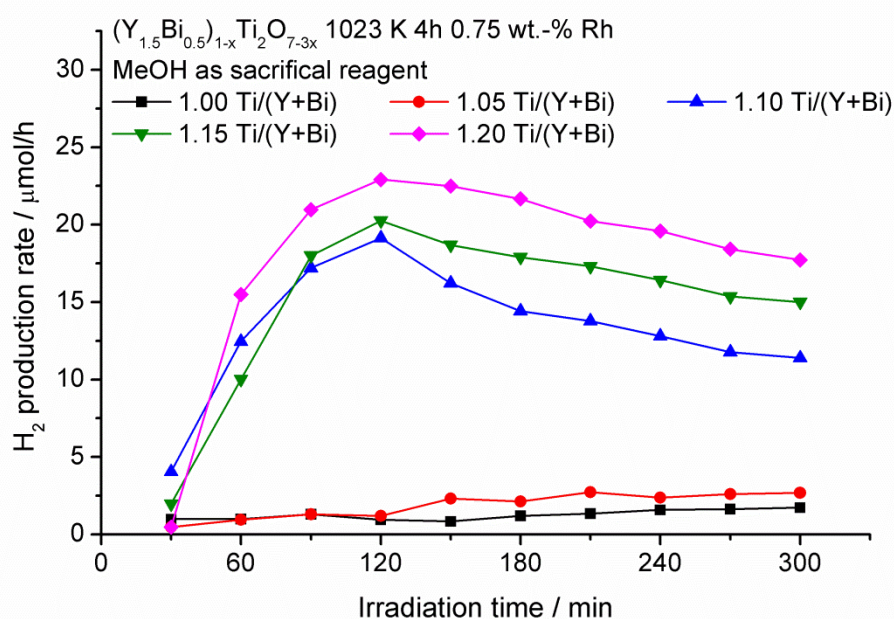


Figure A6: Photocatalytic activity regarding hydrogen production over $(Y_{1.5}Bi_{0.5})_{1-x}Ti_2O_{7-3x}$ calcined at 1023 K for 4h with 0.75 wt.-% rhodium as co-catalyst in the presence of 10 vol.-% methanol as sacrificial reagent.

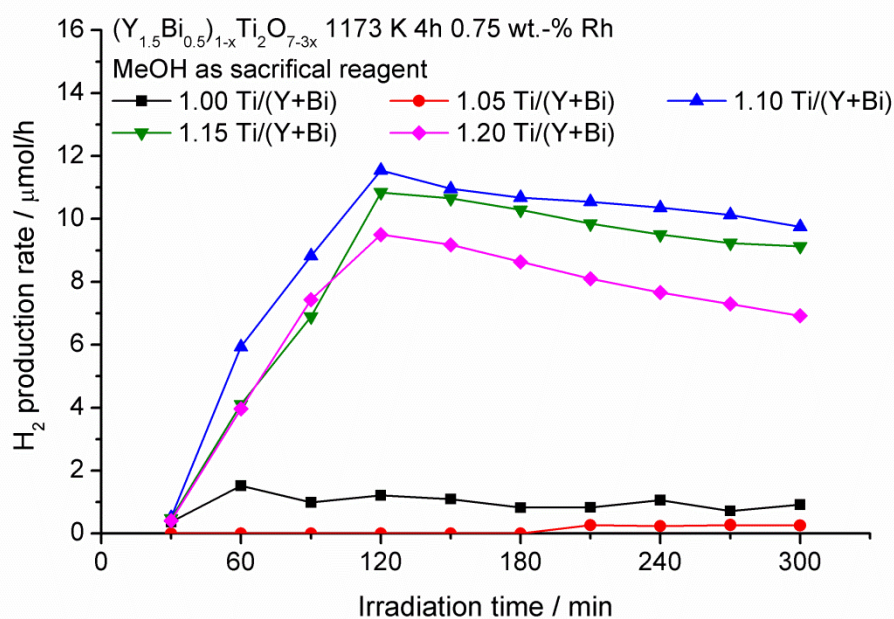


Figure A7: Photocatalytic activity regarding hydrogen production over $(Y_{1.5}Bi_{0.5})_{1-x}Ti_2O_{7-3x}$ calcined at 1173 K for 4h with 0.75 wt.-% rhodium as co-catalyst in the presence of 10 vol.-% methanol as sacrificial reagent.

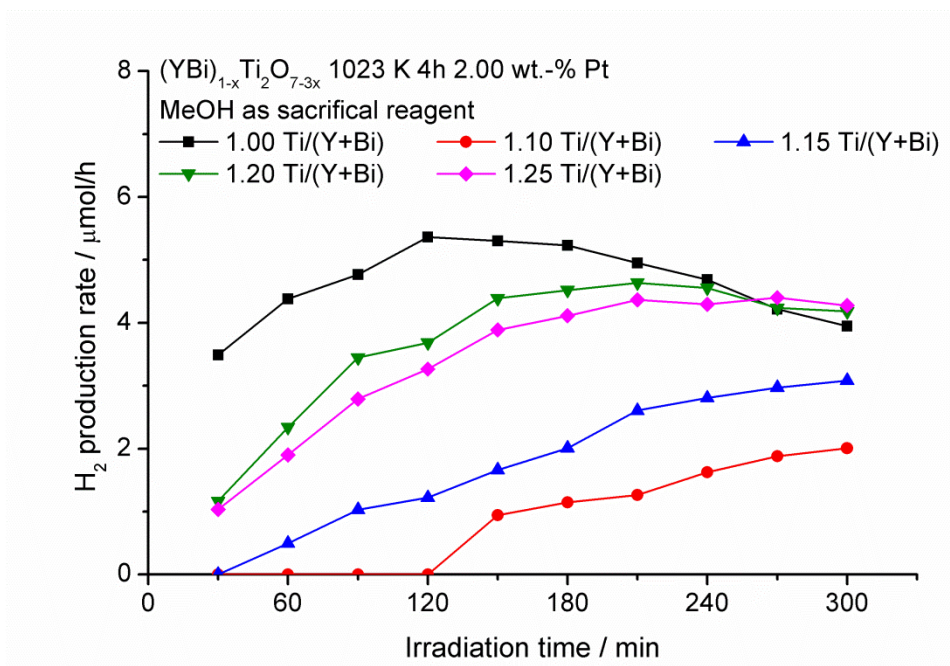


Figure A8: Photocatalytic activity regarding hydrogen production over $(YBi)_{1-x}Ti_2O_{7-3x}$ calcined at 1023 K for 4h with 2.00 wt.-% platinum as co-catalyst in the presence of 10 vol.-% methanol as sacrificial reagent.

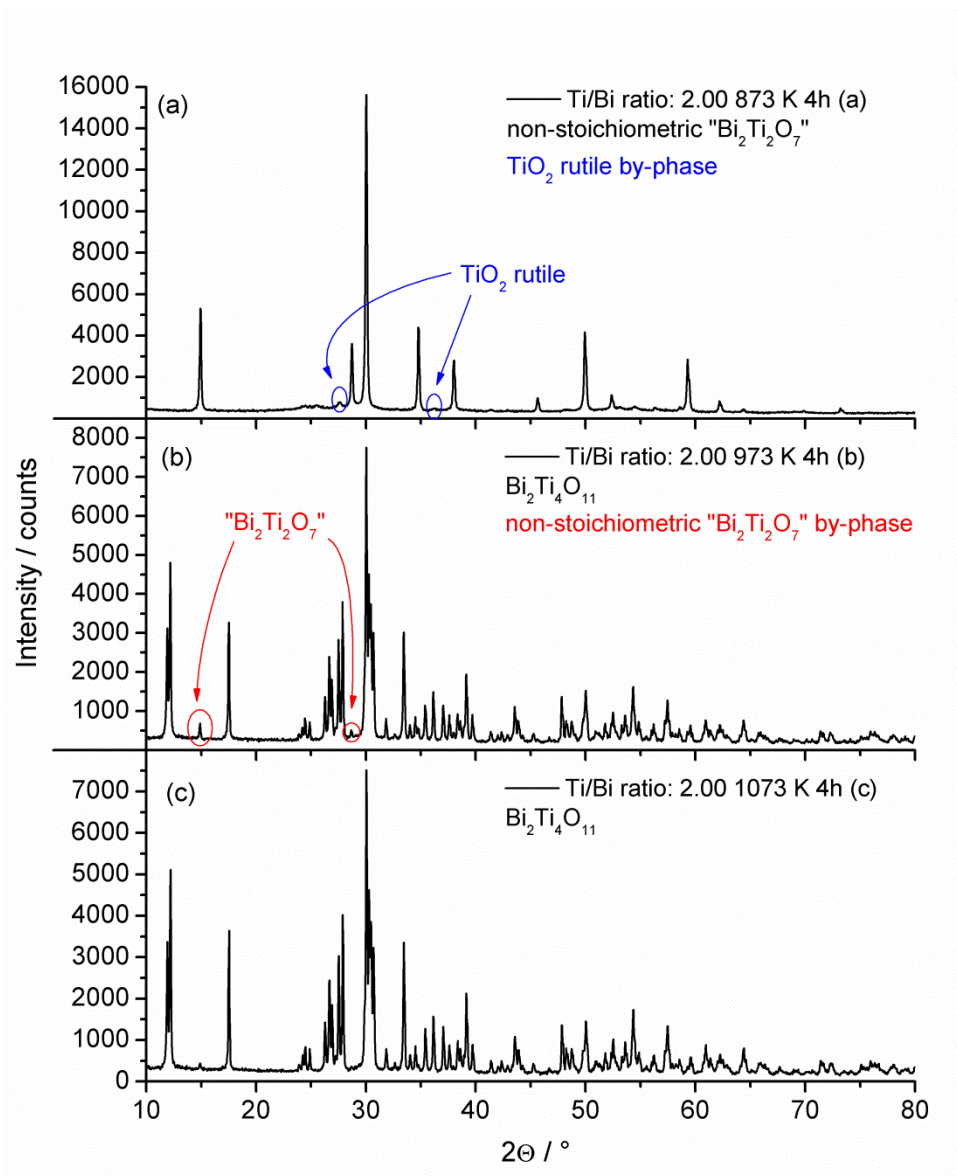


Figure A9: X-ray diffraction data of the sample featuring a Ti/Bi ratio of 2.00 as a function of the annealing temperature. At 873 K, a phase mixture of pyrochlore ($\text{Bi}_{2-x}\text{Ti}_{0.75x}\text{Ti}_2\text{O}_7$) and TiO_2 rutile is obtained. Being spiked with a small amount of the pyrochlore at 973 K, $\text{Bi}_2\text{Ti}_4\text{O}_{11}$ is obtained at 1073 K as a pure phase.

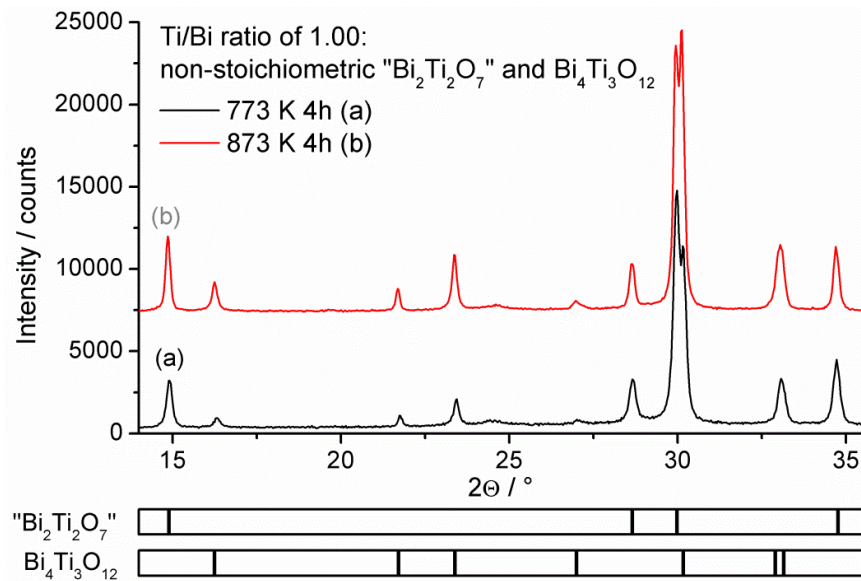


Figure A10: X-ray diffraction data of the sample featuring a Ti/Bi ratio of 1.00 as a function of the annealing temperature. A phase mixture of pyrochlore $(\text{Bi}_{2-x}\text{Ti}_{0.75x})\text{Ti}_2\text{O}_7$ and $\text{Bi}_4\text{Ti}_3\text{O}_{12}$ is obtained at 773 K and 873 K. The amount of $\text{Bi}_4\text{Ti}_3\text{O}_{12}$ as well as the degree of vacancies in $(\text{Bi}_{2-x}\text{Ti}_{0.75x})\text{Ti}_2\text{O}_7$ increase with increasing annealing temperature.

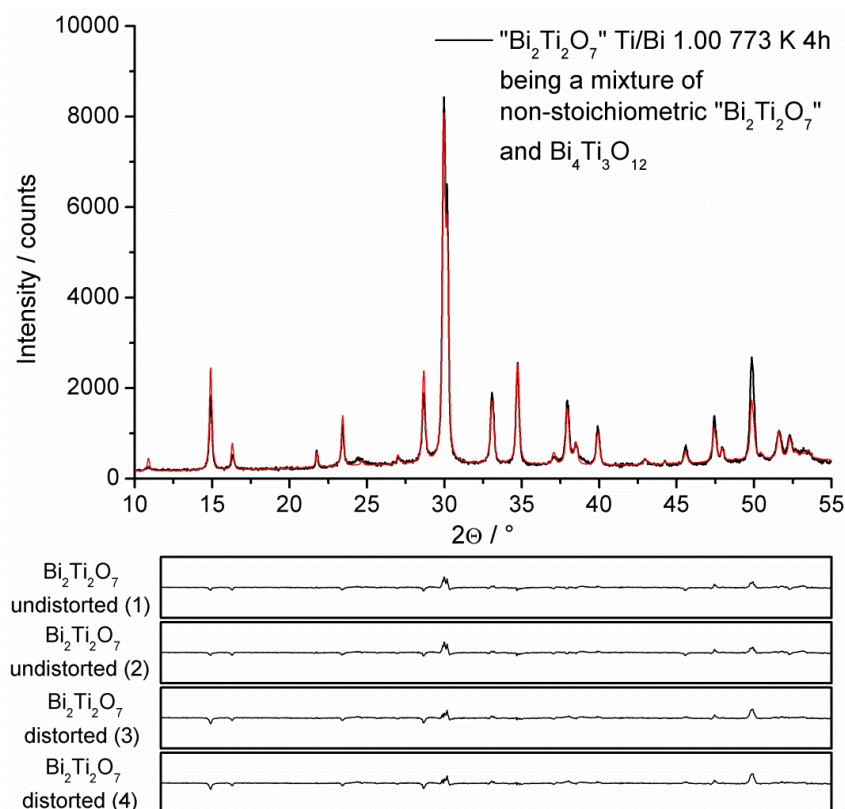


Figure A11: Rietveld refinement of the bismuth titanate sample featuring a stoichiometric Ti/Bi ratio of 1.00 annealed at 773 K for 4 hours. The sample is composed of a mixture of $(\text{Bi}_{2-x}\text{Ti}_{0.75x})\text{Ti}_2\text{O}_7$ and $\text{Bi}_4\text{Ti}_3\text{O}_{12}$. The main part shows the raw data and the calculated fit for structure suggestion 4. The difference plots for all four structures are given in the bottom each providing the same scale ranging from -3000 to +3000 counts. It should be pointed out that the measurement was conducted in a reduced range from 10 to $55^\circ 2\theta$.

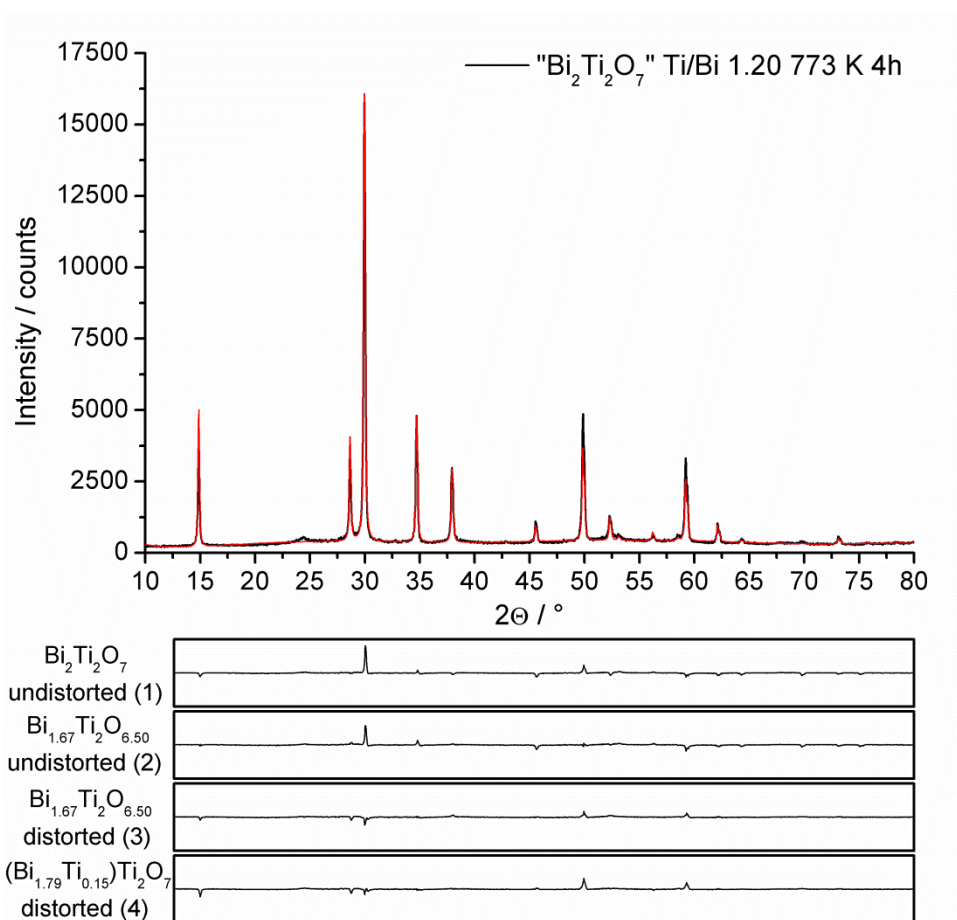


Figure A12: Rietveld refinement of $(\text{Bi}_{2-x}\text{Ti}_{0.75x})\text{Ti}_2\text{O}_7$ featuring a Ti/Bi ratio of 1.20 annealed at 773 K for 4 hours. The main part shows the raw data and the calculated fit for structure suggestion 4. The difference plots for all four structures are given in the bottom each providing the same scale ranging from -4500 to +4500 counts.

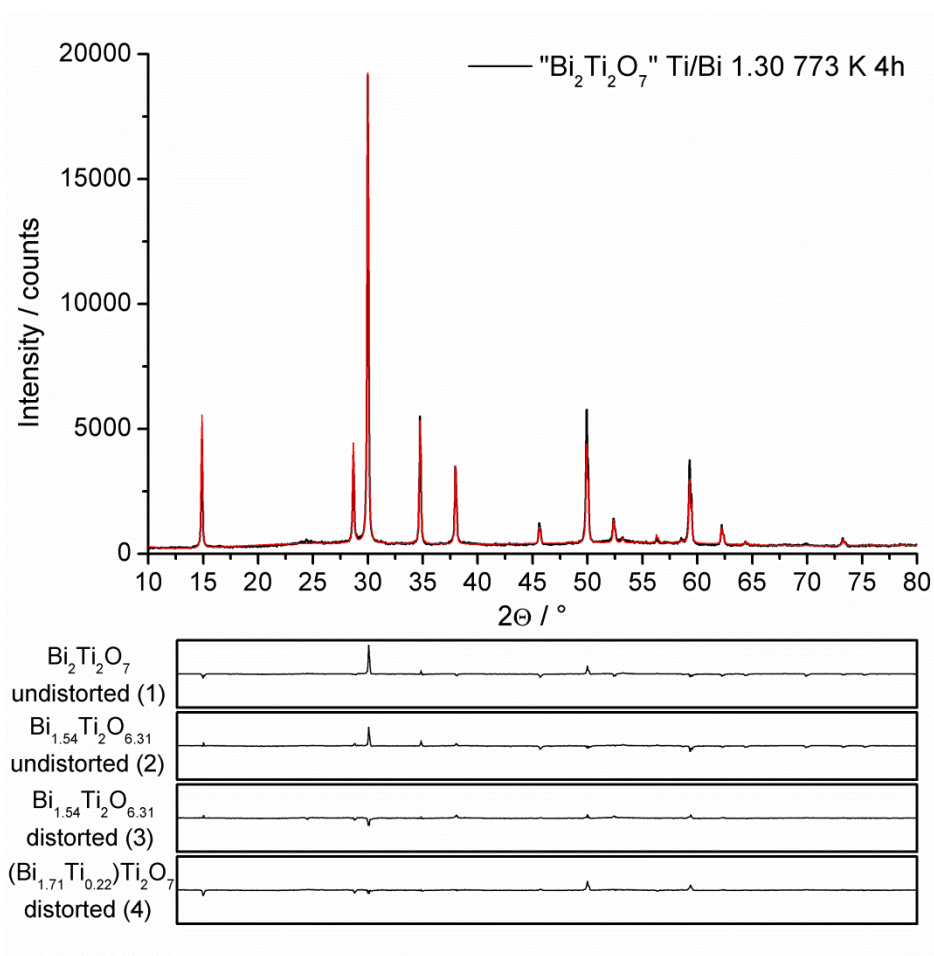


Figure A13: Rietveld refinement of $(\text{Bi}_{2-x}\text{Ti}_{0.75x})\text{Ti}_2\text{O}_7$ featuring a Ti/Bi ratio of 1.30 annealed at 773 K for 4 hours. The main part shows the raw data and the calculated fit for structure suggestion 4. The difference plots for all four structures are given in the bottom each providing the same scale ranging from -6000 to +6000 counts.

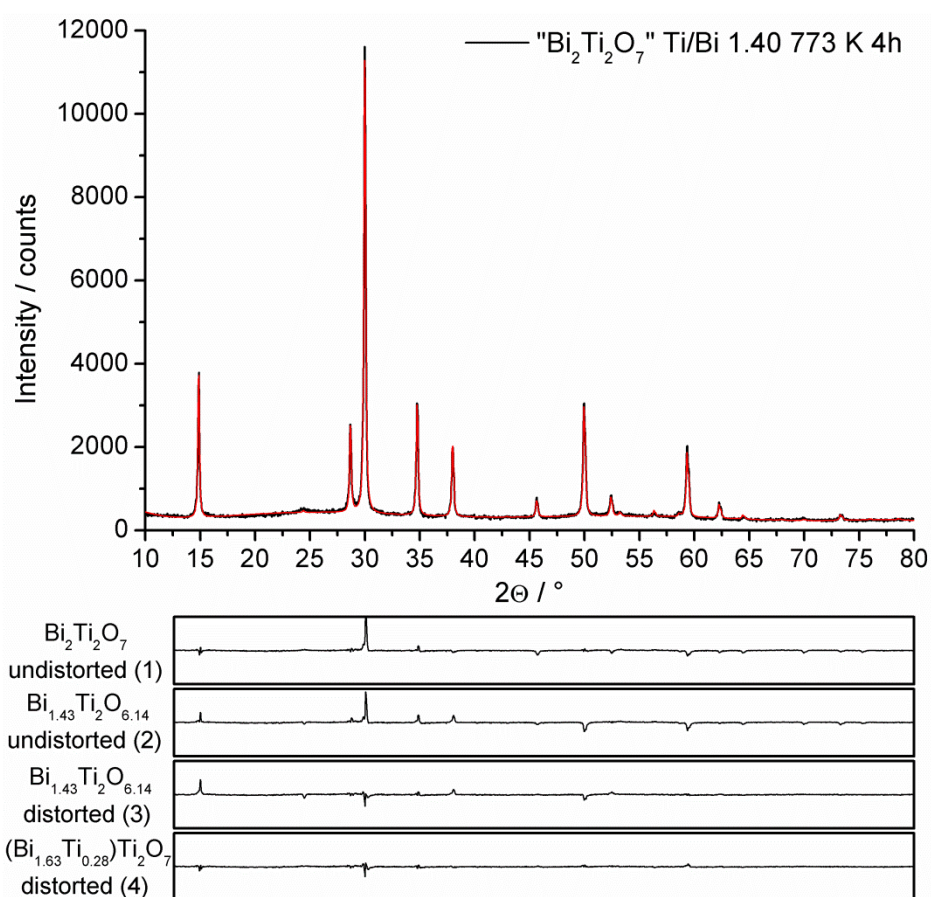


Figure A14: Rietveld refinement of $(\text{Bi}_{2-x}\text{Ti}_{0.75x})\text{Ti}_2\text{O}_7$ featuring a Ti/Bi ratio of 1.40 annealed at 773 K for 4 hours. The main part shows the raw data and the calculated fit for structure suggestion 4. The difference plots for all four structures are given in the bottom each providing the same scale ranging from -3000 to +3000 counts.

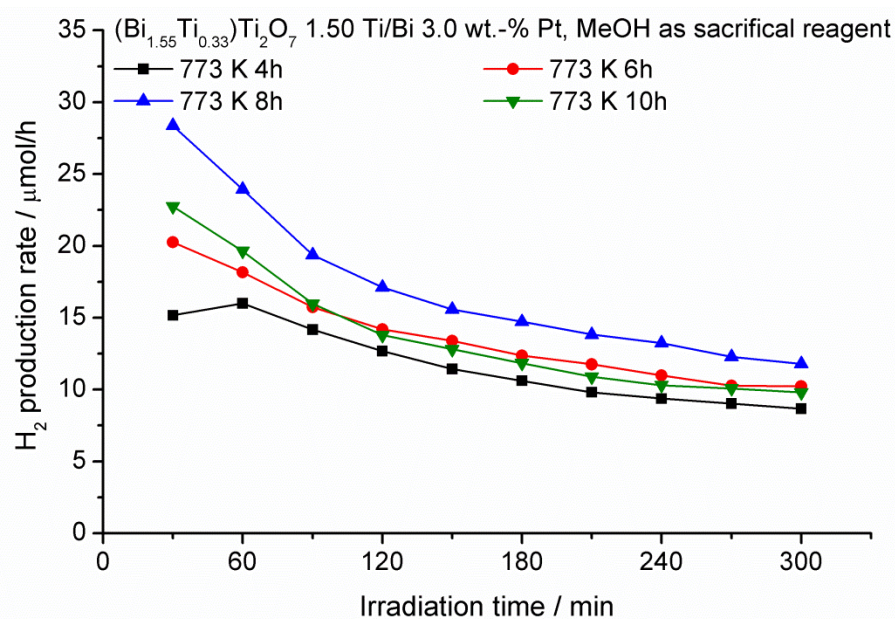


Figure A15: Photocatalytic activity regarding hydrogen production over $(\text{Bi}_{1.55}\text{Ti}_{0.33})\text{Ti}_2\text{O}_7$ annealed at 773 K loaded with 3.0 wt.-% of platinum as co-catalyst and in the presence of 10 vol.-% of methanol as a function of the annealing time.

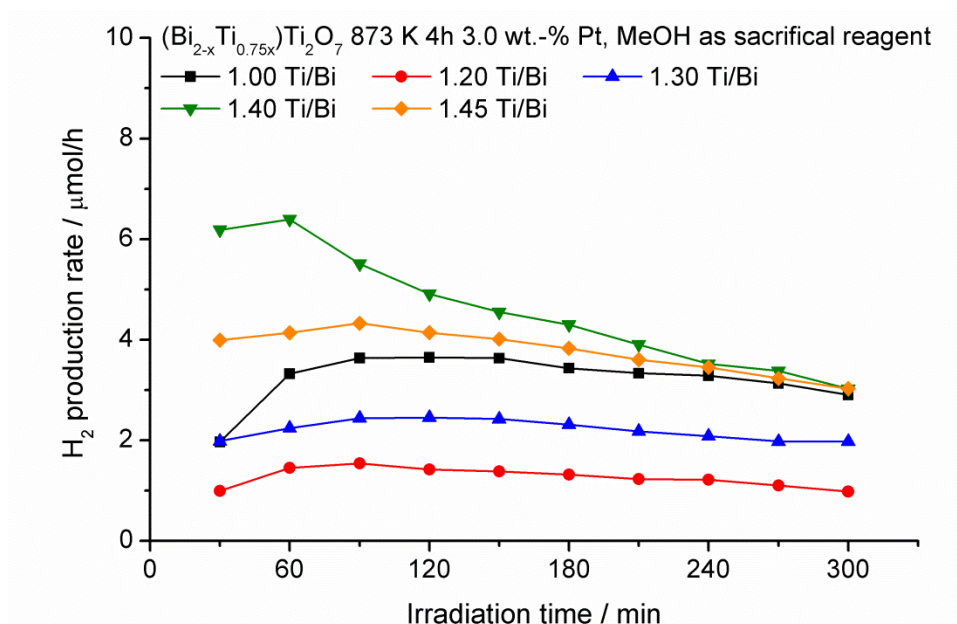


Figure A16: Photocatalytic activity regarding hydrogen production over (Bi_{2-x}Ti_{0.75x})Ti₂O₇ calcined at 873 K for 4 hours with 3.0 wt.-% of platinum as co-catalyst and in the presence of 10 vol.-% methanol as sacrificial reagent.

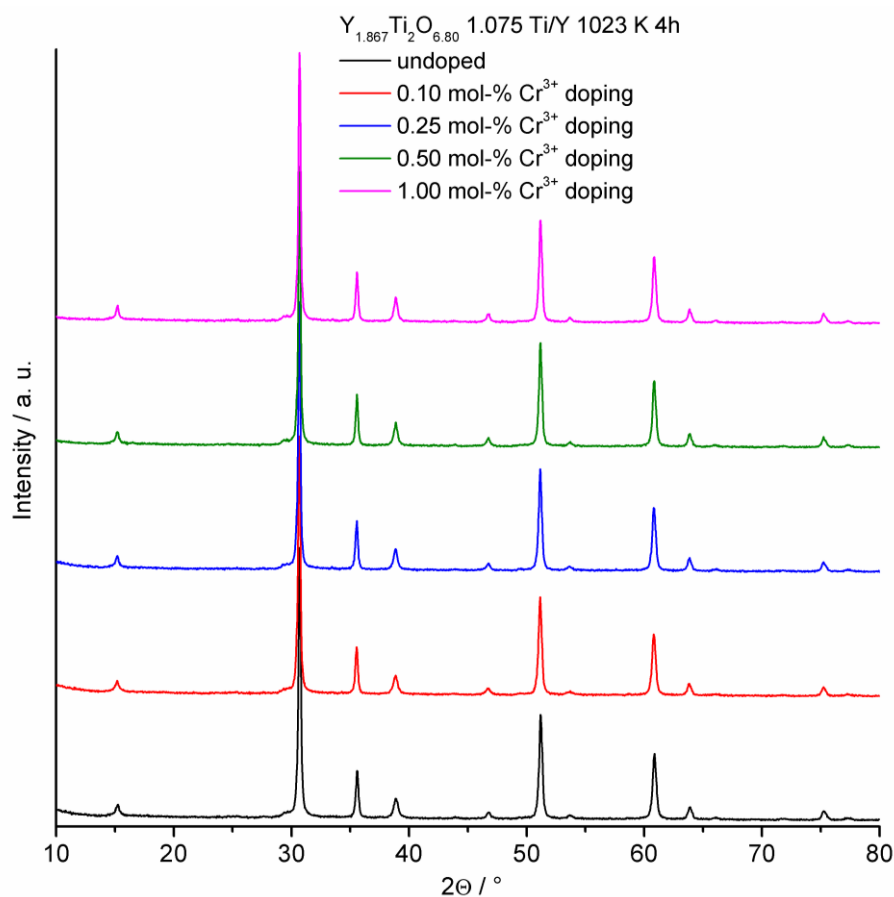


Figure A17: XRD pattern of Y_{1.867}Ti₂O_{6.80} doped with 0.10, 0.25, 0.50 and 1.00 mol-% of Cr³⁺. Additionally, the undoped sample is included. Annealing was performed at 1023 K for 4h and all samples feature a Ti/Y ratio of 1.075.

7.1.2 Additional Tables

wt.-% of metal	0.40 %	0.75 %	1.35 %	2.00 %	3.00 %	4.00 %
H ₂ PtCl ₆ solution	0.80 mL	1.49 mL	2.69 mL	3.98 mL	5.97 mL	7.96 mL
Na ₃ RhCl ₆ solution	1.12 mL	2.10 mL	3.78 mL	5.60 mL	8.41 mL	11.21 mL

Table A1: Needed volumes of platinum and rhodium precursor solutions prepared with 100 mg of H₂PtCl₆·6H₂O or Na₃RhCl₆·6H₂O in 100 mL solution.

wt.-% of metal	0.40 %	0.75 %	1.35 %	2.00 %	3.00 %	4.00 %
H ₂ PtCl ₆ solution	0.80 mL	1.49 mL	2.69 mL	3.98 mL	5.97 mL	7.96 mL
Na ₃ RhCl ₆ solution	1.12 mL	2.10 mL	3.78 mL	5.60 mL	8.41 mL	11.21 mL
wt.-% of Cr	0.60 %	1.125 %	2.025 %	3.00 %	4.50 %	6.00 %
K ₂ CrO ₄ solution	0.45 mL	0.84 mL	1.51 mL	2.24 mL	3.36 mL	4.48 mL

Table A2: Needed volumes of platinum and rhodium precursor solutions prepared with 100 mg of H₂PtCl₆·6H₂O or Na₃RhCl₆·6H₂O in 100 mL solution and the corresponding volume of the chromium precursor solution made of 500 mg K₂CrO₄ in 100 mL distilled water. A Cr/metal wt.-%-ratio of 1.5 is adjusted.

	molar mass / g·mol ⁻¹	density / g·cm ⁻³	mass / g	volume / mL	molar amount / mmol	eq.
Y(NO ₃) ₃ ·6H ₂ O	382.91	-	2.45	-	6.39	2
Ti(O-iPr) ₄	284.23	0.955	1.73	1.81	6.07	1.9
EDTA	292.25	-	3.82	-	13.08	4.095
C ₆ H ₈ O ₇ ·H ₂ O	210.14	-	3.93	-	18.69	5.85
Y₂(Y_{0.05}Ti_{1.95})O_{6.97}	387.20	-	1.18	-	3.035	0.95

Table A3: Synthesis of Y₂(Y_{0.05}Ti_{1.95})O_{6.97} (Ti/Y ratio of 0.95).

	molar mass / g·mol ⁻¹	density / g·cm ⁻³	mass / g	volume / mL	molar amount / mmol	eq.
Y(NO ₃) ₃ ·6H ₂ O	382.91	-	2.45	-	6.39	2
Ti(O-iPr) ₄	284.23	0.955	1.91	2.00	6.71	2.1
EDTA	292.25	-	4.02	-	13.75	4.305
C ₆ H ₈ O ₇ ·H ₂ O	210.14	-	4.13	-	19.65	6.15
Y_{1.90}Ti₂O_{6.86}	374.75	-	1.26	-	3.355	1.05

Table A4: Synthesis of Y_{1.90}Ti₂O_{6.86} (Ti/Y ratio of 1.05).

	molar mass / g·mol ⁻¹	density / g·cm ⁻³	mass / g	volume / mL	molar amount / mmol	eq.
Y(NO ₃) ₃ ·6H ₂ O	382.91	-	2.45	-	6.39	2
Ti(O-iPr) ₄	284.23	0.955	1.95	2.04	6.87	2.15
EDTA	292.25	-	4.07	-	13.92	4.3575
C ₆ H ₈ O ₇ ·H ₂ O	210.14	-	4.18	-	19.89	6.225
Y_{1.86}Ti₂O_{6.80}	369.75	-	1.27	-	3.435	1.075

Table A5: Synthesis of Y_{1.86}Ti₂O_{6.80} (Ti/Y ratio of 1.075).

	molar mass / g·mol ⁻¹	density / g·cm ⁻³	mass / g	volume / mL	molar amount / mmol	eq.
Y(NO ₃) ₃ ·6H ₂ O	382.91	-	2.45	-	6.39	2
Ti(O-iPr) ₄	284.23	0.955	2.00	2.09	7.03	2.2
EDTA	292.25	-	4.12	-	14.09	4.41
C ₆ H ₈ O ₇ ·H ₂ O	210.14	-	4.23	-	20.13	6.3
Y_{1.82}Ti₂O_{6.73}	364.98	-	1.28	-	3.515	1.1

Table A6: Synthesis of Y_{1.82}Ti₂O_{6.73} (Ti/Y ratio of 1.10).

	molar mass / g·mol ⁻¹	density / g·cm ⁻³	mass / g	volume / mL	molar amount / mmol	eq.
Y(NO ₃) ₃ ·6H ₂ O	382.91	-	2.45	-	6.39	2
Ti(O-iPr) ₄	284.23	0.955	2.09	2.19	7.35	2.3
EDTA	292.25	-	4.22	-	14.43	4.515
C ₆ H ₈ O ₇ ·H ₂ O	210.14	-	4.33	-	20.61	6.45
Y_{1.74}Ti₂O_{6.61}	356.05	-	1.31	-	3.674	1.15

Table A7: Synthesis of Y_{1.74}Ti₂O_{6.61} (Ti/Y ratio of 1.15).

	molar mass / g·mol ⁻¹	density / g·cm ⁻³	mass / g	volume / mL	molar amount / mmol	eq.
Y(NO ₃) ₃ ·6H ₂ O	382.91	-	1.84	-	4.79	1.5
Bi(NO ₃) ₃ ·5H ₂ O	485.07	-	0.77	-	1.60	0.5
Ti(O-iPr) ₄	284.23	0.955	1.73	1.81	6.07	1.9
EDTA	292.25	-	3.82	-	13.08	4.095
C ₆ H ₈ O ₇ ·H ₂ O	210.14	-	3.93	-	18.69	5.85
(Y_{1.49}Bi_{0.51}) (Y_{0.05}Ti_{1.95})O_{6.97}	448.77	-	1.36	-	3.035	0.95

Table A8: Synthesis of (Y_{1.49}Bi_{0.51})(Y_{0.05}Ti_{1.95})O_{6.97} (Ti/(Y+Bi) ratio of 0.95).

	molar mass / g·mol ⁻¹	density / g·cm ⁻³	mass / g	volume / mL	molar amount / mmol	eq.
Y(NO ₃) ₃ ·6H ₂ O	382.91	-	1.84	-	4.79	1.5
Bi(NO ₃) ₃ ·5H ₂ O	485.07	-	0.77	-	1.60	0.5
Ti(O-iPr) ₄	284.23	0.955	1.91	2.00	6.71	2.1
EDTA	292.25	-	4.02	-	13.75	4.305
C ₆ H ₈ O ₇ ·H ₂ O	210.14	-	4.13	-	19.65	6.15
Y_{1.43}Bi_{0.48}Ti₂O_{6.86}	431.93	-	1.45	-	3.355	1.05

Table A9: Synthesis of Y_{1.43}Bi_{0.48}Ti₂O_{6.86} (Ti/(Y+Bi) ratio of 1.05).

	molar mass / g·mol ⁻¹	density / g·cm ⁻³	mass / g	volume / mL	molar amount / mmol	eq.
Y(NO ₃) ₃ ·6H ₂ O	382.91	-	1.84	-	4.79	1.5
Bi(NO ₃) ₃ ·5H ₂ O	485.07	-	0.77	-	1.60	0.5
Ti(O-iPr) ₄	284.23	0.955	2.00	2.09	7.03	2.2
EDTA	292.25	-	4.12	-	14.09	4.41
C ₆ H ₈ O ₇ ·H ₂ O	210.14	-	4.23	-	20.13	6.3
Y_{1.36}Bi_{0.45}Ti₂O_{6.73}	419.56	-	1.47	-	3.515	1.1

Table A10: Synthesis of Y_{1.36}Bi_{0.45}Ti₂O_{6.73} (Ti/(Y+Bi) ratio of 1.10).

	molar mass / g·mol ⁻¹	density / g·cm ⁻³	mass / g	volume / mL	molar amount / mmol	eq.
Y(NO ₃) ₃ ·6H ₂ O	382.91	-	1.84	-	4.79	1.5
Bi(NO ₃) ₃ ·5H ₂ O	485.07	-	0.77	-	1.60	0.5
Ti(O-iPr) ₄	284.23	0.955	2.09	2.19	7.35	2.3
EDTA	292.25	-	4.22	-	14.43	4.515
C ₆ H ₈ O ₇ ·H ₂ O	210.14	-	4.33	-	20.61	6.45
Y_{1.30}Bi_{0.43}Ti₂O_{6.61}	408.26	-	1.50	-	3.674	1.15

Table A11: Synthesis of Y_{1.30}Bi_{0.43}Ti₂O_{6.61} (Ti/(Y+Bi) ratio of 1.15).

	molar mass / g·mol ⁻¹	density / g·cm ⁻³	mass / g	volume / mL	molar amount / mmol	eq.
Y(NO ₃) ₃ ·6H ₂ O	382.91	-	1.84	-	4.79	1.5
Bi(NO ₃) ₃ ·5H ₂ O	485.07	-	0.77	-	1.60	0.5
Ti(O-iPr) ₄	284.23	0.955	2.18	2.28	7.67	2.4
EDTA	292.25	-	4.31	-	14.76	4.62
C ₆ H ₈ O ₇ ·H ₂ O	210.14	-	4.43	-	21.09	6.6
Y_{1.25}Bi_{0.42}Ti₂O_{6.50}	397.90	-	1.53	-	3.834	1.2

Table A12: Synthesis of Y_{1.25}Bi_{0.42}Ti₂O_{6.50} (Ti/(Y+Bi) ratio of 1.20).

	molar mass / g·mol ⁻¹	density / g·cm ⁻³	mass / g	volume / mL	molar amount / mmol	eq.
Y(NO ₃) ₃ ·6H ₂ O	382.91	-	1.22	-	3.20	1
Bi(NO ₃) ₃ ·5H ₂ O	485.07	-	1.55	-	3.20	1
Ti(O-iPr) ₄	284.23	0.955	2.00	2.09	7.03	2.2
EDTA	292.25	-	4.12	-	14.09	4.41
C ₆ H ₈ O ₇ ·H ₂ O	210.14	-	4.23	-	20.13	6.3
Y_{0.91}Bi_{0.91}Ti₂O_{6.73}	474.14	-	1.67	-	3.515	1.1

Table A13: Synthesis of Y_{0.91}Bi_{0.91}Ti₂O_{6.73} (Ti/(Y+Bi) ratio of 1.10).

	molar mass / g·mol ⁻¹	density / g·cm ⁻³	mass / g	volume / mL	molar amount / mmol	eq.
Y(NO ₃) ₃ ·6H ₂ O	382.91	-	1.22	-	3.20	1
Bi(NO ₃) ₃ ·5H ₂ O	485.07	-	1.55	-	3.20	1
Ti(O-iPr) ₄	284.23	0.955	2.09	2.19	7.35	2.3
EDTA	292.25	-	4.22	-	14.43	4.515
C ₆ H ₈ O ₇ ·H ₂ O	210.14	-	4.33	-	20.61	6.45
Y_{0.87}Bi_{0.87}Ti₂O_{6.61}	460.46	-	1.69	-	3.674	1.15

Table A14: Synthesis of Y_{0.87}Bi_{0.87}Ti₂O_{6.61} (Ti/(Y+Bi) ratio of 1.15).

	molar mass / g·mol ⁻¹	density / g·cm ⁻³	mass / g	volume / mL	molar amount / mmol	eq.
Y(NO ₃) ₃ ·6H ₂ O	382.91	-	1.22	-	3.20	1
Bi(NO ₃) ₃ ·5H ₂ O	485.07	-	1.55	-	3.20	1
Ti(O-iPr) ₄	284.23	0.955	2.18	2.28	7.67	2.4
EDTA	292.25	-	4.31	-	14.76	4.62
C ₆ H ₈ O ₇ ·H ₂ O	210.14	-	4.43	-	21.09	6.6
Y_{0.83}Bi_{0.83}Ti₂O_{6.50}	447.93	-	1.72	-	3.834	1.2

Table A15: Synthesis of Y_{0.83}Bi_{0.83}Ti₂O_{6.50} (Ti/(Y+Bi) ratio of 1.20).

	molar mass / g·mol ⁻¹	density / g·cm ⁻³	mass / g	volume / mL	molar amount / mmol	eq.
Y(NO ₃) ₃ ·6H ₂ O	382.91	-	1.22	-	3.20	1
Bi(NO ₃) ₃ ·5H ₂ O	485.07	-	1.55	-	3.20	1
Ti(O-iPr) ₄	284.23	0.955	2.27	2.38	7.99	2.5
EDTA	292.25	-	4.41	-	15.10	4.725
C ₆ H ₈ O ₇ ·H ₂ O	210.14	-	4.53	-	21.57	6.75
Y_{0.80}Bi_{0.80}Ti₂O_{6.40}	436.40	-	1.74	-	3.994	1.25

Table A16: Synthesis of Y_{0.80}Bi_{0.80}Ti₂O_{6.40} (Ti/(Y+Bi) ratio of 1.25).

	molar mass / g·mol ⁻¹	density / g·cm ⁻³	mass / g	volume / mL	molar amount / mmol	eq.
Y(NO ₃) ₃ ·6H ₂ O	382.91	-	1.22	-	3.20	1
Bi(NO ₃) ₃ ·5H ₂ O	485.07	-	1.55	-	3.20	1
Ti(O-iPr) ₄	284.23	0.955	2.36	2.47	8.31	2.6
EDTA	292.25	-	4.51	-	15.43	4.83
C ₆ H ₈ O ₇ ·H ₂ O	210.14	-	4.63	-	22.05	6.9
Y_{0.77}Bi_{0.77}Ti₂O_{6.31}	425.76	-	1.77	-	4.154	1.3

Table A17: Synthesis of Y_{0.77}Bi_{0.77}Ti₂O_{6.31} (Ti/(Y+Bi) ratio of 1.30).

	molar mass / g·mol ⁻¹	density / g·cm ⁻³	mass / g	volume / mL	molar amount / mmol	eq.
Bi(NO ₃) ₃ ·5H ₂ O	485.07	-	3.10	-	6.39	2
Ti(O-iPr) ₄	284.23	0.955	2.18	2.28	7.67	2.4
EDTA	292.25	-	4.31	-	14.76	4.62
C ₆ H ₈ O ₇ ·H ₂ O	210.14	-	4.43	-	21.09	6.6
(Bi_{1.79}Ti_{0.15})Ti₂O₇	590.20	-	2.10	-	3.56	1.2

Table A18: Synthesis of (Bi_{1.79}Ti_{0.15})Ti₂O₇ (Ti/Bi ratio of 1.20).

	molar mass / g·mol ⁻¹	density / g·cm ⁻³	mass / g	volume / mL	molar amount / mmol	eq.
Bi(NO ₃) ₃ ·5H ₂ O	485.07	-	3.10	-	6.39	2
Ti(O-iPr) ₄	284.23	0.955	2.27	2.38	7.99	2.5
EDTA	292.25	-	4.41	-	15.10	4.725
C ₆ H ₈ O ₇ ·H ₂ O	210.14	-	4.53	-	21.57	6.75
(Bi_{1.75}Ti_{0.19})Ti₂O₇	582.43	-	2.13	-	3.65	1.25

Table A19: Synthesis of (Bi_{1.75}Ti_{0.19})Ti₂O₇ (Ti/Bi ratio of 1.25).

	molar mass / g·mol ⁻¹	density / g·cm ⁻³	mass / g	volume / mL	molar amount / mmol	eq.
Bi(NO ₃) ₃ ·5H ₂ O	485.07	-	3.10	-	6.39	2
Ti(O-iPr) ₄	284.23	0.955	2.36	2.47	8.31	2.6
EDTA	292.25	-	4.51	-	15.43	4.83
C ₆ H ₈ O ₇ ·H ₂ O	210.14	-	4.63	-	22.05	6.9
(Bi_{1.71}Ti_{0.22})Ti₂O₇	575.04	-	2.15	-	3.74	1.3

Table A20: Synthesis of (Bi_{1.71}Ti_{0.22})Ti₂O₇ (Ti/Bi ratio of 1.30).

	molar mass / g·mol ⁻¹	density / g·cm ⁻³	mass / g	volume / mL	molar amount / mmol	eq.
Bi(NO ₃) ₃ ·5H ₂ O	485.07	-	3.10	-	6.39	2
Ti(O-iPr) ₄	284.23	0.955	2.45	2.57	8.63	2.7
EDTA	292.25	-	4.61	-	15.77	4.935
C ₆ H ₈ O ₇ ·H ₂ O	210.14	-	4.73	-	22.52	7.05
(Bi_{1.67}Ti_{0.25})Ti₂O₇	568.01	-	2.18	-	3.83	1.35

Table A21: Synthesis of (Bi_{1.67}Ti_{0.25})Ti₂O₇ (Ti/Bi ratio of 1.35).

	molar mass / g·mol ⁻¹	density / g·cm ⁻³	mass / g	volume / mL	molar amount / mmol	eq.
Bi(NO ₃) ₃ ·5H ₂ O	485.07	-	3.10	-	6.39	2
Ti(O-iPr) ₄	284.23	0.955	2.54	2.66	8.95	2.8
EDTA	292.25	-	4.71	-	16.10	5.04
C ₆ H ₈ O ₇ ·H ₂ O	210.14	-	4.83	-	23.00	7.2
(Bi_{1.63}Ti_{0.28})Ti₂O₇	561.30	-	2.20	-	3.93	1.4

Table A22: Synthesis of (Bi_{1.63}Ti_{0.28})Ti₂O₇ (Ti/Bi ratio of 1.40).

	molar mass / g·mol ⁻¹	density / g·cm ⁻³	mass / g	volume / mL	molar amount / mmol	eq.
Bi(NO ₃) ₃ ·5H ₂ O	485.07	-	3.10	-	6.39	2
Ti(O-iPr) ₄	284.23	0.955	2.63	2.76	9.27	2.9
EDTA	292.25	-	4.80	-	16.44	5.145
C ₆ H ₈ O ₇ ·H ₂ O	210.14	-	4.93	-	23.48	7.35
(Bi_{1.59}Ti_{0.31})Ti₂O₇	554.90	-	2.23	-	4.02	1.45

Table A23: Synthesis of (Bi_{1.59}Ti_{0.31})Ti₂O₇ (Ti/Bi ratio of 1.45).

	molar mass / g·mol ⁻¹	density / g·cm ⁻³	mass / g	volume / mL	molar amount / mmol	eq.
Bi(NO ₃) ₃ ·5H ₂ O	485.07	-	3.10	-	6.39	2
Ti(O-iPr) ₄	284.23	0.955	2.72	2.85	9.59	3
EDTA	292.25	-	4.90	-	16.77	5.25
C ₆ H ₈ O ₇ ·H ₂ O	210.14	-	5.04	-	23.96	7.5
(Bi_{1.55}Ti_{0.33})Ti₂O₇	548.78	-	2.25	-	4.11	1.5

Table A24: Synthesis of (Bi_{1.55}Ti_{0.33})Ti₂O₇ (Ti/Bi ratio of 1.50).

	molar mass / g·mol ⁻¹	density / g·cm ⁻³	mass / g	volume / mL	molar amount / mmol	eq.
Bi(NO ₃) ₃ ·5H ₂ O	485.07	-	3.10	-	6.39	2
Ti(O-iPr) ₄	284.23	0.955	1.36	1.43	4.79	1.5
EDTA	292.25	-	3.43	-	11.74	3.675
C ₆ H ₈ O ₇ ·H ₂ O	210.14	-	3.52	-	16.77	5.25
Bi₄Ti₃O₁₂	1171.45	-	1.87	-	1.598	0.5

Table A25: Synthesis of Bi₄Ti₃O₁₂ (Ti/Bi ratio of 0.75).

	molar mass / g·mol ⁻¹	density / g·cm ⁻³	mass / g	volume / mL	molar amount / mmol	eq.
Bi(NO ₃) ₃ ·5H ₂ O	485.07	-	3.10	-	6.39	2
Ti(O-iPr) ₄	284.23	0.955	3.63	3.80	12.78	4
EDTA	292.25	-	5.88	-	20.13	6.3
C ₆ H ₈ O ₇ ·H ₂ O	210.14	-	6.04	-	28.76	9
Bi₂Ti₄O₁₁	785.36	-	2.51	-	3.195	1

Table A26: Synthesis of Bi₂Ti₄O₁₁ (Ti/Bi ratio of 2.00).

site	Atom	Ti/Bi ratio								
		1.00	1.20	1.25	1.30	1.35	1.40	1.45	1.50	
A	16c	Bi	1	5/6	4/5	10/13	20/27	5/7	20/29	2/3
B	16d	Ti	1	1	1	1	1	1	1	1
O	48f	O	1	1	1	1	1	1	1	1
O [⋄]	8a	O	1	1/2	2/5	4/13	2/9	1/7	2/29	0

Table A27: Occupancies of bismuth, titanium and oxygen on different Wyckoff positions for a predicted structure of non-stoichiometric Bi_{2-x}Ti₂O_{7-1.5x} corresponding to structure suggestion 2. Atomistic displacements of bismuth and O[⋄] oxygen have not been taken into consideration.

site	Atom	Ti/Bi ratio								
		1.00	1.20	1.25	1.30	1.35	1.40	1.45	1.50	
A	96g	Bi	1/6	5/36	2/15	5/39	10/81	5/42	10/87	1/9
B	16d	Ti	1	1	1	1	1	1	1	1
O	48f	O	1	1	1	1	1	1	1	1
O [⋄]	48f	O	1/6	1/12	1/15	2/39	1/27	1/42	1/87	0

Table A28: Occupancies of bismuth, titanium and oxygen on different Wyckoff positions for a predicted structure of non-stoichiometric Bi_{2-x}Ti₂O_{7-1.5x} corresponding to structure suggestion 3. This structural model includes the atomistic displacements of bismuth and O[⋄] oxygen.

site		Atom	Ti/Bi ratio							
			1.00	1.20	1.25	1.30	1.35	1.40	1.45	1.50
A	96g	Bi	1/6	35/234	7/48	35/246	5/36	35/258	35/264	7/54
	16c	Ti	0	1/13	3/32	9/82	1/8	6/43	27/176	1/6
B	16d	Ti	1	1	1	1	1	1	1	1
O	48f	O	1	1	1	1	1	1	1	1
O [•]	48f	O	1/6	35/234	7/48	35/246	5/36	35/258	35/264	7/54
	8a	O	0	4/39	1/8	6/41	1/6	8/43	9/44	2/9

Table A29: Occupancies of bismuth, titanium and oxygen on different Wyckoff positions for a predicted structure of non-stoichiometric $(\text{Bi}_{2-x}\text{Ti}_{0.75x})\text{Ti}_2\text{O}_7$ corresponding to structure suggestion 4. This structural model includes the atomistic displacements of bismuth and O[•] oxygen.

7.2 Abbreviations and symbols

A	absorption coefficient
a	distance between two spheres
a_m	required space of a nitrogen molecule
a_0	lattice parameter
Å	Angstrom
C	BET constant
c	velocity of light: $2.99 \cdot 10^8$ m/s
cb	conduction band
$c.n.$	coordination number
D	average crystallite size
d	distance between lattice planes
DOS	density of states
E	extinction
E	energy
E_A	activation energy
E_{bg}	band gap energy
$EDXS$	energy-dispersive X-ray spectroscopy
eV	electron volt
$F(R_\infty)$	Kubelka-Munk function
$FWHM$	full width at half maximum

<i>g</i>	gram
<i>GOF</i>	goodness of fit
<i>h</i>	Planck`s constant: $6.6256 \cdot 10^{-34}$ Js
<i>h</i>	hour
<i>HOMO</i>	highest occupied molecular orbital
<i>h, k, l</i>	Miller indices
<i>I</i>	intensity of irradiation
<i>K</i>	absorption
<i>k</i>	Scherrer constant
<i>k</i>	wavenumber
\vec{k}	wavevector
<i>k_r</i>	recombination rate
<i>L</i>	liter
<i>LUMO</i>	lowest unoccupied molecular orbital
<i>M</i>	molar
<i>m</i>	meter
<i>min</i>	minute
<i>N_A</i>	Avogadro constant: $6.023 \cdot 10^{23}$ 1/mol
<i>NHE</i>	normal hydrogen electrode
<i>O_{sp}</i>	specific surface area
<i>p</i>	momentum
<i>R_∞</i>	reflection
<i>R_{exp}</i>	expected R-factor
<i>R_{wp}</i>	weighted profile R-factor
<i>S</i>	scattering
<i>s</i>	second
<i>SSR</i>	solid state reaction
<i>V</i>	volume
<i>V_m</i>	volume of a monolayer
<i>vb</i>	valence band
<i>W</i>	watt
°C	degree Centigrade

α	optical absorption coefficient
β	integrated peak width
θ	glancing angle
λ	wavelength
$\zeta(\%)$	photonic efficiency
χ_n	contribution of an l_s wave function to the BLOCH function
ψ_k	BLOCH function

7.3 Table of Figures

Figure 1: Wavefunctions.	8
Figure 2: Fundamental reaction steps in the process of photocatalysis.	12
Figure 3: The process of platinum co-catalyst photodeposition.	13
Figure 4: Corner-sharing network of TiO_6 octahedra in the cubic pyrochlore structure of $\text{Y}_2\text{Ti}_2\text{O}_7$.	15
Figure 5: Scheme of the hypothetical phase transition of $\text{Y}_2\text{Ti}_2\text{O}_7$ from the pyrochlore structure into the parental defect fluorite structure.	17
Figure 6: ASTM standard spectrum ^[65] AM1.5 (G159) being in good accordance with the overall yearly average irradiation in mid-latitude regions.	18
Figure 7: The positions of the conduction band bottom and the valence band top proposed for binary oxides.	20
Figure 8: The additional transitions and reaction steps in $\text{Y}_2\text{Ti}_2\text{O}_7$ doped by transition metal cations.	23
Figure 9: The proposed positions of energy levels created by doping the pyrochlore $\text{Y}_2\text{Ti}_2\text{O}_7$ with Fe^{3+} , Cr^{3+} , Mn^{3+} and Ti^{3+} .	24
Figure 10: Alteration of the surface charge by changing the pH value.	26
Figure 11: The typical irradiation spectrum of a xenon arc lamp.	28
Figure 12: Photocatalysis setup.	36
Figure 13: Preparation procedure of mixed oxide pyrochlores via the modified Pechini sol-gel method.	42
Figure 14: XRD pattern of stoichiometric $\text{Y}_2\text{Ti}_2\text{O}_7$ annealed at 1173 K for 4h.	51
Figure 15: XRD pattern of $\text{Y}_2\text{Ti}_2\text{O}_7$ annealed at 1173 K 4h featuring different Ti/Y ratios in the angular range of $34.5\text{-}39.5^\circ 2\theta$.	52

- Figure 16: Quotient of the intensities of the (400) and (331) reflections as a function of the Ti/Y ratio for $Y_2Ti_2O_7$ calcined at 1023 K and 1173 K. 53
- Figure 17: Lattice parameter as a function of the Ti/Y ratio for $Y_2Ti_2O_7$ calcined at 1023 K and 1173 K. 54
- Figure 18: Tauc-plots (for indirect band gap transition) calculated from the UV-vis diffuse reflectance spectra of $Y_2Ti_2O_7$ with different Ti/Y ratios. 56
- Figure 19: Average crystallite sizes and TiO_2 rutile fractions obtained by Rietveld refinement of the X-ray diffraction data of $Y_2Ti_2O_7$ samples as a function of the Ti/Y ratio. 59
- Figure 20: TEM micrographs in dark field mode of $Y_2Ti_2O_7$ Ti/Y 1.00 calcined at 1023 K for 4h. 60
- Figure 21: Photocatalytic activity regarding hydrogen production over $Y_2Ti_2O_7$ calcined at 1023 K for 4h with 0.75 wt.-% platinum as co-catalyst. 61
- Figure 22: Photocatalytic activity regarding hydrogen production over $Y_2Ti_2O_7$ calcined at 1173 K for 4h with 0.75 wt.-% platinum as co-catalyst. 62
- Figure 23: Steadiness of photocatalytic hydrogen production over $Y_2Ti_2O_7$ 1.10 Ti/Y 1023 K 4h and $Y_2Ti_2O_7$ 1.00 Ti/Y 1173 K 4h loaded with 0.75 wt.-% rhodium or 0.75 wt.-% platinum as co-catalyst. 64
- Figure 24: Photocatalytic activities and photonic efficiencies regarding hydrogen production over $Y_2Ti_2O_7$ calcined at 1023 K or 1173 K for 4h with 0.75 wt.-% of rhodium or platinum as co-catalyst. 65
- Figure 25: Cationic lattice distortion and average particle sizes of the $Y_2Ti_2O_7$ catalysts are classified and rated by quality marks. 66
- Figure 26: Correlation between the cationic lattice distortion in the $Y_{2-x}Ti_2O_{7-1.5x}$ structure at 1023 K annealing and the photocatalytic activity as a function of the Ti/Y ratio. 68
- Figure 27: Photocatalytic activity regarding hydrogen production over $Y_{1.867}Ti_2O_{6.80}$ (Ti/Y=1.075) calcined at 1023 K for 4h as a function of the co-catalyst loading of platinum (A) and rhodium (B). 69
- Figure 28: Phase analysis of $(Y_{1.5}Bi_{0.5})_{1-x}Ti_2O_{7-3x}$ and $(YBi)_{1-x}Ti_2O_{7-3x}$ samples annealed at 873 K, 1023 K or 1173 K for 4h as a function of the Ti/(Y+Bi) ratio. 71

- Figure 29: Tauc-plots (for indirect bad gap transition) calculated from the UV-vis diffuse reflectance spectra of $Y_2Ti_2O_7$ (a), $Y_{1.43}Bi_{0.48}Ti_2O_{6.86}$ (b) and $(YBi)_{0.91}Ti_2O_{6.73}$ (c) annealed at 1023 K 4h exhibiting Ti/(Y+Bi) ratios of 1.00, 1.05 and 1.10, respectively. 72
- Figure 30: Tauc-plots (for indirect bad gap transition) calculated from the UV-vis diffuse reflectance spectra of $(Y_{1.5}Bi_{0.5})_{1-x}Ti_2O_{7-3x}$ and $(YBi)_{1-x}Ti_2O_{7-3x}$ samples annealed at 1173 K for band gap energy calculation and the analysis of the titania by-phase rutile. 73
- Figure 31: XRD pattern of $Y_{1.36}Bi_{0.45}Ti_2O_{6.73}$ (part A) and $(YBi)_{0.87}Ti_2O_{6.61}$ (part B) annealed at 1173 K for 4h featuring Ti/(Y+Bi) ratios of 1.10 and 1.15, respectively. 74
- Figure 32: Detail of the X-ray diffraction data in the angular range of 24.5 to 31.5 ° 2 θ for analysis of the titania by-phases rutile and anatase of $(Y_{1.5}Bi_{0.5})_{1-x}Ti_2O_{7-3x}$ and $(YBi)_{1-x}Ti_2O_{7-3x}$ samples annealed at 1023 K or 1173 K as a function of the Ti/(Y+Bi) ratio. 75
- Figure 33: Quotients of the intensities of the (400) and (331) reflections as a function of the Ti/(Y+Bi) ratio for $(Y_{1.5}Bi_{0.5})_{1-x}Ti_2O_{7-3x}$, $(YBi)_{1-x}Ti_2O_{7-3x}$ and $Y_{2-x}Ti_2O_{7-1.5x}$ calcined at 873 K, 1023 K and 1173 K. 76
- Figure 34: The lattice parameters as a function of the Ti/(Y+Bi) ratio for $(YBi)_{1-x}Ti_2O_{7-3x}$ (A), $(Y_{1.5}Bi_{0.5})_{1-x}Ti_2O_{7-3x}$ (B) and $Y_{2-x}Ti_2O_{7-1.5x}$ (C) calcined at 873 K, 1023 K and 1173 K. 77
- Figure 35: XRD pattern of $YBiTi_2O_7$ (part A) and $Y_{1.5}Bi_{0.5}Ti_2O_7$ (part B) annealed at 1023 K 4h and featuring Ti/(Y+Bi) ratios of 1.00 and 0.95, respectively. 78
- Figure 36: TEM micrographs in dark field mode of $Y_{1.36}Bi_{0.45}Ti_2O_{6.73}$ Ti/(Y+Bi) 1.10 calcined at 1023 K for 4h and $(YBi)_{0.77}Ti_2O_{6.31}$ Ti/(Y+Bi) 1.30 annealed at 873 K for 4h loaded by photodeposition with 1.35 wt.-% of rhodium and 3.0 wt.-% of platinum, respectively. 79
- Figure 37: TEM micrograph in dark field mode and EDXS analysis of $(YBi)_{0.77}Ti_2O_{6.31}$ Ti/(Y+Bi) 1.30 annealed at 873 K for 4h and loaded with 3.0 wt.-% of platinum. 80
- Figure 38: Photocatalytic activity regarding hydrogen production over $(Y_{1.5}Bi_{0.5})_{1-x}Ti_2O_{7-3x}$ calcined at 1023 K for 4h with 0.75 wt.-% platinum as co-catalyst. 81

- Figure 39: Maximum photocatalytic activities in hydrogen production over $(Y_{1.5}Bi_{0.5})_{1-x}Ti_2O_{7-3x}$ calcined at 1023 K or 1173 K for 4h with 0.75 wt.-% of rhodium or platinum as co-catalyst. 82
- Figure 40: Photocatalytic activity regarding hydrogen production over $(YBi)_{1-x}Ti_2O_{7-3x}$ calcined at 873 K for 4h with 2.00 wt.-% platinum as co-catalyst. 83
- Figure 41: Maximum photocatalytic activities in hydrogen production over $(YBi)_{1-x}Ti_2O_{7-3x}$ calcined at 873 K, 1023 K or 1173 K for 4h with 2.00 wt.-% platinum as co-catalyst. 84
- Figure 42: Photocatalytic activity regarding hydrogen production over $Y_{1.36}Bi_{0.45}Ti_2O_{6.73}$ ($Ti/(Y+Bi)=1.10$) calcined at 1023 K for 4h as a function of the co-catalyst loading of platinum (A) and rhodium (B). 85
- Figure 43: Photocatalytic activity regarding hydrogen production over $(YBi)_{0.77}Ti_2O_{6.31}$ ($Ti/(Y+Bi)=1.30$) calcined at 873 K for 4h as a function of the co-catalyst loading of platinum (A) and rhodium (B). 86
- Figure 44: Photocatalytic activities and photonic efficiencies regarding hydrogen production over $(Y_{1.5}Bi_{0.5})_{1-x}Ti_2O_{7-3x}$ 1.10 $Ti/(Y+Bi)$ annealed at 1023 K for 4h and $(YBi)_{1-x}Ti_2O_{7-3x}$ 1.30 $Ti/(Y+Bi)$ annealed at 873 K for 4h as a function of the co-catalyst loading. 88
- Figure 45: XRD patterns of various bismuth titanates $Bi_4Ti_3O_{12}$ (a), “ $Bi_2Ti_2O_7$ ” ($Ti/Bi = 1.40$) (b) and $Bi_2Ti_4O_{11}$ (c) annealed at 873 K, 773 K and 1073 K for 4 hours, respectively. 91
- Figure 46: XRD patterns and UV-vis diffuse reflectance spectra (inset) of “ $Bi_2Ti_2O_7$ ” samples ($Ti/Bi = 1.50$) annealed at 773 K for 4 hours (a), 6 hours (b) and 8 hours (c). The degree of crystallinity is improved with prolonged annealing. 92
- Figure 47: The lattice parameter of non-stoichiometric “ $Bi_2Ti_2O_7$ ” samples annealed at 773 K and 873 K as a function of the Ti/Bi ratio. 93
- Figure 48: Tauc-plots (for indirect band gap transition) calculated from the UV-vis diffuse reflectance spectra for band gap energy calculations of $Bi_4Ti_3O_{12}$ (a), “ $Bi_2Ti_2O_7$ ” ($Ti/Bi = 1.40$) (b) and $Bi_2Ti_4O_{11}$ (c) annealed at 873 K, 773 K and 1073 K for 4 hours, respectively. 94

- Figure 49: Displacements in the $O\text{Bi}_4$ tetrahedron in non-stoichiometric " $\text{Bi}_2\text{Ti}_2\text{O}_7$ " samples predicting six possible positions for bismuth and O' oxygen. 97
- Figure 50: Rietveld refinement of non-stoichiometric " $\text{Bi}_2\text{Ti}_2\text{O}_7$ " featuring a Ti/Bi ratio of 1.50 annealed at 773 K for 8 hours. 99
- Figure 51: Maximum photocatalytic activities and photonic efficiencies regarding hydrogen production over $(\text{Bi}_{2-x}\text{Ti}_{0.75x})\text{Ti}_2\text{O}_7$ annealed at 773 K for 4h as a function of the Ti/Bi ratio. 100
- Figure 52: Photocatalytic activity regarding hydrogen production over $(\text{Bi}_{2-x}\text{Ti}_{0.75x})\text{Ti}_2\text{O}_7$ calcined at 773 K for 4 hours with 3.0 wt.-% of platinum as co-catalyst. 101
- Figure 53: Photocatalytic activity regarding hydrogen production over $\text{Bi}_4\text{Ti}_3\text{O}_{12}$ (Ti/Bi = 0.75) annealed at 773 K and 873 K for 4 hours, $(\text{Bi}_{1.55}\text{Ti}_{0.33})\text{Ti}_2\text{O}_7$ (Ti/Bi = 1.50) calcined at 773 K for 8 hours, and $\text{Bi}_2\text{Ti}_4\text{O}_{11}$ (Ti/Bi = 2.00) annealed at 873 K, 973 K and 1073 K for 4 hours. 102
- Figure 54: The x positional parameter of O oxygen obtained from Rietveld refinement as a function of the Ti/Bi ratio in $(\text{Bi}_{2-x}\text{Ti}_{0.75x}\square_{0.25x})\text{Ti}_2\text{O}_7$. 103
- Figure 55: Change of the geometry in the TiO_6 octahedra as a function of the Ti/Bi ratio in $(\text{Bi}_{2-x}\text{Ti}_{0.75x}\square_{0.25x})\text{Ti}_2\text{O}_7$. 104
- Figure 56: Evolution of the O-Ti-O angle in the TiO_6 octahedra obtained from Rietveld refinement as a function of the Ti/Bi ratio in $(\text{Bi}_{2-x}\text{Ti}_{0.75x}\square_{0.25x})\text{Ti}_2\text{O}_7$. 105
- Figure 57: Evolution of the Ti-O-Ti angle in the TiO_6 octahedral network obtained from Rietveld refinement as a function of the Ti/Bi ratio in $(\text{Bi}_{2-x}\text{Ti}_{0.75x}\square_{0.25x})\text{Ti}_2\text{O}_7$. 106
- Figure 58: Evolution of the Ti-O distance in the TiO_6 octahedra obtained from Rietveld refinement as a function of the Ti/Bi ratio in $(\text{Bi}_{2-x}\text{Ti}_{0.75x}\square_{0.25x})\text{Ti}_2\text{O}_7$. 107
- Figure 59: Activity and stability of photocatalytic hydrogen production over $(\text{Bi}_{1.55}\text{Ti}_{0.33})\text{Ti}_2\text{O}_7$ (Ti/Bi = 1.50) annealed at 773 K for 8 hours loaded with bare Pt or core-shell Pt/Cr₂O₃ as a function of the co-catalyst loading. 108

- Figure 60: Proposed scheme of how the Cr_2O_3 shell inhibits the photoreduction of Bi^{3+} in the $(\text{Bi}_{1.55}\text{Ti}_{0.33})\text{Ti}_2\text{O}_7$ photocatalyst occurring under illumination, if bare Pt acts as co-catalyst. 110
- Figure 61: Crystal field splitting in the MO_6 octahedra with $\text{M}^{3+} = \text{Cr}^{3+}, \text{Mn}^{3+}$ and Fe^{3+} providing *high spin* configuration. 111
- Figure 62: Potential modes of excitation in M^{3+} -doped $\text{Y}_2\text{Ti}_2\text{O}_7$ with $\text{M}^{3+} = \text{Cr}^{3+}, \text{Mn}^{3+}$ and Fe^{3+} . The excitation with $\Delta E < E_{bg}$ is enabled by the generation of acceptor and donor energy levels within the band gap. 112
- Figure 63: XRD pattern of $\text{Y}_{1.867}\text{Ti}_2\text{O}_{6.80}$ doped with 0.25 mol-% of $\text{Cr}^{3+}, \text{Mn}^{3+}$ or Fe^{3+} . Additionally, a co-doped sample with 0.25 mol-% of each Cr^{3+} and Ta^{5+} , and the undoped sample are included. 113
- Figure 64: Tauc-plots (for indirect band gap transition) calculated from the UV-vis diffuse reflectance spectra of $\text{Y}_{1.867}\text{Ti}_2\text{O}_{6.80}$ doped with 0.25 mol-% of $\text{Cr}^{3+}, \text{Mn}^{3+}$ or Fe^{3+} . Additionally, a co-doped sample with 0.25 mol-% of each Cr^{3+} and Ta^{5+} , and the undoped sample are included. 114
- Figure 65: Photocatalytic activity regarding hydrogen production over $\text{Y}_{1.867}\text{Ti}_2\text{O}_{6.80}$ (Ti/Y ratio of 1.075) doped with 0.25 mol-% of $\text{Cr}^{3+}, \text{Mn}^{3+}$ or Fe^{3+} calcined at 1023 K for 4h. Additionally, a co-doped sample with 0.25 mol-% of each Cr^{3+} and Ta^{5+} , and the undoped sample are included. 115
- Figure 66: Photocatalytic activity regarding hydrogen production over $\text{Y}_{1.867}\text{Ti}_2\text{O}_{6.80}$ (Ti/Y ratio of 1.075) doped with 0.25 mol-% of $\text{Cr}^{3+}, \text{Mn}^{3+}$ or Fe^{3+} calcined at 1023 K for 4h. Additionally, a co-doped sample with 0.25 mol-% of each Cr^{3+} and Ta^{5+} , and the undoped sample are included. 116
- Figure 67: Tauc-plots (for indirect band gap transition) calculated from the UV-vis diffuse reflectance spectra of $\text{Y}_{1.867}\text{Ti}_2\text{O}_{6.80}$ doped with 0.10, 0.25, 0.50 or 1.00 mol-% of Cr^{3+} . The data for the undoped sample is included as well. 118
- Figure 68: Photocatalytic activity regarding hydrogen production over $\text{Y}_{1.867}\text{Ti}_2\text{O}_{6.80}$ (Ti/Y ratio of 1.075) doped with 0.10, 0.25, 0.50 or 1.00 mol-% of Cr^{3+} . The data for the undoped sample is included as well. 119

- Figure 69: Photocatalytic activity regarding hydrogen production over $Y_{1.867}Ti_2O_{6.80}$ (Ti/Y ratio of 1.075) doped with 0.10, 0.25, 0.50 or 1.00 mol-% of Cr^{3+} . The data for the undoped sample is included as well. 120
- Figure 70: XRD pattern of $Y_{1.867}Ti_2O_{6.80}$, $Y_{1.867}Ti_{1.6}Ta_{0.4}O_7$ and $Y_{1.867}Ti_{1.8}W_{0.2}O_7$ featuring (Ti+Ta+W)/Y ratios of 1.075. Annealing was performed at 1023 K for 4h. 122
- Figure 71: XRD pattern of $Y_{1.867}Ti_{1.6}Ta_{0.4}O_7$ (part (a)) and $Y_{1.867}Ti_{1.8}W_{0.2}O_7$ (part (b)) featuring (Ti+Ta+W)/Y ratios of 1.075 and annealed at 1023 K, 1273 K and 1323 K for 4h. 124
- Figure 72: Tauc-plots (for indirect band gap transition) calculated from the UV-vis diffuse reflectance spectra of $Y_{1.867}Ti_2O_{6.80}$, $Y_{1.867}Ti_{1.6}Ta_{0.4}O_7$ and $Y_{1.867}Ti_{1.8}W_{0.2}O_7$ annealed at 1023 K for 4h and featuring (Ti+Ta+W)/Y ratios of 1.075. 125
- Figure 73: Tauc-plots (for indirect band gap transition) calculated from the UV-vis diffuse reflectance spectra of $Y_{1.867}Ti_2O_{6.80}$, $Y_{1.867}Ti_{1.6}Ta_{0.4}O_7$ and $Y_{1.867}Ti_{1.8}W_{0.2}O_7$ annealed at 1173 K and 1323 K for 4h and featuring (Ti+Ta+W)/Y ratios of 1.075. 126
- Figure 74: Photocatalytic activity regarding hydrogen production over $Y_{1.867}Ti_{1.6}Ta_{0.4}O_7$ and $Y_{1.867}Ti_{1.8}W_{0.2}O_7$ featuring a (Ti+W+Ta)/Y ratio of 1.075 as function of the annealing temperature (1023 K, 1173 K and 1323 K). The samples were loaded with 0.75 wt.-% of platinum by in-situ photodeposition. 127
- Figure 75: X-ray diffraction data of the monoclinic M' - $YTaO_4$ phase (a), the pyrochlore " $Y_2Ta_2O_5N_2$ " contaminated with Ta_3N_5 (b), and pure Ta_3N_5 obtained by ammonolysis of commercial Ta_2O_5 (c). 130
- Figure 76: Tauc-plots (for indirect band gap transition) calculated from the UV-vis diffuse reflectance spectra of pyrochlore " $Y_2Ta_2O_5N_2$ " contaminated with Ta_3N_5 , and pure Ta_3N_5 obtained by ammonolysis of commercial Ta_2O_5 . 131

- Figure A1: Photocatalytic activity regarding hydrogen production over $Y_2Ti_2O_7$ calcined at 1023 K for 4h with 0.75 wt.-% rhodium as co-catalyst. 147
- Figure A2: Photocatalytic activity regarding hydrogen production over $Y_2Ti_2O_7$ calcined at 1173 K for 4h with 0.75 wt.-% rhodium as co-catalyst. 147
- Figure A3: X-ray diffraction data of $YBiTi_2O_7$ annealed at 873 K for 4h (part A) and $Y_{1.5}Bi_{0.5}Ti_2O_7$ annealed at 1023 K for 4h (part B) and 1173 K for 4h (part C). 148
- Figure A4: TEM micrograph in dark field mode (a) and EDXS analysis of $(YBi)_{0.77}Ti_2O_{6.31} Ti/(Y+Bi) 1.30$ annealed at 873 K for 4h and loaded with 3.0 wt.-% of platinum. 149
- Figure A5: Photocatalytic activity regarding hydrogen production over $(Y_{1.5}Bi_{0.5})_{1-x}Ti_2O_{7-3x}$ calcined at 1173 K for 4h with 0.75 wt.-% platinum as co-catalysts. 149
- Figure A6: Photocatalytic activity regarding hydrogen production over $(Y_{1.5}Bi_{0.5})_{1-x}Ti_2O_{7-3x}$ calcined at 1023 K for 4h with 0.75 wt.-% rhodium as co-catalyst. 150
- Figure A7: Photocatalytic activity regarding hydrogen production over $(Y_{1.5}Bi_{0.5})_{1-x}Ti_2O_{7-3x}$ calcined at 1173 K for 4h with 0.75 wt.-% rhodium as co-catalyst. 150
- Figure A8: Photocatalytic activity regarding hydrogen production over $(YBi)_{1-x}Ti_2O_{7-3x}$ calcined at 1023 K for 4h with 2.00 wt.-% platinum as co-catalyst. 151
- Figure A9: X-ray diffraction data of the sample featuring a Ti/Bi ratio of 2.00 as a function of the annealing temperature. 152
- Figure A10: X-ray diffraction data of the sample featuring a Ti/Bi ratio of 1.00 as a function of the annealing temperature. 153
- Figure A11: Rietveld refinement of the bismuth titanate sample featuring a stoichiometric Ti/Bi ratio of 1.00 annealed at 773 K for 4 hours. 153
- Figure A12: Rietveld refinement of $(Bi_{2-x}Ti_{0.75x})Ti_2O_7$ featuring a Ti/Bi ratio of 1.20 annealed at 773 K for 4 hours. 154
- Figure A13: Rietveld refinement of $(Bi_{2-x}Ti_{0.75x})Ti_2O_7$ featuring a Ti/Bi ratio of 1.30 annealed at 773 K for 4 hours. 155
- Figure A14: Rietveld refinement of $(Bi_{2-x}Ti_{0.75x})Ti_2O_7$ featuring a Ti/Bi ratio of 1.40 annealed at 773 K for 4 hours. 156

- Figure A15: Photocatalytic activity regarding hydrogen production over $(\text{Bi}_{1.55}\text{Ti}_{0.33})\text{Ti}_2\text{O}_7$ annealed at 773 K loaded with 3.0 wt.-% of platinum as co-catalyst as a function of the annealing time. 156
- Figure A16: Photocatalytic activity regarding hydrogen production over $(\text{Bi}_{2-x}\text{Ti}_{0.75x})\text{Ti}_2\text{O}_7$ calcined at 873 K for 4 hours with 3.0 wt.-% of platinum as co-catalyst. 157
- Figure A17: XRD pattern of $\text{Y}_{1.867}\text{Ti}_2\text{O}_{6.80}$ doped with 0.10, 0.25, 0.50 and 1.00 mol-% of Cr^{3+} . Additionally, the undoped sample is included. Annealing was performed at 1023 K for 4h and all samples feature a Ti/Y ratio of 1.075. 157

7.4 Tables

- Table 1: Changes in the crystallographic coordinates of Y^{3+} , Ti^{4+} and O^{2-} in a hypothetical phase transition of $\text{Y}_2\text{Ti}_2\text{O}_7$ from the pyrochlore structure into the parental defect fluorite structure. 16
- Table 2: Summary of the crystal information file of $\text{Y}_2\text{Ti}_2\text{O}_7$. 35
- Table 3: Synthesis of $\text{Y}_2\text{Ti}_2\text{O}_7$ (Ti/Y ratio of 1.00). 41
- Table 4: Synthesis of $\text{Y}_{1.5}\text{Bi}_{0.5}\text{Ti}_2\text{O}_7$ (Ti/(Y+Bi) ratio of 1.00). 43
- Table 5: Synthesis of YBiTi_2O_7 (Ti/(Y+Bi) ratio of 1.00). 44
- Table 6: Synthesis of $\text{Bi}_2\text{Ti}_2\text{O}_7$ (Ti/Bi ratio of 1.00). 45
- Table 7: Synthesis of $\text{Y}_{1.86}\text{Ti}_2\text{O}_{6.80}$ (Ti/Y ratio of 1.075) doped with Cr^{3+} , $\text{Mn}^{2+,3+}$, Fe^{3+} . 47
- Table 8: Synthesis of $\text{Y}_{1.86}\text{Ti}_{1.6}\text{Ta}_{0.4}\text{O}_7$ and $\text{Y}_{1.86}\text{Ti}_{1.8}\text{W}_{0.2}\text{O}_7$ ((Ti+Ta+W)/Y ratio of 1.075). 48
- Table 9: Synthesis of $\text{M}^- \text{-YTaO}_4$. 49
- Table 10: Structure models for the Rietveld refinement of the “ $\text{Bi}_2\text{Ti}_2\text{O}_7$ ” series annealed at 773 K. 95
- Table 11: Results of the Rietveld refinement for structures 1-4 each describing a slightly different structure of “ $\text{Bi}_2\text{Ti}_2\text{O}_7$ ” by systematically combining non-stoichiometry, atomistic distortion of bismuth and O` oxygen, and different vacancy distributions. 98

Table 12: Summary of the lattice parameters, the average crystallite sizes, the optical band edge energies and photocatalytic activities regarding hydrogen production of 0.25 mol-% Cr^{3+} , Mn^{3+} and Fe^{3+} doped $\text{Y}_{1.867}\text{Ti}_2\text{O}_{6.80}$ (Ti/Y ratio of 1.075).	117
Table 13: Summary of the lattice parameters, the average crystallite sizes, the optical band edge energies and photocatalytic activities regarding hydrogen production of $\text{Y}_{1.867}\text{Ti}_2\text{O}_{6.80}$ (Ti/Y ratio of 1.075) samples doped with 0.10, 0.25, 0.50 and 1.00 mol-% of Cr^{3+} .	121
Table 14: Summary of the lattice parameters, the I(400)/I(331) ratios, the average crystallite sizes, the band gap energies and the photocatalytic activities regarding hydrogen production of samples of $\text{Y}_{1.867}\text{Ti}_{1.6}\text{Ta}_{0.4}\text{O}_7$ and $\text{Y}_{1.867}\text{Ti}_{1.8}\text{W}_{0.2}\text{O}_7$ ((Ti+Ta+W)/Y ratio of 1.075) annealed at temperatures of 1023 K, 1173 K and 1323 K for 4 hours, respectively.	128
Table 15: Summary of the band gap energies, the BET surface areas, the average crystallite sizes and the photocatalytic activities regarding hydrogen production of M^-YTao_4 , Ta_3N_5 and $\text{Y}_2(\text{Ta}_{2-x}\text{Y}_x)\text{O}_{4.85-x}\text{N}_{2.10}$.	132
Table A1: Needed volumes of platinum and rhodium precursor solutions.	158
Table A2: Needed volumes of platinum, rhodium and chromium precursor solutions.	158
Table A3: Synthesis of $\text{Y}_2(\text{Y}_{0.05}\text{Ti}_{1.95})\text{O}_{6.97}$ (Ti/Y ratio of 0.95).	158
Table A4: Synthesis of $\text{Y}_{1.90}\text{Ti}_2\text{O}_{6.86}$ (Ti/Y ratio of 1.05).	158
Table A5: Synthesis of $\text{Y}_{1.86}\text{Ti}_2\text{O}_{6.80}$ (Ti/Y ratio of 1.075).	159
Table A6: Synthesis of $\text{Y}_{1.82}\text{Ti}_2\text{O}_{6.73}$ (Ti/Y ratio of 1.10).	159
Table A7: Synthesis of $\text{Y}_{1.74}\text{Ti}_2\text{O}_{6.61}$ (Ti/Y ratio of 1.15).	159
Table A8: Synthesis of $(\text{Y}_{1.49}\text{Bi}_{0.51})(\text{Y}_{0.05}\text{Ti}_{1.95})\text{O}_{6.97}$ (Ti/(Y+Bi) ratio of 0.95).	159
Table A9: Synthesis of $\text{Y}_{1.43}\text{Bi}_{0.48}\text{Ti}_2\text{O}_{6.86}$ (Ti/(Y+Bi) ratio of 1.05).	160
Table A10: Synthesis of $\text{Y}_{1.36}\text{Bi}_{0.45}\text{Ti}_2\text{O}_{6.73}$ (Ti/(Y+Bi) ratio of 1.10).	160
Table A11: Synthesis of $\text{Y}_{1.30}\text{Bi}_{0.43}\text{Ti}_2\text{O}_{6.61}$ (Ti/(Y+Bi) ratio of 1.15).	160
Table A12: Synthesis of $\text{Y}_{1.25}\text{Bi}_{0.42}\text{Ti}_2\text{O}_{6.50}$ (Ti/(Y+Bi) ratio of 1.20).	160
Table A13: Synthesis of $\text{Y}_{0.91}\text{Bi}_{0.91}\text{Ti}_2\text{O}_{6.73}$ (Ti/(Y+Bi) ratio of 1.10).	161
Table A14: Synthesis of $\text{Y}_{0.87}\text{Bi}_{0.87}\text{Ti}_2\text{O}_{6.61}$ (Ti/(Y+Bi) ratio of 1.15).	161
Table A15: Synthesis of $\text{Y}_{0.83}\text{Bi}_{0.83}\text{Ti}_2\text{O}_{6.50}$ (Ti/(Y+Bi) ratio of 1.20).	161
Table A16: Synthesis of $\text{Y}_{0.80}\text{Bi}_{0.80}\text{Ti}_2\text{O}_{6.40}$ (Ti/(Y+Bi) ratio of 1.25).	161

Table A17: Synthesis of $Y_{0.77}Bi_{0.77}Ti_2O_{6.31}$ (Ti/(Y+Bi) ratio of 1.30).	162
Table A18: Synthesis of $(Bi_{1.79}Ti_{0.15})Ti_2O_7$ (Ti/Bi ratio of 1.20).	162
Table A19: Synthesis of $(Bi_{1.75}Ti_{0.19})Ti_2O_7$ (Ti/Bi ratio of 1.25).	162
Table A20: Synthesis of $(Bi_{1.71}Ti_{0.22})Ti_2O_7$ (Ti/Bi ratio of 1.30).	162
Table A21: Synthesis of $(Bi_{1.67}Ti_{0.25})Ti_2O_7$ (Ti/Bi ratio of 1.35).	163
Table A22: Synthesis of $(Bi_{1.63}Ti_{0.28})Ti_2O_7$ (Ti/Bi ratio of 1.40).	163
Table A23: Synthesis of $(Bi_{1.59}Ti_{0.31})Ti_2O_7$ (Ti/Bi ratio of 1.45).	163
Table A24: Synthesis of $(Bi_{1.55}Ti_{0.33})Ti_2O_7$ (Ti/Bi ratio of 1.50).	163
Table A25: Synthesis of $Bi_4Ti_3O_{12}$ (Ti/Bi ratio of 0.75).	164
Table A26: Synthesis of $Bi_2Ti_4O_{11}$ (Ti/Bi ratio of 2.00).	164
Table A27: Occupancies of bismuth, titanium and oxygen on different Wyckoff positions for a predicted structure of non-stoichiometric $Bi_{2-x}Ti_2O_{7-1.5x}$ corresponding to structure suggestion 2.	164
Table A28: Occupancies of bismuth, titanium and oxygen on different Wyckoff positions for a predicted structure of non-stoichiometric $Bi_{2-x}Ti_2O_{7-1.5x}$ corresponding to structure suggestion 3.	164
Table A29: Occupancies of bismuth, titanium and oxygen on different Wyckoff positions for a predicted structure of non-stoichiometric $(Bi_{2-x}Ti_{0.75x})Ti_2O_7$ corresponding to structure suggestion 4.	165

7.5 Scientific publications

7.5.1 Journal publications

O. Merka, V. Yarovy, D. W. Bahnemann, M. Wark

“pH-Control of the Photocatalytic Degradation Mechanism of Rhodamine B over $\text{Pb}_3\text{Nb}_4\text{O}_{13}$ ”

J. Phys. Chem. C **2011**, *115*, 8014-8023.

O. Merka, D. W. Bahnemann, M. Wark

“Improved Photocatalytic Hydrogen Production by Structure Optimized Non-Stoichiometric $\text{Y}_2\text{Ti}_2\text{O}_7$ ”

ChemCatChem **2012**, DOI: 10.1002/cctc.201200148.

O. Merka, O. Raisch, D. W. Bahnemann, M. Wark

“Effects of Non-Stoichiometry and Co-catalyst Loading on the Photocatalytic Hydrogen Production with $(\text{Y}_{1.5}\text{Bi}_{0.5})_{1-x}\text{Ti}_2\text{O}_{7-3x}$ and $(\text{YBi})_{1-x}\text{Ti}_2\text{O}_{7-3x}$ Pyrochlores”

J. Am. Ceram. Soc. **2012**, DOI: 10.1111/jace.12013.

O. Merka, D. W. Bahnemann, M. Wark

“Photocatalytic Hydrogen Production with non-stoichiometric Pyrochlore $(\text{Bi}_{2-x}\text{Ti}_{0.75x})\text{Ti}_2\text{O}_7$, $\text{Bi}_4\text{Ti}_3\text{O}_{12}$ and $\text{Bi}_2\text{Ti}_4\text{O}_{11}$ ”

ACS Catalysis **2012**, submitted.

7.5.2 Talks on conferences

O. Merka, M. Wark

“Rh Photodeposition on Yttrium depleted and Bismuth doped Yttrium Titanate for Photocatalytic Hydrogen Production”

The 16th International Conference on TiO₂ Photocatalysis: Fundamentals and Applications (TiO₂-16), 07.11.2011 - 10.11.2011, San Diego, United States of America.

O. Merka, V. Yarovy, D. W. Bahnemann, M. Wark

“Stoichiometry-optimized Pyrochlores of Y₂Ti₂O₇ and Y_{1.5}Bi_{0.5}Ti₂O₇ for Photocatalytic Hydrogen Production”

Festkörperseminar des Instituts für Technische Chemie an der Ruhr-Universität Bochum, 28.11.2011, Bochum, Germany.

O. Merka, O. Raisch, D. W. Bahnemann, M. Wark

“Improved Photocatalytic Hydrogen Production by Structure optimized non-stoichiometric Yttrium Bismuth Titanate Pyrochlores”

7th European Meeting on Solar Chemistry and Photocatalysis: Environmental Applications (SPEA 7), 18.06.2012 - 20.06.2012, Porto, Portugal.

7.5.3 Posters on conferences

O. Merka, V. Yarovy, D. W. Bahnemann, M. Wark

“pH-Control of the Photocatalytic Degradation Mechanism of Rhodamine B over Silica Aerosil supported Pb₃Nb₄O₁₃”

6th European Meeting on Solar Chemistry and Photocatalysis: Environmental Applications (SPEA 6), 14.06.2010 - 18.06.2010, Prague, Czech Republic.

O. Merka, V. Yarovy, M. Wark

“Rh photodeposition on yttrium and bismuth titanate for photocatalytic hydrogen production”

44. Jahrestreffen Deutscher Katalytiker und Jahrestreffen Reaktionstechnik, 16.03.2011 - 18.03.2011, Weimar, Germany.

O. Merka, V. Yarovy, M. Wark

“Rh Photodeposition on Yttrium depleted and Bismuth doped Yttrium Titanate for Photocatalytic Hydrogen Production”

International Conference on Photocatalytic and Advanced Oxidation Technologies for the Treatment of Water, Air, Soil and Surfaces (PAOT 2011), 04.07.2011 - 08.07.2011, Gdańsk, Poland.

O. Merka, V. Yarovy, R. Marschall, M. Wark

“Photocatalytic Hydrogen Production with Yttrium depleted and Bismuth doped Yttrium Titanate”

9th International Meeting of Pacific Rim Ceramic Societies (PACRIM 9), 10.07.2011 - 14.07.2011, Cairns, Australia.

O. Merka, A.-C. Möller, M. Wark

“Non-stoichiometric Bismuth doped Yttrium Titanate and Yttrium Tantalum Oxynitride for Photocatalytic Hydrogen Production”

Bunsen International Discussion meeting “Photocatalysis”, 13.10.2011 - 14.10.2011, Heidelberg, Germany.

O. Merka, V. Yarovy, M. Wark

“Improved Photocatalytic Hydrogen Production by Structure optimized non-stoichiometric $Y_2Ti_2O_7$ ”

45. Jahrestreffen Deutscher Katalytiker, 14.03.2012 - 16.03.2012, Weimar, Germany

O. Merka, O. Raisch, D. W. Bahnemann, M. Wark

“Improved Photocatalytic Hydrogen Production by Structure optimized non-stoichiometric Yttrium Bismuth Titanate Pyrochlores”

7th European Meeting on Solar Chemistry and Photocatalysis: Environmental Applications (SPEA 7), 18.06.2012 - 20.06.2012, Porto, Portugal.

7.6 Curriculum vitae

Personal data

Name: Oliver Merka
Date of birth: 01. März 1983
Place of birth: Alfeld (Leine)
Family status: single

School education

09/1989 – 06/1993 Grundschule Delligsen, Germany
09/1993 – 06/1995 Orientierungsstufe Duingen, Germany
09/1995 – 06/2002 Abitur (general qualification for university entrance) at the
Gymnasium Alfeld (Leine), Germany

Civilian service

08/2002 – 05/2003 Employee in the internal patient transport at the
Universitätsklinikum in Göttingen, Germany

University education

10/2003 – 01/2009 Student of chemistry (diploma) at the Leibniz University of
Hannover, Germany
Diploma thesis at the Institut für Physikalische Chemie und
Elektrochemie on: “Synthese von Bleiniobaten und ihre
Anwendung in der Photokatalyse“
02/2009 – 10/2012 PhD student at the Institut für Physikalische Chemie und
Elektrochemie at the Leibniz University of Hannover, Germany
PhD thesis on: “Photocatalytic hydrogen production with
pyrochlore mixed oxides“